



UNIVERSITE DE REIMS CHAMPAGNE - ARDENNE
ECOLE DOCTORALE SCIENCES TECHNOLOGIE SANTE



AKADEMIA GÓRNICZO - HUTNICZA
WYDZIAŁ METALI NIEŻELAZNYCH

A thesis submitted in fulfillment of the requirements for the degree of

**DOCTOR OF THE UNIVERSITY OF REIMS CHAMPAGNE-ARDENNE
AND THE UNIVERSITY OF SCIENCE AND TECHNOLOGY**

Discipline : Material Science and Engineering

presented and publicly defended by

Agnieszka FRAN CZAK

Subject :

Experimental and theoretical studies of the electrodeposition mechanism of Co-based films: modeling and structure-properties relationship by a multi-scale approach

Reims, 26th September 2013

Jury Members :

Ivan SKORVANEK	Professeur (Slovak Academy of Sciences, Slovaquie)	Président de Jury
Qiang WANG	Professeur (Northeastern University, Chine)	Rapporteur
Wanda GUMOWSKA	Professeur (AGH Academy of Science and Technology, Pologne)	Rapporteuse
Marco COISSON	Maitre de Conférences (INRIM, Italy)	Examineur
Frédéric BOHR	Professeur (Université de Reims Champagne-Ardenne, France)	Directeur
Krzysztof FITZNER	Professeur (AGH Academy of Science and Technology, Pologne)	Directeur
Alexandra LEVESQUE	Maitre de Conférences HDR (Université de Reims Champagne-Ardenne, France)	Co-Directrice
Piotr ZABINSKI	Maitre de Conférences (AGH University of Science and Technology, Pologne)	Co-Directeur



UNIVERSITE DE REIMS CHAMPAGNE - ARDENNE
ECOLE DOCTORALE SCIENCES TECHNOLOGIE SANTE



AKADEMIA GÓRNICZO - HUTNICZA
WYDZIAŁ METALI NIEŻELAZNYCH

THESE

pour obtenir le grade de

**DOCTEUR DE L'UNIVERSITE DE REIMS CHAMPAGNE-ARDENNE
ET AKADEMII GÓRNICZO-HUTNICZEJ**

Discipline : Ingénierie et Sciences des Matériaux

présentée et soutenue publiquement par

Agnieszka FRAN CZAK

Titre :

Etude expérimentale et théorique du mécanisme de l'électrodéposition de films à base de cobalt : modélisation et relation structure-propriétés par approche multi-échelle

le 26 Septembre 2013, à Reims

Membres du Jury :

Ivan SKORVANEK	Professeur (Slovak Academy of Sciences, Slovaquie)	Président de Jury
Qiang WANG	Professeur (Northeastern University, Chine)	Rapporteur
Wanda GUMOWSKA	Professeur (AGH Academy of Science and Technology, Pologne)	Rapporteuse
Marco COISSON	Maitre de Conférences (INRIM, Italy)	Examineur
Frédéric BOHR	Professeur (Université de Reims Champagne-Ardenne, France)	Directeur
Krzysztof FITZNER	Professeur (AGH Academy of Science and Technology, Pologne)	Directeur
Alexandra LEVESQUE	Maitre de Conférences HDR (Université de Reims Champagne-Ardenne, France)	Co-Directrice
Piotr ZABINSKI	Maitre de Conférences (AGH University of Science and Technology, Pologne)	Co-Directeur

Résumé

Cette étude porte sur les études expérimentales et théoriques du mécanisme d'électrodéposition de différents revêtements à base de cobalt : le cobalt métallique, les alliages binaires Co-Ni, Co-Cu et l'alliage ternaire Co-Ni-Cu. L'étude de la relation procédé-structure-propriétés est réalisée par une approche multi-échelle.

Ce travail s'articule autour de 5 chapitres. Le premier chapitre résume les différents sujets abordés dans ce travail, en particulier les bases de l'électrodéposition, une revue bibliographique des films base cobalt électrodéposés notamment en présence d'un champ magnétique. Les deuxième et troisième chapitres présentent les différents résultats expérimentaux concernant respectivement l'électrodéposition et les propriétés magnétiques des films obtenus. Enfin, le dernier chapitre concerne une approche théorique basée sur des calculs DFT (Théorie de la Fonctionnelle de la Densité) en vue d'apporter des nouveaux éléments pour la compréhension des phénomènes mis en jeu à l'électrode lors de l'application d'un champ magnétique.

Une étude préliminaire a permis la détermination et l'optimisation des paramètres d'électrodéposition afin d'obtenir des films nanocristallins. La qualité et les propriétés de ces films dépendent fortement des paramètres expérimentaux tels que le pH de l'électrolyte, la nature du substrat ou encore le temps de dépôt.

Dans cette étude, deux valeurs de pH sont considérées respectivement égales à 2,7 et 4,7. La nature des phases cristallographiques formées, la composition de phase et la morphologie des films Co et alliages Co-Ni sont fortement influencées par le pH de l'électrolyte. Pour les deux valeurs de pH, les films électrodéposés sont constitués d'un mélange des deux phases cristallographiques du cobalt: la structure hexagonale (hcp : hexagonal close packed) et la structure cubique centrée (fcc : face centered cubic). En fonction du pH, les intensités des pics de diffraction varient. Les différences observées au niveau de la composition de phase et de la morphologie des films sont expliquées notamment par la réaction de dégagement d'hydrogène et l'évolution des espèces intermédiaires adsorbées, tels que les hydroxydes de cobalt et de nickel à la surface de la cathode.

L'élaboration des films de Co et Co-Ni a été réalisée sur différents substrats tels que le titane ou des substrats de verre recouverts par un dépôt d'oxyde d'indium dopé à l'étain (ITO). Pour

ce dernier, une couche de nickel est électrodéposée avant le dépôt des films base cobalt afin de garantir leur bonne adhérence. Les études microstructurales montrent que le type de substrat affecte la composition de phase des dépôts du métal pur Co et alliages Co-Ni. Les films de Co et films Co-Ni sur Ti sont caractérisés par un mélange biphasique : structure hexagonale (hcp) et cubique faces centrées (fcc). Les films de Co déposés sur substrat Ni / ITO ne possèdent que la structure hcp, tandis que dans le cas des films de Co-Ni, la phase prédominante est la structure cubique. Les différences de composition de phase sont confirmées par l'étude morphologique menée par microscopie électronique à balayage qui permet de visualiser la présence de cristallites dont la forme caractéristique est associée à la structure hexagonale dans certains dépôts. De façon générale, dans le cas de l'utilisation des substrats de verre, la qualité de la surface des films est améliorée. En effet, les films sont en apparence plus homogènes et moins rugueux.

Enfin, différents temps d'électrodéposition sont testés afin d'évaluer leur effet sur la morphologie des dépôts. La diminution du temps de dépôt entraîne une réduction de la taille des cristallites et est donc favorable à la réalisation de films nanocristallins.

Les propriétés d'un dépôt peuvent être fortement affectées par l'application d'un champ magnétique externe sur la cellule d'électrolyse. Dans ce travail, un champ magnétique est superposé parallèlement à la surface de l'électrode de travail avec des amplitudes de champ pouvant aller jusqu'à 12T. Dans ces conditions, la convection induite par la force de Lorentz dans l'électrolyte, que l'on appelle effet MHD (Magneto Hydro Dynamique), peut modifier différents paramètres expérimentaux de l'électrolyse à la surface de l'électrode (pH, espèces adsorbées...) et donc influencer sur la structure et la morphologie des films obtenus. D'une façon générale, les effets du champ magnétique sur la composition de phase ne sont pas significatifs sauf dans le cas des dépôts d'alliage Co-Ni sur des substrats de titane. En effet dans ce dernier cas, la composition de phase des alliages CoNi déposés sur titane évolue différemment en fonction du champ magnétique B_{el} appliqué durant l'électrolyse comparativement aux dépôts réalisés sur substrat de verre recouvert d'ITO où le substrat impose une autre structure cristallographique. L'orientation cristallographique (220) de la phase CoNi est favorisée par B_{el} . Classiquement, de nombreux paramètres expérimentaux liés au procédé d'électrolyse influent sur la structure cristallographique et la morphologie des dépôts du matériau obtenu: composition du bain, température du bain, le courant d'électrolyse

ou encore le pH. Dans ce cas précis, l'application d'un champ magnétique parallèle à l'électrode va jouer le même rôle qu'une diminution de pH dans le bain sur la structure cristallographique. L'application d'un champ magnétique parallèle à l'électrode pour laquelle la force de Lorentz est maximale, conduit à une forte agitation MHD de l'électrolyte qui peut être responsable des effets observés. Toutefois, même si les effets du champ magnétique sur la composition de phase ne sont pas significatifs sur les autres systèmes Co sur Ti, Co et Co-Ni sur Ni/ITO, l'intensité relative des pics de diffraction de rayons X est légèrement affectée par le champ magnétique.

L'effet du champ magnétique appliqué durant l'électrolyse affecte d'autres propriétés des dépôts. D'une part, la taille des cristallites et la rugosité de surface des dépôts sont affectés, conduisant ainsi à l'obtention de surfaces plus homogènes. Cet effet classique est souvent attribué dans la littérature à l'effet d'agitation de l'électrolyte lié à l'effet convectif MHD. Dans ce cas, l'épaisseur de la couche de diffusion est réduite, ce qui améliore le transport de masse vers la surface de l'électrode et donc dans le même temps permet la désorption de bulles de gaz à la surface de l'électrode de travail. La conséquence est alors l'obtention de films base-Co avec des états de surface plus homogènes.

D'autre part, lors de l'élaboration des alliages Co-Ni et Co-Cu, le processus de codéposition anormale caractérisé par un plus grand rapport atomique Co/Ni dans les films que d'ions $\text{Co}^{2+} / \text{Ni}^{2+}$ dans la solution électrolytique est observé. Ce processus est également légèrement affecté par le champ magnétique. En particulier, dans le cas des alliages Co-Cu, la quantité de cuivre dans les dépôts augmente considérablement avec l'amplitude du champ magnétique. Une approche par une étude électrochimique (cinétique et dynamique) est réalisée sur les systèmes Co, Co-Ni et Co-Cu afin de mieux comprendre les actions du champ magnétique. Dans le cas de l'étude cinétique, les investigations sont basées sur des mesures chronoampérométriques, où le régime transitoire courant-temps du système Co est étudié et le mode de nucléation est évalué. Les résultats montrent que le processus de nucléation est relativement proche du mécanisme instantané, mais avec un écart non négligeable par rapport au modèle théorique ce qui peut s'expliquer par la réduction de l'hydrogène. Les différences observées en présence d'un champ magnétique dans le cas du système Co et Co-Ni sont dues à la variation des conditions hydrodynamiques dans l'électrolyte induites par celui-ci. Dans le cas de l'étude par spectroscopie d'impédance électrochimique sur le système Co-Cu, il est montré qu'un champ magnétique homogène ne modifie pratiquement pas les paramètres de transfert de charge du processus. Les faibles effets observés en présence du champ

magnétique ne sont dus qu'à la variation de la surface de l'électrode au cours de l'électrodéposition métallique et à l'effet de la convection MHD.

Les phénomènes observés lors de l'application d'un champ parallèle à l'électrode sur une cellule d'électrolyse tels que la variation de la forme des grains, les changements de rugosité ou encore les modifications de phase cristallographique résultent principalement de l'effet magnétohydrodynamique (MHD) induit par la force de Lorentz et éventuellement d'un autre champ de force : la force magnétique, qui ne dépend pas de la densité de courant et n'agit sur les particules qu'à travers leurs susceptibilités magnétiques. L'effet MHD augmente le transfert de masse des ions dans la solution et agit sur les espèces adsorbées à la surface. Ces espèces adsorbées peuvent empêcher la diffusion en surface des atomes et conduire à des surfaces plus lisses. Les morphologies des couches sont alors gouvernées par la compétition entre phénomènes de diffusion en surface déterminée par les paramètres électrochimiques expérimentaux tels que la densité de courant et les vitesses de croissance des espèces adsorbées. La croissance de différents plans cristallographiques en fonction du champ magnétique B peut être notamment une conséquence de l'adsorption compétitive entre l'hydrogène et les espèces intermédiaires. Les hypothèses émises dans cette étude concernant principalement l'effet MHD et ses conséquences sur l'évolution du pH et la nature des espèces adsorbées à la surface de l'électrode sont confrontées dans le dernier chapitre aux calculs de l'énergie d'adsorption de l'atome d'hydrogène et de l'ion H^+ sur différentes faces cristallographique du cobalt obtenue par la modélisation DFT.

Le troisième chapitre est consacré à l'étude de la réponse magnétique des différents systèmes élaborés Co/Ni/ITO, Co-Ni/ITO, Co-Cu/Cu/ITO et Co-Ni-Cu/Cu/ITO. Les mesures sont réalisées par les techniques de magnétométrie à échantillon vibrant (VSM) et microscopie à force magnétique (MFM). Avant d'être testés, les échantillons sont traités thermiquement. Dans le cadre du projet ANR COMAGNET, ces traitements thermiques sont aussi menés en présence d'un champ magnétique. De façon générale, le traitement permet l'obtention de dépôts mieux cristallisés et une modification de la morphologie des dépôts avec ou sans champ magnétique. Dans le cas de bicouches Co/Ni/ITO, il est montré que l'application d'un champ magnétique pendant le recuit permet une augmentation des coefficients d'interdiffusion. Cette zone d'interdiffusion à l'interface Co/Ni va affecter la réponse magnétique du système. En effet, les mesures par microscopie à force magnétique

montrent l'apparition d'une légère anisotropie perpendiculaire lorsque le traitement thermique est réalisé sous un champ magnétique.

Dans le cadre de l'étude du système CoNi/ITO, les caractérisations par microscopie à force atomique AFM mettent en évidence une augmentation de la taille des grains et de la rugosité jusqu'à une amplitude de 9T puis une diminution jusqu'à 12T. Le champ magnétique induit dans un même temps une augmentation du taux de Co dans les alliages. L'influence du couplage des procédés d'électrolyse et de traitement thermique sous champ magnétique intense est ensuite montrée. D'un point de vue cristallographique, ces alliages CoNi de structure cubique présentent une légère orientation préférentielle (111) lorsqu'un champ magnétique est appliqué durant l'électrodéposition (B_{el}). Cette orientation reste stable quelque soit l'amplitude du champ magnétique appliqué B_{el} . Des recuits sont ensuite réalisés à une température de 473 K sous flux d'argon et champ magnétique B_{HT} ($0T < B_{HT} < 12 T$). Lorsque les alliages sont recuits, l'orientation préférentielle est favorisée quelque soit le champ magnétique appliqué B_{HT} durant le traitement thermique. Après traitement thermique, le matériau garde en quelque sorte « la mémoire du champ appliqué B_{el} durant l'électrolyse ». En effet, lorsque l'amplitude du champ magnétique appliqué durant l'électrodéposition croît, l'orientation préférentielle (111) de l'alliage CoNi augmente proportionnellement dans les alliages recuits. L'application d'un champ magnétique durant l'électrolyse favorise une augmentation de la coercivité alors que le champ magnétique B_{HT} appliqué durant le traitement thermique induit une diminution de celle-ci.

L'application d'un champ magnétique durant l'électrodéposition affecte les propriétés magnétiques des systèmes Co-Cu/Cu/ITO et Co-Ni-Cu/Cu/ITO. D'une part, les mesures magnétiques révèlent que les propriétés magnétiques des films dépendent fortement de la composition chimique du film, en effet, la quantité de cuivre augmente dans les films en fonction de l'amplitude du champ magnétique B_{el} appliqué. D'autre part, les changements morphologiques et structuraux observés, notamment l'augmentation du ratio surface / volume du dépôt permet de modifier l'anisotropie de forme.

La dernière partie de ce manuscrit concerne l'approche théorique. Des calculs DFT (Théorie de la Fonctionnelle de la Densité) avec trois fonctionnelles différentes ont été effectués pour examiner l'énergie d'adsorption de l'atome d'hydrogène et de l'ion H^+ sur des surfaces de cobalt représentées par différents indices : système cubique – (100), (110), (111), (220) et

système hexagonal – (100), (110), (101), (011). Les sites d'adsorption préférentiels ont aussi été déterminés. Pour toutes les surfaces de cobalt, les résultats DFT montrent que l'hydrogène se lie préférentiellement aux sites correspondant à la plus grande coordination, qui est ici un site ponté. Cependant, dans le cas du cobalt cubique, l'adsorption sur un site triplement coordonné est également observée. Suivant l'orientation de la surface, le site d'adsorption et la fonctionnelle utilisée, les énergies d'adsorption de l'atome ou de l'ion varient légèrement. Parmi toutes les surfaces de cobalt examinées (fcc et hcp), les énergies d'adsorption obtenues montrent des tendances pour les plans plus ou moins favorables à l'adsorption, en fonction de la fonctionnelle choisie. L'étude DFT de l'adsorption de l'hydrogène est donc une aide pour comprendre la formation des phases dans le film de cobalt en cours de croissance à un faible pH (2,7), pour lequel un film biphasique est obtenu. Le calcul de l'énergie d'adsorption montre que l'adsorption de l'hydrogène est la plus favorable sur la surface (220) du cobalt cubique, ce qui peut ensuite conduire à la formation d'hydrure de cobalt. On peut donc estimer que la fraction volumique de la phase fcc dans les dépôts de cobalt est plus grande que celle de la phase hcp. D'autre part, la croissance dans la direction fcc-(220) est supprimée et la croissance selon d'autres plans du cobalt est observée, comme par exemple hcp-(110). Pour un pH plus grand (4,7), la formation des phases dépend plutôt de la formation et de l'adsorption d'hydroxydes sur les surfaces de cobalt, et non plus d'un hydrogène seul. Pour confirmer cette observation, des calculs quantiques complémentaires sont nécessaires pour examiner l'adsorption des hydroxydes.

Cet ouvrage présente un intérêt particulier sur différents aspects cités ci-après : 1- un apport en magnétoélectrochimie en ce qui concerne les systèmes base cobalt ; 2- il est montré qu'un couplage des procédés d'électrolyse et de traitement thermique sous champ magnétique intense permettent d'influer sur les propriétés des matériaux magnétiques ; 3- l'apport d'une nouvelle approche pour la compréhension de résultats expérimentaux concernant l'électrodéposition sous champ magnétique par l'introduction d'une étude théorique. Cette étude ouvre la discussion sur l'apport de la modélisation moléculaire dans la compréhension des phénomènes se déroulant à l'électrode en présence de l'effet MHD.



UNIVERSITE DE REIMS CHAMPAGNE - ARDENNE
ECOLE DOCTORALE SCIENCES TECHNOLOGIE SANTE



AKADEMIA GÓRNICZO - HUTNICZA
WYDZIAŁ METALI NIEŻELAZNYCH

PRACA DOKTORSKA

Eksperymentalne i teoretyczne badania mechanizmu katodowego osadzania powłok na osnowie kobaltu: modelowanie i zależność pomiędzy strukturą a właściwościami poprzez wielozakresowe podejście

mgr inż. Agnieszka Franczak

Promotorzy pracy:

Prof. Frédéric Bohr, Université de Reims Champagne-Ardenne

Dr hab. Alexandra Levesque, Université de Reims Champagne-Ardenne

Prof. dr hab. inż. Krzysztof Fitzner, Akademia Górniczo-Hutnicza

Dr Piotr Żabiński, Akademia Górniczo-Hutnicza

Reims, 26 września 2013

Abstrakt

Praca oparta jest na eksperymentalnym i teoretycznym badaniu mechanizmu katodowego osadzania powłok na osnowie kobaltu. Badano kolejno powłoki: kobaltowe (Co), kobaltowo-niklowe (Co-Ni), kobaltowo-miedziane (Co-Cu) i kobaltowo-niklowo-miedziane (Co-Ni-Cu). Część eksperymentalna pracy obejmuje katodowe osadzanie powłok, charakterystykę ich właściwości strukturalnych, zmiany strukturalne spowodowane procesem wygrzewania, prowadzonym także w wysokim polu magnetycznym oraz badania właściwości magnetycznych. Część teoretyczna pracy poświęcona jest modelowemu badaniu procesu adsorpcji wodoru na powierzchni powłok kobaltowych poprzez zastosowanie technik mechaniki kwantowej. W zakres tej części wchodzi również próba opisanie i wyjaśnienia zmian strukturalnych powłok kobaltowych spowodowanych współwydzielającym się wodorem podczas procesu katodowego osadzania.

Praca ta składa się z czterech rozdziałów, w których:

Rozdział I – zawiera przegląd literatury dotyczący problematyki rozpatrywanej w pracy:

- podstaw elektrochemicznego osadzania metali, głównej metody wytwarzania powłok,
- porównania możliwych mechanizmów elektrochemicznego osadzania powłok kobaltowych,
- wpływu parametrów elektrochemicznego osadzania (pH, dodatki organiczne, etc.), oraz warunków procesu (obecność zewnętrznego pola magnetycznego) na właściwości strukturalne, które są głównym przedmiotem badań części eksperymentalnej,
- charakterystyki właściwości strukturalnych powłok kobaltowych i stopowych na osnowie kobaltu, w odniesieniu do części eksperymentalnej związanej z zastosowaniem otrzymanych powłok.

Rozdział II – poświęcony jest części eksperymentalnej pracy, która oparta jest na wyznaczeniu i optymalizacji parametrów procesu katodowego osadzania, takich jak: pH roztworu, rodzaju

podkładki katodowej i czasu osadzania. W następnej kolejności badano wpływ przyłożonego zewnętrznego pola magnetycznego na właściwości strukturalne otrzymanych powłok. Ponadto, rozdział ten zawiera także określenie wpływu pola magnetycznego na procesy elektrochemiczne, w tym przypadku elektrokryształizację i kinetykę procesu.

Rozdział III – badania przedstawione w tym rozdziale są częścią pracy należącej do projektu *COMAGNET*. Projekt ten prowadzony jest we współpracy dwóch laboratoriów: Laboratoire d'Ingenierie et Sciences des Materiaux w Reims i Key Laboratory of Electromagnetic Processing of Materials w Shenyang. Rozdział ten opisuje badania wpływu wygrzewania i wygrzewania w zewnętrznym polu magnetycznym powłok otrzymanych w wyniku katodowego osadzania, opisanych w *Rozdziale II*, na ich właściwości strukturalne oraz badaniu właściwości magnetycznych.

Rozdział IV – jest częścią teoretyczną pracy, która skupia się na modelowaniu procesu adsorpcji wodoru poprzez zastosowanie mechaniki kwantowej oraz relacji wyników teoretycznych z wynikami eksperymentalnymi.

Rozdział I – Przegląd literatury

Właściwości danego materiału ściśle zależą od jego budowy strukturalnej, która z kolei uzależniona jest od metody i warunków prowadzenia procesu jego produkcji. Wydaje się więc być interesującym badanie zależności pomiędzy właściwościami strukturalnymi a parametrami procesu, których kontrola pozwala na otrzymanie materiału o pożądanym właściwościach.

Proces katodowego osadzania jest jedną z wielu metod powszechnie stosowanych przy wytwarzaniu powłok monometalicznych, stopowych, czy wielowarstwowych. Wiąże się to przede wszystkim z relatywnie niskimi kosztami procesu, jego prostotą i wysoką wydajnością. Ponadto, katodowe osadzanie charakteryzuje się dużym stopniem kontroli, który jest osiąganym poprzez zmianę parametrów jego prowadzenia. Jednym z takich parametrów jest zastosowanie zewnętrznego pola magnetycznego, który zmieniając warunki hydrodynamiczne w roztworze elektrolitu wpływa na właściwości strukturalne osadzonej powłoki. Istnieje również możliwość zmiany otrzymanej struktury za pomocą niektórych metod fizycznych, takich jak wygrzewanie,

bądź wygrzewanie w polu magnetycznym, w wyniku których osadzane katodowo powłoki charakteryzują się dodatkowymi właściwościami.

Postęp w rozwoju inżynierii materiałowej odbywa się przede wszystkim poprzez wielozakresowe podejście, co w praktyce oznacza wykorzystywanie osiągnięć z innych dziedzin nauki, znajdowanie wspólnych relacji i ich stosowanie w celu otrzymania komplementarnego zrozumienia rozpatrywanego problemu. Modelowanie i symulacja procesu wytwarzania powłok, a ściślej ujmując procesów zachodzących podczas ich osadzania, umożliwia wizualizację jego przebiegu, dając tym samym możliwość zaprojektowania materiału o pożądanych właściwościach. Jedną z nich jest wykorzystanie nowatorskich technik mechaniki kwantowej, które dają szansę na modelowe określenie właściwości materiału zanim zostanie on wyprodukowany.

Rozdział II – Część eksperymentalna: optymalizacja procesu

Rozdział ten poświęcony jest badaniom wpływu pH roztworu, rodzaju podkładki katodowej i czasu osadzania na właściwości i strukturę osadzanych powłok. Rozpatrywane tutaj wartości pH są przypisane kolejno jako niskie – 2.7 i wysokie – 4.7. Rodzaje badanych podkładek katodowych to krążek tytanowy i szkło napyłane warstwą tlenku indu (ITO), dodatkowo wzmocnione powłoką niklową. Ponadto, badano wpływ przyłożenia zewnętrznego pola magnetycznego na strukturę i morfologię osadzanych powłok, a także zjawiska elektrochemiczne, tj. proces elektrokryształizacji, za pomocą krzywych chronoamperometrycznych i topografii powłok, oraz kinetykę procesu osadzania poprzez elektrochemiczną spektroskopię impedancyjną (EIS).

Przeprowadzone badania pokazują, że pH roztworu jest znaczącym parametrem w procesie wzrostu powłok i formowania się faz metalicznych. Osadzane katodowo powłoki Co i Co-Ni charakteryzują się obecnością dwóch struktur krystalograficznych: heksagonalnej gęstego ułożenia (hcp) i kubicznej (regularnej) ściennie centrowanej (fcc). Różnice obserwowane w składzie fazowym i morfologii powłok, w zależności od pH roztworu, związane są ze współdzielającym się wodorem i adsorbującymi na powierzchni powłok związkami przejściowymi, takimi jak wodorotlenki niklu i kobaltu.

Podczas katodowego osadzania na podkładkach tytanowych większość powłok Co i Co-Ni odznaczało się wysoką chropowatością powierzchni. Celem jej zmniejszenia, tytanowa

podkładka katodowa została zastąpiona podkładką Ni/ITO. Badania strukturalne pokazały, że rodzaj podkładki ma również wpływ na skład fazowy osadzanych powłok. W przypadku osadzania na Ti, powłoki kobaltowe charakteryzują się obecnością obu faz: hcp i fcc, podczas gdy powłoki Co i Co-Ni osadzone na Ni/ITO są jednofazowe (fcc). Obserwowane różnice składów fazowych powłok osadzanych na różnych podkładkach katodowych zostały potwierdzone przez analizę morfologii powłok, która wskazuje na obecność kryształów w kształtach charakterystycznych dla obu faz. Dodatkowo, powłoki osadzone na podkładkach Ni/ITO są bardziej homogeniczne, a ich powierzchnia mniej chropowata niż u powłok osadzanych na podkładkach tytanowych.

Czas osadzania wpływa na rozmiar ziaren osadu katodowego. Podczas długiego procesu katodowego osadzania, proces wzrostu kryształów pełni dominującą rolę nad procesem zarodkowania i osadzone powłoki są w rezultacie grubokrystaliczne. Ze względu na to, że celem tej pracy jest uzyskanie powłok nanokrystalicznych, zredukowano czas procesu katodowego osadzania, ograniczając tym samym etap wzrostu kryształów osadu.

Właściwości osadzanych powłok mogą być także uzależnione od warunków prowadzenia procesu, w tym wypadku od obecności przyłożonego równoległego w stosunku do powierzchni elektrody zewnętrznego pola magnetycznego o natężeniu do 12T. W takich warunkach procesu obserwuje się dodatkową konwekcję wzbudzaną w roztworze poprzez siłę Lorentza (efekt magneto-hydro-dynamiczny), która wpływa na zmianę warunków hydrodynamicznych przy powierzchni elektrody, a przez to strukturę i morfologię osadzanych powłok. Otrzymane wyniki pokazują, że przyłożenie zewnętrznego pola magnetycznego podczas procesu osadzania nie wpływa znacząco na zmiany składu fazowego powłok. Zmienia się względną intensywność refleksów dyfrakcyjnych poszczególnych faz. Odosobnionym przypadkiem jest powłoka Co-Ni osadzana na podkładce tytanowej, której skład fazowy w porównaniu ze składem powłok Co-Ni osadzanych na podkładkach Ni/ITO zmienia się w obecności przyłożonego pola magnetycznego. W tym przypadku, wpływ pola magnetycznego na skład fazowy jest podobny do wpływu niskiego pH, gdzie obserwowany jest uprzywilejowany wzrost płaszczyzny (220). Obserwowane zmiany są prawdopodobnie spowodowane wtórnym działaniem pola magnetycznego poprzez zmianą pH przy powierzchni elektrody, czy adsorpcję współwydzielającego się wodoru i innych związków pośrednich.

Przyłożenie zewnętrznego pola magnetycznego podczas katodowego osadzania wpływa na morfologię i chropowatość powierzchni osadzanych powłok. Powłoki kobaltowe osadzone w obecności pola magnetycznego są generalnie bardziej homogeniczne, co związane jest z obecnością dodatkowej konwekcji w roztworze. Konwekcja powstała na skutek przyłożenia pola magnetycznego powoduje mieszanie roztworu przy powierzchni elektrody, co zmniejsza grubość powłoki dyfuzyjnej i przyspiesza transport jonów w kierunku jej powierzchni. W konsekwencji bąbelki współdzielającego się wodoru są szybciej usuwane z powierzchni elektrody i powierzchnia osadzanych powłok jest jednorodniejsza.

Katodowe osadzanie powłok Co-Ni i Co-Cu wykazuje anomalny charakter, który skutkuje wyższym stosunkiem zawartości Co/Cu w powłoce niż jonów $\text{Co}^{2+}/\text{Cu}^{2+}$ w roztworze. Obecność zewnętrznego pola magnetycznego podczas procesu katodowego osadzania wpływa również na skład ilościowy metali w powłoce, w których zawartość Co w Co-Ni oraz Cu w Co-Cu i Co-Ni-Cu jest wyższa, kiedy proces prowadzony jest w polu magnetycznym.

Z punktu widzenia elektrochemii, badanie wpływu przyłożonego zewnętrznego pola magnetycznego na elektrokryształizację powłok Co i Co-Ni oraz kinetykę procesu osadzania powłok Co-Cu pokazuje, że obserwowane zmiany są głównie spowodowane efektem obecności pola magnetycznego, tj. jego wpływem na adsorpcję współdzielanego wodoru i innych związków pośrednich, takich jak wodorotlenki osadzanych metali. W przypadku procesu elektrokryształizacji badanego na podstawie analizy krzywych chronoamperometrycznych, proces zarodkowania osadzanych powłok katodowych jest zbliżony charakterem do natychmiastowego, niemniej jednak z odchyleniem od modelu teoretycznego. Różnica ta spowodowana jest zmianą warunków hydrodynamicznych pod wpływem przyłożonego pola magnetycznego i współdzielającym się wodorem, który determinuje przebieg zależności gęstości prądowej w funkcji czasu. Podobnie jest w przypadku kinetyki procesu. Przyłożenie zewnętrznego pola magnetycznego praktycznie nie wpływa na zmianę przeniesienia ładunku, a zmiany w kinetyce procesu są głównie związane ze zmianami powierzchni elektrody poprzez adsorpcję współdzielających się związków pośrednich, tj. wodoru i wodorotlenków.

Efekty przyłożonego zewnętrznego pola magnetycznego podczas procesu katodowego osadzania sprowadzają się głównie do jego wpływu na zmianę proporcji składu fazowego, kształtu i rozmiaru kryształów oraz chropowatości powierzchni powłoki. Obserwowane zmiany spowodowane są efektem magneto-hydrodynamicznym (MHD) wzbudzonym w roztworze

elektrolitycznym przez siłę Lorentza. MHD przyspiesza transport jonów w roztworze, ponieważ wzbudzona obecnością pola magnetycznego konwekcja miesza roztwór przy powierzchni elektrody, zmniejszając powłokę dyfuzyjną i przyspieszając redukcję metali na powierzchni elektrody. Jednocześnie przyspieszana jest adsorpcja współwydzielających się związków pośrednich, tj. wodoru i wodorotlenków metali, które zmieniają warunki hydrodynamiczne na powierzchni elektrody. Właściwości strukturalne osadzonej powłoki są głównie uzależnione od dwóch procesów, tj. dyfuzji na powierzchni elektrody, zależnej od parametrów procesu, oraz adsorpcji związków pośrednich. Zakłada się więc, że zmiany proporcji składu fazowego w powłoce są wynikiem zmiany pH przy powierzchni elektrody i konkurencyjnej adsorpcji pomiędzy współwydzielającym się wodorem a wodorotlenkami osadzanych metali na powierzchni powłoki. Problem ten jest szerzej rozpatrywany w *Rozdziale IV*, który skupia się na modelowym badaniu procesu adsorpcji, celem wyjaśnienia zmian strukturalnych obserwowanych w tej części pracy.

Rozdział III – Część eksperymentalna: zastosowanie

W drugiej części eksperymentalnej badany jest wpływ wygrzewania i wygrzewania w zewnętrznym polu magnetycznym powłok kobaltowych oraz określenie właściwości magnetycznych osadzanych katodowo powłok kobaltowych. Wyniki pokazują, że proces wygrzewania poprawia strukturę krystalograficzną osadzanych powłok, a prowadzenie procesu w zewnętrznym polu magnetycznym zachowuje ten efekt. Wygrzewanie powoduje również powstawanie obszarów dyfuzyjnych pomiędzy warstwą pośrednią niklu, osadzonego na ITO i warstwą właściwą powłoki. Efekt ten jest powiększony pod wpływem przyłożonego pola magnetycznego i wpływa na właściwości magnetyczne osadzanych katodowo powłok, czego przykładem są powłoki Co/Ni/ITO. Analiza przeprowadzona przy użyciu mikroskopu sił magnetycznych (MFM) powłok Co/Ni/ITO wskazuje na pojawienie się niewielkiej prostopadłej anizotropii magnetycznej, która wzrasta w procesie wygrzewania z przyłożonym polem magnetycznym.

W przypadku powłok Co-Ni/ITO, podczas katodowego osadzania w polu magnetycznym obserwuje się wzrost rozmiaru kryształów powłoki i chropowatości powierzchni. Wygrzewanie w polu magnetycznym zwiększa efekt pola magnetycznego przyłożonego podczas procesu katodowego osadzania. Osadzone katodowo powłoki Co-Ni/ITO charakteryzują się strukturą

regularną o płaszczyźnie (111), której wzrost nie jest zależny od obecności zewnętrznego pola magnetycznego. Późniejszy proces wygrzewania powłok powoduje silny wzrost tej płaszczyzny, która nie ulega wpływowi przyłożonego pola magnetycznego w czasie ponownego procesu. Obserwowane zmiany strukturalne wpływają znacząco na właściwości magnetyczne powłok. W wyniku procesu katodowego osadzania w polu magnetycznym powłoki Co-Ni/ITO charakteryzują się wysokim polem koercji, którego wartość wzrasta wraz ze wzrostem natężenia pola magnetycznego. Wygrzewanie w polu magnetycznym przynosi efekt odwrotny, tj. pole koercji powłok wygrzewanych w polu magnetycznym ulega redukcji, gdy natężenie pola wzrasta.

Badanie właściwości magnetycznych prowadzono również dla powłok Co-Cu/Cu/ITO i Co-Ni-Cu/Cu/ITO osadzanych katodowo w polu magnetycznym o natężeniu pola do 1T. W tym przypadku, właściwości magnetyczne są głównie zależne od składu chemicznego powłok. W warunkach procesu prowadzonego w zewnętrznym polu magnetycznym obserwuje się wzrost zawartości Cu w obu powłokach i zmiany w ich morfologii. Powłoki osadzone w polu magnetycznym charakteryzują się silnie rozwiniętą strukturą dendrytyczną, która wpływa na stosunek powierzchnia/objętość powodując zmiany anizotropii magnetycznej powłok.

Rozdział IV – Część teoretyczna: modelowe badanie procesu adsorpcji

Modelowe badanie procesu adsorpcji wodoru oparte je na technikach mechaniki kwantowej i teorii funkcjonału gęstości (*ang.* Density Functional Theory, DFT). Na ich podstawie dokonano obliczenia energii adsorpcji (E_{ads}) atomowego (H) i jonowego (H^+) wodoru na powierzchni kobaltu. W modelowym badaniu procesu adsorpcji uwzględniono oba rodzaje sieci krystalicznych tego metalu, tj. strukturę heksagonalną gęstego ułożenia (hcp) oraz strukturę regularną ściennie centrowaną (fcc). Spośród nich wybrano płaszczyzny atomowe, które najczęściej pojawiają się w powłoce kobaltowej osadzonej katodowo z roztworów podstawowych, tj. roztworów niezawierających dodatków organicznych. W przypadku struktury heksagonalnej, obliczenia dotyczą wyznaczenia E_{ads} pomiędzy wodorem a płaszczyznami: (100), (110), (101) i (011); dla struktury kubicznej są to kolejno: (100), (110), (111) oraz (220). Ponadto, modelowe badanie procesu adsorpcji wodoru pozwoliło określić rodzaj najstabilniejszego wiązania pomiędzy wodorem a powierzchnią adsorpcyjną.

Na podstawie otrzymanych wyników stwierdzono, że najstabilniejszym położeniem adsorbującego się wodoru jest położenie pomostowe dwojaki (z *ang.* bridge site), które

tworzone jest z większością rozpatrywanych powierzchni kobaltu. Niemniej jednak, adsorpcja na powierzchni struktury kubicznej wskazuje również na możliwość występowania położenia pomostowego trojaka (z ang. 3-fold site) na powierzchniach płaszczyzn o większych wartościach wskaźników, np. (220). Zgodnie z obliczeniami, E_{ads} uzależniona jest od rodzaju powierzchni adsorpcyjnej, rodzaju tworzonego wiązania pomiędzy wodorem a powierzchnią adsorpcyjną oraz zastosowanym funkcjonałem obliczeniowym. W związku z tym, otrzymane wartości E_{ads} wykazują pewną tendencję, na podstawie której można wyodrębnić powierzchnie bardziej bądź mniej podatne na adsorpcję wodoru. Dzięki temu, możliwe jest hipotetyczne wyjaśnienie formowania się faz w powłokach kobaltowych otrzymanych w procesie katodowego osadzania, diskutowanych w *Rozdziale II*.

W części eksperymentalnej powłoki kobaltowe były osadzane katodowo z roztworów o dwóch wartościach pH. W przypadku osadzania z roztworu o niskim pH (2.7), dyfrakcyjna analiza rentgenowska wskazuje na obecność obu faz kobaltu: heksagonalnej o płaszczyźnie (110) oraz kubicznej o płaszczyźnie (220). W odniesieniu do E_{ads} , faza kubiczna jest bardziej podatna na adsorpcję wodoru niż faza heksagonalna. W związku z tym, udział objętościowy fazy kubicznej jest prawdopodobnie wyższy niż fazy heksagonalnej, ze względu na zwiększoną ilość wiązanego z jej powierzchnią wodoru. Powstające w rezultacie związki wodorków kobaltu prawdopodobnie blokują dalszy wzrost powłoki w płaszczyźnie (220) pozwalając tym samym na jej wzrost w innych płaszczyznach, w tym przypadku heksagonalnej - (110). W przypadku powłok kobaltowych osadzanych z roztworów o wyższym pH (4.7), skład fazowy powłoki jest bardziej uzależniony od powstających związków wodorolenków kobaltu niż jego wodorków i dalsze obliczenia E_{ads} są potrzebne, by jednoznacznie stwierdzić odgrywaną przez nich rolę w procesie formowania się faz. Przypuszcza się, że ich wpływ na proces formowania się faz w powłoce jest podobny do wpływu wodorków kobaltu.

W dalszej części określony został wpływ przyłożonego zewnętrznego pola magnetycznego podczas katodowego osadzania na zmiany proporcji składu fazowego. Badania pokazują, że wpływ pola magnetycznego opiera się przede wszystkim na zmianie warunków hydrodynamicznych w roztworze, przy powierzchni elektrody. Przyłożenie zewnętrznego pola magnetycznego powoduje przyspieszenie transportu jonów do powierzchni elektrody poprzez wzbudzoną dodatkową konwekcję. W rezultacie obserwowany jest konkurencyjny proces

redukcji jonów osadzanego metalu i jonów wodorowych na powierzchni elektrody, który bezpośrednio wpływa na skład fazowy osadzonej powłoki.

Niniejsza praca przedstawia wkład Autora w dziedzinę magneto-elektrochemii poprzez badania oparte na powłokach, których podstawowym składnikiem jest kobalt. Celem pracy było poszerzenie wiedzy i wyjaśnienie roli odgrywanej przez przyłożenie zewnętrznego pola magnetycznego w procesie wzrostu powłok. Ponadto, pokazano rolę powiązanych ze sobą procesów katodowego osadzania i wygrzewania w przyłożonym zewnętrznym polu magnetycznym, które znacząco wpływają na właściwości magnetyczne otrzymanych powłok. Zaproponowano także nowatorskie rozwiązanie, którego celem jest osiągnięcie lepszego wyjaśnienia i zrozumienia otrzymanych wyników eksperymentalnych, otwierając dyskusję nad znaczeniem modelowego badania procesów elektrochemicznych zachodzących w obecności zewnętrznego pola magnetycznego, poprzez wykorzystanie technik mechaniki kwantowej.

Acknowledgements

U lala! So this is it! Every time, when I have been wondering, what should I begin from, I always used to hum:

“This is the end,

Hold your breath and count to ten...”

Skyfall, Adele

Yes, very at place! Now, what I am thinking about is that completing my PhD degree is probably one of the most challenging activities of my first 27 years of life. All the moments of my doctoral journey have been shared with many people. It has been a great privilege to spend these three years in Laboratoire d'Ingénierie et Sciences des Matériaux (LIMS) at Université de Reims Champagne-Ardenne, and its members will always remain dear to me.

I would like to begin these acknowledgements from a person, from who whole this PhD adventure has been started; who saw some scientific potential and gave me a chance to develop it; who is always right on place and right on time. I would kindly like to thank to my Master supervisor and co-supervisor of my Doctoral thesis, Dr Piotr Zabinski from the Laboratory of Electrochemistry and Physical Chemistry at AGH University of Science and Technology. I appreciate all the help, which you have always provided to me whenever I visited Krakow. Thank you for always well welcome, even if I was just coming to bother you and taking your time for the all and nothing talks. Thanks to you I am where I am and doing what I am doing and what is worse, I simply like it! But now I need to worry you a little bit... you have a concurrency! Because coming to Reims, to follow my PhD study, I would have never imagined having better supervisor than she was. I would like to thank Alexandra Levesque for her friendly and openhearted support in the planning and conduction of my research period in LISM. Alex, I have learnt a lot from you and I am grateful about the fruitful time to have spent with you. Not only the excellent discussions within the project, but also your constant support in all my efforts, which I have put in this work were amazing. Thank you so much!

The greatest thanks to the supervisors of my thesis, Prof. Frédéric Bohr and Prof. Krzysztof Fitzner. Thank you for the support, discussions, listening, advising and kind help. It was my honor to be your student.

I would also like to thank the Director of Ecole Doctorale and LISM Laboratory, Prof. Jean-Paul Chopart, for acceptance of my candidature as a PhD student, for the leadership and all of the fruitful discussions.

Many thanks to the Champagne-Ardenne Region Council, ANR Agency and Materalia for the financial support provided by the University Research Grants: n° 2010-INTB-903-01, as well as the Romeo Calculation Platform at University of Reims Champagne-Ardenne and LNCMI Laboratory in Grenoble for a high magnetic field facility.

I would also like to thank my jury members: Prof. Wanda Gumowska, Prof. Ivan Skorvanek and Prof. Qiang Wang, for providing encouraging and constructive feedback. I suppose that reviewing a thesis is not an easy task to do and I am grateful for all your thoughtful and detailed comments.

Many heartwarm thanks go to some wonderful people, who I had a pleasure to meet during the last three years and whose have been extremely helpful in my research. I would like to thank Dr Maciej Czapkiewicz, Dr Pierre Mohlo, Dr Andrzej Baczmański, Dr Roman Wawszczak, Dr Marianna Marciszko, Dr Gabriele Barrera, Dr Federica Celegato, Prof. Paola Tiberto, Dr Margitta Uhlemann and Dr Tomasz Tokarski, for their help in analyses and discussions. Special thanks to Dr Marco Coisson from INRIM Electromagnetic Division in Torino, Italy, for the magnetic analyses, cooperative discussions, enormous help, contribution and fantastic friendship. I am also grateful to Dr Remigiusz Kowalik, Dr Krzysztof Mech and Dr Piotr Handzlik, for the help in AFM, XRD and WD-XRF analyses as well as always well welcome in the Laboratory. Moreover, I am deeply thankful to Prof. Omar Aaboubi for spending his time to explain me the mystery of EIS, for discussions and kindness, which he surrounded me during my thesis.

I would like to thank Prof. Qiang Wang, the head of EPM Group from Shenyang in China, for allowance me to stay in his group and take advantage to enlarge my professional experience as well as for huge generosity. Special thanks go also to the members of EPM Group: Zhao Yue, Liu Tie, Wang Kai, Du Jiaojiao, Ma Yonghui, Li Guojian, Li Dejun, Pang Hongxuan, Shui Guangliang, Liu Wenjun, Wang Wenli, Cai Haishan, Ouyang Renhua, Li Hongxia, Liu Xingan, with some special thanks to Wu Chun, Liu Qiang, Zhou Xiangkui, Liu Yin, Wang Yan, Mao Jun, Shao Jianguo, Gao Pengfei and my lovely "sister" Yinglong (Dragon) Li. You all have been very kind and helpful to me during my two months stay in the Key Laboratory. Besides the experiments and analyses, I would like to thank you first of all for your friendship, all the hot-spots, dumplings and soups evenings; all the fantastic time spent together on talks, QQ chattings and jokes. You are special. In addition, I would like to thank Dr Donggang Li for the last two years in LISM, for helpful discussions related to the COMAGNET project as well as for being so generous with his expertise and friendship.

Some extremely great thanks go to the most amazing people I have ever known! Thank you: Céline Rousse, Patrick Fricoteaux, Valérie Mancier, Samuel Crequy and Prof. Jacques Douglade. I will be missing the morning coffee services, shouting out loud: "Bibi!", teasing you with something like: "t'es méchant!", resolving sudoku and all the positive fluctuations appearing every time you were around!

Many thanks to Martin Noel, Anne-Lise Daltin, Hicham Benhayoune, Sébastien Murer, who saved my pc out of trouble and Patrick Baudart - the best technician in the world! Warm thanks to the other members of LISM and Laboratory of Electrochemistry and Physical Chemistry at AGH, especially: Marek, Justyna, Przemek, Tomek, Michal, Justyna, Iwona, Ania, Dr Krzysztof Paclawski and Dr Dominika Jendrzeczyk-Handzlik. Thank you for your kindness, smiling faces, curiosity and making effort in understanding my "polish-english" french.

I can think of no finer individual than Jérémy Mallet, who has been exceptional friend to me during these years. You are the source of inspiration with your enthusiasm and amazing outlook on life. You have been one of my strongest supporters, and I am grateful for your encouragement, motivation, faith, understanding and what is the most important, trust.

Last, but not least, I would like to thank some good friends of mine, living here and there, but always being around: Raffi, Ania, Honor, Cisek, Kasia, Gosia, Manel, Sam, Ahmad, Clara, Ali, Alexander, Iva, Karima, Hakim, Yan, Karin, Pedro, Ari and Arla. Some special ones need to go to Antonietta, Lilly, Angel and Aigi, my four musketeers, as well as Agatka, my privet source of information. Thank you for being genuinely happy for my success and good fortune, as if it were your own; thanks for letting me vent, and trusting me enough to tell me what's bothering you; thank you for hugs, smiles, inside jokes, and memories and thanks for understanding that I could never write long enough acknowledgements to express how much you all mean to me.

Furthermore, I would like to thank my best friends, Francesca and Ibi. You will always be the most important persons in my life. There is nobody else who can support as much as you, who loves disinterestedly, who sacrifices all when the help is needed, who is there every time whenever I need.... Thank you for being my friends always, not just when it was convenient; for making time for me, even on your busiest days; for being honest with me when I really needed you to be; for asking how I am doing, and actually wanting to hear the answer; for not letting time or distance affect our friendship... Love you!

Moreover, I would like to deeply thank to Francesca's family: parents, grandma, Giuli, Giova and Fede. Thank you for surrounding me so huge kindness, happiness and sympathy. Since two years you are mine as well and I like this feeling! You are simply the best!

At least, I would like to thank my little family: mom, dad, Olenka, Piotrek and Malgosia. You have always been there for me, supported me every day, always listen, never interrupt. Thank you for your patience, for understanding my way, my choices and always waiting for my come back. Thanks to my grandma, who has been waiting for this moment... I hope you are proud there now.

Coming together is a beginning;

keeping together is progress;

working together is success.

~ Henry Ford

For Alexandra.

My supervisor. My friend.

Abstract

The present work is focused on the experimental and theoretical studies of the electrodeposition mechanism of Co-based films, including single Co, binary Co-Ni, Co-Cu and ternary Co-Ni-Cu alloy films. The modeling and structure-properties relationship by a multi-scale approach are investigated.

The preliminary study involves determination and optimization of the electrodeposition parameters in order to obtain nanocrystalline films with satisfied surface quality and promising magnetic properties. It is shown that the electrolytic pH, to-be-deposited type of substrate and deposition time are of high importance in the fabrication of nanoscale materials. Among them, the electrolytic pH is the one, which has the greatest effect on the structure formation. The film growth as well as its quality can be strongly affected by a superimposition of an external magnetic field. The electrodeposition process was carried out under parallel to the electrode surface magnetic fields with magnets strength up to 12T. The results reveal that the induced forced convection in the electrolyte changes the hydrodynamic conditions and thus, affects the structure and morphology of the obtained films. Furthermore, the process kinetics and crystal growth are enhanced under magnetic electrodeposition conditions.

Microstructure formed by the electrochemical processing is characterized by some significant magnetic properties, which may result in soft and/or hard magnetic materials, depending on their application approach. Additionally, the microstructure of films has been improved by the magnetic annealing treatment. Thus, the recrystallization and interdiffusion phenomena are observed, and modification of the magnetic properties is induced.

Considering the electrodeposition process carried out in aqueous solutions the secondary process, which is the hydrogen evolution reaction (HER), needs to be taken into account. The theoretical study based on the tools of quantum mechanics (QM) and density functional theory (DFT) is used to determine the adsorption energies of hydrogen. In this work, the calculation results are related with the experimental study and may explain the structure formation assisted by the simultaneous evolution of hydrogen at the electrode surface.

Résumé

Des études expérimentales et théoriques du mécanisme d'électrodéposition de différents revêtements à base de cobalt : le cobalt métallique, les alliages binaires Co-Ni, Co-Cu et l'alliage ternaire Co-Ni-Cu sont menés.

Les propriétés de ces films dépendent fortement des paramètres expérimentaux tels que le pH de l'électrolyte, la nature du substrat, etc.. Un champ magnétique jusqu'à 12T est superposé parallèlement à la surface de l'électrode de travail. La convection forcée induite dans l'électrolyte modifie les conditions hydrodynamiques et par conséquent, influe sur la structure et la morphologie des films obtenus. Par ailleurs, la cinétique des processus et la croissance des cristaux sont améliorées dans des conditions magnéto électrochimique. Les microstructures obtenues suite au procédé électrochimique en présence d'un champ magnétique sont caractérisées par différentes propriétés magnétiques trouvant un intérêt potentiel en tant que matériaux magnétiques doux et / ou dur. Dans le cadre du projet ANR COMAGNET, les matériaux subissent ensuite un traitement thermique en présence d'un champ magnétique, des phénomènes de recristallisation et interdiffusion sont mis en évidence induisant des modifications des propriétés magnétiques.

Enfin, des calculs de l'énergie d'adsorption de l'atome d'hydrogène et de l'ion H^+ sur différentes faces cristallographiques du cobalt sont menés par modélisation DFT (Théorie de la Fonctionnelle de la Densité). Ces résultats, mis en relation avec l'étude expérimentale, montrent le lien entre la formation de certaines structures cristallographiques et l'évolution simultanée de l'hydrogène à la surface de l'électrode pendant l'électrolyse.

Abstrakt

Praca oparta jest na eksperymentalnym i teoretycznym badaniu mechanizmu katodowego osadzania powłok na osnowie kobaltu. Badano kolejno powłoki: kobaltowe (Co), kobaltowo-niklowe (Co-Ni), kobaltowo-miedziane (Co-Cu) i kobaltowo-niklowo-miedziane (Co-Ni-Cu). Część eksperymentalna pracy obejmuje katodowe osadzanie powłok, charakterystykę ich właściwości strukturalnych, zmiany strukturalne spowodowane procesem wygrzewania, prowadzonym także w wysokim polu magnetycznym oraz badania właściwości magnetycznych. Część teoretyczna pracy poświęcona jest modelowemu badaniu procesu adsorpcji wodoru na powierzchni powłok kobaltowych poprzez zastosowanie technik mechaniki kwantowej. W zakres tej części wchodzi również próba opisanie i wyjaśnienia zmian strukturalnych powłok kobaltowych spowodowanych współwydzielającym się wodorem podczas procesu katodowego osadzania.

Niniejsza praca przedstawia wkład Autora w dziedzinę magneto-elektrochemii poprzez badania oparte na powłokach, których podstawowym składnikiem jest kobalt. Celem pracy jest poszerzenie wiedzy i wyjaśnienie roli odgrywanej przez przyłożenie zewnętrznego pola magnetycznego w procesie wzrostu powłok. Ponadto, pokazano rolę powiązanych ze sobą procesów katodowego osadzania i wygrzewania w przyłożonym zewnętrznym polu magnetycznym, które znacząco wpływają na właściwości magnetyczne otrzymanych powłok. Zaproponowano także nowatorskie rozwiązanie, którego celem jest osiągnięcie lepszego wyjaśnienia i zrozumienia otrzymanych wyników eksperymentalnych, otwierając dyskusję nad znaczeniem modelowego badania procesów elektrochemicznych zachodzących w obecności zewnętrznego pola magnetycznego, poprzez wykorzystanie technik mechaniki kwantowej.

Content

Abstracts:

❖ English	7
❖ French	8
❖ Polish	9
List of Tables	14
List of Figures	15
List of Symbols	20
List of Abbreviations	22
<i>General introduction</i>	24
CHAPTER I - Literature review	
I.1. Introduction	27
I.2. Background of electrochemical deposition	28
I.2.1. Steps involved in the electrochemical deposition process	29
I.2.2. Pathways for the growth of electrodeposit	30
I.2.2.1. Thermodynamics and kinetics of the electrodeposition process	31
I.3. Electrodeposition mechanism of Co and Co-based alloys	32
I.3.1. Structural characteristic of the electrodeposited cobalt	34
I.3.2. Parameters affecting electrodeposition process	36
I.3.2.1. Effect of current density and deposition potential	36
I.3.2.2. Effect of electrolyte pH	38
I.3.2.3. Effect of temperature	39
I.3.2.4. Effect of electrolyte additives	41
I.3.2.4.1. Boric acid	42
I.3.2.4.2. Saccharin	43
I.3.3. Co-electrodeposition with less noble metal	45
I.3.3.1. Hydrogen evolution reaction (HER)	46

I.3.3.2. Microstructure dependence	48
I.3.4. Co-electrodeposition with more noble metal	48
I.3.4.1. Displacement reactions	49
I.3.4.2. Underpotential deposition	50
I.4. Electrodeposition under superimposed magnetic field	51
I.4.1. Magnetic forces generated in the electrolyte	51
I.4.2. Magnetic forces and convection	54
I.4.3. Magnetic field and microstructure formation	55

Chapter II - *Experimental results*

II.1. Introduction	58
II.2. Experimental methodology	59
II.2.1. Electrolyte composition	59
II.2.2. Electrolytic cell and electrodes	60
II.2.3. Electrochemical deposition methods	61
II.2.4. Superimposed magnetic field	62
II.3. Preliminary study - optimization of the electrodeposition parameters	63
II.3.1. Electrolyte pH	64
II.3.1.1. pH effect on the structure of Co and Co-Ni films	64
II.3.1.2. pH effect on the morphology of Co and Co-Ni films	67
II.3.2. Substrate type and deposition time	70
II.3.2.1. Electrodeposited Co films	71
II.3.2.2. Electrodeposited Co-Ni films	74
II.4. Electrodeposition under external magnetic field	75
II.4.1. Effect of a low magnetic field (LMF)	76
II.4.1.1. Co and Co-Ni films electrodeposited on Ti substrate	76
II.4.1.2. Co films electrodeposited on Ni/ITO substrate	80
II.4.1.3. Electrochemical kinetic study	82
II.4.1.3.1. Effect of a magnetic field on the current-transients	85
II.4.1.3.2. Effect of a magnetic field on the crystal growth	86
II.4.1.4. Co-Cu and Co-Ni-Cu films electrodeposited on Cu/ITO substrate	88

IV.4.2. Face-centered cubic structure	
IV.4.3. Hexagonal closed-packed structure	155
IV.5. Structure formation determined by hydrogen evolution reaction	157
IV.5.1. Effect of pH	157
IV.5.2. Effect of magnetic field	159
IV.6. Conclusion	161
<i>General conclusion</i>	162
Annexes	165
I. Magnetohydrodynamic (MHD) effect	165
I.1. MHD in electrochemical processing	168
I.2. Nucleation determined by the electrochemical fluctuations	169
I.3. Early stages of electrodeposition and MHD	172
II. Electrochemical stationary techniques	173
II.1. Chronoamperometry	173
II.2. Voltammetry	174
III.3. Electrochemical Impedance Spectroscopy	175
III. Characterization techniques	178
III.1. X-ray Diffraction (XRD)	178
III.2. Scanning Electron Microscopy (SEM)	179
III.3. Energy-Dispersive X-ray Spectroscopy (EDXS)	180
III.4. Wavelength-Dispersive X-ray Fluorescence (WD-XRF)	181
III.5. X-ray Photoelectron Spectroscopy (XPS)	181
III.6. Atomic Force Microscopy (AFM)	181
III.7. Magnetic Force Microscopy (MFM)	182
III.8. Vibrating Sample Magnetometer (VSM)	182
III.9. Alternating Field Gradient Magnetometer (AFGM)	183
List of References	184

List of Tables

Chapter II - Experimental study

- Table 1. Composition of the electrolytic solutions according to the electrodeposition of different systems considered in the preliminary study, together with the electrodeposition conditions.
- Table 2. Conditions of the electrodeposition process of Co and Co-Ni films deposited on Ti substrate.
- Table 3. Conditions of the electrodeposition process of Co and Co-Ni films deposited on Ni/ITO substrate.
- Table 4. Composition of the electrolytic solutions according to the electrodeposition of different systems under LMF, together with the electrodeposition conditions.
- Table 5. Parameters obtained from fitting of EIS model to the experimental data.
- Table 6. Composition of the electrolytic solutions according to the electrodeposition of different systems under HMF, together with the electrodeposition conditions.

Chapter III - Application approach

- Table 7. The electrodeposition conditions of Co-based thin films subjected to the magnetic annealing treatment and magnetic properties analysis.
- Table 8. Characteristic features of the Co-Cu/Cu/ITO films influencing magnetic properties.
- Table 9. Characteristic features of the Co-Cu/Cu/ITO and Co-Ni-Cu/Cu/ITO films influencing magnetic properties.

Chapter IV - Theoretical study

- Table 10. Calculation results for the different planes of Co-cubic system.
- Table 11. Calculation results for the different planes of Co-hexagonal system.

List of Figures

Chapter I – Literature review

- Fig.1. Schematic diagram of the electrodeposition process.
- Fig.2. Approximate regions in which the various stages of ion transport occur, leading for electrodeposition.
- Fig.3. Schematic representation of the steps involved in electrodeposition.
- Fig.4. The Bravais crystalline systems representing hexagonal and cubic structures [16].

Chapter II – Experimental study

- Fig.5. Three-electrode double-wall cell used during the electrochemical deposition.
- Fig.6. Experimental setups for (a) LMF and (b) HMF investigations.
- Fig.7. Phase composition of the Co films deposited on Ti substrate at different pH levels: (a) 2.7 (b) 4.7; $i = -20\text{mA/cm}^2$, $t = 12\text{min}$.
- Fig.8. Phase composition of the Co-Ni films deposited on Ti substrate at different pH levels (a) with the overlap lines of two cobalt phases (b); $i = -20\text{mA/cm}^2$, $t = 18\text{min}$.
- Fig.9. Morphology of the Co films electrodeposited on Ti substrate at pH (a) 4.7 and (b) 2.7; $i = -20\text{mA/cm}^2$, $t = 12\text{min}$.
- Fig.10. Morphology of the Co-Ni films electrodeposited on Ti substrate at pH (a) 4.7 and (b) 2.7; $i = -20\text{mA/cm}^2$, $t = 18\text{min}$.
- Fig.11. Substrates used as the working electrodes: (a) – titanium, (b) – ITO/glass.
- Fig.12. Comparison of the phase composition and morphology of Co films electrodeposited on: (a) Ti and (b) Ni/ITO substrates; **Ti**: $i = -20\text{mA/cm}^2$, $t = 12\text{min}$, $\text{pH} = 4.7$; **Ni/ITO**: $i = -10\text{mA/cm}^2$, $t = 4\text{min}$, $\text{pH} = 4.7$.
- Fig.13. Morphology of the Co films electrodeposited on Ni/ITO substrate at different times: (a) 4 minutes and (b) 1 minute; $i = -10\text{mA/cm}^2$, $\text{pH} = 4.7$.
- Fig.14. Comparison of the phase composition and morphology of Co-Ni films electrodeposited on (a) Ni/ITO and (b) Ti substrates; **Ti**: $i = -20\text{mA/cm}^2$, $t = 18\text{min}$, $\text{pH} = 4.7$; **Ni/ITO**: $i = -10\text{mA/cm}^2$, $t = 1\text{min}$, $\text{pH} = 4.7$.
- Fig.15. Comparison of the surface morphology of Co (a) and Co-Ni (b) films electrodeposited on Ni/ITO substrate; $i = -10\text{mA/cm}^2$, $t = 1\text{min}$, $\text{pH} = 4.7$.
- Fig.16. Magnetic field flux in parallel orientation to the electrode surface placed horizontally (a) and vertically (b).
- Fig.17. X-ray diffraction patterns and morphology of the Co films electrodeposited on Ti substrate under: (a) 0T, (b) 0.5T and (c) 1T magnetic field; $i = -20\text{mA/cm}^2$, $t = 12\text{min}$, $\text{pH} = 4.7$.

- Fig.18. X-ray diffraction patterns and morphology of the Co-Ni films electrodeposited on Ti substrate under: (a) 0T, (b) 0.5T and (c) 1T magnetic field; $i = -20\text{mA/cm}^2$, $t = 18\text{min}$, $\text{pH} = 4.7$.
- Fig.19. X-ray diffraction patterns and morphology of the Co films electrodeposited on Ni/ITO substrate under: (a) 0T, (b) 0.5T and (c) 1T magnetic field; $i = -10\text{mA/cm}^2$, $t = 1\text{min}$, $\text{pH} = 4.7$.
- Fig.20. Current-time transient for the electrodeposition of Co/Ti at -1.4V vs. SSE, $\text{pH} = 4.7$.
- Fig.21. The theoretical instantaneous and progressive nucleation modes compared with normalized $(i/i_{\text{max}})^2$ vs. t/t_{max} plots obtained from the experimental data in Fig.20.
- Fig.22. Dependence of i versus (a) $t^{1/2}$ and (b) $t^{3/2}$ plots for the initial transient portion for Co/Ti electrodeposition; $E = -1.4\text{V}$ vs. SSE, $\text{pH} = 4.7$.
- Fig.23. The adjustment of current-time transients for: (a) Co/Ti and (b) Co-Ni/Ti films electrodeposited at -1.4V vs. SSE under LMF.
- Fig.24. The AFM images of (a) Co/Ti and (b) Co-Ni/Ti films electrodeposited under LMF; Scanning area $10 \times 10 \mu\text{m}$; $i = -20\text{mA/cm}^2$, $t = 12/18\text{min}$, $\text{pH} = 4.7$.
- Fig.25. X-ray diffraction patterns of the Co-Cu/Cu/ITO (a) and Co-Ni-Cu/Cu/ITO (b) films electrodeposited under LMF; $i = -20\text{mA/cm}^2$, $t = 1\text{min}$, $\text{pH} = 4$.
- Fig.26. Morphology of the Co-Cu/Cu/ITO (a) and Co-Ni-Cu/Cu/ITO (b) films electrodeposited under LMF; $i = -20\text{mA/cm}^2$, $t = 1\text{min}$, $\text{pH} = 4$.
- Fig.27. Chemical composition of the Co-Cu/Cu/ITO (a) and Co-Ni-Cu/Cu/ITO (b) films electrodeposited under LMF; $i = -20\text{mA/cm}^2$, $t = 1\text{min}$, $\text{pH} = 4$.
- Fig.28. Comparison of the flower-like features of Co-Cu/Cu/ITO (a) and Co-Ni-Cu/Cu/ITO (b) films electrodeposited under 1T magnetic field; $i = -20\text{mA/cm}^2$, $t = 1\text{min}$, $\text{pH} = 4$.
- Fig.29. Schematic representation of the dendrite formation related to the hydrogen evolution reaction [186].
- Fig.30. The current-potential curves for Co-Cu/Cu/ITO films electrodeposited under LMF; $E = -1.4\text{V}$ vs. SSE, $\text{pH} = 4$.
- Fig.31. Nyquist diagram of the Co-Cu/Cu/ITO films electrodeposited under LMF; $E = -1.4\text{V}$ vs. SSE, $\text{pH} = 4$.
- Fig.32. The equivalent circuit for modeling the impedance of electrodeposition of Co-Cu/Cu/ITO films under LMF.
- Fig.33. Phase composition of: (a) Co-Ni/Ni/ITO and (b) Co-Ni/ITO electrodeposited under HMF; $i = -10\text{mA/cm}^2$, $t = 1\text{min}$, $\text{pH} = 4.7$.
- Fig.34. Morphology of the Co-Ni/Ni/ITO films electrodeposited under: (a) 0T, (b) 6T and (c) 12T magnetic field; $i = -10\text{mA/cm}^2$, $t = 1\text{min}$, $\text{pH} = 4.7$, without saccharin additive.
- Fig.35. Morphology of the Co-Ni/ITO films electrodeposited under: (a) 0T, (b) 6T and (c) 12T magnetic field; $i = -10\text{mA/cm}^2$, $t = 1\text{min}$, $\text{pH} = 4.7$, with saccharin additive.

Fig.36. Roughness and crystallite size characteristics of the Co-Ni/ITO films electrodeposited under HMF; $i = -10\text{mA/cm}^2$, $t = 1\text{min}$, $\text{pH} = 4.7$.

Fig.37. Chemical composition of the Co-Ni films electrodeposited on: (a) Ni/ITO and (b) ITO substrates under HMF; $i = -10\text{mA/cm}^2$, $t = 1\text{min}$, $\text{pH} = 4.7$.

Fig.38. Phase composition of the Co-Cu films electrodeposited on Cu/ITO substrate under HMF; $i = -20\text{mA/cm}^2$, $t = 1\text{min}$, $\text{pH} = 4$.

Fig.39. Morphological characteristic of the Co-Cu films electrodeposited on Cu/ITO substrate under HMF; $i = -20\text{mA/cm}^2$, $t = 1\text{min}$, $\text{pH} = 4$.

Fig.40. Chemical composition of the Co-Cu films electrodeposited on Cu/ITO substrate under HMF; $i = -20\text{mA/cm}^2$, $t = 1\text{min}$, $\text{pH} = 4$.

Chapter III – Application approach

Fig.41. Schematic view of the annealing setup under high magnetic field.

Fig.42. X-ray diffraction patterns of the Co/Ni/ITO films before and after annealing under high magnetic field; *Electrodeposition*: $i = -10\text{mA/cm}^2$, $t = 1\text{min}$, $\text{pH} = 4.7$; *Annealing*: $t = 4\text{h}$, $T = 673\text{K}$.

Fig.43. Zoom at the 2θ angles, where the growth of biphasic diffraction peaks of Co/Ni/ITO films is observed; *Electrodeposition*: $i = -10\text{mA/cm}^2$, $t = 1\text{min}$, $\text{pH} = 4.7$; *Annealing*: $t = 4\text{h}$, $T = 673\text{K}$.

Fig.44. The composition distribution of Co/Ni/ITO films along the cross-section. Δx stands for the diffusion distance [195]; *Electrodeposition*: $i = -10\text{mA/cm}^2$, $t = 4\text{min}$, $\text{pH} = 4.7$; *Annealing*: $t = 4\text{h}$, $T = 673\text{K}$.

Fig.45. Morphological comparison of the Co/Ni/ITO bilayer thin films as-deposited under 0T (a) and post-annealed under 0T (b), 6T (c) and 12T (d) magnetic field; *Electrodeposition*: $i = -10\text{mA/cm}^2$, $t = 1\text{min}$, $\text{pH} = 4.7$; *Annealing*: $t = 4\text{h}$, $T = 673\text{K}$.

Fig.46. Comparison of the hysteresis loops of Co/Ni/ITO bilayer films electrodeposited without and with a superimposed magnetic field; *Electrodeposition*: $i = -10\text{mA/cm}^2$, $t = 1\text{min}$, $\text{pH} = 4.7$.

Fig.47. Comparison of the hysteresis loops of Co/Ni/ITO bilayer films electrodeposited under 0 and 1T and annealed under 0, 6 and 12T; *Electrodeposition*: $i = -10\text{mA/cm}^2$, $t = 1\text{min}$, $\text{pH} = 4.7$; *Annealing*: $t = 4\text{h}$, $T = 673\text{K}$.

Fig.48. Comparison of the coercivity field of Co/Ni/ITO bilayer films before (as-deposited) and after (post-annealed) annealing treatment; *Electrodeposition*: $i = -10\text{mA/cm}^2$, $t = 1\text{min}$, $\text{pH} = 4.7$; *Annealing*: $t = 4\text{h}$, $T = 673\text{K}$.

Fig.49. MFM analysis of the Co/Ni/ITO films; *Electrodeposition*: $i = -10\text{mA/cm}^2$, $t = 1\text{min}$, $\text{pH} = 4.7$; *Annealing*: $t = 4\text{h}$, $T = 673\text{K}$.

Fig.50. X-ray diffraction patterns the Co-Ni/ITO alloy films before and after annealing under high magnetic field; *Electrodeposition*: $i = -10\text{mA/cm}^2$, $t = 1\text{min}$, $\text{pH} = 4.7$; *Annealing*: $t = 4\text{h}$, $T = 673\text{K}$.

- Fig.51. Dependence of the crystal orientation index Y(111) of Co-Ni fcc phase on magnetic flux density. B_{el} – magnetic field during electrodeposition, B_{HT} – magnetic field during annealing; *Electrodeposition: $i = -10\text{mA/cm}^2$, $t = 1\text{min}$, $pH = 4.7$; Annealing: $t = 4\text{h}$, $T = 673\text{K}$.*
- Fig.52. Morphological comparison of the electrodeposited Co-Ni/ITO films before and after annealing process; *Electrodeposition: $i = -10\text{mA/cm}^2$, $t = 1\text{min}$, $pH = 4.7$; Annealing: $t = 4\text{h}$, $T = 673\text{K}$.*
- Fig.53. Hysteresis loops of the post-annealed Co-Ni/ITO films deposited without magnetic field; *Electrodeposition: $i = -10\text{mA/cm}^2$, $t = 1\text{min}$, $pH = 4.7$; Annealing: $t = 4\text{h}$, $T = 673\text{K}$.*
- Fig.54. Coercivity field of the as-deposited Co-Ni/ITO films after annealing process; *Electrodeposition: $i = -10\text{mA/cm}^2$, $t = 1\text{min}$, $pH = 4.7$; Annealing: $t = 4\text{h}$, $T = 673\text{K}$.*
- Fig.55. X-ray diffraction patterns of Co-Cu/Cu/ITO alloy films before and after annealing under high magnetic field; *Electrodeposition: $i = -20\text{mA/cm}^2$, $t = 1\text{min}$, $pH = 4$; Annealing: $t = 4\text{h}$, $T = 623\text{K}$.*
- Fig.56. Morphological changes of as-deposited Co-Cu/Cu/ITO films by the annealing process under magnetic field; *Electrodeposition: $i = -20\text{mA/cm}^2$, $t = 1\text{min}$, $pH = 4$; Annealing: $t = 4\text{h}$, $T = 623\text{K}$.*
- Fig.57. Comparison of the hysteresis loops field of Co-Cu/Cu/ITO alloy films electrodeposited without and with an applied magnetic field; *Electrodeposition: $i = -20\text{mA/cm}^2$, $t = 1\text{min}$, $pH = 4$.*
- Fig.58. Topographical characteristics of the Co-Cu/Cu/ITO films electrodeposited under high magnetic field. Images were obtained by applying a differentiation procedure to the AFM images by Nova software; *Electrodeposition: $i = -20\text{mA/cm}^2$, $t = 1\text{min}$, $pH = 4$.*
- Fig.59. Comparison of the hysteresis loops measured in-plane of Co-Ni-Cu/Cu/ITO films electrodeposited without and with an applied magnetic field; *Electrodeposition: $i = -20\text{mA/cm}^2$, $t = 1\text{min}$, $pH = 4$.*
- Fig.60. Topography of (a) Co-Cu under 12T and (b) Co-Ni-Cu under 1T magnetic field; *Electrodeposition: $i = -20\text{mA/cm}^2$, $t = 1\text{min}$, $pH = 4$.*
- Fig.61. Comparison of the hysteresis loops measured out-of-plane of Co-Ni-Cu/Cu/ITO films electrodeposited without and with an applied magnetic field; *Electrodeposition: $i = -20\text{mA/cm}^2$, $t = 1\text{min}$, $pH = 4$.*

Chapter IV – Theoretical study

- Fig.62. Schematic representation of the current distribution together with direction of Lorentz force (left hand side) and characteristic convection patterns (right hand side) in the vicinity of a bubble obtained in the parallel-to-electrode magnetic field configuration. (Krause et al. [216]).

- Fig.63. Schematic representation of the current distribution together with direction of Lorentz force (left hand side) and characteristic convection patterns (right hand side) in the vicinity of a bubble obtained in the perpendicular-to-electrode magnetic field configuration (a), and surface tensions between gas/liquid/solid interfaces (b). (Krause et al. [217], Koza et al. [220]).
- Fig.64. Optical micrographs of CoFe deposits: (a) deposited without magnetic field and (b) deposited with $B = 1\text{T}$ [220].
- Fig.65. H atom adsorption sites on Fe(111) surface (Huo et al.[240]).
- Fig.66. The Bravais lattice indicating hexagonal simple structure of cobalt.
- Fig.67. The Bravais lattice indicating a simple hexagonal structure of cobalt with marked calculation part.
- Fig.68. Crystallographic structures of cobalt with marked planes determined by CaRIne 3.1 software and geometrical parameters.
- Fig.69. Example of the adsorption sites of hydrogen at cubic-Co surface: (a) – bridge site, (b) – 3-fold site.
- Fig.70. X-ray diffraction patterns of the electrodeposited Co at different bath pH.
- Fig.71. X-ray diffraction patterns of the electrodeposited Co films under 1T magnetic field.

List of Symbols

- F_P – paramagnetic force, $N.m^{-3}$
 F_L – Lorentz force, $N.m^{-3}$
 F_B – field gradient force, $N.m^{-3}$
 F_E – electrokinetic force, $N.m^{-3}$
 F_D – magnetic damping force, $N.m^{-3}$
 q – electrical charge, C
 v - velocity, $m.s^{-1}$
 B – magnetic flux density, T
 t – time, sec
 ρ – density, $g.cm^{-3}$
 P – pressure, Pa
 i – electrical current, $A.cm^{-2}$
 σ_d - charge density in the diffusion layer, $C.m^{-1}$
 E_{II} – induced non-electrostatic field, $N.C^{-1}$
 σ - solution conductivity, $S.m^{-1}$
 μ_0 – permeability of the free space, m^{-2}
 μ – magnetic moment
 χ_m – susceptibility, mM
 B_z – Boltzmann constant, $1.38.10^{-23} J.K^{-1}$
 T – temperature, K
 d – grain size, nm
 k – shape factor
 λ – X-ray wavelength, nm
 β – full width at half maximum intensity
 θ – Bragg angle
 Z_{HF} – high frequency electrochemical impedance,
 R_s – resistance, ohm
 Q – constant phase element
 γ – surface tension

E – electrochemical potential, V

R – gas constant, $8.314 \text{ J.K}^{-1}.\text{m}^{-1}$

a – activity of ion

List of Abbreviations

MEMS – microelectromechanical system
QM – quantum mechanics
DFT – density functional theory
fcc – face-centered cubic
hcp – hexagonal closed-packed
MED – magneto-electrodeposition
EQCM – Electrochemical Quartz Crystal Microbalance
HER – hydrogen evolution reaction
UPD – underpotential deposition
MHD – magnetohydrodynamics
MMC – micro-magneto convection
LISM – Laboratoire d'Ingénierie et Sciences des Matériaux
LNCMI – Laboratoire National des Champs Magnétiques Intenses
ITO – indium tin oxide
SEM – Scanning Electron Microscope
AFM – Atomic Force Microscope
EIS – Electrochemical Impedance Spectroscopy
XRD – X-ray Diffraction
EDS – Energy-Dispersive X-ray Spectroscopy
WD-XRF – Wavelength-Dispersive X-ray Fluorescence
MFM – Magnetic Force Microscope
AGFM – Alternating Gradient Force Magnetometer
VSM – Vibrating Sample Magnetometer
WE – working electrode
AUX – reference electrode
CE – counter electrode
SSE – Saturated Sulphate Electrode
PDF – Powder Diffraction File
JCPDS – Joint Committee on Powder Diffraction Standards
FWHM – full width at half maximum

HMF – high magnetic field

LMF – low magnetic field

3D – three-dimensional

2D – two-dimensional

MBE – molecular beam epitaxy

HT – heat treatment

WFT – Wave Function Theory

LDA – Local Density Approximation

GGA – generalized type orbital

GTO – Gaussian type orbital

General Introduction

In the age of nanostructured materials and well performed magnetic devices it seems reasonable to provide investigations on the improvement of relationship between structure and properties. Ferromagnetic films consisting of transition metals (e.g. Co, Ni, Fe) or their alloys have a wide range of applications in data storage devices, write-read heads, and sensor technology. Especially Co-based magnetic films are used in microelectromechanical systems (MEMSs), including microactuators, sensors, micromotors, etc.. In this way, magnetic nanostructures are vastly examined due to their functional and technological properties.

The magnetic behaviour of Co-based materials is currently a field of very active research due to the ability for exhibition new, stable and beneficial magnetic properties. Moreover, the production of such films using several deposition techniques has aroused great interest, because many of their properties may be changed with preparation methods as well as deposition parameters. Electrodeposition has been one of the techniques used to produce ferromagnetic single-element, alloy and multilayer films for a long time, since it has some advantages such as low cost, simplicity and fast production. Moreover, it is attractive due to a high degree of control, which can be obtained by varying the experimental conditions.

Since the material properties are affected by the structure, which in turn depends on the production method, it seems interesting to investigate its formation under different process conditions. One of them is a superimposed magnetic field on the electrolytic cell, which is well known to influence the hydrodynamic conditions in the electrolyte and thus, affects the microstructure formation of material. Furthermore, the material microstructure formation may be modified by some external routes, such as annealing and/or magnetic annealing processes. As a consequence, the resulted material microstructure performs different characteristics and properties.

Development of the material science is generally done by a multidisciplinary approach. Modeling and simulating of the fabrication processing allow predicting the final microstructure of material with required properties. The quantum mechanics (QM) and density functional theory (DFT) are novel routes in the materials design. The possibility of their use creates a new opportunity to model and predict the material form, before it will be fabricated.

The aim of this work is to model and to investigate the relationship between structure and properties of the electrodeposited Co-based films, such as single Co, binary Co-Ni and Co-Cu, and ternary Co-Ni-Cu alloy films, by a multi-scale approach.

The thesis consists of four chapters organized as follows:

Chapter I – is the literature review section, which summarizes the main subjects involved in the thesis. In the first order the basics of electrodeposition process are described and refer to the examples of electrodeposition mechanism of cobalt and Co-based alloy films. The parameters affecting electrodeposition process and effect of a superimposed magnetic field is considered as well.

Chapter II – is the experimental results section. It consists of the experimental methodology route followed by the preliminary study, where firstly, the determination and optimization of the electrodeposition parameters are investigated. Secondly, the effect of a superimposed magnetic field on the microstructure of cobalt and Co-based alloys is determined. Additionally, this section contains also the electrochemical investigations related to the kinetics and dynamics of deposition process influenced by an external magnetic field.

Chapter III - is the application approach section. It is focused on the determination of magnetic properties and structure improvement by annealing and magnetic annealing treatments. The magnetic characterization and annealing effects are described and the relation between structure and properties is discussed.

Chapter IV – is the theoretical study section. The Quantum Mechanics (QM) and Density Functional Theory (DFT) studies are involved in the modeling of hydrogen adsorption process onto cobalt surfaces. It consists of description of QM and DFT techniques and calculation of the adsorption energies of hydrogen onto cobalt structures: hexagonal closed-packed (hcp) and face-centered cubic (fcc). The relationship between theoretical and experimental studies is presented.

Chapter I

Literature review

1.1. Introduction

In parallel with development of the new processes, considerable effort has been devoted to gain a fundamental understanding of electrodeposition. Electrochemical deposition processing, among many other advantages, is mainly used to reflect material properties and to improve contact resistance and friction properties. It is also a good method to improve corrosion resistance or particular desired physical and/or mechanical properties of the metal surface. The material properties are determined by nucleation process that occurs at the early stages of electrodeposition. They are strongly dependent on deposition parameters, such as current density, deposition potential, pH, additives, bath temperature, etc.. The main problem involved in the production of films by electrodeposition method is roughening. Numerous studies can be found considering the possibilities to resolve the problem with rough deposits surface. One of the methods of tackling this problem is magneto-electrodeposition (MED). MED is an electrodeposition phenomenon occurring under the influence of a magnetic field on the formation of a substance layer on an appropriate substrate in externally imposed magnetic field. An important role of superimposed magnetic field during electrodeposition process is also modification of deposit morphology, depending on the magnetic character of deposited metal. Hence, it seems reasonable to investigate the electrodeposition process of materials, which can be affected by external conditions, as magnetic field, and thus, improving the properties of deposited films.

The followed sections are based on the problematic considered in this thesis and thus, present:

- principles of the electrodeposition process, since it has been the main production route of Co-based films in this work,
- description of the possible electrodeposition mechanism of cobalt, due to the investigations of different Co-based systems and theoretical study part,
- effects of the electrodeposition parameters (e.g. electrolyte pH, additives, etc.) and conditions (superimposed external magnetic field) on microstructural formation of Co-based films in relation with the experimental study part,
- characteristics of the obtained microstructure, according to the application approach study.

1.2. Background of electrochemical deposition

Electrodeposition is a process in which the metal atoms are deposited on a conducting substrate by passing a current through electrolytic solution containing the to-be-deposited metal(s). The schematic diagram explaining the electrodeposition is shown in Fig.1.

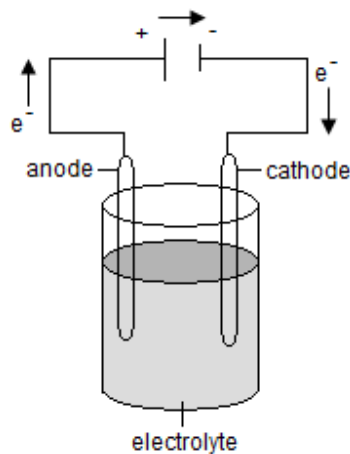


Fig.1. Schematic diagram of the electrodeposition process.

The typical electrodeposition setup consists of following components:

- electrolytic solution,
- cathode and anode,
- source of electricity.

When the current passed through cathode and anode immersed in electrolyte containing the to-be-deposited metal(s) ions, the metal ions get attracted towards cathode neutralized electrically by receiving electrons and get deposited cathode. Deposition is controlled by controlling the amount and rate of charge passing through the electrolyte. Thus, the electrical energy is used to cause chemical change. The net result is that the metal (cation) is deposited on the cathode from a solution of metal ions according to following process:



On the other hand, if the electrolyte contains more than one ionic species that can be simultaneously deposited, then the electrodeposition process for, say two types of ionic species can be written as:



Accordingly, one can deposit a compound or an alloy of a multicomponent system. When electrolysis is carried out in the electrolyte, metal is deposited on the cathode and at the same time anode can be dissolved in the solution or another reaction can occur, i.e. water oxidation. The amount of dissolution and deposition is determined by the quantity of electricity passed and by the electrochemical reactions that occur (deposition, dissolution, metal reduction or oxidation).

1.2.1. Steps involved in the electrochemical deposition process

Electrodeposition of ionic species from the electrolyte occurs in the following successive steps:

- ionic transport,
- discharge,
- breaking of ion-ligand bond (if the bath is complexed),
- incorporation of ad-atoms onto the substrate followed by nucleation and growth processes.

All above steps occur within 1-1000 angstroms from the substrate. However, each of them has its own region of operation. These various processes can be classified with respect to the distance from the electrolyte (Fig.2), as:

(a) in the electrolyte

1 – Migration. Ions in the electrolyte can move towards the electrode under influence of potential gradient and mechanical convection, leading to ion drift.

(b) near the electrode surface

2 – Diffusion; 3 – Rearrangement of the ionic atmosphere; 4 – Reorientation of the solvent dipoles; 5 – Modification of the distances between ligands and central ions.

Ionic species are normally surrounded by a hydration sheath or by other complex forming ion or ligand present in the electrolyte. They move together as a single entity and arrive near the electrode surface, where the ion-ligand system either accepts electrons from the cathode, or donates electrons to the anode.

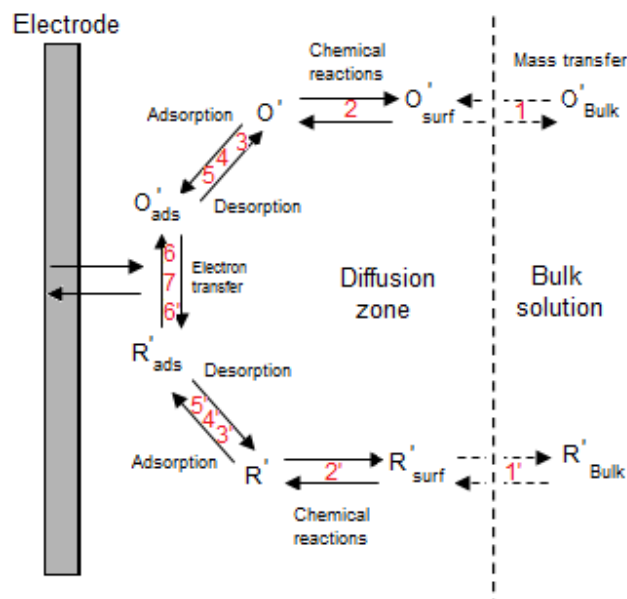


Fig.2. Approximate regions in which the various stages of ion transport occur, leading for electrodeposition.

(c) at the electrode surface

6 – Adsorption-surface diffusion-electrocrystallization; 7 – Electron transfer.

The ions arrive near the electrode, where step by step they lead to the formation of a new solid phase or the growth of an electrodeposit. The atoms deposited have a tendency to form either an ordered crystalline phase, or a disordered amorphous phase. The electrodeposit formation steps of transport, discharge, nucleation and growth are interlinked.

1.2.2. Pathways for the growth of electrodeposit

Four types of fundamental areas are involved in the electrochemical deposition process (Fig.3):

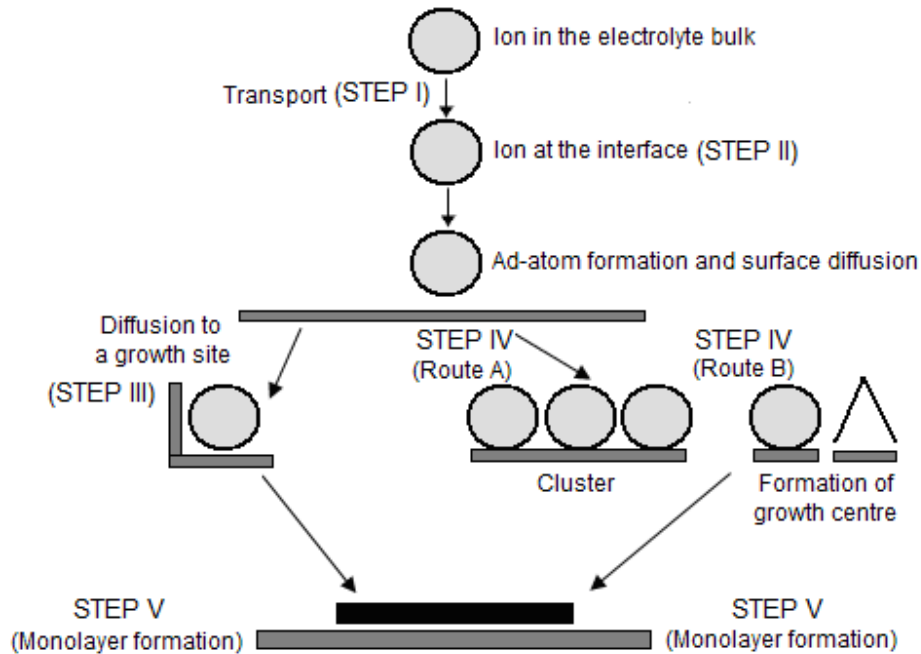


Fig.3. Schematic representation of the steps involved in electrodeposition.

- electrode/electrolytic solution interface as the locus of deposition process – STEP I,
- thermodynamics and kinetics of the deposition process – STEP II,
- nucleation and growth processes of deposits, where again alternative routes are possible:
 - (a) growth assisted by surface diffusion - STEP III,
 - (b) growth assisted by formation of clusters and critical nuclei - STEP IV,
 - (c) formation of monolayer and final growth of electrodeposit - STEP V,
- structure and properties of the deposits.

Among them the first two: electrode-electrolyte solution interface and thermodynamics and kinetics, are the most important in the whole electrodeposition process, because they determine the early stages of nucleation and growth modes of electrodeposit. Thus, the followed section provides a brief discussion on these areas.

1.2.2.1. Thermodynamics and kinetics of the electrodeposition process

Thermodynamics and kinetics of the electrochemical deposition process are generally related to the nucleation mode, which is strongly affected by temperature at which the process is undertaken. Alternations in the temperature range used may affect kinetics in the following way: decreasing temperature increases the activity of ions, causing faster nucleation rather than nuclei growth. Thus, the critical nucleating condition will occur at low temperature. The relationship between morphology and early stages of electrodeposition (electrocrystallization) is an open area of research.

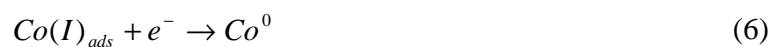
In the formation and growth of ad-ion clusters, two processes are of fundamental importance:

- (i) the arrival and adsorption of ions (atoms) at the surface,
- (ii) the motion of these adsorbed ions (ad-ions, ad-atoms) at the surface.

An ad-ion deposited at the surface of a perfect crystal stays at this surface as an ad-ion only temporarily, since its binding energy to the crystal is small. It is not a stable entity on the surface, but it can increase its stability by formation of clusters. The transfer of ions is purely a thermodynamic conceptual origin. Under the state of thermodynamic equilibrium in an electrochemical system comprising metal ions in electrolytic solution, metal ad-atoms on an electrode, and metal atoms in the deposit, the system is stable.

1.3. Electrodeposition mechanism of Co and Co-based alloys

Several mechanisms for cobalt electrodeposition have been proposed in the literature [1-5]. The main idea lies on assumption that the pH in vicinity of the cathode surface increases due to the hydrogen evolution reaction and cobalt hydroxide can be formed. In general, the most comprehensive studies report that deposition occurs similarly to that of other iron-group metals as for example iron and nickel, by involving the consecutive one-electron transfer steps [6-13]. The first step involves formation of an intermediate ad-ion $Co(I)_{ads}$ (Eq. (5)), which is then consumed in the second step to produce metal (Eq. (6)) [14]:

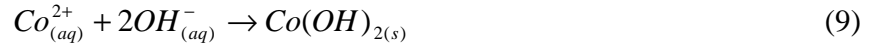


Pradhan et al. [4] and Ciu et al. [5] reported that the cobalt electrodeposition mechanism is thought to occur via the formation of CoOH^+ and Co(OH)_2 species. The formation of hydroxide species depends on the pH of deposition bath. For solution pH lower than 4.0, the authors proposed that Co^{2+} and OH^- ions react with each other producing CoOH^+ , which is in the form of “unstable complex”. The reaction that follows next is the reduction of this complex and its reaction with adsorbed hydrogen to form metallic cobalt. For solution pH between 4.0 and 4.5 they proposed that Co^{2+} and OH^- ions reacts producing cobalt hydroxide, which is then reduced to produce metallic cobalt. The last reaction involving reduction of the adsorbed hydroxide causes an increase of OH^- ions concentration near the electrode, which changes the surface pH. Since OH^- ions are formed during the cobalt reduction, at pH 4.0 and 4.5, this mechanism does not result in hydrogen evolution reaction. On the other hand, Jeffrey et al. [3] proposed an alternative mechanism involving CoOH^+ ions, whereas the authors did not mention if these ions are free or adsorbed on the electrode surface. Furthermore, the authors did not consider the dissociation constant of those ions under their experimental conditions, leaving their proposed mechanism very unpredictable. Moreover, they suggested that the limiting step for the proposed mechanism is the reduction of CoOH^+ to metallic cobalt. Unfortunately, again the authors did not mention how these particularly unstable species were formed. Another mechanism for cobalt electrodeposition have been proposed by Jiang et al. [1,2], who investigated different reaction paths that involve the formation of cobalt hydroxides and oxides species, as well as mentioned unstable cobalt complex ions, as the prior products before effective deposition of metallic cobalt.

Considering aboved descriptions, Matsushima et al. [15] presented a study aiming the usage of Electrochemical Quartz Crystal Microbalance (EQCM) technique simultaneously with cyclic voltammetry in order to compare past results and to propose a practical and alternative mechanism for cobalt electrodeposition at different pH unbuffered solutions. It was reported that only two different reactions, i.e. direct cobalt reduction and cobalt hydroxide formation, describe the current process without further intermediates. The last reaction is a consequence of the parallel hydrogen evolution reaction. A flux model considering these proposals was made and fitted the experimental data. For the purpose of elaborating a mathematical flux model, it was assumed that only the direct reduction of cobalt takes place, as shown by the equation below:



On the other hand, during metal electrodeposition from an aqueous solution at negative potentials, the parallel reaction of water electrolysis occurs. Such a reaction can be related to the formation of Co hydroxides:

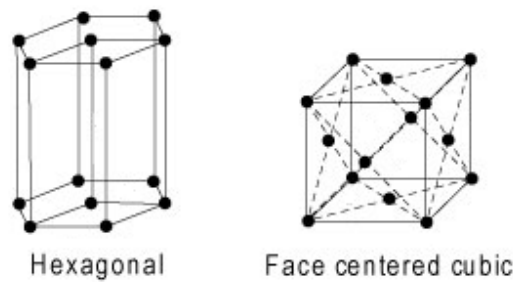


Summarizing, Eqs. (8) and (9) are related to the formation of $Co(OH)_2$, while equation (7) stands for the direct deposition of cobalt. Cobalt hydroxide reduction requires a much more negative potential than direct cobalt reduction. Considering the simultaneous reaction of water electrolysis (Eq. (8)) and Co^{2+} ions reduction, it can be proposed that the amount of generated OH^- ions is directly proportional to the amount of formed $Co(OH)_2$ species (Eq. (9)).

1.3.1. Structural characteristic of the electrodeposited cobalt

The review of publications in the past twenty years shows that the interest in cobalt containing alloys grows due to the expansion of their application areas. Among the iron-group metals, cobalt is an important ferromagnetic element, which due to its various structure and morphology formation with other elements, exhibits some unique properties of high importance.

Electrolytic cobalt crystallizes with both hexagonal closed-packed (hcp) and face centred-cubic (fcc) lattice structures (Fig.4.).



Crystal system	Edge length	Interaxial angle
Hexagonal	$a = b \neq c$	$\alpha = \beta = 90^\circ, \gamma = 120^\circ$
Cubic	$a = b = c$	$\alpha = \beta = \gamma = 90^\circ$

Fig.4. The Bravais crystalline systems representing hexagonal and cubic structures [16].

The hcp phase is thermodynamically stable at temperature below 417°C [17]. The transformation energy between stable hcp phase and high-temperature fcc phase is determined by the stacking fault energy, which is very low for cobalt. A magnetically induced phase transformation is in principle possible, when the mobility of the atoms is high enough and the magnetically induced energy is in the same order of magnitude as the transformation energy [18].

The formation of fcc-Co by electrodeposition has been studied in details and still remains a research topic of primary relevance, although in recent years the attention has been particularly focused on phase selection as related to substrate influence [19,20] and deposition conditions [19,21,22]. The first extensive reports on the crystal structure of electrodeposited hcp-Co appeared in 1966, by Cadorna and Cavallotti [23] and by Pangarov and Vitkova [24]. According to the latter, the experimental results were in substantial agreement with the theory of 2D nucleation [25]. The following investigations were almost exclusively focused on deposition from Watts's type electrolyte or from buffered sulphate solution. Deposits having biphasic composition show a hcp-(110)+fcc-(110) texture, from buffered sulphate [26,25-28] or sulphamate [23] solution, in agreement with the early observation of Finch *et al.* [29]. With increase of pH the structure becomes completely of the hcp-phase and deposits texture depends mainly on solution pH [23,27-30] and, to a minor extent, on temperature [27] and current density [31]. The prevailing orientations and their stability with respect to the operative conditions are characterized in details for both sulphate [23,26-28,32] and chloride based electrolytes [33].

Early attempts to interpret the growth modes of electrodeposited cobalt followed Reddy's views on nickel electrocrystallization [34]. The different growth textures were explained as a consequence of competitive adsorption between hydrogen and intermediate species [27] or classified according to growth conditions related to different degree of inhibition [26]. Subsequently, the main importance of the electrolyte pH was recognized. It was suggested [35] or explicitly stated [36] that the surface pH and the related chemical phenomena at the cathode surface were the major factors responsible for the development of different textures [30,37]. The structural bearing of hydrolytic phenomena received further support from the work of Croll [30], who reported that depositing from CoSO₄ electrolyte, in the absence of boric acid, a sharp change from (100)+(110)-hcp to (001)-hcp preferential orientation takes place at pH about 4 within a short range. When boric acid is present the (100)+(110)-hcp preferred orientation weakens gradually as the pH raises and the transition pH is higher, about 6.4. The possibility of obtaining the three main growth orientations of hcp-Co by autocatalytic deposition [38] and the assessment

of the conditions giving Co cellular growth [39,40] with strong (001)-hcp texture definitely pointed out the decisive contribution of reactive hydrolysis in determining the deposits structure.

1.3.2. Parameters affecting electrodeposition process

In the electrodeposition process, the main objective is to produce a uniform deposit on the metal to-be-coated. From this reason as well as from the fact that the properties of an electrodeposit are significantly changing depending on the operating conditions, a systematic study about the parameters affecting properties of an electrodeposit is required. In the electrodeposition process, the main parameters to be considered generally include current density or deposition potential, bath type, electrolyte pH, temperature and presence of additives. Among them the deposition current/potential, electrolyte pH and additives are found to be the most significant. The effect of current density on the structure of electrodeposits is particularly important because it greatly changes the cathodic potential. However, a secondary process – hydrogen evolution reaction, will also be produced at the cathode. Temperature and pH control are always desirable in deposition conditions because they affect the characteristic of deposition solution and/or the deposit. Agitation of deposition solution is also usually helpful in influencing the structures of deposits. Although agitation causes the formation of coarse-grained deposits, it permits the use of higher current densities. Nevertheless, by adjusting the electrochemical deposition conditions as well as physical parameters, such as substrate type, it is possible to control and optimize the structural, mechanical and magnetic properties of electrodeposited films.

1.3.2.1. Effect of current density and deposition potential

In the electrodeposition process, the sheer amount of material deposited on a cathode is practically not uniform and greatly influenced by the current distribution. In practice, the metal ions do not deposit as continuous sheets from one edge of the cathode to the other. In general, the metal ions are attached to the cathode at certain favoured sites. This condition will possibly result in the presence of discontinuities in the form of pores, cracks or other irregularities. Thus, the current density and its distribution play a key role in determining the quality of final deposit.

Cojocaru *et al.* [41] investigated the Co-Ni system deposited at different current densities. With their experimental conditions, compact, no fragile and very fine-grained deposits were

always obtained. All Co-Ni deposits showed diffraction peaks corresponding to the fcc structure. The position of diffraction peaks indicating alloy formation was shifted to lower angles than those corresponding to pure Ni, as a consequence of incorporation of Co atoms in the fcc crystalline lattice of Ni. An increase of current density favoured the decrease of Co percentage. This behaviour was ascribed to a nickel deposition process controlled by activation, whereas Co deposition process can be controlled by a mass transfer. Bahadormanesh *et al.* [42] showed that higher current densities used during electrodeposition provide more reductive circumstance and consequently more activation energy for deposition. This is more beneficial for deposition of the species controlled kinetically than that controlled by diffusion. Therefore, increasing the current density, the contribution of Ni ions in the electron transfer is enhanced and their content in the deposits increases, which is equivalent to the reduction of relative amount of cobalt in the deposits. Zhao *et al.* [43] proposed an original approach to design of a self-lubricant coating based on the electrodeposition of nanostructured columnar or cellular cobalt films. The investigated effect of current density on the morphology and crystal structure of Co deposits showed that by an applied low current density a faceted morphology consisting of crystal of either polyhedral or pyramidal shape, with a relatively large distribution of grain size was obtained. Occasionally, either in-plane or slightly inclined hexagonal facets appeared at the surface, denoting the lower quality of basal orientation of the layer. At higher current densities, a larger population of smaller grains and an increasingly mound shape top was observed. The faceted growth at low current density or the extent of it at higher current density was linked to the nucleation intensity, which increased with current density increase.

Some of the publications consider also the effect of deposition potential. For instance, Karaagac *et al.* [44] reported the role of cathode potential on crystal structure and magnetic properties of Co-Cu films electrodeposited on polycrystalline Cu substrates. It was observed that the crystal structure of Co-Cu films changed with Co:Cu ratio, which was affected by the cathode potential. The films had mostly fcc and partly hcp mixed phase. The (111) peak of fcc structure splits into two as Co(111) and Cu(111). Intensities of the (111) peaks changed with composition of the film caused by changes in the values of deposition potential. Surface morphology indicated dendritic growth when they grown at a low potential (-1.0V), while at high cathode potential value (-1.6V) the detected growth was dominated by a roundish cauliflower shape. It was also found that the Cu-Co properties change significantly with the cathode potential. A decrease of deposition potential resulted in an increase of the Cu content in the film. Hence, the magnetic

properties of the films were affected strongly. Qiu et al. [45] in their study on tunable electrochemical preparation of micro/nanostructured cobalt showed that cobalt can exhibit series of morphologies, i.e. bumps, flowers and dendrites, when subjected to variations in the applied crystal growth potential and at the same precursor concentration and temperature of the electroplating bath.

1.3.2.2. Effect of electrolyte pH

The electrodeposition process is dominated by the dissolution of freshly deposited metal atoms, formation and adsorption of metals hydroxides and normal electrodeposition of metals. A lower pH value favours the dissolution of freshly deposited metal and depresses the formation and adsorption of metal hydroxides. The process is predominated by normal deposition of metal, resulting in lower Co content in the coatings due to the lower Co^{2+} concentration in electrolyte. Nevertheless, a higher pH value favours formation and adsorption of the metal hydroxides and depresses the dissolution of freshly deposited metal. The process is predominated by the second factor, the preferential adsorption of cobalt hydroxides, results in higher cobalt content in the coatings [46]. At lower pH value, higher H^+ concentration favours the evolution of hydrogen (HER) and more current is consumed on hydrogen reduction, resulting in the lower current efficiency. However, when the pH is high, lower H^+ concentration depresses HER and less current is consumed, leading to a higher current efficiency.

It has been reported by Mentar [47] that electrochemical deposition from a bath at pH more than 2.9 results mainly in hcp-Co. However, in the literature the formation of fcc-Co phase by electrodeposition route at room temperature is due to the presence of co-discharge and dissolved hydrogen distorting the hcp lattice to an extent that is finally transformed to the fcc structure. Moreover, it has been shown that when the electrolyte has a pH value about 3, and the stirring of electrolyte is absent, the fcc structure is favoured. According to the work of Tian et al. [48], at lower pH value (2.0 and 3.1) atomic hydrogen and hydroxides dominate in the coatings. At higher pH value (4.3 and 5.4) the influence of hydrogen and hydroxides become less apparent and the visible dark circle holes appearing at the surface at low pH nearly disappear. Simultaneously, the deposition ratio becomes larger with the increase of pH. The higher deposition ratio causes a situation where there is not enough time for internal stress release and cracking of coating may occur [49]. The coatings tend to be more compact with the increase of

pH value because of the weakening of hydrogen evolution at higher pH. Alper *et al.* [50] made a comparison between electrodeposited Ni-Cu alloys at low and high pH levels, deposited on the Ti substrates. Their results indicated that the texture formation of Ni-Cu films changed depending on the electrolyte pH. The X-ray diffraction data showed that the (100) texture of fcc structure in the films grown at high pH (3.3) develops preferentially, while for the films deposited at low pH (2.0) the crystal planes are randomly oriented as in a powder pattern of bulk Ni (or Cu). It has also been reported elsewhere (Mizushima *et al.* [51]), that the electrolyte pH hardly affects the crystallographic structure of Ni-Cu alloy films, which were deposited on Cu substrate with the presence of some complexing agents.

The surface morphology of deposited films is also significantly affected by the electrolyte pH [50]. Films deposited at high pH were characterized by rougher surface consisted of larger crystallites, compared to those grown at low pH. The change of surface morphology with the electrolyte pH may be explained by hydrogen evolution that occurs at the cathode surface. Fenineche *et al.* [52] studied the effect of chloride bath plating conditions on the microstructure of Co-Ni deposits. They noticed that the quality of Co-Ni deposits depends markedly on the pH of electrolytic bath. A study of the variation of surface morphology with pH revealed that low pH values (1-3) tend to favour the formation of smooth bright deposits. However, medium pH values (3-4) tend to enhance the rate of nucleation, resulting in a higher cathode current efficiency. Hardness values also tend to decline when the pH is increased. At low pH, the cathode current efficiency is limited by hydrogen evolution on cathode, but at higher pH it seems to be a tendency for basic insoluble hydroxides to be incorporated in the deposit, leading to imperfect deposits. The observed differences in the behaviour of deposited films may be due to the bath type and/or the used substrates [53,54]. However, the textured structure of films electrodeposited on several polycrystalline substrates, is known to evolve depending on deposition conditions, such as the electrolyte composition, pH, deposition potential and additives. The changes in texture degrees of deposited films from the electrolytes based on Ni has been usually attributed to the presence of inhibiting species, such as hydrogen and nickel hydroxide [55,56]. This may lead to the formation of different dendrites as well as affecting strongly the magnetic properties.

1.3.2.3. Effect of temperature

An effective control of the deposition process by operating temperature is vital for the consistent performance of any deposition bath. Deviation of more than 5°C from optimum temperature is sufficient to harm deposit quality, deposition rate and other properties. Electrolytic bath can usually be formulated and can operate satisfactorily at any given temperature within a relatively wide range, 20°C to 80°C [43,57-59].

Santos *et al.* [57] investigated the effect of temperature on the Co electrodeposition mechanism in sulphate solutions containing boric acid during potentiostatic depositions, using the Electrochemical Quartz Crystal Microbalance technique (EQCM). From the analyses of profile of voltammograms they pointed out that (i) the overpotential of cobalt deposition in the experiment carried out at 48°C was smaller than one at 25°C, (ii) the mass-potential curves showed an increase in the deposited mass over the working electrode for the measurements performed at 48°C, (iii) the total deposited mass on electrode was dissolved and (iv) the dissolution current peak related to the rich hydrogen phase was more evident in the electrodeposition carried out at 48°C. A local increase of the temperature in electrode surface may strongly affect the adsorption rate of intermediate species and change the cobalt deposition efficiency. As a result, the proton reduction rate will increase favouring the formation of hydroxylate species due to the OH⁻ formation. Also Elsherief [58], who studied the effect of temperature upon cobalt electrowinning from sulfate solutions, has shown that temperature has an effect on the cobalt deposition and dissolution reaction. Increasing the electrolyte temperature appeared to enhance the deposition reaction. However, it was found that the hydrogen evolution reaction occurs more readily at higher temperature [59]. The increase in temperature was also found to affect cathodic cobalt deposition more than the cobalt concentration of the electrolyte [60].

The performed experiments at different values of electrolyte temperatures have been also shown to cause some structural changes. Zhao *et al.* [43] observed a decreasing intensity of the (0002) reflection for the temperature of 50°C and the appearance of (0001)-hcp line at $T \geq 50^\circ\text{C}$, which were the main effects induced by deposition temperature during nanostructured cobalt electrodeposition. These observations in particular point to a destabilizing effect of a high deposition temperature on the (0001)-hcp texture growth of cobalt, possibly related to stronger inhibition at the surface due to the enhanced precipitation of cobalt hydroxide at higher temperatures. Another observation was noticed on the morphology modifications, where the

deposition temperature caused a progressive change from a mixed globular-faceted growth at 30°C, to a fully developed pyramidal growth at 50°C and finally, at 70°C, to the formation of polyhedral isolated large crystals. This modification was accompanied by a coarsening of the grain structure, which was probably caused by the reduction of nucleation intensity with raising bath temperature. Fenineche *et al.* [52] studied the effect of electrodeposition parameters on the microstructure and mechanical properties of Co-Ni alloys. They observed a decrease in cathode current efficiency and hardness with increasing temperature. For the lower temperatures, deposits were bright and smooth, while at higher temperatures (over 40°C) they were blackish.

1.3.2.4. Effect of electrolyte additives

Additives in galvanotechnology belong to a large variety of compounds. They can be salts with as simple anion as chloride ion, organic compounds with some heteroatom like S or N, aromatic compounds, complex-forming molecules with chelating capability, soluble polymers with polar groups and so on. Besides their chemical variety, the common features of these bath components are that (i) they bear one or several non-bonding electron pair(s) which (ii) can interact with either the electrode surface or metal ions in the solution. Therefore (iii) they are capable of substantially modifying the reaction kinetics and hence leading to a desired deposit property. Moreover, the impact of an additive is usually not universal in the sense that an additive with favourable influence on the deposition of a particular metal might be even harmful to the deposition of another metal.

It is clear that additives adsorb at the electrode surface during electrodeposition process and as such, they can modify the thermodynamics of nucleation process and grain boundary formation. As a result, the grain structure and level of stress in the deposit could be changed. It is also known that additives incorporate into magnetic films in the form of a low surface energy phase, such as sulfur related inclusions, molecular fragments or S- and C-containing intermetallic compounds [61-63]. They are segregated at the grain boundaries, affecting their specific energy or acting as stress relievers during the grain zipping process. Other additives used in galvanotechnology are classified as stress relievers, levelers and brighteners. These additives are usually applied in a very little concentration (a few millimol/liter as a maximum), as opposed to the metal salts and the complexing agents. They have a fundamental impact on the properties of deposits. The additives are used for regulating the residual internal stress, hardness, tensile stress,

corrosion resistance and the smoothness and brightness of the surface [64]. The followed sections include the description of two additives, usually added to the electrolytic solutions, which have been also used in this work.

1.3.2.4.1. Boric acid

It is known that during electrodeposition process pH changes near the electrode surface are possible, especially when the process is carried out from the simple bath. To avoid this situation it is common to add boric acid (H_3BO_3) in the electrolyte to inhibit the formation of hydroxide species [65-68]. The protons released from the aqueous solution of boric acid



in the cathodic diffusion layer, reacts with the hydroxide ions to form water. As a result, more energy is required for the reduction of water, thereby shifting its potential to more negative values. Thus, the use of boric acid offsets the increase in pH associated with the onset of water electrolysis. Hence, the deposition can be accomplished without interference from hydrogen evolution [66]. This specificity of boric acid may be the primarily responsible for the growth of dendrites. It acts also as a brightening agent and as a cathode polarizer for electrodeposition. The silent features of boric acid include:

- (i) pH buffering agent [69],
- (ii) catalyst for deposition [70],
- (iii) suppresser for hydrogen evolution [70]
- (iv) accelerator for the growth of deposits [71].

Unfortunately, the real function of this additive in electrodeposition is yet a matter of controversy and a lot of propositions have been done.

Most of the authors proposed that the boric acid acts mainly as a buffer agent. This effect is thought to be a dynamic process occurring during hydrogen evolution reaction. Consequently, the dissociation kinetics of buffer must be fast enough to supply protons during molecules discharge occurring at the electrode surface. Horkans [72] concluded that the dissociation of HSO_4^- as well as H_3BO_3 is so slow that the overall buffer contribution is ineffective during HER in sulphate electrolyte. However, it was suggested that this additive may act as a homogeneous catalyst, which decreases the metal electrodeposition overpotential. Moreover, Yin and Lin [70]

proposed that boric acid works as a selective membrane inhibiting movement of the ions during diffusion-controlled process at the electrode.

Despite all mechanism propositions for Co electrodeposition, Santos *et al.* [57] investigated the effect of temperature on the Co electrodeposition mechanism with a presence of boric acid in the solution. The results indicated that the boric acid remains effective after the experiment performed at 48°C, in which the additive was ineffective. The explanation of this behaviour was followed by the observations made by Jeffrey *et al.* [3] and Elsherief [58] who proposed that HER contribution is intense in experiments carried out at high temperatures. If the hydrogen evolution reaction is more effective at 48°C, the formation of OH⁻ ions must be larger than in the case of experiment carried out at 25°C. The results showed that only metallic Co was deposited at 25°C, whereas a large amount of Co(OH)₂ was detected at 48°C. If considered the kinetics of boric acid dissociation, it can be proposed that this dissociation is the rate-determining step during HER. In this case, the dissociation rate is not fast enough to provide the increase of concentration of OH⁻ at the surface of electrode for the experiments performed at 48°C. These results suggested that, under chosen condition, the buffer contribution of boric acid is not effective in the electrodeposition process at high temperature.

Vazquez-Arenas *et al.* [73] have investigated the effect of boric acid on the electrodeposition of Co-Ni alloy coatings. Boric acid has been shown to play a strong role and have a different effect on Co-Ni deposition that has been reported in some previous studies on iron-group alloys. They found that its presence had a little influence on coating composition whenever a significant amount of deposition occurred. However, the same cannot be said for the effect of boric acid on the current efficiency. In the absence of boric acid, the current efficiency never rose above 60% and the drop-off to near zero values occurred at relatively low current densities. On the other hand, in the presence of boric acid much higher current efficiencies were achieved over wide range current densities. Thus, for the conditions of this study, alloy deposition was not effectively possible, when boric acid was absent. Further analysis of the results suggested that some differences in the structure of film and dynamics of its formation occur, depending on whether it occurs in the presence or absence of boric acid.

1.3.2.4.2. Saccharin

Saccharin is one of the well known additive that influences the electrode kinetics during electrodeposition, producing levelled bright deposits. The HER is strongly inhibited in presence of saccharin. Current density is reduced, when sodium saccharin is added to the electrolyte indicating that in the presence of this organic additive the electrodeposition kinetics is reduced. The relationship between the molecular structure of saccharin and its action on the electrodeposition process is not completely clarified. This kinetic reduction has been related to the surface coverage by molecules, reducing the active area for the deposition process [74,75]. On the other hand, a complexation process may also be involved, as saccharin is known to form a complex with cobalt [76] and therefore may slow down Co ion diffusion. The addition of saccharin promotes morphological changes. By adding saccharin to the electrolyte, the nuclei size decrease and the silicon surface becomes more covered by the Co deposit. Visually it is possible to see that the increase of saccharin concentration promotes brighter deposits and adherence is also increased. In the work of Manhabosco *et al.* [77] it was found that the deposits obtained from the electrolyte without saccharin presented two phases, hcp and fcc. In the deposits obtained from the electrolyte with saccharin only presence of hcp phase was identified. Lallemand *et al.* [75] also found that in the absence of additives, cobalt-rich Co-Fe films present both hcp and fcc phases. In the presence of saccharin they also reported the presence of only a single phase. This difference can be related to the substrate, bath and film composition as well as electrochemical parameters.

Moreover, the authors [77] noticed that the magnetic properties were also affected by this additive. The remanent magnetization and coercive field rise as the saccharin concentration increased and the nuclei size become smaller. The addition of saccharin brings about a reduction of the Co content, i.e. the saccharin addition facilitates the deposition of Ni and hinders that of Co [78]. In the case of Cu-Co heterogeneous alloys electrodeposited from complexed citrate bath by pulse current electrolysis, reported in work of Ghosh *et al.* [79], an addition of saccharin within the electrolyte enhanced a phase segregation tendency, resulting in more evenly distributed two-phase microstructure. Brankovic *et al.* [80] investigated the effect of saccharin as a stress reducing additive in electrodeposition process of Co-Fe alloy films. The saccharin adsorption on the growing Co-Fe surface effectively change the driving force for Co-Fe grain zipping process

and consequently it changed the maximum level of stress in the film. This was possible by a control of saccharin coverage of the film surface.

In some cases, the hardening effect by saccharin addition is observed. This is understandable, when the grain refinement effect is taken into account. It is clear that the strength and hardness of a metallic material significantly increase with the grain size decreasing [74]. Increase in saccharin content leads to hardness decline of the Ni-Co alloy.

1.3.3. Co-electrodeposition with less noble metal

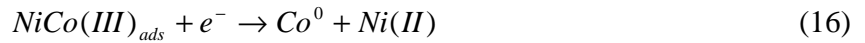
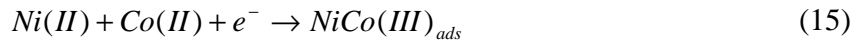
The Co-electrodeposition with less noble metal is described in term of anomalous co-deposition and refers to the preferential deposition of less noble metal rather than the more noble one. The phenomenon of anomalous co-deposition has been reported mainly in co-deposition process of iron-group metals, such as Co, Ni, Fe, and it can be attributed to the three factors:

- (i) dissolution of freshly deposited metal atoms on the substrate because of acid circumstances in the electrolyte,
- (ii) formation and adsorption of metal hydroxides on the electrode surface,
- (iii) normal electrodeposition of metals.

The effect of the second factor is more important, because the normal co-deposition always exists and the dissolution of freshly deposited metal atoms is less apparent at low pH [48].

The well known example of anomalous co-deposition process is the electrodeposition of Co-Ni alloys, where Co as a less noble metal is preferentially deposited [81,82]. In different studies, the anomalous Co-Ni deposition was explained by several mechanisms: an increase of pH near the deposit-electrolyte interface during HER and therefore, precipitation of the cobalt hydroxide at the surface, or two-step mechanism containing the adsorption of a monovalent intermediate and its reduction to the elemental state, competitive adsorption of electroactive species, underpotential deposition and fast kinetics of cobalt species under diffusion control [81-99]. In the case of Co-Ni system, when the pH value exceeds the critical value for forming metal hydroxide, both Co and Ni hydroxides may be formed. The anomalous co-deposition occurs because of the preferential adsorption of cobalt hydroxides. When pH value remains below the critical value, Co^{2+} and Ni^{2+} ions exist as the form of CoOH^+ and NiOH^+ [49]. It is believed that both the monohydroxides and hydroxides of Co are favored in aqueous solution [100].

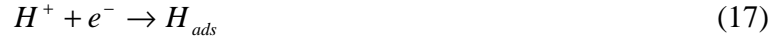
A model that more comprehensively captures the phenomena occurring during co-deposition of iron-group metals was presented by Zech *et al.* [101,102]. The authors compared the measured partial current densities for metal co-deposition during an alloy formation with deposition of the single metal alone. Their results demonstrated that not only the Ni deposition is inhibited in the presence of Fe^{2+} or Co^{2+} ions during alloy formation, but also the deposition of less noble metal, i.e. Fe or Co, is accelerated when Ni^{2+} ions are presented in the solution. The inhibiting effect is generally stronger when the reaction rate of the less noble metal is kinetically controlled and diminished as the limiting current is reached. In view of these findings, Zech *et al.* proposed a model considering the acceleration of co-deposition of the less noble component and inhibition of the more noble one. The model accounts for three parallel reactions occurring in one-electron transfer step: reduction of the more noble (Eqs. (11) and (12)) and less noble component (Eqs. (13) and (14)) by independent reactions and catalytic-inhibiting reduction reactions, in which two components interact with each other (Eqs. (15) and (16)).



Reactions (15) and (16) can be considered to be catalytic for Co(II) reduction in that they provide another pathway to deposit cobalt, but are inhibited toward nickel deposition in that the participating Ni(II) is never reduced and the NiCo(III)_{ads} adsorbed intermediate can block sites otherwise available to Ni(I)_{ads} and Co(I)_{ads} . This model also considers side reaction due to H^+ and water reduction via two-electron transfer steps and mass-transport by diffusion. To date, this is the most comprehensive analysis of anomalous behaviour. However, as stressed by these authors, some gaps particularly with regard to the quantitative prediction of an alloy composition exist in this model. One of these aspects is associated with a role played by HER in co-deposition of metals.

1.3.3.1. Hydrogen evolution reaction (HER)

It is accepted that HER involves the formation of an adsorbed species, i.e. H_{ads} , not considered in the model of Zech *et al.* [101,102]:



H_{ads} can block active sites at the surface of electrode, otherwise occupied by $Ni(I)_{ads}$, $Co(I)_{ads}$ and $NiCo(III)_{ads}$ species. Given the importance of competition between the different adsorbed species, this interaction may be significant and consequently its effect should be considered. Reaction (17) tends to increase the pH at the electrode/solution interface and can eventually become limited by mass transfer, particularly when carried out at higher overpotentials. These conditions lead to a third cathodic reaction in which water itself is reduced:



In addition, the buffering effect of boric acid, which is commonly added to iron-group metal baths, needs to be also considered. In single metal deposition of cobalt and nickel, this effect has been found to be very important, since the calculated surface pH is significantly affected by whether or not they are included. Since a similar situation should also exist during the co-deposition of Co-Ni alloys, this phenomenon should be included in the model. Also, since most of the deposition studies have been conducted using a rotating disk electrode, convective mass transport becomes important and should also be considered. Other important limitations in these previous studies were that the models were not statistically fit to the experimental data and not used to predict the alloy compositions or current efficiencies at different bath compositions. This incorporation of many or all of these phenomena into a model for Co-Ni alloy deposition would represent a significant advance over previous ones and presumably provide better insight into the behaviour of electrodeposited system.

A steady state model for Co-Ni alloy deposition applicable to polarization experiments was developed by Vazquez-Arenas and Pritzker [103]. By this, it was possible to fit the measurements obtained at different Ni^{2+}/Co^{2+} ion concentration ratios into the model in order to evaluate the kinetic parameters for proposed by Zech *et al.* [101,102] reaction mechanism and diffusion coefficients of the dissolved species. The model can predict the alloy composition and

current efficiency at different bath compositions extremely well on the basis of these parameters. In addition, it can be used to determine the total current densities, partial current densities of Ni deposition, Co deposition and hydrogen evolution reaction, as well as current efficiency for metal deposition. Further analysis of the model revealed that very little mixed intermediate $\text{NiCo(III)}_{\text{ads}}$ species form at the surface of electrode during alloy co-deposition and that the presence of these species is not required to explain the anomalous behaviour of this system, contrary to the proposed mechanism of Zech *et al.* The model also revealed that the preferential surface coverage of $\text{Co(I)}_{\text{ads}}$ over that of $\text{Ni(I)}_{\text{ads}}$ species is not required in order to accurately model the anomalous behaviour of Co-Ni system. Instead, the model indicates that the main factor accounting for anomalous Co-Ni electrodeposition is the much faster charge transfer of Co(II) reduction compared to that of Ni(II) reduction.

1.3.3.2. Microstructure dependence

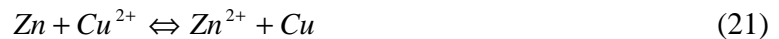
The electrodeposited Co-Ni alloys present a Co/Ni ratio considerably higher than in the bath. Thus, the composition of coatings strongly affects the morphology, what has been shown by Lupi *et al.* [104]. For the used electrodeposition conditions the cobalt content in alloy increase (up to approximately 40%), inducing the formation and growth of globular crystallites. When Co content was very low (quasi-nickel alloy) the hydrogen evolution became higher and thus, the local pH increased, allowing for a growth of (111) preferential orientation and formation of an acicular morphology. Results of [66,104] revealed the co-existence of hexagonal (hcp) and cubic (fcc) phases, which were observed in the literature either for pure cobalt and cobalt rich Ni-Co electrodeposits [83,105]. The presence of both phases in pure Co deposits is generally attributed to the small difference between the free energies of hexagonal and cubic cobalt structures [105]. In alloy containing less than 70wt.% of cobalt the cubic phase is favourite [106], as the Co atoms are substituted by Ni atoms and the preferred structure of fcc Ni leads to the alloy cubic structure. The different textures can be probably associated with the electrodeposition parameters, such as current density, solution pH, metal concentration, additive elements and their concentration. Moreover, the co-deposition of hydrogen can be associated with the presence of stacking faults and twins in alloy films with hcp and fcc structures [107], affecting the growth rate of a crystal face.

1.3.4. Co-electrodeposition with more noble metal

The other example of anomalous co-deposition behaviour is an electrodeposition of cobalt with more noble metals, such as Cu. Principally, the deposition of more noble metal can be carried out either by the current or by potential control. Regarding the concentration ratio of a salt of more noble metal to other ionic components, one can say that diffusion is the major mass transport process of more noble metal ions and migration is negligible. By applying a current control for the deposition of non-magnetic metal, e.g. copper, the actual diffusion layer thickness will be higher than the nominal one, i.e. that calculated from Faraday's law. This is because the leftover ions of more noble metal, i.e. those not discharged by the fixed current, can oxidize less noble metal deposited previously. In fact, it is very difficult to maintain accurately the diffusion limited current density by current control. Small concentration fluctuations can lead to either the exchange reaction or the incorporation of magnetic metal into non-magnetic layer. Both processes are undesirable. For this reason, potential control can rather be recommended for the deposition of non-magnetic layers. In the case of potentiostatic deposition of the non-magnetic layer, potential can be selected so that dissolution of the previously deposited magnetic layer does not occur. In the simplest approximation, the deposition of non-magnetic metal should be performed at the rest potential of less noble metal, as measured in an electrolyte void of the ions of more noble metal. Since the standard potential differences between the common magnetic and non-magnetic metals is quite large (several hundred of minivolts), the deposition of more noble metal surely takes place in the diffusion-limited current density regime. The situation can be more complex if the magnetic layer consists of several magnetic metals. In this case, all constituents have different dissolution potential and whichever conditions are applied for the deposition of more noble metal the partial dissolution of the magnetic layer is practically unavoidable. The good strategy in this case, is the minimization of loss of magnetic layer by analyzing the current transients. The simplest guideline is that the deposition potential of more noble metal has to be close to the dissolution potential of the main component of magnetic layer [108].

1.3.4.1. Displacement reactions

Peter et al. [109] has shown that Zn in Co-Cu-Zn/Cu multilayers obtained in the high-current pulse deposition induces an anomalous co-deposition in presence of Cu. The anomaly of deposition can be clearly observed even if the deposit contains 50at% Cu. The composition change with the current density of Cu deposition can be explained by the consideration of both deposition and displacement reactions. If the magnetic layer contains both Co and Zn, two displacement reactions can be formulated as follow:



The reaction stops when the cathode surface becomes completely covered by more noble metal. The driving force of Zn displacement is higher than that of Co, since the standard potential of Zn is lower than the standard potential of Co. However, the composition data of [109] showed that Zn content in the sample remains almost constant, while Co is displaced. Zinc can only be displaced when the time for displacement is high enough and when all Co has already been displaced by Cu. The reason why Co is displaced first is that Zn is deposited selectively at the early stages of high-current pulse, then it is followed by Co deposition when Zn²⁺ ions content of the electrolyte around the substrate is depleted. Hence, the selective Co displacement is caused by the anomalous nature of displacement reaction.

1.3.4.2. Underpotential deposition

The feature of reaction mechanism that results in anomalous co-deposition has not been well agreed. Some authors consider a catalytic mechanism in which the intermediate contains two different metallic atoms, but finally less noble metal atom is reduced only [110]. For this type of mechanism, the existence of thermodynamic driving force of the reaction is doubtful. Another assumption is that the ions of less noble element are adsorbed at the cathode and adsorbate is reduced, giving rise to the growth of no more than a monolayer (underpotential deposition (UPD)). The more noble metal can be deposited again onto less noble one; hence the entire process can be referred to an accumulative underpotential deposition [111]. Permitting that the origin of anomalous co-deposition may be UPD, it must be emphasized that the diagnostic criteria of UPD have never been observed for any metal pair exhibiting anomalous co-deposition. Namely, there is no information on whether:

- (i) the ions of less noble metal can form a monoatomic layer at the surface of more noble metal,
- (ii) the oxidation of UPD layer of less noble metal takes place at the same potential at which it can form.

I.4. Electrodeposition under superimposed magnetic field

Electrodeposition is an effective and efficient method to produce cobalt and cobalt-based alloys. Unfortunately, the thin cobalt-based films formed using this traditional technique contains some defects, such as rough surface, high air hole rate, etc.. According to this, a number of researchers have investigated the effects of superimposed magnetic fields on the electrochemical behaviour of deposited films. An imposition of magnetic field is another degree of reaction freedom, which may provide promising technique to uniquely control the surface microstructure, and in consequence the film's properties. Magnetic fields applied during the deposition may result in a textured film structure [112-114], affect its phase composition [115] and reduce an internal stress of the layers [116,117]. The morphology of obtained structures is the most affected [116,118-122]. It was observed during deposition of Fe [122] and Co [123], that a superimposition of magnetic field parallel to the electrode surface, where the Lorentz force is maximal, led to better quality deposited layers, i.e. lower roughness, they are more compact and grains are smaller. Those results suggest that the amount of organic additives in the electrolyte might be reduced by a superimposition of magnetic field. Therefore, the contamination of deposited layers with these compounds would be suppressed. Currently, the effects of homogeneous magnetic fields on electrochemical processes are widely understood, and the effects of heterogeneous magnetic fields on electrochemical processes got into focus. This interest is based on the fact that non-homogeneous magnetic fields are of higher interest from an application point of view, as high performance permanent magnets are cheap and easily available today.

1.4.1. Magnetic forces generated in the electrolyte

In the absence of magnetic field the mass transport factors, which can control the electrode process are diffusion, ionic migration and convection (natural and forced) [124]. For magneto-electrochemical processing, due to a superimposition of an external magnetic field the electrochemical systems receives various forces, such as paramagnetic force (F_P), field gradient force (F_B), Lorentz force (F_L), electrokinetic force (F_E) and magnetic damping force (F_D), which can become prominent in an electrode reaction and all forces have units of force per unit volume ($N\cdot m^{-3}$).

Three types of forces which depend on the interaction of current or movement of ions with the magnetic field are Lorentz force, electrokinetic force and the magnetic damping force, while the other two depend on properties of the ions in a magnetic field [125]. The Lorentz force arises from the interaction of a moving electric charge and a magnetic field. When it moves in a magnetic field, an electrically charged particle receives a Lorentz force F_L :

$$F_L = qv \times B \quad (22)$$

where q is the electrical charge of a particle, v is the velocity of the particle, and B is the magnetic flux density. It induces a torque on particle in the plane perpendicular to B and induces rotational motion. The direction of torque is reversed, when the direction of B is reversed. In solution, ions and charged particles cannot move alone due to the collision with solvent and other solutes. As a result, the Lorentz force induces convection of the solution. The mechanism is called the magnetohydrodynamics (MHD) mechanism. It is important in not only electrochemical reactions, where electric current moves in solution, but also in processes in solution, where ions move to a specific reaction zone such as the solid/liquid interface. Generally speaking, the speed of convection induced by the Lorentz force in an electrochemical reaction can be estimated from the following equation:

$$\frac{\partial u}{\partial t} + (u \cdot \nabla)u = -\left(\frac{1}{\rho}\right)\nabla P + \nu \nabla^2 u + \left(\frac{1}{\rho}\right)i \times B \quad (23)$$

where u is the velocity of solution, t is the time, ρ is the density of solution, P is the pressure, ν is the dynamic viscosity of solution, i is the electric current and B is the magnetic flux density. The

solution of this equation depends on the experimental conditions. MHD-induced convection is quite fast and very significantly affects transportation from bulk solution to a reaction zone [126].

Electrokinetic force, proposed by Olivier *et al.* [127] and Chopart *et al.* [128]:

$$F_E = \frac{\sigma_d E_{II}}{\delta_0} \quad (24)$$

is from the effects of Lorentz force on the charge density in a diffuse layer, which gives rise to a non-electrostatic field parallel to the working electrode surface, which induces motion of the solution near the interface. σ_d is the charge density in the diffuse layer, E_{II} is the induced non-electrostatic field and δ_0 is the diffusion layer thickness.

The magnetic damping force results from the damping of the flow of ions,

$$F_D = \sigma v \times B \times B \quad (25)$$

where $v \times B$ is the electrostatic force from the interaction between current and magnetic field, and σ is the solution conductivity.

A still controversially discussed force is the paramagnetic force, presented by O'Brien and Santhanam [129,130], Waskaas and Kharkats [131,132], Bund *et al.* [133] and Rabah *et al.* [134]:

$$F_P = \chi_m \frac{B^2}{2\mu_0} \nabla c \quad (26)$$

It is caused by the difference of paramagnetic susceptibility, which arises from the concentration gradient of paramagnetic ions in the diffusion layer. It is expected to balance the concentration of paramagnetic ions in a homogeneous magnetic field and thus, is directed towards higher concentration gradients and points the same direction as diffusion [129,135]. This force has a short range and thus acts only near the electrode surface. However, some authors pointed out that this force, if it exists at all, will not show an influence on electrochemical processes [124,136,137].

The field gradient force, discussed widely by Uhlemann and co-workers [138-142]

$$F_B = \chi_m \frac{cB\nabla B}{\mu_0} \quad (27)$$

where B is the magnetic field strength, c is concentration, ∇B is the magnetic field gradient, ∇c is the concentration gradient and μ_0 is the permeability of free space, arises from the non-uniformity of the magnetic field or is induced by ferromagnetic substrates and can sufficiently influence the transport of paramagnetic or diamagnetic active species. This force can be effective in the whole volume as well as close to the electrode surface for ferromagnetic substrates.

Thematically, the two forces F_P and F_B depend on magnetic moment (μ) and molar susceptibility (χ_m) of elements, which are related to the number of unpaired valence electrons. The field gradient force and paramagnetic force depend on the magnetic susceptibility of the atoms or ions. From elementary theory of magnetochemistry, the magnetic susceptibility can be expressed as

$$\chi_m = \frac{N\mu_0\mu^2}{3B_z T} \quad (28)$$

where N is the number of molecules per unit volume, μ_0 is the magnetic permeability of vacuum, μ is the magnetic moment of the an atom or ion, B_z is the Boltzmann constant and T is the absolute temperature. The molar susceptibility for paramagnetic ($\chi_m > 0$) and diamagnetic ($\chi_m < 0$) materials is maximum, if the applied magnetic field is perpendicular to the current density and vice versa [125].

1.4.2. Magnetic forces and convection

Since the magnetic field effect on electrodeposition has been discovered, many researchers started to investigate its action on different metal systems due to the changes in electrochemical behaviour as well as in the structure and morphology. Yu et al. [143] investigated the influence of magnetic fields on the electroless deposition of Co-W-P films from an alkali-metal-free bath. They have shown that the field gradient force induces the convection effect during deposition to affect the mass transfer, which results in the improvement of a reaction speed. Tschulik et al. [139,140] demonstrated that structuring process cannot be due to the action of Lorentz force only, but requires a remarkable effect of the field gradient force during deposition of Cu in patterned magnetic gradient force. It was found that with increasing Cu^{2+} concentration the intensity of structuring effect diminishes. This observation was explained

by the field gradient force induced convection, which depends on the concentration gradient established during the Cu deposition. Grant et al. [144] and Pullins et al. [145] showed that uniform magnetic fields acted at the microelectrode surface in order to induce rotational flow of the electrolyte, causes either an increase or a decrease in the limiting currents, depending solely on the size of electrode. For inlaid disk electrodes with radii less than 100 μm , the magnetic field driven flow results in a decrease of the transport limited current as a consequence of rotational solution flow adjacent to the surface, preventing gravity-driven natural convection. Similar increase in the limiting current due to the act of a magnetic field was observed by Motoyama et al. [146] and Bund et al. [133]. The magnitude of different magnetically induced forces and influence on a fluid motion were estimated by Hinds et al. [124]. Recently, Sugiyama et al. [147] have visualized and quantitatively examined that heterogeneous convection takes place on microdisk electrodes in non-uniform vertical magnetic fields. It has been concluded that the current density is controlled by magnetoconvection and is proportional to the power of one third of the magnetic flux density and its gradient as well as of the gradient of magnetic susceptibility. With increasing radius of the disk electrode the diffusion current is increasingly determined by MHD convection, inducing rotating and magnetic susceptibilities respectively, and gradients of magnetic flux density. Both phenomena, magnetoconvection and MHD effect, overlap and have to be taken into account.

Krause et al. [148] in the investigation on influence of magnetic force on the deposition of Co, Ni and Cu, showed that the electrodeposition in magnetic fields is not exceptionally influenced by the MHD effect in the hydrodynamic layer, but also by micro-magneto convection phenomena inside the diffusion layer (MMC effect). The latter is driven by gradient forces and especially by the paramagnetic force. However, among all the magnetic forces the Lorentz force is generally predominant in the electrochemical reactions, so that the effects induced by Lorentz force, magnetohydrodynamic (MHD) and micro-MHD effects have been studied from the beginning (*Annex I*).

1.4.3. Magnetic field and microstructure formation

A magnetic field remarkably influences the microstructural properties [120,149-151]. In the works of Matsushima et al. [152-154] the microstructural variation of electrodeposited iron films has been investigated under the MHD flow conditions. The surface morphology changes

into roundish and finer precipitates depending on the direction of a magnetic field. The texture formations drastically changed from uniaxial to biaxial grow by the convection, which probably influenced the surface pH value. The experimental results of Koza et al. [155] on electrodeposited Co-Fe alloy films showed that there is no influence of the magnetic field neither on structure nor on texture of deposited layer. However, the internal stress state of the deposits has been affected by the external magnetic field in the way that it decreased, when the deposition was carried out under magnetic field conditions. This is valid for the thin layer films investigation, but it has to be stressed that the texture development may required thicker layers to introduce a significant changes. From the quality point of view, a parallel-to-electrode magnetic field applied during the deposition results in a very homogeneous and compact layer. The obtained deposits exhibit a finer grain structure and, except for the buffered electrolytes, where the influence of a magnetic field is not so significant, a reduced roughness is obtained, when compared to those deposited without a magnetic field.

A number of research groups have investigated the effects of magnetic fields during the electrodeposition process. They have reported that the surface morphology [104,121,151,156,157] and the crystal structure [146,154,158-160] of deposits are considerably changed in the presence of magnetic field. These phenomena are explained by the MHD convection, which enhances mass transport of ionic species, thus changing the electrode interfacial conditions, such as the surface pH and ionic adsorption [161]. On the other hand, there are only few papers [153,162,163], which investigated the initial stage of electrocrystallization, such as nucleation and underpotential deposition processes in the magnetic field, because the general tent is that the chief magnetic field effects are related to MHD convection and that molecular processes are hardly affected [135,164-166]. For instance, it has been shown by Ispas et al. [167], by analysis of the $i(t)$ transients obtained during potentiostatic deposition of Ni without and with a magnetic field, that the steady state nucleation rate has been increased by a magnetic field applied parallel-to-electrode configuration resulting in finer grain structure of the deposit. Daltin et al. [168-170] studied the influence of an external magnetic field on the electrocrystallization of Cu_2O and they have also found a convective impact on the nucleation and the early stages of layer growth.

Chapter II

Experimental study

II.1. Introduction

Chapter II is related to the experimental investigations of electrodeposited cobalt and Co-based alloy films. The involved here Co-based systems are: binary Co-Ni and Co-Cu alloys and ternary Co-Ni-Cu alloy. The main objectives of this chapter are focused on the following points:

- (1) optimization of the electrochemical parameters, based on the investigations on Co and Co-Ni alloy.

This point is related to the electrochemical deposition process and determination of its experimental conditions. Thus, in the first order the electrolyte pH has been investigated by the electrodeposition of cobalt single layer and Co-Ni alloy film. The considered pH levels are ascribed to low and high values, i.e. 2.7 and 4.7, respectively. Secondly, the type of to-be-deposited substrate is determined. The considered substrates types are: titanium (Ti), tin indium oxide (ITO) covered by Ni seed-layer and pure ITO. Since one of the purposes of this study is to obtain nanocrystalline films, the deposition time is examined as well. These experimental parameters are studied in order to determine their influence on structure and morphology of the obtained films.

- (2) effect of an external magnetic field, primarily on the structure and morphology of Co, Co-Ni, Co-Cu and Co-Ni-Cu alloys, and additionally on the electrochemical aspect of deposition process.

This part is focused on the effects of an external magnetic field on the microstructure of electrodeposited films. First of all, the effect of low (up to 1T) magnetic field on the electrodeposition processes of Co and Co-Ni alloy films is studied. Next, the considerations are enlarged to investigations of the effects of high magnetic field (up to 12T) on the structure formation of Co-Ni, Co-Cu and Co-Ni-Cu films. Additionally, the effects of magnetic field on the electrochemical aspect are involved. These investigations are based on the kinetic and dynamic studies. The kinetic study involves the chronoamperometric examinations as well as topographical analysis of the growth of Co and Co-Ni films. The dynamic study considers the

Co-Cu electrodeposition process investigated by means of Electrochemical Impedance Spectroscopy (EIS).

II.2. Experimental methodology

The following section considers the experimental conditions of electrochemical deposition experiments performed according to the thesis subject, as well as the description of characterization techniques used for the samples analysis.

The conditions of electrodeposition process involve the electrolyte compositions and parameters of the experimental process, such as pH of the solution, temperature, current density, deposition time and magnetic field amplitude.

From the electrochemical techniques used during experimental investigation, i.e. chronopotentiometry, chronoamperometry, voltammetry and electrochemical impedance spectroscopy (EIS), the chronopotentiometry method is described, as a basic route of film deposition in the thesis. Other considered methods are wider discussed in the ***Annex II*** attached in the end of this manuscript. Similarly: structural, morphological, compositional and topographical characterization techniques of the deposit surface, including: X-ray Diffraction (XRD), Scanning Electron Microscope (SEM), Energy-Dispersive X-ray Spectroscopy (EDS), Wavelength-Dispersive X-ray Fluorescence (WD-XRF), X-ray Photoelectron Spectroscopy (XPS), Atomic Force Microscope (AFM), Magnetic Force Microscope (MFM) as well as tools for magnetic properties measurements: Alternating Gradient-Force Magnetometer (AGFM) and Vibrating Sample Magnetometer (VSM), are described in the attached ***Annex III***.

II.2.1. Electrolyte composition

The electrolytic solutions were the so-called simple electrolytic baths, consisted of cobalt sulfate, nickel sulfate, copper sulfate, boric acid and in some cases, saccharin. Their chemical composition and process operating conditions, regarding on the electrodeposited system, are presented in Table 1. Besides boric acid and saccharin none of the other chemical additives, which are usually added to avoid the effect of hydrogen evolution on the morphology, have been used. The solution pH was adjusted to the proper level by an addition of sulfuric acid or sodium

hydroxide. The volume of used solutions was 120 cm³ and the solution temperature was 50°C, which is a temperature commonly used in the industrial processing.

Table 1. Composition of the electrolytic solutions according to the electrodeposition of different systems considered in the preliminary study, together with the electrodeposition conditions.

System	Chemical agent	Concentration mol/L	Solution pH	Solution temperature °C	Current density mA/cm ²	Deposition time min	Magnetic field amplitude T
Co / Ti	CoSO ₄ ·7H ₂ O H ₃ BO ₃	0.6 0.4	2.7 and 4.7	50	-20	12	≤ 1
Co-Ni / Ti	CoSO ₄ ·7H ₂ O NiSO ₄ ·6H ₂ O H ₃ BO ₃	0.4 0.6 0.4	2.7 and 4.7	50	-20	18	≤ 12
Ni / ITO	NiSO ₄ ·7H ₂ O H ₃ BO ₃	0.6 0.4	2.7	30	-10	1 6	0
Co/Ni / ITO	CoSO ₄ ·7H ₂ O H ₃ BO ₃	0.6 0.4	4.7	50	-10	1 4	≤ 1
Co-Ni/Ni/ITO	CoSO ₄ ·7H ₂ O NiSO ₄ ·6H ₂ O H ₃ BO ₃	0.4 0.6 0.4	4.7	50	-10	1	≤ 12
Co-Ni / ITO	CoSO ₄ ·7H ₂ O NiSO ₄ ·6H ₂ O H ₃ BO ₃ saccharin	0.3 0.7 0.4 0.015	4.7	50	-10	1	≤ 12
Cu / ITO	CuSO ₄ ·6H ₂ O H ₃ BO ₃	0.03 0.4	4.0	50	-20	5 sec	0
Co-Cu/Cu/ITO	CoSO ₄ ·7H ₂ O CuSO ₄ ·6H ₂ O H ₃ BO ₃	0.4 0.03 0.4	4.0	50	-20	1	≤ 12
Co-Ni-Cu/Cu/ITO	CoSO ₄ ·7H ₂ O NiSO ₄ ·6H ₂ O CuSO ₄ ·6H ₂ O H ₃ BO ₃	0.015 0.2 0.01 0.4	4.0	50	-20	1	≤ 1

II.2.2. Electrolytic cell and electrodes

Electrodeposition process has been carried out in a cylindrical double-wall cell with a conventional three-electrode system, as shown in Fig.5. The electrochemical cell consisted of

working (WE), reference (AUX) and counter (CE) electrodes. Two types of working electrodes (WE) were used: a titanium disk with an area of 1 cm^2 embedded in an epoxy resin and glass covered by a thin layer (100 nm) of indium tin oxide (ITO) in the shape of $25 \times 25 \times 1.1 \text{ mm}$ square. Before each experiment the Ti-electrode was grounded with an emery paper and polished. An ITO/glass electrode was washed in alcohol and installed in a Teflon holder. The to-be-deposited substrate areas were equal to 1 cm^2 . The counter electrode was made of platinum rectangular with an area of 2.5 cm^2 and the reference electrode was a saturated mercury sulphate electrode (SSE).

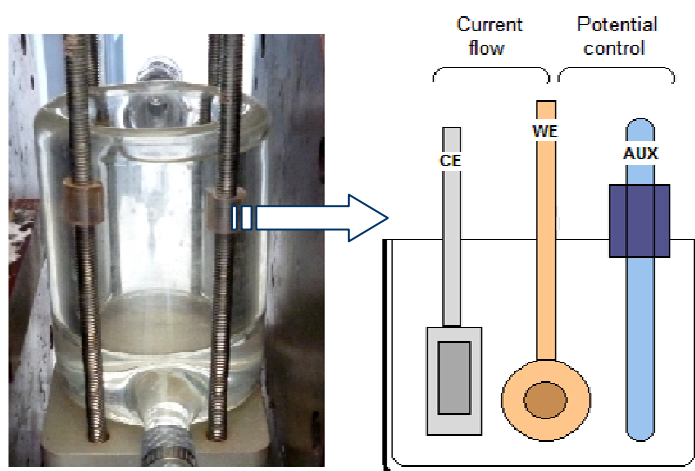


Fig.5. Three-electrode double-wall cell used during electrochemical deposition.

II.2.3. Electrochemical deposition methods

All of the electrochemical investigations were carried out using the chronopotentiometry method, where the constant current density was applied and controlled by means of a potentiostat-galvanostat PGZ 100 Radiometer Analytical and VersaSTAT 4.

In chronopotentiometry, a current is applied to the working electrode and its resulting potential is measured against a reference electrode as a function of time. At the moment when the current is first applied, the measured potential is abruptly changed due to the iR loss, and after that it gradually changed, because concentration overpotential is developed as the concentration of the reactant is exhausted at the electrode surface. If the current is larger than the limiting current, the required flux for the current cannot be provided by the diffusion process and,

therefore, the electrode potential rapidly rises until it reaches the electrode potential of the next available reaction, and so on.

In constant current chronopotentiometry, the constant anodic/cathodic current applied to the electrode causes the electroactive species to be oxidized/reduced at a constant rate. The electrode potential accordingly varies with time as the concentration ratio of reactant to product changes at the electrode surface. This process is sometimes used in titrating the reactant around the electrode, resulting in a potentiometric titration curve. After the concentration of the reactant drops to zero at the electrode surface, the reactant might be insufficiently supplied to the surface to accept all of the electrons being forced by the application of a constant current. The electrode potential will then sharply change to more anodic/cathodic values. The shape of the curve is governed by the reversibility of the electrode reaction.

II.2.4. Superimposed magnetic field

For the electrochemical investigations of the effect of external magnetic field the electrochemical cell was plunged into the gap of electromagnet, which delivers a uniform magnetic field to the electrode surface. The experiments under magnetic field were carried out in two laboratories. Low magnetic field (LMF) investigations were conducted in Laboratoire d'Ingénierie et Sciences des Matériaux (LIMS, Reims; Drusch EAM 20G electromagnet), where the generated magnetic field density is up to 1T and the magnetic flux was directed horizontally. The high magnetic field (HMF) investigations were provided in Laboratoire National des Champs Magnétiques Intenses (LNCMI) in Grenoble, where the magnetic field is oriented vertically to the electrode surface and the considered flux density was up to 12T. In both cases, the parallel orientation of magnetic field to the electrode surface has been used. The schematic representation of this experimental setup is presented in Figure 6.

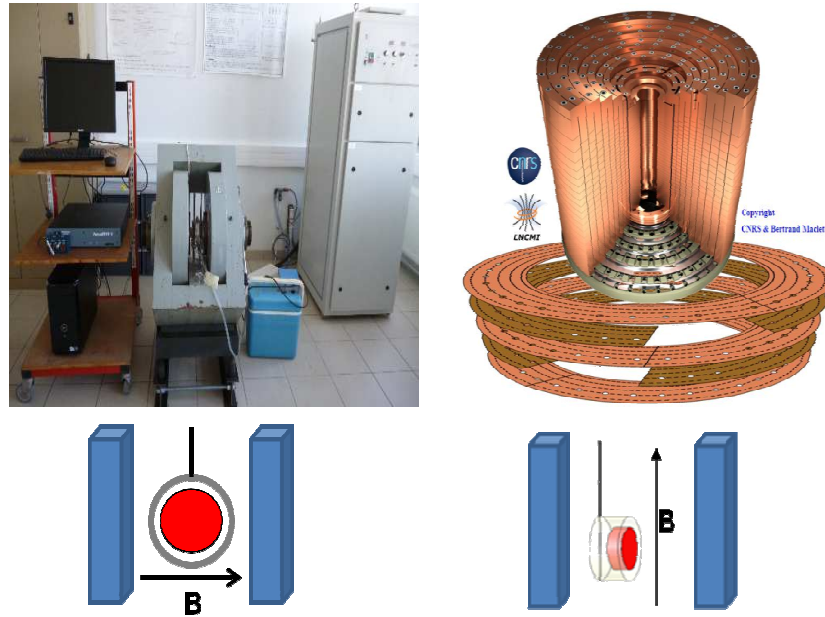


Fig.6. Experimental setups for (a) LMF and (b) HMF investigations.

II.3. Preliminary study - optimization of the electrodeposition parameters

As it was discussed in Chapter I, in each electrochemical deposition process the determination and optimization of the processing conditions are of a high importance. Besides the effect on electrochemical process the formation and growth of deposit is strongly affected. Among many electrodeposition parameters the electrolyte pH was shown as one of the most important, determining the microstructure of a final deposit.

Since this work is based on the electrochemical processing of Co-based film formation, it seems reasonable to investigate firstly the proper process conditions. Thus, the following section plays a role of preliminary study. It is focused on the investigations of electrochemical parameters, such as electrolyte pH, to-be-deposited substrate type, deposition time and in the next order, the effect of an external magnetic field is considered. These experimental parameters, with regard on the structure and morphology of electrodeposited cobalt and Co-Ni films, respectively, are investigated.

II.3.1. Electrolyte pH

In accordance to investigate the effects of solution pH on structure formation and morphology of cobalt and Co-Ni alloy films, two values of pH were used: 2.7, assigned as low pH level, and 4.7 stands for the high one. The effect of solution pH has been determined by the electrodeposition of Co and Co-Ni films on titanium (Ti) substrate. The processing conditions for both depositions are reminded in Table 2.

Table 2. Conditions of the electrodeposition process of Co and Co-Ni films deposited on Ti substrate.

System	Chemical agent	Concentration mol/L	Solution pH	Solution temperature °C	Current density mA/cm ²	Deposition time min
Co / Ti	CoSO ₄ ·7H ₂ O H ₃ BO ₃	0.6 0.4	2.7 and 4.7	50	-20	12
Co-Ni / Ti	CoSO ₄ ·7H ₂ O NiSO ₄ ·6H ₂ O H ₃ BO ₃	0.4 0.6 0.4	2.7 and 4.7	50	-20	18

II.3.1.1. pH effect on the structure of Co and Co-Ni films

In the first order, the structure of cobalt deposits was investigated. Figure 7.(a) and Figure 7.(b) present the X-ray diffraction (XRD) patterns of cobalt films deposited at high and low pH levels, respectively. For the Co films deposited at high pH level the X-ray diffractograms demonstrate the reflections from three characteristic cobalt crystal planes: (100), (101) and (110) of the hexagonal centered-packed (hcp) structure, clearly appearing at $2\theta \cong 41^\circ, 47^\circ$ and 76° , respectively. Moreover, at $2\theta \cong 76^\circ$ the face-centered cubic (fcc) structure in (220) orientation is associated together with the growth of (110) hcp phase. A reliable assignment of the peak of the one or the other phase is not possible at this point because of the small difference between the two XRD line positions (Fig.7.(b)).

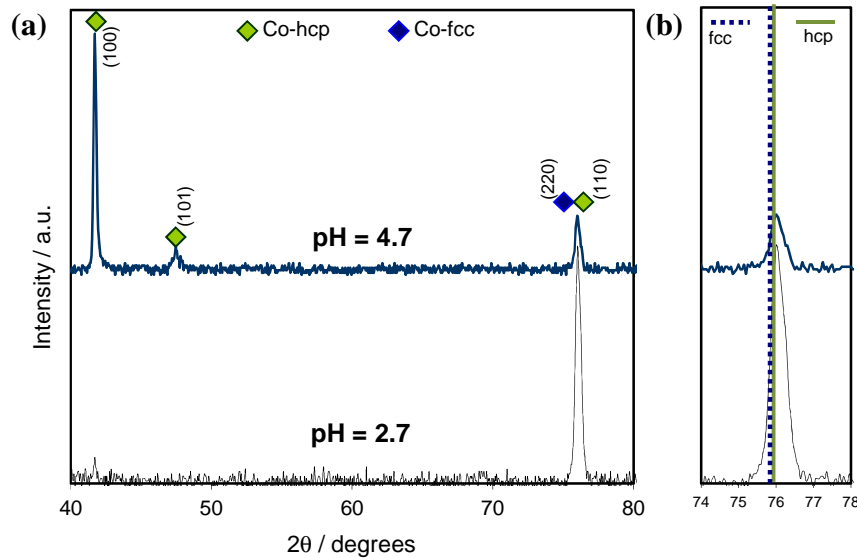


Fig.7. Phase composition of the Co films deposited on Ti substrate at different pH levels (a) with overlapping of two Co phases (b); $i = -20\text{mA/cm}^2$, $t = 12\text{min}$.

According to the Powder Diffraction Files (PDFs) published by the JCPDS – International Centre for Diffraction Data, the fcc-Co phase is localized at $2\theta \cong 75.855^\circ$ (JCPDS 05-0727), while that of hcp-Co at $2\theta \cong 75.941^\circ$ (JCPDS 15-0806). Thus, the difference between diffraction lines for both phases is 0.086° and a clear assignment for the presence of only one phase is not possible. Hence, the structure of electrodeposited cobalt film is ascribed as a biphasic and intensive growth of (100)-hcp plane indicates the crystallites orientation in the film. At low pH level equal to 2.7, a strong decrease in the X-ray peak intensity of (100) and disappearance of (101) plane of Co-hcp is observed, whereas the (220)-fcc+(110)-hcp peak at $2\theta \cong 76^\circ$ become majority.

Going forward, the nickel element has been introduced to the deposition solution in order to investigate the effect of pH on the growth of binary system and compare it with the single metal deposition. The X-ray diffraction patterns of Co-Ni films grown at high and low pH, respectively, are shown in Fig.8. Similarly, as in the electrodeposited Co films case, the binary Co-Ni deposits consist of a biphasic structure, regardless on the pH value.

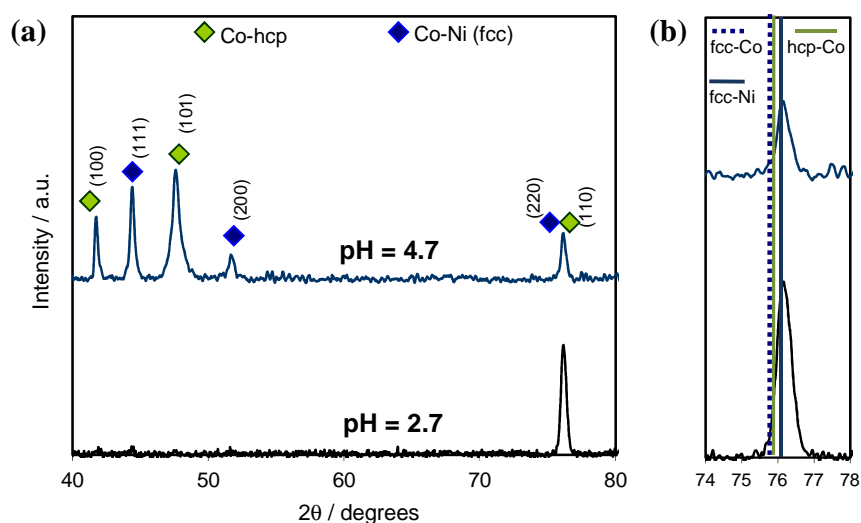


Fig.8. Phase composition of the Co-Ni films deposited on Ti substrate at different pH levels (a) with the overlap lines of two cobalt phases (b); $i = -20\text{mA/cm}^2$, $t = 18\text{min}$.

At high pH (4.7) the alloy formation is indicated by the presence of crystallographic (111) and (200) planes of Co-Ni-fcc phase. Additionally, the diffraction peak at $2\theta \cong 76^\circ$ may be attributed to the growth of a mixed Co-Ni-(220)-fcc and Co-(110)-hcp phases. The presence of Co-hcp phase in the Co-Ni deposits is confirmed by the observation of the growth of (100) and (101) planes of Co-hcp at lower 2θ angles, about 41° and 47° . A decrease of the pH level down to 2.7, shows a similar effect on the Co-Ni structure formation as that of Co. The Co-Ni film electrodeposited at low pH is characterized by a presence of only one diffraction peak, probably related with the growth of both, Co-Ni alloy and Co-hcp phases.

Cohen-Hyams *et al.* [22] and Dini [171] have demonstrated that for a low pH value (<2.7), an fcc phase is always occurred, while at pH values between 2.7 and 5, a mixture of hcp and fcc phase is formed. In contrast, for high value of pH (>5) an hcp phase occurs only. Nevertheless, the experimental results presented in this work reveal the occurrence of fcc and hcp structures at both pH levels, low and high. Thus, it can be assumed that the range of electrolytic pH, when the both varieties of crystallographic structure are observed may vary, depending on the electrodeposition conditions.

According to the literature review, different explanations appear, when considered the phase formation dependence on pH level. Armanyanov [83] reported that the formation of Co-fcc phase at low pH is probably in the form of a metastable cobalt hydride, which is greatly

facilitated by the adsorption and subsequent incorporation of atomic hydrogen into electrodeposits. Orinakova *et al.* [49] gave evidence that hydrogen resulting from the cathodic reaction is chemisorbed or chemically bonded in the electrodeposited layer. The general conclusion is that the highest intensity among hydrogen containing species was detected for OH⁻ ions at all pH values. Furthermore, at lower pH the hydrogen presented in the deposited layer is primarily in the pure form (H, H₂), less as the metallic hydrides (MH, MH₂) and least as the metallic monohydroxide species (MOH). Hence, it can be assumed that the dissolved hydrogen distorts the hcp lattice to an extent that is finally transformed to the fcc structure [172]. Moreover, it has been shown that in the absence of stirring the growth of fcc structure at low pH is favoured [92].

With respect to the occurrence of hcp phase of Co at high pH, an association with the presence of colloidal hydroxides at the cathode surface during the deposition is suggested. Following [83], the investigations on electrodeposited cobalt indicated a high content of both, hydrogen and oxygen in high pH-Co films. Thus, it is suggested that these gases may have been originated from cobalt hydroxides. As stated in [49], in addition to the OH⁻ ions, very high intensities of high pH-Co films were also registered for metallic hydrides (MH, MH₂) as well as mono and dihydroxides (MOH, M(OH)₂). This may also be the case in this study. The biphasic (110)-hcp+(220)-fcc diffraction peak may consist some of the cobalt or cobalt and nickel (in Co-Ni films) hydroxides, which are formed at high pH (4.7). They may slow down the (110)-hcp+(220)-fcc growth rate and as a result favours the growth of cobalt (100) and (101)-hcp planes. Another explanation could be found in the precipitated Co-hcp crystals, which are rotated around the c-axis from (110) to energetically more stable (100) plane. The reason for the formation of non-equilibrium structure may be a lower surface free energy of the fcc phase in comparison to that of the hcp, as shown by Krause *et al.* [18]. The Co-hcp phase is not distributed homogeneously along the substrate, but forms separated crystals in its vicinity. The origin of this behaviour is again the co-deposition of hydrogen, which influences the surface free energy.

II.3.1.2. pH effect on the morphology of Co and Co-Ni films

The differences in phase composition of Co and Co-Ni films, regarding on the pH variations, are well observed in the morphological examinations. Figure 9 presents the SEM

images of Co-films in dependence of electrolyte pH. The surface morphology is strongly affected by the phase composition, which in turn depends on the pH level.

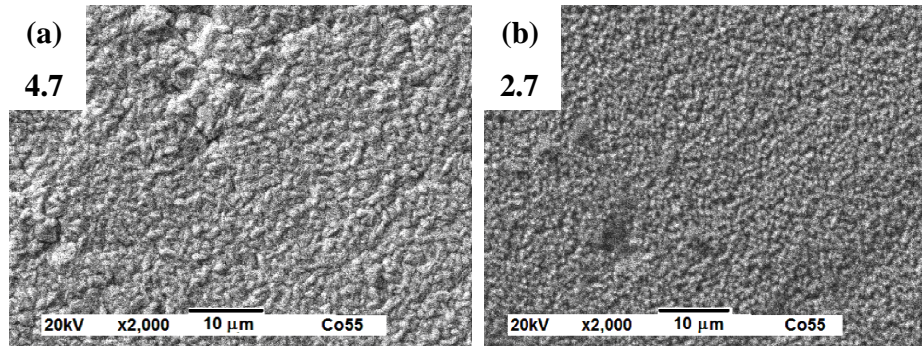


Fig.9. Morphology of the Co films electrodeposited on Ti substrate at pH (a) 4.7 and (b) 2.7; $i = -20\text{mA/cm}^2$, $t = 12\text{ min}$.

The morphology of cobalt film deposited at high pH level (Fig.9.(a)) demonstrates coarse-grained structure. The cobalt crystallites are rather large and in the form of wide needle-like particles. This kind of crystal shape is associated with the presence of hexagonal phase. However, some admixtures of fcc cobalt phase characterized by the growth of small and spherical nucleus may be observed as well. Hence, it can be assumed that the needle-like cobalt crystals grow on the spherical matrix providing formation of a dense film. Furthermore, the quality of the film surface is strongly affected by the simultaneous hydrogen evolution and formation of the cobalt hydroxides during electrodeposition process. Thus, the discontinuity of Co films is observed. Contrary, electrodeposition at low pH (Fig.9.(b)), allows obtaining fine-grained film, much more homogeneous and compact than that deposited at pH 4.7. The presence of small and spherical cobalt crystals could be associated with the Co-fcc phase, which may grow together with Co hcp phase at $2\theta \cong 76^\circ$ (Fig.7).

Similar morphological observations are noticed in the case of electrodeposited Co-Ni films, which characteristic in dependence on pH level is presented in Fig.10. The morphology of deposited film at high pH (Fig.10.(a)) is closely related to that of cobalt film (Fig.9). The Co-Ni film deposited at pH 4.7 possesses a coarse-grained structure with large and wide crystals. When depositing at lower pH the fine-grained structure consisting of small and spherical crystals is observed. The relation between morphology of the Co-Ni films and the phase composition is in the same order as that of the cobalt films.

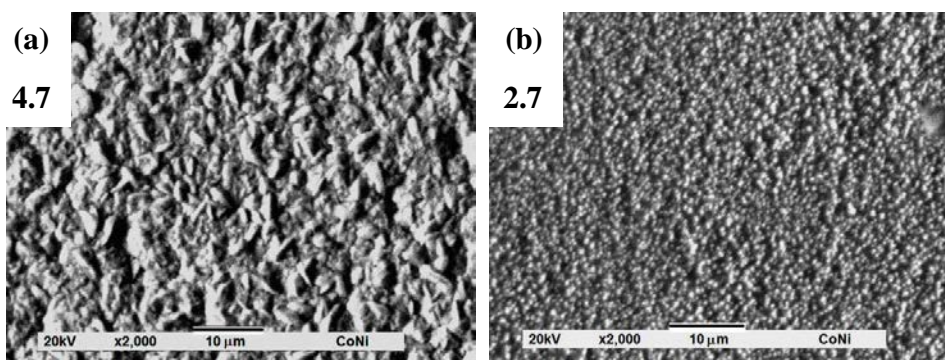


Fig.10. Morphology of the Co-Ni films electrodeposited on Ti substrate at pH (a) 4.7 and (b) 2.7; $i = -20\text{mA/cm}^2$, $t = 18\text{min}$.

The possibility of predominant amount of hexagonal phase of cobalt in the Co-Ni film deposited at pH 4.7 may contribute to the growth of large and elongated crystals. Contrary, the morphological characteristics of films deposited at pH 2.7 could be associated with the larger fraction of fcc phase. Furthermore, the SEM images demonstrate that the quality of deposits surface is more uniform and homogeneous, when cobalt films are alloying with nickel, rather than deposited as a single metal layer, regardless on pH level.

It was deduced in Ref. [49] that the amount of hydrogen incorporated in the deposit is the highest at low pH level (about 2). This corresponds to the highest concentration of hydrogen protons in the electrolyte solution. In spite of the containing the highest level of evolved hydrogen, the quality of both deposited Co and Co-Ni films at low pH (2.7), seems to be smoother and more uniform, compared to that at pH 4.7. Similar observation has been reported by Alper *et al.* [50] and Vincenzo and Cavallotti [17]. The change of surface morphology with the electrolyte pH may be explained by the hydrogen evolution reaction occurred at the cathode surface. If the hydrogen evolution, which is favoured at low pH as stated by Orinakova *et al.* [49], is sufficiently effective then it changes the electrochemical conditions at the vicinity of the electrode. Hence, the value of pH increases near the electrode surface and affects the morphology of deposits. In this case, the boric acid used plays an important role in maintaining the pH of the solution near the electrode surface to be equal to that of bulk solution. The protons released from the aqueous solution of boric acid (Eq.(10)) in the diffusion layer, reacts with the hydroxide ions to form water. As a result, more energy is required for the reduction of water, thereby shifting its potential to more negative values. Thus, the use of boric acid offsets the increase in the pH associated with the onset of water electrolysis. Hence, the deposition can be accomplished

without interference from hydrogen evolution and as a consequence, the hydrogen-free Co and Co-Ni deposits at low pH are obtained.

Unfortunately, the buffering action of boric acid at high pH level is not effective. According to Santos *et al.* [57], the reason lays in the high-temperature (50°C) electrodeposition process. An increase of the solution temperature, similar as a high pH value, enhances the deposition rate, but also increases that of the unwanted hydrogen evolution. If the hydrogen evolution reaction is more effective at high temperature and high pH level, thus, the formation of OH⁻ ions must be larger as well. Considering the kinetics of boric acid, its dissociation is the rate-determining step during hydrogen evolution reaction [57]. In the case of high-temperature process, the dissociation rate of boric acid is not fast enough to provide the increase of OH⁻ ions concentration at the electrode surface. Thus, the Co and Ni hydroxides formed at high pH (4.7) tend to be adsorbed at the cathode surface, affecting the quality of deposited films.

As it is discussed, the problem of hydrogen evolution during the cobalt electrodeposition from aqueous solution is common and fundamental in the microstructure formation. Thus, it is wider discussed in Chapter IV, which investigates the hydrogen adsorption mechanism and its effects on the structure formation of Co films.

II.3.2. Substrate type and deposition time

The followed objectives in the optimization of electrodeposition parameters were lowering the roughness and crystallites size of the deposited Co and Co-Ni films. Thus, in addition with the titanium substrate a thin glass covered by indium tin oxide (ITO) layer (Fig.11) has been used as well.

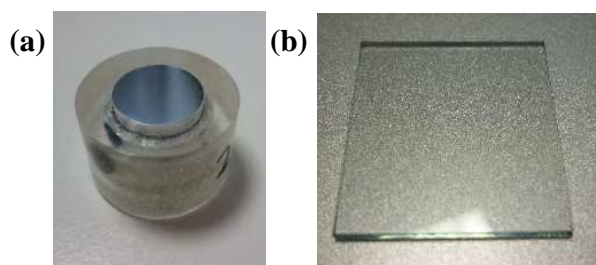


Fig.11. Substrates used as the working electrodes: (a) – titanium, (b) – ITO/glass.

Compared to the electrodeposition at the metal surfaces (Ti), the deposition on semiconductors (ITO) substrates is different at two aspects: the semiconductor characteristics of the substrate and the weak interaction between the semiconductor material and deposited metal. Thus, the ITO substrate has been reinforced with Ni seed-layer in order to improve the adhesion ability of deposited film, which was poor in the case of direct deposition on ITO substrate. Furthermore, the deposition time of electrodeposited Co and Co-Ni films on Ni/ITO substrate on the crystallite size is investigated (Table 3).

Table 3. Conditions of the electrodeposition process of Co and Co-Ni films deposited on Ni/ITO substrate.

System	Chemical agent	Concentration <i>mol/L</i>	Solution pH	Solution temperature <i>°C</i>	Current density <i>mA/cm²</i>	Deposition time <i>min</i>
Ni / ITO	NiSO ₄ ·7H ₂ O H ₃ BO ₃	0.6 0.4	2.7	30	-10	6 1
Co / Ni / ITO	CoSO ₄ ·7H ₂ O H ₃ BO ₃	0.6 0.4	4.7	50	-10	4 1
Co-Ni / Ni / ITO	CoSO ₄ ·7H ₂ O NiSO ₄ ·6H ₂ O H ₃ BO ₃	0.4 0.6 0.4	4.7	50	-10	1

II.3.2.1. Electrodeposited Co films

Figure 12 compares the phase composition and morphological characteristics of Co films electrodeposited on Ti and Ni/ITO substrates.

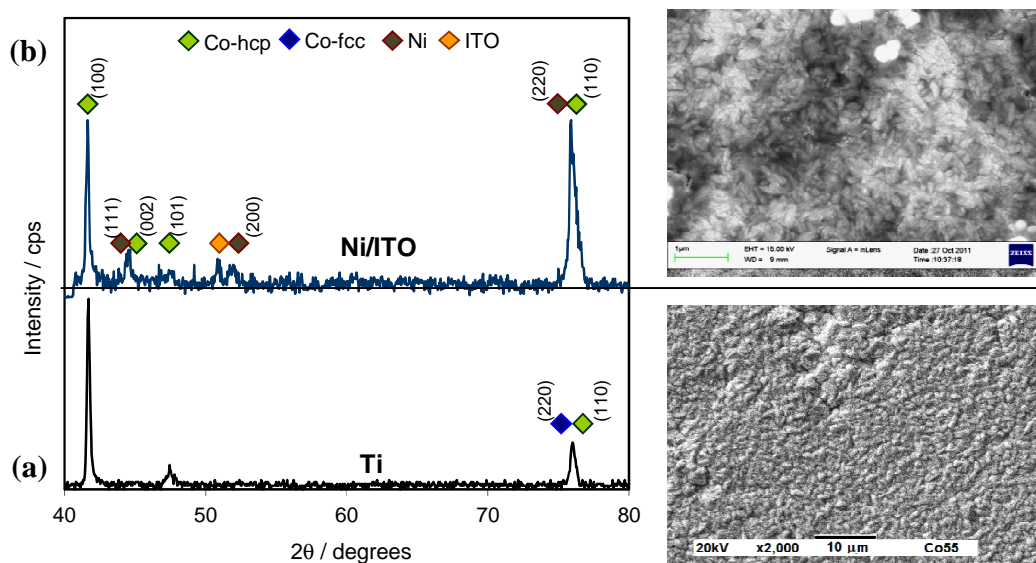


Fig.12. Comparison of the phase composition and morphology of Co films electrodeposited on:
 (a) Ti and (b) Ni/ITO substrates;
Ti: $i = -20\text{mA}/\text{cm}^2$, $t = 12\text{min}$, $\text{pH} = 4.7$; *Ni/ITO*: $i = -10\text{mA}/\text{cm}^2$, $t = 4\text{min}$, $\text{pH} = 4.7$.

The Co films deposited on Ti substrate (Fig.12.(a)) are of biphasic: hcp and fcc structure. The growth of fcc phase at $2\theta \cong 76^\circ$ is accompanied together with Co-(110)-hcp phase. This is confirmed by the morphological investigation, which put into evidence the predominated hcp phase in the Co/Ti films. The electrodeposition of Co on Ni/ITO substrate (Fig.12.(b)) brings about the formation of cobalt film, which is mainly composed with hexagonal phase. Thus, the obtained structure consists of well-defined, wide needle-like crystallites agglomerated in the form of large clusters rather than growing separately along the substrate surface. Furthermore, in both cases the intensive growth of (100)-hcp plane suggests that the Co crystallites are mainly oriented in this direction.

In the further process optimization route, the crystallites size of Co film deposited on Ni/ITO has been reduced by decreasing the deposition time from 4 to 1 minute (Fig.13).

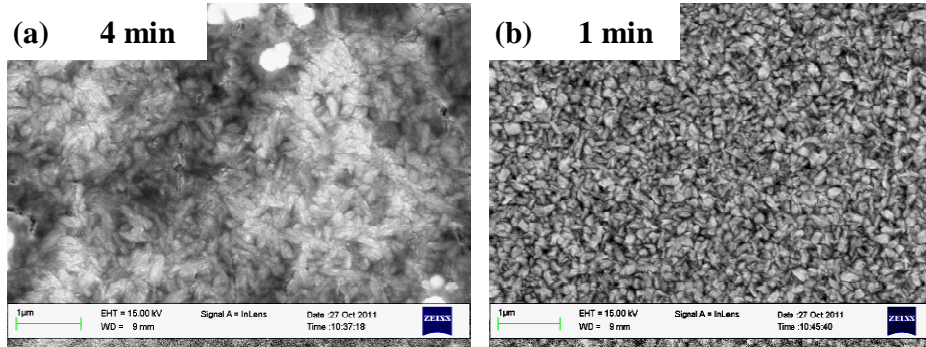


Fig.13. Morphology of the Co films electrodeposited on Ni/ITO substrate at different times: (a) 4 minutes and (b) 1 minute; $i = -10\text{mA}/\text{cm}^2$, $\text{pH} = 4.7$.

The film deposited at longer time (Fig.13.(a)) consists of elongated needle-like crystallites, which are agglomerated into large clusters and grow not uniformly at the substrate surface. A decrease of the deposition time allows obtaining much more homogeneous and uniform structure of Co films (Fig.13.(b)) consisting of typical forms for hexagonal structure. The average crystallite size of cobalt was determined according to the Scherrer formula:

$$d = \frac{k\lambda}{\beta \cos \theta} \quad (29)$$

where d is the mean size of grain, k is a dimensionless shape factor, which value is close to unity and a typical used value of is about 0.9, λ is the X-ray wavelength, β is the full width at half maximum intensity (FWHM) of the X-ray diffraction peak, after the correction for the instrumental line broadening, and θ is the Bragg angle. The mean grain sizes were found to be about 825 nm for the cobalt film grown at high deposition time (4 min) and about 444 nm for that at low deposition time (1 min).

The morphological characteristic shows that decreasing deposition time from 4 to 1 minute brings about reduction in the crystallites size. The deposition time has an effect on the early stages of electrodeposition. At first, the nucleation occurs and the Co nuclei are formed on a whole substrate surface. When all of the active sites on the substrate are occupied the growth process of nuclei follows. During the short-time deposition there is not enough time for long nuclei growth. Thus, the nucleation process is dominated, resulting in the nanocrystallite films. Hence, the reduced deposition time together with a change of to-be-deposited substrate brings about the electrodeposited films characterized by lower roughness and more uniform deposit surface.

II.3.2.2. Electrodeposited Co-Ni films

Much clear difference between both substrates is observed, when alloying Co with Ni element (Fig.14). Again, the Co-Ni film deposited on Ti substrate (Fig.14.(b)) is of biphasic: hcp and fcc structure, with the Co-hcp diffraction peaks at lower 2θ angles. This structural characteristic is followed by the morphological feature, obviously indicating the Co crystallites in hexagonal form (elongated needles), embedded into small and spherical crystallites of Co-Ni-fcc nature.

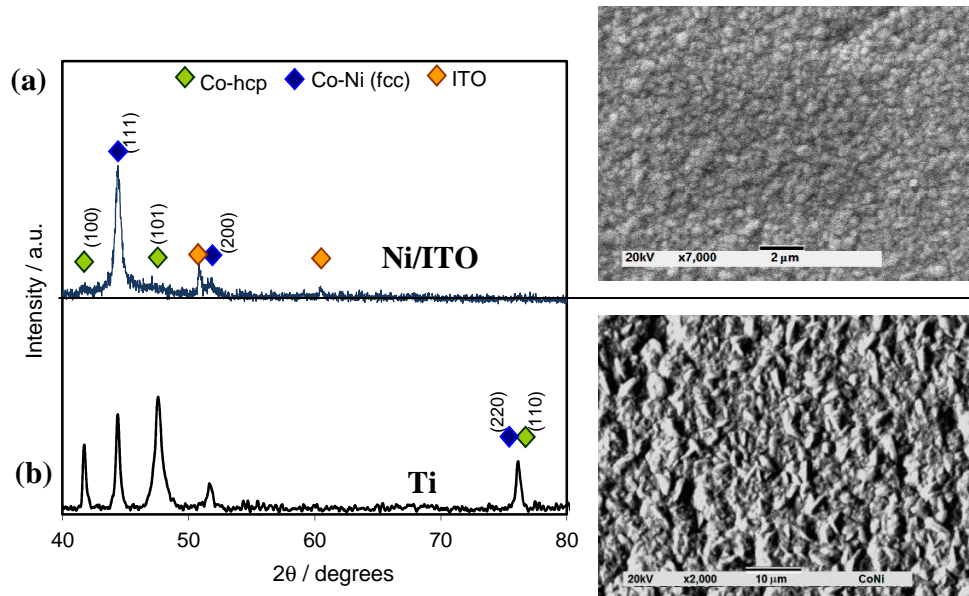


Fig.14. Comparison of the phase composition and morphology of Co-Ni films electrodeposited on (a) Ni/ITO and (b) Ti substrates;
Ti: $i = -20\text{mA/cm}^2$, $t = 18\text{min}$, $\text{pH} = 4.7$; *Ni/ITO*: $i = -10\text{mA/cm}^2$, $t = 1\text{min}$, $\text{pH} = 4.7$.

When the Co-Ni film is electrodeposited on Ni/ITO substrate (Fig.14.(a)), the Co-hcp peaks disappear, whereas the presence of Co-Ni alloys diffraction peaks is observed. Thus, the Co-Ni films consist of small and spherical crystallites, characteristic for the fcc structure.

Regarding on the crystallite size, the alloying of Ni with Co under the electrodeposition conditions allow the formation of nanocrystalline films (Fig.15). In the case of electrodeposited Co and Co-Ni alloys, the films are characterized by a uniform and homogeneous structure, which is fully covered by the small-sized crystallites along the substrate surface.

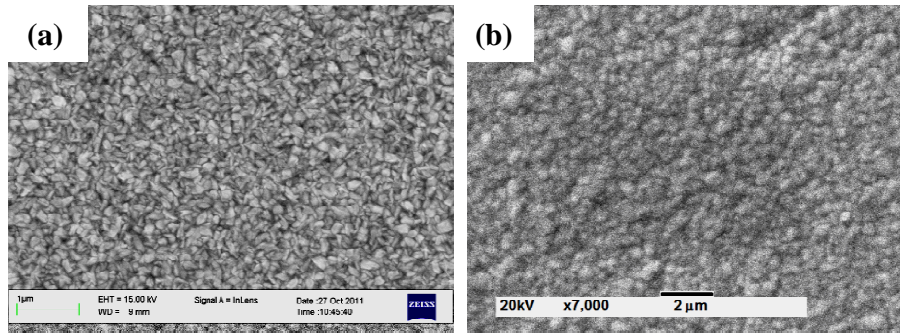


Fig.15. Comparison of the surface morphology of (a) Co and (b) Co-Ni films electrodeposited on Ni/ITO substrate; $i = -10\text{mA}/\text{cm}^2$, $t = 1\text{min}$, $\text{pH} = 4.7$.

II.4. Electrodeposition under external magnetic field

Superimposition of an external magnetic field during electrodeposition process of metals and alloys is another parameter affecting their structure formation and growth. Thus, this section is focused on the investigations of effects of an external magnetic field on the formation and growth of electrodeposited systems described previously: Co and Co-Ni films deposited on Ti and ITO substrates. Furthermore, the binary Co-Cu and ternary Co-Ni-Cu films electrodeposited on Cu/ITO substrate are introduced, since their microstructure formation exhibited some interesting features under superimposed magnetic field.

Because of different magnetic field amplitudes and two varieties of its orientation, this section is divided into two parts including, in the first order, study of the low magnetic fields (LMFs) in horizontal orientation toward electrode surface with magnet strength up to 1T and high magnetic fields with a vertical orientation and magnets strength up to 12T. In both cases the magnetic field flux was oriented parallelly to the electrode surface (Fig.16).

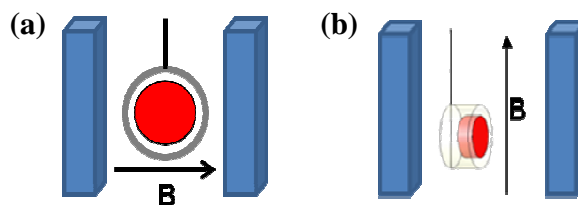


Fig.16. Magnetic field flux in parallel orientation to the electrode surface placed horizontally (a) and vertically (b).

II.4.1. Effect of a low magnetic field (LMF)

This section considers the effect of a superimposed magnetic field up to 1T, on the structure formation and growth of:

- Co and Co-Ni films electrodeposited on Ti substrate,
- Co films electrodeposited on Ni/ITO substrate,
- Co-Cu and Co-Ni-Cu electrodeposited on Cu/ITO substrate.

The parameters of electrochemical deposition process are reminded in Table 4.

Table 4. Composition of the electrolytic solutions according to the electrodeposition of different systems under LMF, together with the electrodeposition conditions.

System	Chemical agent	Concentration <i>mol/L</i>	Solution pH	Solution temperature <i>°C</i>	Current density <i>mA/cm²</i>	Deposition time <i>min</i>	Magnetic field amplitude <i>T</i>
Co / Ti	CoSO ₄ ·7H ₂ O H ₃ BO ₃	0.6 0.4	4.7	50	-20	12	≤ 1
Co-Ni / Ti	CoSO ₄ ·7H ₂ O NiSO ₄ ·6H ₂ O H ₃ BO ₃	0.4 0.6 0.4	4.7	50	-20	18	≤ 1
Ni / ITO	NiSO ₄ ·7H ₂ O H ₃ BO ₃	0.6 0.4	2.7	30	-10	1	0
Co / Ni / ITO	CoSO ₄ ·7H ₂ O H ₃ BO ₃	0.6 0.4	4.7	50	-10	1	≤ 1
Cu / ITO	CuSO ₄ ·6H ₂ O H ₃ BO ₃	0.03 0.4	4.0	50	-20	5 sec	0
Co-Cu / Cu / ITO	CoSO ₄ ·7H ₂ O CuSO ₄ ·6H ₂ O H ₃ BO ₃	0.4 0.03 0.4	4.0	50	-20	1	≤ 1
Co-Ni-Cu / Cu / ITO	CoSO ₄ ·7H ₂ O NiSO ₄ ·6H ₂ O CuSO ₄ ·6H ₂ O H ₃ BO ₃	0.015 0.2 0.01 0.4	4.0	50	-20	1	≤ 1

II.4.1.1. Co and Co-Ni films electrodeposited on Ti substrate

Figure 17 shows the X-ray diffraction patterns associated with the morphological characteristics of Co films electrodeposited without and with 0.5 and 1T magnetic field. The diffractograms indicate that the Co films are of biphasic: hcp and fcc structure. A superimposition

of an external magnetic field does not change the phase composition of Co film, but acts on the relative diffraction peaks intensity. Under magnetic conditions of electrodeposition, two diffraction peaks of Co: (101)-hcp and biphasic (110)-hcp+(220)-fcc increase with the magnetic field amplitude.

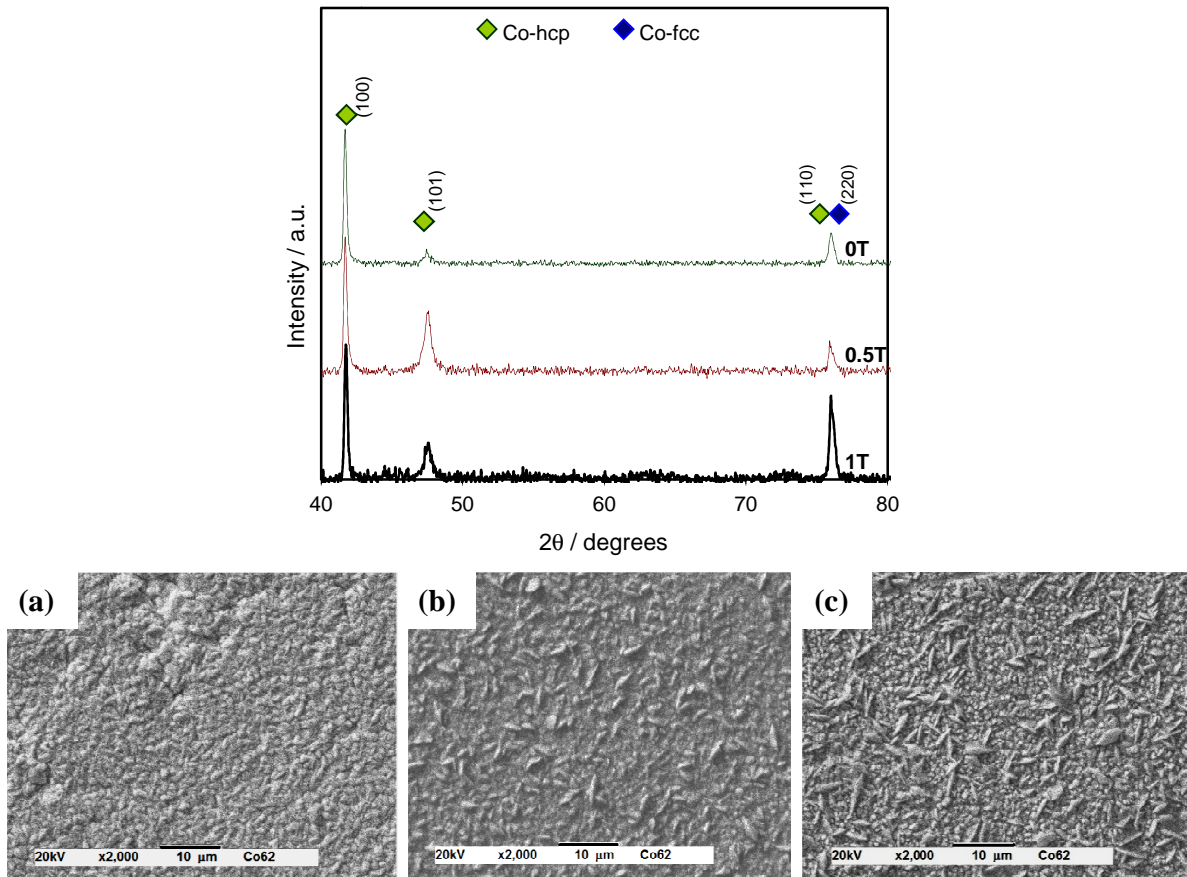


Fig.17. X-ray diffraction patterns and morphology of the Co films electrodeposited on Ti substrate under: (a) 0T, (b) 0.5T and (c) 1T magnetic field; $i = -20\text{mA}/\text{cm}^2$, $t = 12\text{min}$, $\text{pH} = 4.7$.

The effect of magnetic field on the growth of Co phases can be clearly observed, when considering the associated morphological characteristics. At first, when no magnetic field is present during electrodeposition the wide needle-like structure is formed. Under 0.5T magnetic field the intensive growth of (101)-hcp phase is observed, what is related with the improved form and elongation of needle-like crystallites (Fig.17.(b)). Further increase of the magnetic field amplitude causes simultaneous growth of well-defined, needle-like and small, spherical crystallites (Fig.17.(c)). This could be assigned to the increased growth ratio of (101)-hcp and

(110)-hcp+(220)-fcc phases. The needle-like form of crystallites stands for the presence of hexagonal phase, while that of spherical one is related to the growth of fcc phase. Thus, a superimposed magnetic field confirms the formation of biphasic Co films.

The biphasic structure characteristic was also determined in the electrodeposited Co-Ni films (Fig.18). In this case, the effect of a superimposed magnetic field on the phase formation is more obvious than in the electrodeposited single Co films and it acts as a low pH level.

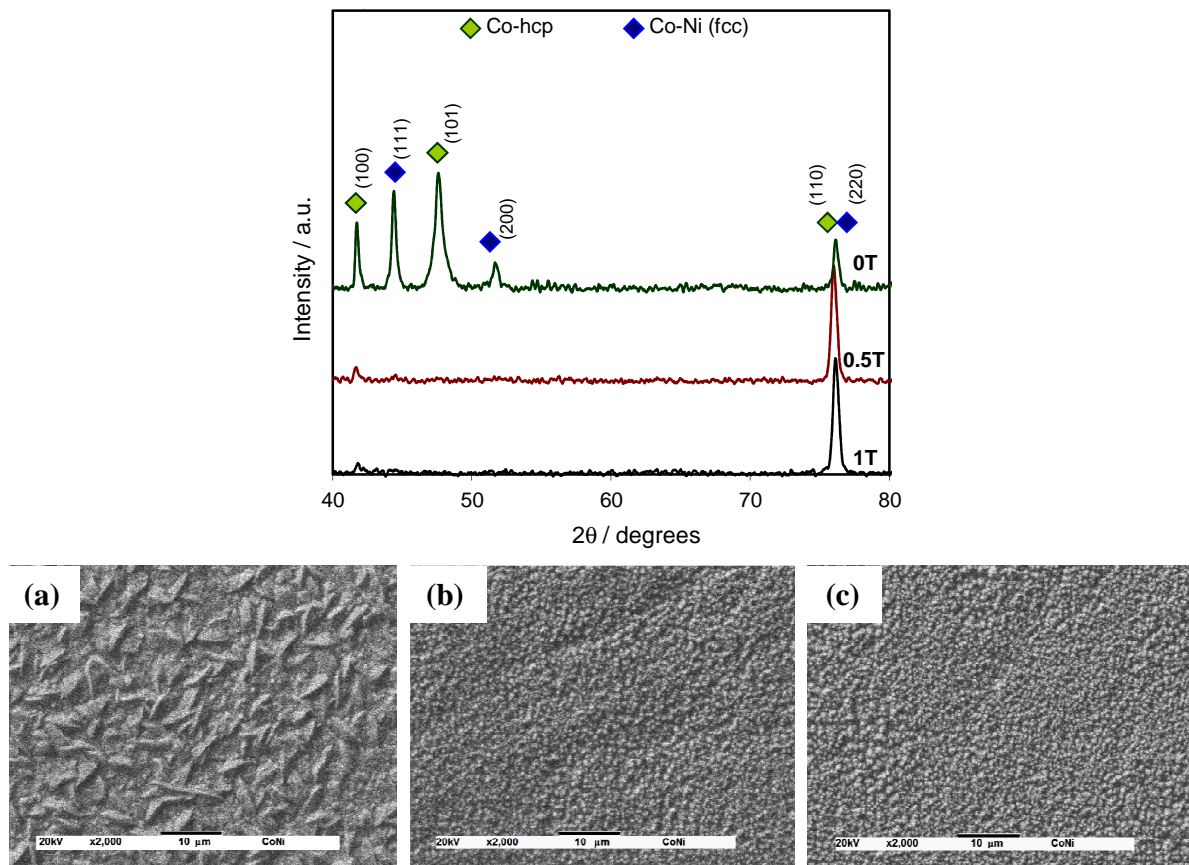


Fig.18. X-ray diffraction patterns and morphology of the Co-Ni films electrodeposited on Ti substrate under: (a) 0T, (b) 0.5T and (c) 1T magnetic field; $i = -20mA/cm^2$, $t = 18min$, $pH = 4.7$.

In absence of an external magnetic field the X-ray diffraction pattern of Co-Ni films indicates five diffraction peaks associated with simultaneous growth of both, hcp and fcc phases. Under magnetic field conditions of 0.5 and 1T most of the diffraction peaks localized at lower 2θ angles are not formed. The (100)-hcp plane of pure Co phase is still observed, but with much lower relative intensity than that in Co film deposited without an applied magnetic field. Similar to the

previous case of Co films, the magnetic field affects the intensity of (110)-hcp+(220)-fcc diffraction peak. Thus, the morphological characteristic is affected as well. The Co-Ni structure consists of broad needle-like crystallites, when no magnetic field was applied (Fig.18.(a)). The morphology is completely transformed in fine-grained structure of small and spherical crystallites under magnetic deposition conditions (Fig.18.(b) and (c)). This suggests that during electrodeposition of Co-Ni films under superimposed magnetic field, the obtained structure could be completely monophasic. In this case, the morphological features confirmed that it is probably the fcc structure.

Regarding on the Co films deposited under magnetic field, there is no effect on the structure formation of deposited films (Fig.17). It was discussed by Krause *et al.* [18], that a magnetic field of at least 30T strength is necessary in order to affect the nucleation. If the nucleation cannot be influenced by laboratory field strengths, an influence on the structure formation is difficult to imagine. Thus, the secondary effects of magnetic field, as for example, on the pH value in the vicinity of electrode surface, are responsible for the structural modifications, as observed in the growth of Co-Ni films under magnetic field (Fig.18). The growth of different structural planes may be explained as a consequence of competitive adsorption between hydrogen and intermediate species [27,170], or according to the growth conditions, related to different degree of inhibition [174]. Also, a change in the intensity of X-ray diffraction peaks of deposited films is usually attributed to the presence of inhibiting species, such as hydrogen and metal hydroxides [175,176]. The additional convection induced by the MHD effect in the electrolyte may be invoked to be responsible for the structural evolution. A superimposed magnetic field increases the hydrogen evolution reaction and adsorption of some inhibiting species, such as H_{ads} and metal hydroxides. As the diffusion layer thickness decreases under magnetic-induced convection, the concentration gradient of hydrogen ions increases. Therefore, the flux of hydrogen ions arriving at the electrode is increased. Diao *et al.* [177] have proposed that an increased HER was observed because of an easier coalescence of hydrogen bubbles due to the MHD stirring of the electrolyte and in turn, decrease in the overpotential of the hydrogen formation. Hence, the crystallite size and layer roughness are improved under magnetic field conditions.

More homogeneous deposit surface, resulting from the processes carried out under magnetic field is also reported in the works of Tabakovic *et al.* [116], Ispas *et al.* [121] and Koza *et al.* [155]. The well-defined quality of deposits is clearly induced by the MHD stirring of the

electrolyte, which reduces the thickness of diffusion layer and in turn improves a mass transport toward the electrode surface. Due to the stirring effect, the MHD convection improves the electrode coverage by removing the gas bubbles sticking to the electrode surfaces and reduces the void fraction in the electrolyte-bubble dispersion zone [178]. The hydrodynamic origin of the smoothing effect is supported by the results obtained by Matsushima *et al.* [152] and Osafo-Acquaah *et al.* [176]. A reduction in the value of growth exponents as well as the roughness with the increased electrolyte flow was reported. It was proposed that the deposition conducted without a forced convection results in a privileged growth of peaks and rough deposits. With an increase of the flow rate the concentration gradient at the electrode surface is reduced, a surface peak growth mode is suppressed and resulting electrodeposit appears smoother [176]. A forced convection is of much higher magnitude than the one caused by Lorentz force. However, the observed changes in a magnetic field have to be of the same nature as the ones reported under a forced convection.

II.4.1.2. Co films electrodeposited on Ni/ITO substrate

In comparison with the Co films electrodeposited on Ti substrate, the magnetic field effect on the Co films deposited on Ni/ITO is less obvious. Figure 19 presents the X-ray diffraction patterns together with associated morphological characteristics of Co/Ni/ITO films. The Co films deposited on Ni/ITO substrate consist of both crystallographic Co phases: hcp and fcc. This phase composition is not changed under magnetic electrodeposition conditions. The superimposition of 0.5 and 1T magnetic field, similar as in previous cases, affects the relative intensity of diffraction peaks. Under magnetic conditions the intensity of diffraction peaks corresponding to the Co-(100)-hcp and mixed Co-(110)-hcp+Co-(220)-fcc+Ni-(200)-fcc orientations increases slightly. Accordingly, no significant modifications in the morphological features are observed (Fig.19.(a),(b) and (c)). The Co films in each case consist of crystallites in the form of small and wide particles.

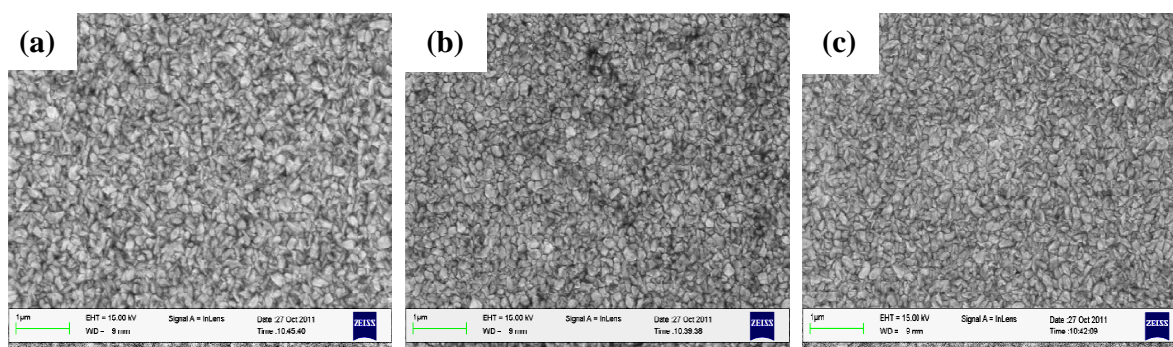
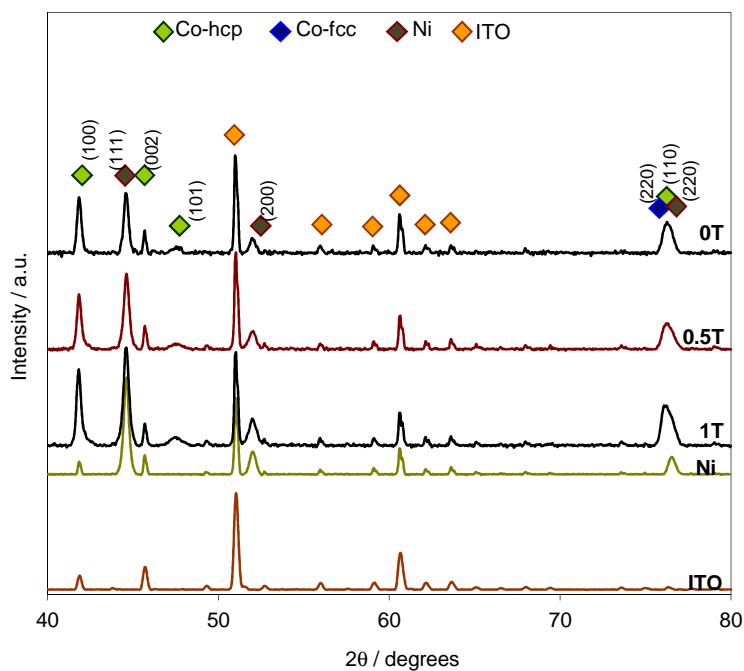


Fig.19. X-ray diffraction patterns and morphology of the Co films electrodeposited on Ni/ITO substrate under: (a) 0T, (b) 0.5T and (c) 1T magnetic field; $i = -10\text{mA/cm}^2$, $t = 1\text{min}$, $\text{pH} = 4.7$.

Change in the diffraction peaks intensity of the Co/Ni/ITO films has been usually attributed to the presence of inhibiting species, such as hydrogen and cobalt hydroxides [49]. Such species can be formed depending on the electrolyte composition and deposition parameters, and can be partially adsorbed at the cathode surface. The amount of inhibiting species can be changed with a superimposed magnetic field. The induced convection in the process carried out under magnetic field conditions increases the transport of both, metal and inhibiting species ions towards the electrode surface. Thus, under magnetic field the hydrogen evolution is faster than in the process, where no magnetic field is superimposed. Hence, the amount of adsorbed hydrogen is higher and the variation of diffraction peak intensities is observed.

II.4.1.3. Electrochemical kinetic study

Chronoamperometry is a method widely used to study nucleation and growth processes. A basic study interprets the electrodeposition process in terms of nucleation followed by growth and generally relies on the use of current transient analysis for determining nucleation rates, saturation nucleus densities and steady-state growth rates. Figure 20 shows the current-time transient of cobalt recorded on the Ti substrate at deposition potential -1.4V vs. SSE.

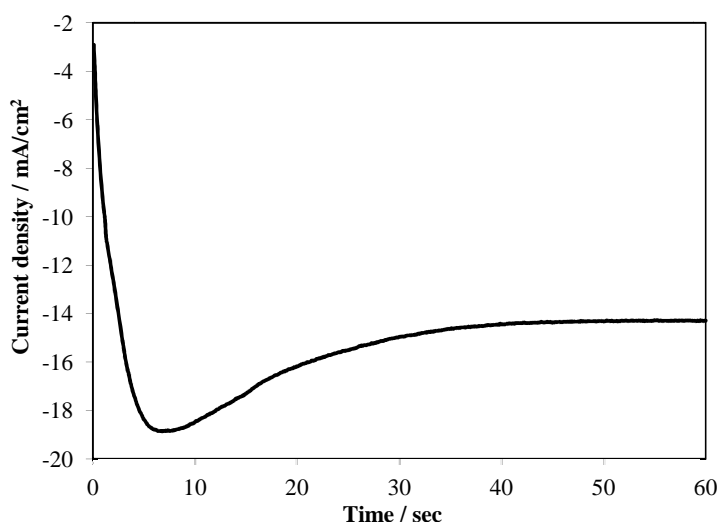


Fig.20. Current-time transient for the electrodeposition of Co/Ti at -1.4V vs. SSE, pH = 4.7.

This feature is consistent with the nucleation and growth processes, indicating 3D-nucleation mechanism with hemispherical nucleus and diffusion control. The initial regime of transient is characterized by a sharp increase in current, which corresponds to formation of the first nuclei at the electrode surface. This is followed by a decrease in the current due to a decrease in the electroactive area associated with crystal growth on the electrode. Finally, the slow decrease in current corresponds to limitation of the reaction process by semi-infinite linear diffusion of the Co^{2+} ions.

The electrodeposition transients can be analyzed by comparing the growth laws normalized in terms of the maximum current, i_{max} , and the time at which the maximum current is observed, t_{max} . According to the model including diffusion-controlled growth of hemispherical nuclei proposed by Scharifker and Hills [179], the electrodeposition transients for instantaneous

and progressive nucleation followed by 3D diffusion-limited growth can be described by the following Equations:

$$\left(\frac{i(t)}{i_{\max}}\right)^2 = \frac{1.9542}{t/t_{\max}} \left\{ 1 - \exp\left[-1.2564\left(\frac{t}{t_{\max}}\right)\right] \right\}^2 \quad (30)$$

$$\left(\frac{i(t)}{i_{\max}}\right)^2 = \frac{1.2254}{t/t_{\max}} \left\{ 1 - \exp\left[-2.3367\left(\frac{t}{t_{\max}}\right)^2\right] \right\}^2 \quad (31)$$

Eq.(30) stands for an instantaneous nucleation, where all the cobalt nuclei are created at the same moment at the beginning of the applied potential, while Eq.(31) is a progressive nucleation, where new crystals are continuously created throughout electrodeposition. A convenient criterion for distinguishing between these two cases of nucleation kinetics is to present the experimental data in a non-dimensional plot $(i(t)/i_{\max})^2$ vs. (t/t_{\max}) and to compare them with the theoretical plots resulting from Eqs. (30) and (31). Figure 21 shows the experimental result for electrodeposited cobalt at potential -1.4V with the two limiting cases of the theoretical 3D nucleation growth models.

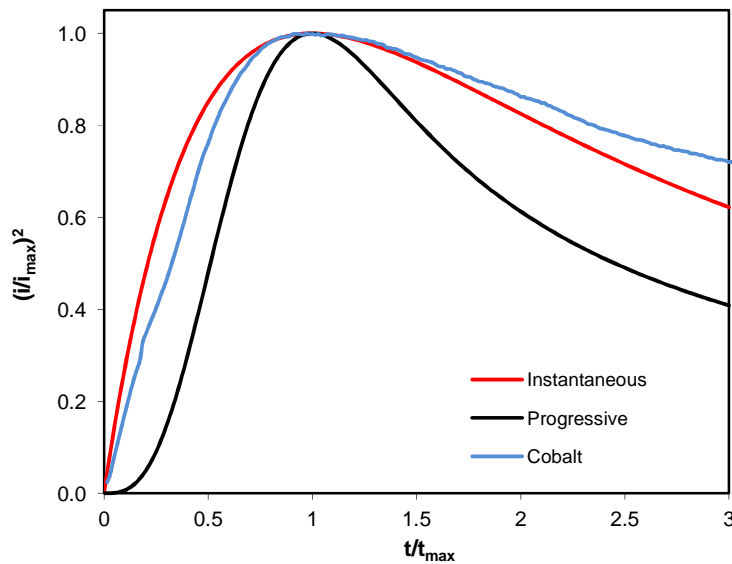


Fig.21. The theoretical instantaneous and progressive nucleation modes compared with normalized $(i/i_{\max})^2$ vs. t/t_{\max} plots obtained from the experimental data in Fig.20.

According to Fig.21, cobalt nucleation seems to follow the instantaneous nucleation model. Negative deviation of chronoamperogram from the models at about $t/t_{max} = 1.5$, is mostly likely related to reduction of hydrogen ions and hydrogen evolution. When the total area of cobalt nuclei is relatively small (before the maximum on the reduced current plot) the contribution from the hydrogen reduction will also be small. While, the surface area of cobalt becomes larger, the contribution from the hydrogen ion reduction to the overall current will become significant, causing a deviation from the theoretical model. This invalidates the interpretation of the result in Fig.21, because the model given by Eqs. (30) and (31) cannot distinguish between the currents contributed by the cobalt and hydrogen ions reduction.

The Scharifker-Hills model also determines the type of nucleation by analyzing the raising parts of the chronoamperogram, prior to the overlap of nuclei diffusion zones. At this stage, the reduction of hydrogen ions is not so prominent and majority of current corresponds to reduction of cobalt ions. Analysis of the raising part of transient is possible by representing, for the initial transient portion, i versus $t^{1/2}$ for instantaneous and i versus $t^{3/2}$ for progressive nucleation. The raising parts of the current-time transient should exhibit linear dependence in either the of i vs. $t^{1/2}$ or i vs. $t^{3/2}$ domains, for instantaneous and progressive nucleation mechanisms, respectively (Fig.22).

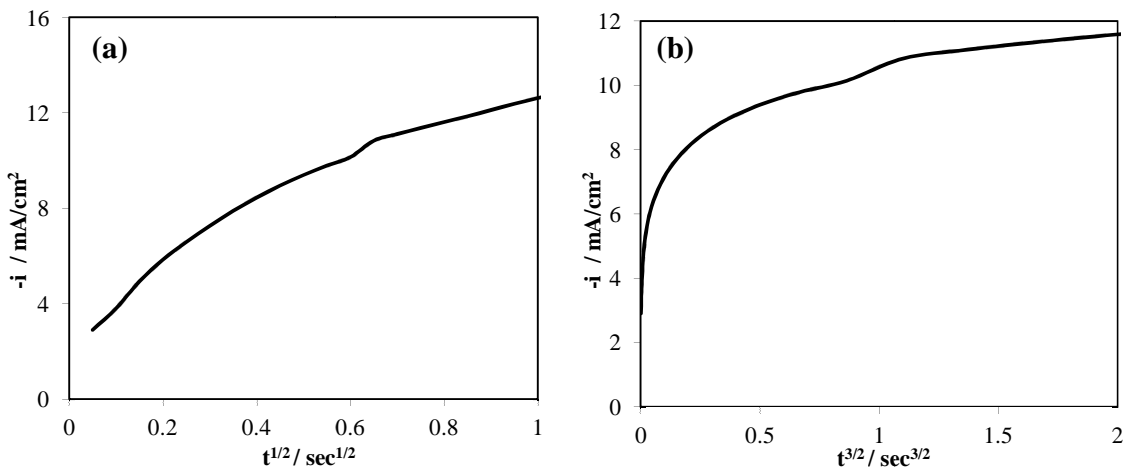


Fig.22. Dependence of i versus (a) $t^{1/2}$ and (b) $t^{3/2}$ plots for the initial transient portion for Co/Ti electrodeposition; $E = -1.4V$ vs. SSE, $pH = 4.7$.

For the experimental data shown in Fig.22, it can be observed that the initial part of chronoamperogram can be better linearized in the $i-t^{1/2}$ domain, which corresponds to the

instantaneous nucleation regime. It should be noted that the linearization is not ideal in either of the two domains.

Because of the apparent discrepancy in unequivocal assigned cobalt nucleation mechanisms, which may be changed depending on the employed diagnostic criteria, another proposed by Palomar-Pardave *et al.* [180] nucleation model may be used. The Palomar-Pardave *et al.* nucleation model takes into account the contribution from the concurrent hydrogen ion reduction and clear identification can be done. However, since the electrochemical aspect is not a main goal of the thesis, the further investigations on this deliberation are not provided. Instead, in the forthcoming sections the topographical analysis is included, which may also resolve the stated problem.

II.4.1.3.1. Effect of a magnetic field on the current-transients

The shape of $i-t$ transients at the very beginning of the deposition, obtained with the same parameters may significantly vary from one to another experiment. Because of that, analysis of a single, independent transient may lead to a misinterpretation in the nucleation and growth mechanism. For this purpose it is more convenient to use transients, which are an average value of many measurements. This procedure was adopted for the present section, where the electrodeposition process was carried out under magnetic field.

Figure 23 presents the differences in $i-t$ transient curves between Co and Co-Ni films electrodeposited with and without an applied magnetic field at potential -1.4V vs. SSE.

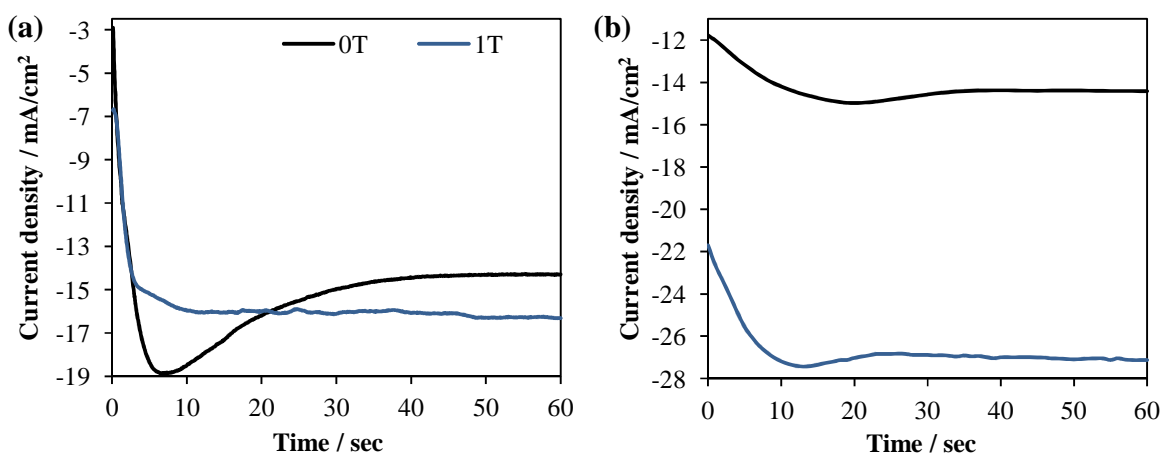


Fig.23. The adjustment of current-time transients for: (a) Co/Ti and (b) Co-Ni/Ti films electrodeposited at -1.4V vs. SSE under LMF.

A magnetic field applied during the process decreases the maximum current density of the transient current of deposited Co (Fig.23.(a)). Opposite situation is observed for deposition of Co with Ni (Fig.23.(b)), where the current density of Co-Ni electrodeposition process increases with applied magnetic field. Moreover, the current maximum is observed at shorter times, indicating faster nucleation rate. The differences in the $i-t$ transients obtained under magnetic condition are related with a simultaneous hydrogen evolution. The hydrogen evolution reaction is a secondary process always assisted deposition from aqueous solution, and needs to be considered. The applied magnetic field during the process enhanced the hydrogen evolution, thus causes the modification of $i-t$ curves. However, the transients indicate a characteristic feature – current maximum, which represents nucleation and 3D growth phenomena with a hemispherical geometry.

The differences observed in the current-time transients of electrodeposited Co and Co-Ni films are due to the change of hydrodynamic conditions in the electrolyte under magnetic field superimposition. The observed shift of the current maximum peak of Co-Ni film toward shorter times in a magnetic field (Fig.23.(b)) suggests that the nucleation and early stages of the layer growth could be affected by a magnetic field. This effect is attributed to the MHD effect acting in the electrolyte, which retards the nucleation rate and favours the growth of nuclei [181]. In consequence, the obtained surface morphology of Co and Co-Ni films differ significantly from, when magnetic field is superimposed.

II.4.1.3.2. Effect of a magnetic field on the crystal growth

The typical AFM images of cobalt and Co-Ni alloy films electrodeposited with and without an applied magnetic field, in 2D view are presented in Figure 24. These images indicate that the substrate surface is completely covered by quite homogeneous in form crystals, which grow onto the substrate through 3D island growth mode (Volmer-Weber growth mode), indicative of instantaneous 3D nucleation. Thus, the instantaneous nucleation mechanism proposed on the base of conventional electrochemical experiments presented before, may be confirmed.

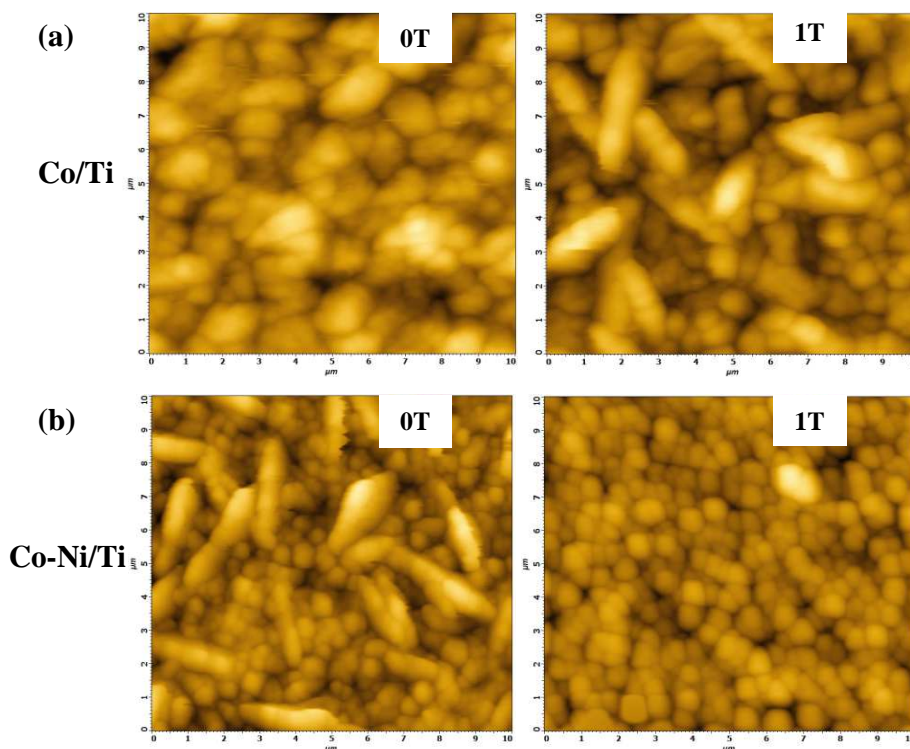


Fig. 24. The AFM images of (a) Co/Ti and (b) Co-Ni/Ti films electrodeposited under LMF; Scanning area $10 \times 10 \mu\text{m}^2$; $i = -20 \text{mA/cm}^2$, $t = 12/18 \text{min}$, $\text{pH} = 4.7$.

Considering the magnetic field effect it can be seen that the Co and Co-Ni crystals evaluated into different shapes and sizes. The topography of cobalt films (Fig.24.(a)) indicates formation of two different varieties of crystals: spherical and needle-like, which grow above the certain level of film. These two varieties of film crystals are characteristic for Co-Ni alloy film deposited in non-magnetic process (Fig.24.(b)). A superimposition of 1T magnetic field causes a transformation of Co-Ni crystals in the monoshape of spherical and separated grains. The reason of this observation is of a hydrodynamic origin. When no magnetic field is present during electrodeposition, the nucleation occurs at many active sites and their growth processes occur simultaneously. Nuclei are at different ages and sizes, as indicated in Fig.24.(a) and (b) in the case of deposition under 0T. When a magnetic field is superimposed, the very beginning of electrocrystallization is unaffected by a magnetic field and a whole situation is identical as in the process with absent magnetic field. As the time goes by, the Lorentz force induced convection arises and increases electroactive species transport towards already existing nuclei. Due to that as soon as metallic Co (or Co and Ni in Co-Ni films) will appear at the electrode surface, it serves as a reaction site for hydrogen evolution. The products of the hydrogen reduction are the hydrogen gas bubbles that

are formed at the electrode surface, grow and eventually prevent further cobalt reduction from taking place on the cobalt nuclei surface. Because cobalt ions could not be reduced at the surface of metallic cobalt, they need to be reduced elsewhere on the electrode substrate, leading for the formation of new cobalt nuclei. As a result, the size of nuclei decreases and population density increases [182,183].

II.4.1.4. Co-Cu and Co-Ni-Cu films electrodeposited on Cu/ITO substrate

The Co-Cu alloy is especially interesting Co-based system, mainly because of its magnetic properties. Moreover, it has been found that alloying the Co-Cu system with low amounts of nickel, the properties of thin films can be improved. Furthermore, both Co-Cu and Co-Ni-Cu alloys are usually prepared by physical vapor deposition technique rather than electrodeposition method. In this case, the electrochemical deposition process seems to be more convenient, since it is easier to maintain the process parameters and thus, control the growth and related with it, properties of the deposited film. Hence, the followed section considers electrodeposition of Co-Cu and Co-Ni-Cu films on Cu/ITO substrate and investigates the effects of magnetic field on their growth process.

II.4.1.4.1. Magnetic field effect on microstructure and chemical composition

Figure 25 reveals the phase composition of Co-Cu and Co-Ni-Cu films electrodeposited on Cu/ITO substrate with and without a superimposed magnetic field. The X-ray diffraction patterns indicate that the films of both systems are polycrystalline in nature.

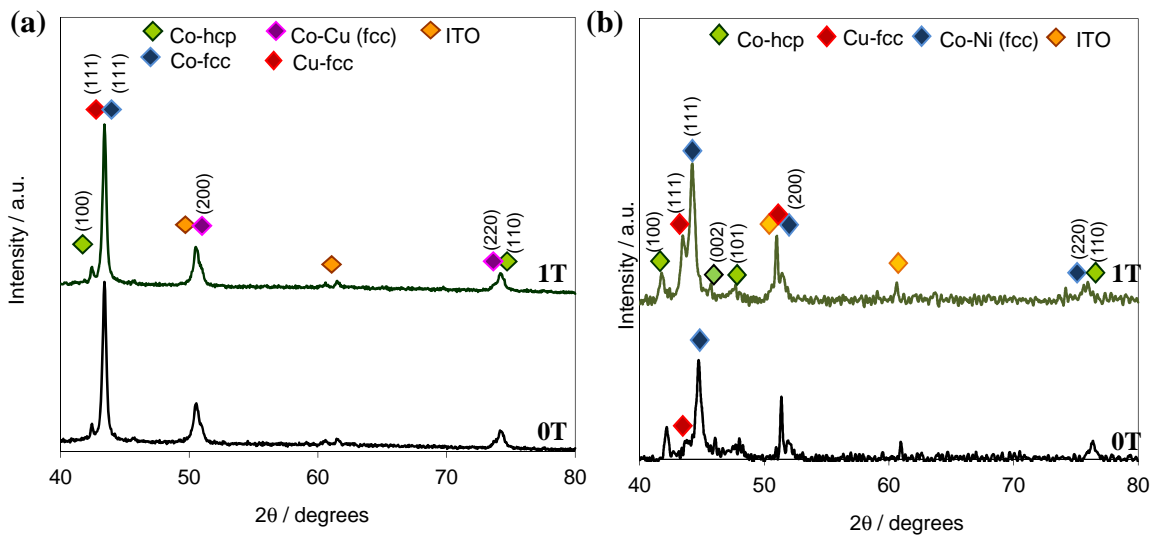


Fig.25. X-ray diffraction patterns of the Co-Cu/Cu/ITO (a) and Co-Ni-Cu/Cu/ITO (b) films electrodeposited under LMF; $i = -20\text{mA/cm}^2$, $t = 1\text{min}$, $\text{pH} = 4$.

In the case of Co-Cu films, each pattern shows the diffraction peaks of fcc structure of alloy, as well as a weak peak at $2\theta = 41^\circ$, which is attributed to the reflection of (100) plane of hexagonal structure of cobalt, appearing also at higher angles as (110) plane together with Cu (220)-fcc phase. The presence of Co-hcp phase may suggest that Co grains exist within the Co-Cu solid solution matrix. The intensive diffraction peak at 2θ angle about 41° indicates that the Co-Cu film crystallites grown favorably in the direction of (111)-fcc plane. A superimposed magnetic field does not provide any effect neither on the phase composition nor on the relative diffraction peak intensities. The act of superimposed magnetic field is observed, when alloying Co-Cu system with Ni element (Fig.25.(b)). The X-ray diffraction pattern indicates the growth of Cu on the Co-Ni matrix during electrodeposition without an applied magnetic field. Moreover, this growth is associated with the simultaneous growth of single Co-hcp phase. Under magnetic condition of 1T an intensive growth of Co-Ni-(111)-fcc matrix and embedded in it Cu-(111)-fcc crystals is observed. Thus, it is suggested that under magnetic condition the growth of Cu crystallites may be more stable and they can grow separately from the Co-Ni matrix.

In contrast to the X-ray diffraction patterns, the morphological characteristics of both films (Co-Cu and Co-Ni-Cu) are closely related to each other (Fig.26).

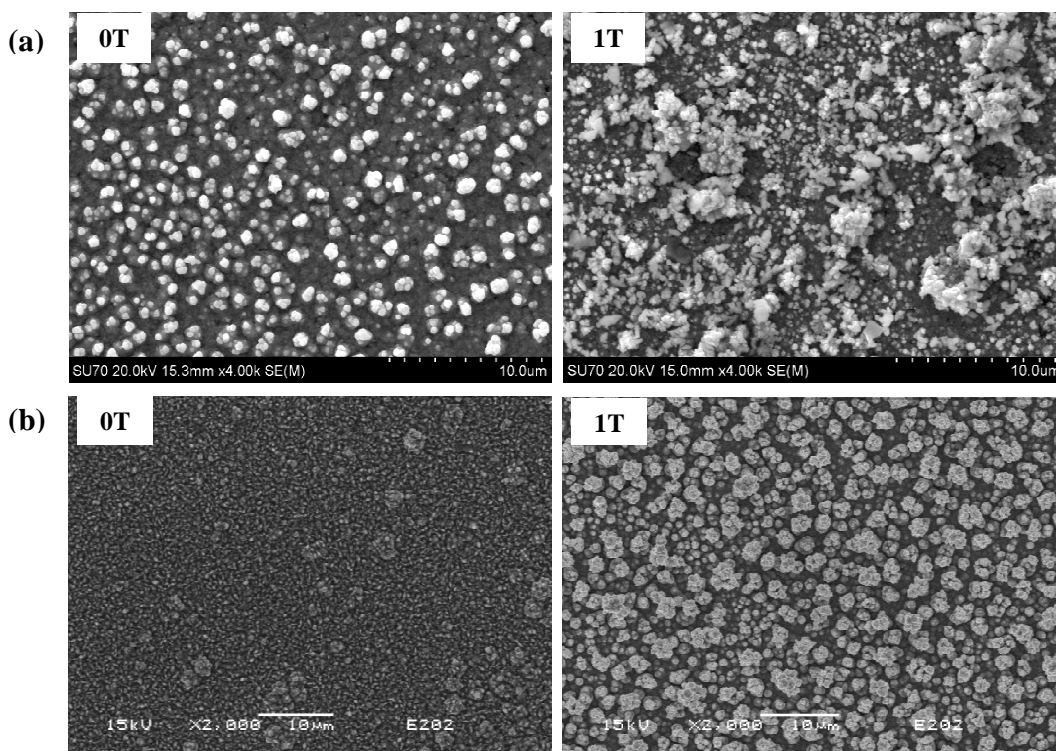


Fig.26. Morphology of the Co-Cu/Cu/ITO (a) and Co-Ni-Cu/Cu/ITO (b) films electrodeposited under LMF; $i = -20\text{mA}/\text{cm}^2$, $t = 1\text{min}$, $\text{pH} = 4$.

The SEM observation shows that the electrodeposited Co-Cu/Cu/ITO and Co-Ni-Cu/Cu/ITO deposits could be composed of two layers. This feature is especially well observed in the Co-Cu and Co-Ni-Cu films are deposited without magnetic field. The bottom layer is a compact thin film, whereas the surface layer consists of submicron-scale crystallites that adhere to the bottom layer. Comparing both films, when the Co-Cu system is alloyed with Ni, the morphological feature of the Co-Ni-Cu film is characterized by more homogeneous structure (Fig.26.(b)). The surface morphology of both alloy films is strongly dependent on a superimposed magnetic field, more exactly on the concentration of each ions affected by an external magnetic field. When the weight percent of Cu atoms increases from 48wt.% to 58wt.% in the Co-Cu layer (Fig.27.(a)) and from 14wt.% to 35wt.% in the Co-Ni-Cu layer (Fig.27.(b)), due to the magnetic condition, the morphology of the bi and tri-metallic films changes from individual particles to submicron-scale flower-shaped Co-Cu and Co-Ni-Cu crystallites (Fig.26).

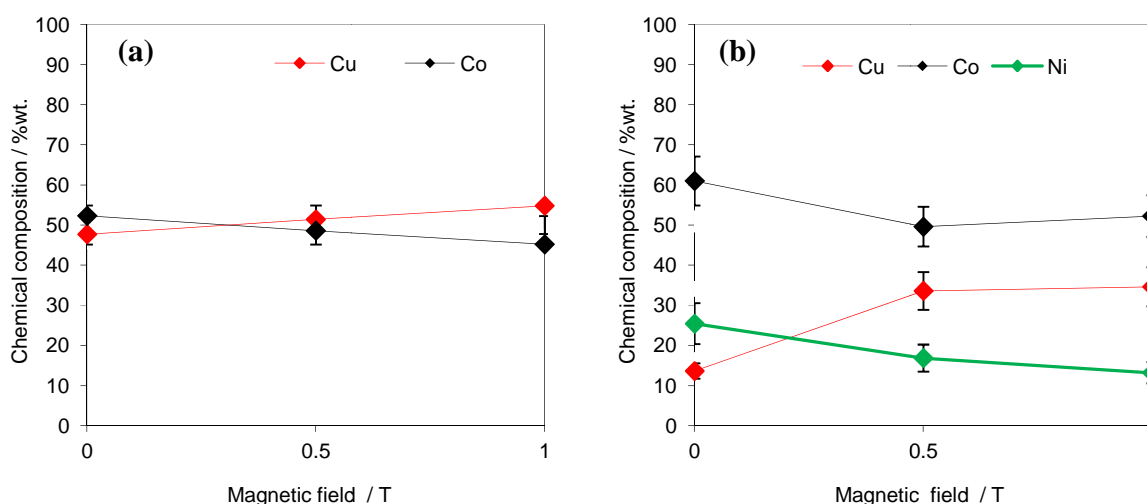


Fig.27. Chemical composition of the Co-Cu/Cu/ITO (a) and Co-Ni-Cu/Cu/ITO (b) films electrodeposited under LMF; $i = -20\text{mA/cm}^2$, $t = 1\text{min}$, $\text{pH} = 4$.

The typical multi-branched flower form of Co-Cu and Co-Ni-Cu films is presented in Figure 28. Comparing both films, it is observed that Co-Cu crystallites grown not uniformly at the electrode surface (Fig.28.(a)), while that of Co-Cu-Ni are more uniform in crystallite sizes and its population density is much higher (Fig.28.(b)). However, both multi-directional 3-dimensional film growth indicates an instantaneous nucleation process, perpendicular to the electrode surface.

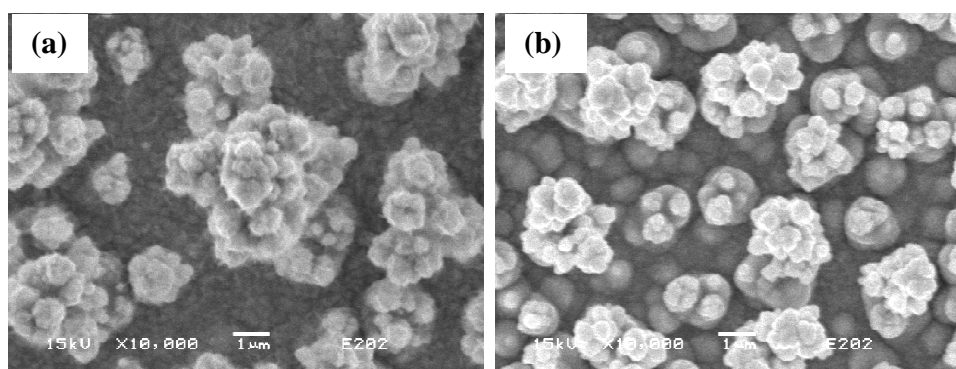


Fig.28. Comparison of the flower-like features of Co-Cu/Cu/ITO (a) and Co-Ni-Cu/Cu/ITO (b) films electrodeposited under 1T magnetic field; $i = -20\text{mA/cm}^2$, $t = 1\text{min}$, $\text{pH} = 4$.

As a result of structural analysis, it could be proposed that the separation of the (111) peaks in Co-Ni-Cu film is reinforced by the magnetic electrodeposition conditions and the

intensity of the peaks increase with development of the flower-like morphology. It is known that the favour growth orientation of electrodeposited films containing Cu is an fcc phase in (111) orientation [184,185]. Moreover, an increase of the diffraction peak intensity is probably a result of the increased Cu content in the electrodeposits. In the mass-controlled region of Co-Cu and Co-Ni-Cu deposition, the deposited mass of Cu increases with increasing magnetic field. This is due to the MHD effect caused by a higher convection in the electrolyte, as a result of the Lorentz force (Eq.(22)). It is expected that the surface concentration of Cu^{2+} ions increase accompanying with decreasing H^+ ion concentration at cathode surface under magnetic field. That is, the surface concentration of Cu^{2+} ion is still maintained at higher value due to MHD convection [114]. The deposition of Co and Ni in the Co-Cu and Co-Ni-Cu films is overlapped by the deposition of Cu and also by the reduction of protons. A decrease of the deposited Co and Ni masses can be related to a preferential hydrogen reduction in an applied magnetic field. Hydrogen reduction as a transport-controlled reaction is subjected to the same magnetically induced enhancement of convection.

A possible explanation for the flower-like growth in the surface morphology of the films might be the diffusive growth of Cu. Branched flower-like structure of Co-Cu and Co-Ni-Cu deposits may be explained by the co-deposition of hydrogen. Therefore, a change of the morphology of deposited films might be attributed to the hydrogen evolution reaction, which is favoured under magnetic field conditions. Without a magnetic field, the only driving force for the reduction is the diffusion of hydrogen ions towards the electrode surface. The natural convection is negligible since the electrode is oriented horizontally. A short time after switching on the magnetic field, an additional force is influencing the hydrogen ion reduction. The flow of hydrogen ions towards the cathode is perpendicularly oriented to the magnetic field. Thus, due to the Lorentz force (Eq.(22)), an additional convection is generated. As a result, the thickness of diffusion layer decreases and the concentration gradient of hydrogen ions increase [159]. Therefore, the number of hydrogen ions arriving at the electrode surface is increased (Fig.29). One of the consequences of hydrogen evolution is that H_2 bubbles are attached to the surface during the deposition and therefore, can cause growth of the deposit around the bubbles before they are released.

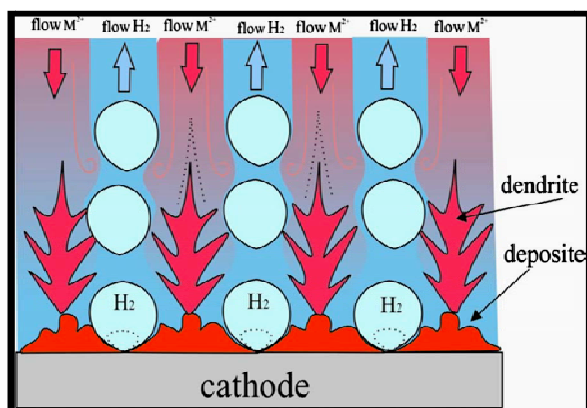


Fig.29. Schematic representation of the dendrite formation related to the hydrogen evolution reaction [186].

II.4.1.4.2. Electrochemical dynamic study

To obtain a complimentary overview on the electrochemical aspect of deposition, besides the electrokinetics investigated by the chronoamperometry, it is also useful to determine the electrochemical dynamics of studied system. Since the best reproducibility of experiments was obtained for the Co-Cu films the present section is focused on the study of dynamic process as a function of an applied magnetic field, by means of potentiostatic polarization curves and Electrochemical Impedance Spectroscopy (EIS).

The results shown in Figure 30 demonstrate the magnetic field effect observed during electrodeposition of Co-Cu alloy films. A slight increase of current density in the presence of a magnetic field is found in the cathodic potential range up to -1.6 V vs. SSE.

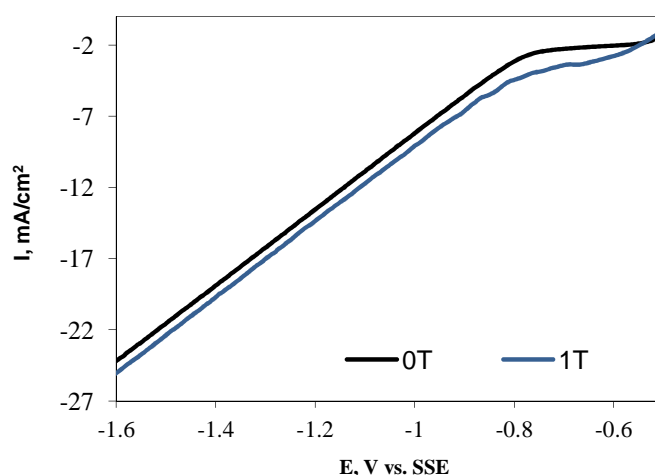


Fig.30. Current-potential curves for the Co-Cu/Cu/ITO films electrodeposited under LMF; $E = -1.4V$ vs. SSE, $pH = 4$.

The first current increase observed at potential range of -0.6 to -0.8 V vs. SSE is due to the MHD convective effect on the cathode of inhibiting Co(II) species that are under mass control. The further increase of potential, up to -1.6 V vs. SSE is explained by the MHD convective effect on the H(I) species that leads to a strong gaseous hydrogen bubbling from the cathode.

Figure 31 presents the impedance diagrams in the frequency range from 59.7 kHz to 7.59 Hz, for a deposition potential of -1.4 V vs. SSE. The impedance diagrams are composed with two loops. The high frequency capacitive loops characterize the charge transfer processes in parallel with the double-layer charging. In addition, the second capacitive loop is composed with inductive compartment, which may be localized in the negative imaginary part of the plot for high applied potential values. In this high frequency domain the first loop of the diagram arises from coupling the electrons exchange reactions with the double layer charge phenomena. Usually, the first process is represented by the charge transfer resistance, R_{ct} and the second by the double layer capacitance, C_{dl} . From this, the potential dependence of charge transfer resistance may be regarded in term of the potential evolution of electrode kinetics. Taking into account that at chosen potential the Co-Cu electrodeposition is dominated by the simultaneous hydrogen evolution (Fig.30), the effect of magnetic field is measurable.

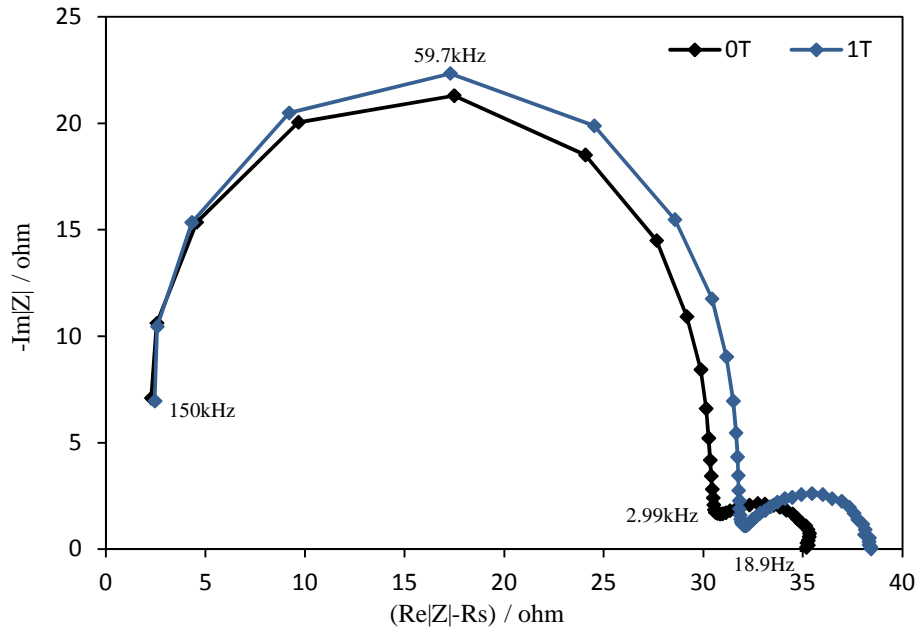


Fig.31. Nyquist diagram of the Co-Cu/Cu/ITO films electrodeposited under LMF; $E = -1.4V$ vs. SSE, $pH = 4$.

The differences between both plots, 0 and 1T, are due to the enhanced hydrogen evolution reaction under magnetic conditions. In this case, the magnetic field acts on the kinetics of the adsorption process, leading to a modification of the covering state of electrode by the adsorbed species. The high frequency electrochemical impedance Z_{HF} is given by the expression:

$$Z_{HF} = R_s + [R_{ct} / (1 + R_{ct} (j\omega)^\alpha 2Q)] \quad (39)$$

where R_s is the solution resistance, R_{ct} is the charge-transfer resistance, Q is the constant phase element, that is a term of representative of the double layer phenomenon, and α is an empirical constant ranging between 0 and 1. For α equal to 1, the constant phase element Q is completely identifiable to the double layer capacity, C_{dl} . To examine the effect of magnetic field on EIS characteristic parameters the experimental data were analyzed using a fitting procedure, which has been performed using commercial software ZSimpWin 3.21. This method is based on the comparison of experimental data with an equivalent circuit, which component values are dependent on a superimposed magnetic field during electrodeposition process. As an example, the equivalent circuit depicted in Figure 32 was used to quantify the evolutions of both capacitive and inductive loops with respect to the magnetic condition.

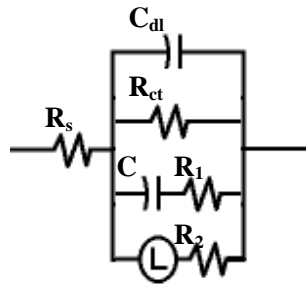


Fig.32. The equivalent circuit for modeling the impedance of electrodeposition of Co-Cu/Cu/ITO films under LMF.

The experimental parameters of impedances are listed in Table 5, in accordance to the electrodeposition conditions (with or without magnetic field). The parameters of R_s , C_{dl} and R_{ct} are constant, while that of R_1 , R_2 , L and C vary with a superimposed magnetic field, indicating the magnetic field effect on the adsorption of intermediate species and alloy activity.

Table 5. Parameters obtained from fitting of EIS model to the experimental data.

Feature \ B-field	0T	1T
R_s, ohm	2	2
C_{dl}, F	$1.3 \cdot 10^{-7}$	$1.3 \cdot 10^{-7}$
R_{ct}, ohm	$4.5 \cdot 10^7$	$4.5 \cdot 10^7$
C, F	$1.9 \cdot 10^{-6}$	$1.0 \cdot 10^{-6}$
R_1, ohm	152	140
L, H	$8.8 \cdot 10^{-5}$	$1.0 \cdot 10^{-4}$
R_2, ohm	33	36

The weak effects observed in the presence of magnetic field are only due to the change of the electrode area during the metallic electrodeposition and to the effect of MHD convection. Similar observations were reported by Devos *et al.* [166], who studied the magnetic field effect on electrochemical kinetics of different electrochemical systems. From the current-potential curves (Fig.30) it is clear that the Co-Cu electrodeposition is assisted with simultaneous hydrogen

evolution reaction. In a magnetic field the MHD convection enhances the mass transfer rate of Co^{2+} and Cu^{2+} ions toward the electrode surface as well as hydrogen. The hydrogen is adsorbed at the active sites of substrates, blocking them for the metal ions reduction. Thus, the conditions of electrodeposited substrate surface are changed and the electrochemical response is modified.

II.4.2. Effect of high magnetic field (HMF)

The electrochemical deposition process of Co-Ni and Co-Cu films was then carried out in a high magnetic field (HMF) up to 12T, in order to determine if the larger change of hydrodynamic conditions in the electrolytic solution caused by high magnetic field (larger magnetic forces than in LMF) will keep or induce further microstructural changes in the deposited films. Table 6 shows the considered systems in this section, together with the electrodeposition parameters.

Table 6. Composition of the electrolytic solutions according to the electrodeposition of different systems under HMF, together with the electrodeposition conditions.

System	Chemical agent	Concentration mol/L	Solution pH	Solution temperature °C	Current density mA/cm ²	Deposition time min	Magnetic field amplitude T
Ni / ITO	NiSO ₄ ·7H ₂ O H ₃ BO ₃	0.6 0.4	2.7	30	-10	1	0
Co-Ni/Ni/ITO	CoSO ₄ ·7H ₂ O NiSO ₄ ·6H ₂ O H ₃ BO ₃	0.4 0.6 0.4	4.7	50	-10	1	≤ 12
Co-Ni / ITO	CoSO ₄ ·7H ₂ O NiSO ₄ ·6H ₂ O H ₃ BO ₃ saccharin	0.3 0.7 0.4 0.015	4.7	50	-10	1	≤ 12
Cu / ITO	CuSO ₄ ·6H ₂ O H ₃ BO ₃	0.03 0.4	4.0	50	-20	5 sec	0
Co-Cu/Cu/ITO	CoSO ₄ ·7H ₂ O CuSO ₄ ·6H ₂ O H ₃ BO ₃	0.4 0.03 0.4	4.0	50	-20	1	≤ 12

II.4.2.1. Electrodeposited Co-Ni films

The Co-Ni films were electrodeposited under high magnetic field in two routes: on Ni/ITO substrate and directly on ITO substrate. The growth of Co-Ni films at the pure ITO surface was possible after introduction of saccharin additive to the electrolytic solution. Figure 33 presents the comparison of phase composition between Co-Ni films electrodeposited on Ni/ITO and ITO substrates. The X-ray diffraction patterns indicate the Co-Ni alloy formation at 2θ angle about 45° and additionally, for the Co-Ni/Ni/ITO at 2θ angle about 51° . Other detected diffraction peaks are associated with the Ni seed-layer and ITO substrate. Under high magnetic conditions of electrodeposition the phase composition in each deposit is not modified, even when the amplitude of magnetic field increases up to 12T.

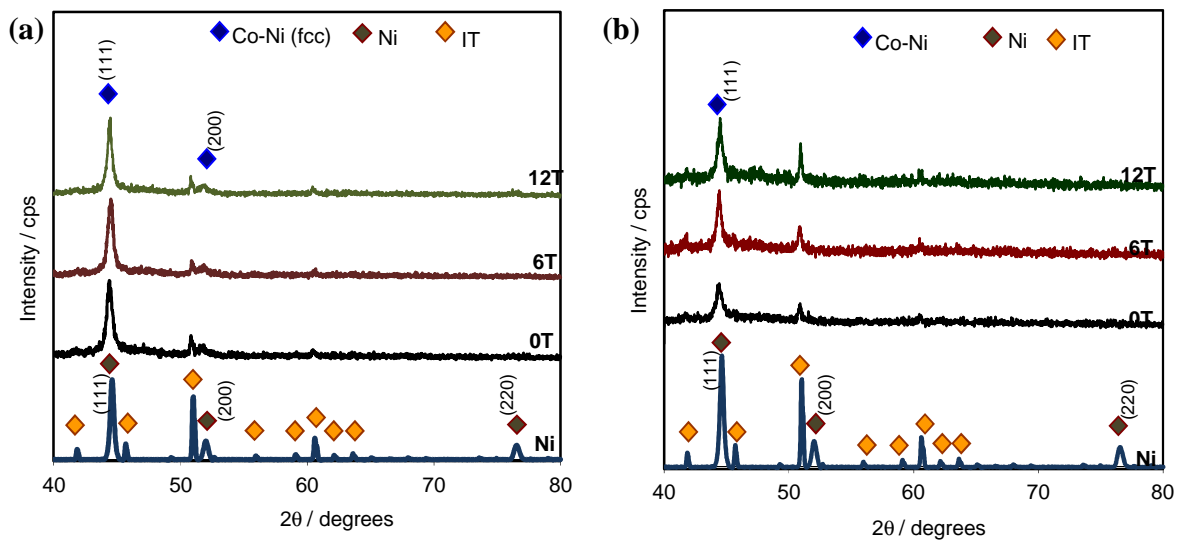


Fig.33. Phase composition of: (a) Co-Ni/Ni/ITO and (b) Co-Ni/ITO electrodeposited under HMF; $i = -10\text{mA}/\text{cm}^2$, $t = 1\text{min}$, $\text{pH} = 4.7$.

Similarly as in the previous case of Co films electrodeposited under low magnetic field, the slight variations observed in the diffraction peak intensity, when magnetic field is superimposed, are related with the hydrogen evolution reaction during electrodeposition. The magnetic field increases the HER increasing as the same time adsorption of some inhibiting species, such as H_{ads} or/and hydroxides. Moreover, according to Tabakovic *et al.* [116] and Ispas *et al.* [121], it can also lead to a preferential growth of the grains, if their easy axis of magnetization is in the

direction of a superimposed magnetic field. Both cases can be responsible for the modification of diffraction peak intensities. Furthermore, the additional convection in the electrolyte, induced by the MHD effect can be invoked to be responsible for the texture evolution, as stated by Matsushima *et al.* [154].

The morphological characteristics of Co-Ni films differ according to the deposited surface. The Co-Ni films electrodeposited on Ni/ITO substrate demonstrates less obvious modifications under magnetic field (Fig.34). The films consist of thin and needle-like crystallites, growing along the substrate surface. Moreover, in each magnetic case their size and shape is very similar.

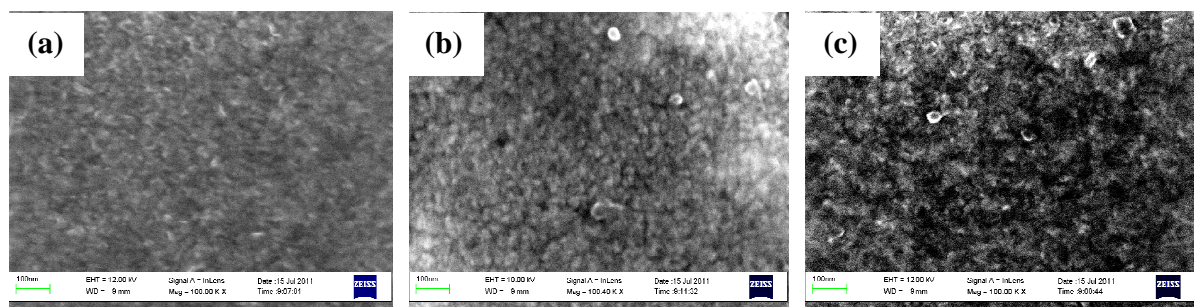


Fig.34. Morphology of the Co-Ni/Ni/ITO films electrodeposited under: (a) 0T, (b) 6T and (c) 12T magnetic field; $i = -10\text{mA}/\text{cm}^2$, $t = 1\text{min}$, $\text{pH} = 4.7$, without saccharin additive.

Much more interesting observation is noticed, when the Co-Ni films are electrodeposited directly on ITO substrate (Fig.35). The morphology of Co-Ni film deposited without a magnetic field (Fig.35.(a)) is similar to the previous observations of films deposited on ITO covered with Ni seed-layer (Fig.35.(a)).

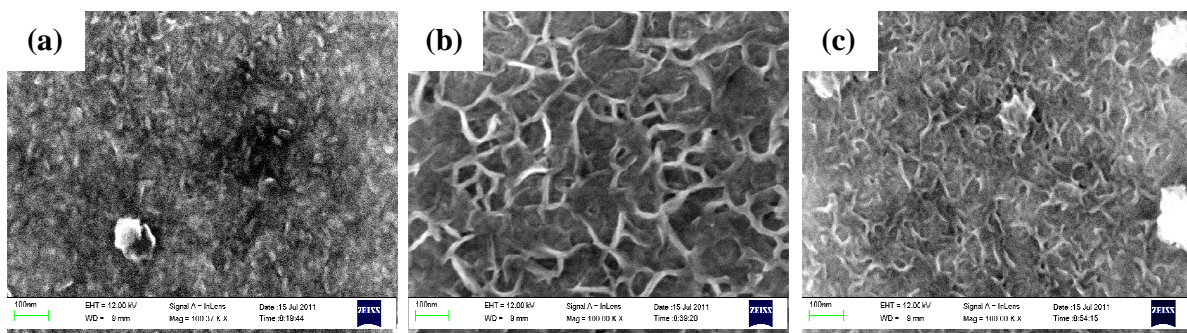


Fig.35. Morphology of the Co-Ni/ITO films electrodeposited under: (a) 0T, (b) 6T and (c) 12T magnetic field; $i = -10\text{mA}/\text{cm}^2$, $t = 1\text{min}$, $\text{pH} = 4.7$, with saccharin additive.

A significant morphological modification is caused, when a magnetic field is superimposed. The morphology of Co-Ni films appears in form of long and maze-like nanowired structure (Fig.35.(b)). This effect is kept with an increase of magnetic field amplitude up to 12T (Fig.35.(c)). However, the shape of these features is more like nanofibres characterized by a smaller size and higher population density along the substrate surface. The presence of saccharin in the electrolytic solution could influence the behaviour observed in this case. The modification of morphology by a superimposed magnetic field is confirmed by the calculated particles size, listed together with the roughness variations in Fig.36, obtained by the AFM analysis.

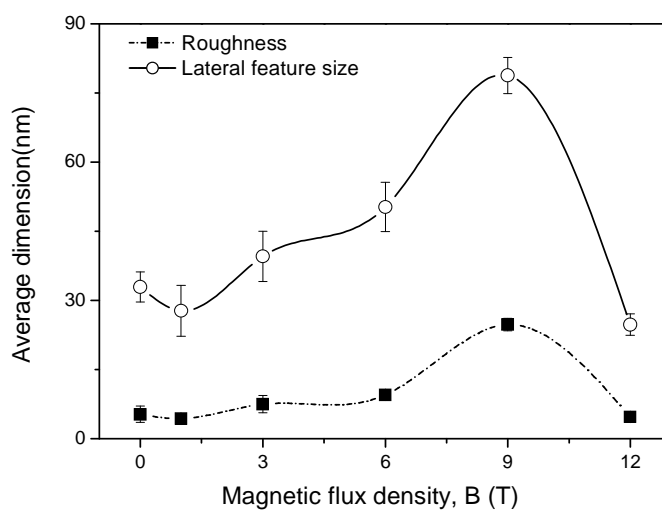


Fig.36. Roughness and crystallite size characteristics of the Co-Ni/ITO films electrodeposited under HMF; $i = -10\text{mA/cm}^2$, $t = 1\text{min}$, $\text{pH} = 4.7$.

The curves of feature size and roughness exhibit non-monotonic increase up to 9T. In contrast, these features decrease dramatically with further magnetic field increase up to 12T. Tabakovic *et al.* [116] have reported that a superimposed magnetic field gave larger crystallite size of electrodeposited Co-based films because of an increased mass transport. An increased mass transport of cobalt (Co and Ni ions in the case of Co-Ni alloy) diminishes the effect of hydrogen evolution reaction under magnetic field, which gives larger crystallites size, improved substrate surface and more dense deposits. Since the surface roughness is determined by the structural characteristics, the increased crystallites size causes simultaneous increase of deposit roughness.

The electrodeposition process of Co-Ni alloys is known as an anomalous co-electrodeposition. This means that the less noble metal (Co) is preferentially deposited on the

substrate than the more noble one (Ni). Fan and Piron [187] reported that anomalous co-deposition occurred only for current densities lower than 100 mA/cm^2 and related this phenomenon to the kinetics of deposition, which is intrinsically faster for cobalt than for nickel. The anomalous behaviour of Co-Ni films deposited in this work, with and without an applied magnetic field is shown in Fig.37. Each quantitative diagram shows that the amount of Co in the films is much higher than that of Ni. Comparing both deposition routes, on ITO substrate covered by Ni seed-layer (Fig.37.(a)) and ITO substrate without a seed-layer (Fig.37.(b)), there is no significant differences in the amount of each element in process with absent magnetic field.

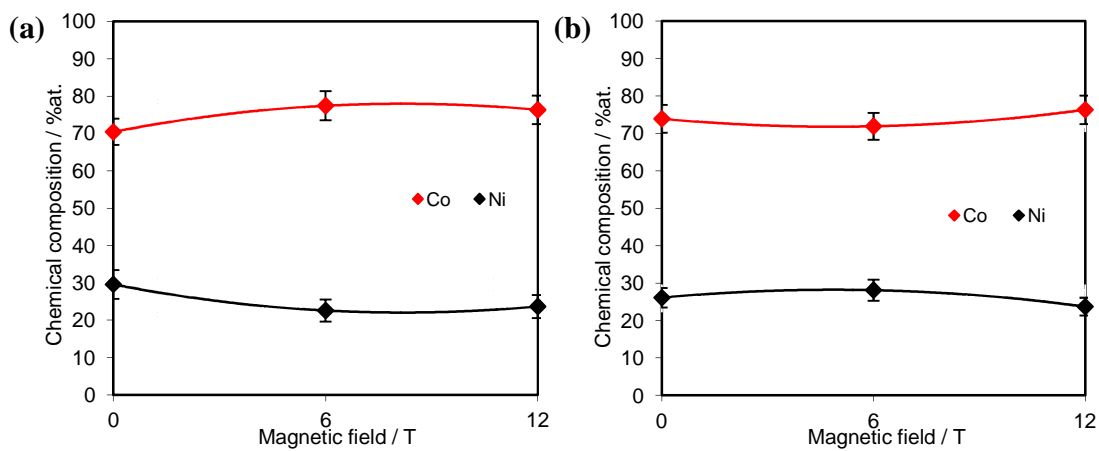


Fig.37. Chemical composition of the Co-Ni films electrodeposited on: (a) Ni/ITO and (b) ITO substrates under HMF; $i = -10 \text{ mA/cm}^2$, $t = 1 \text{ min}$, $\text{pH} = 4.7$.

In the Co-Ni film deposited on Ni/ITO substrate the amount of Co is about 70at.% and that of Ni about 30at.%, while the direct deposition on ITO results in 73at.% of Co and 27at.% of Ni. The chemical composition of Co-Ni films is slightly changed during the electrodeposition under magnetic conditions. The amount of Co in the film increases with simultaneous decrease that of Ni. According to Correia and Machado [188] an attempt was made to explain the anomalous co-deposition by the following steps:

- (i) at the initial stage of electrodeposition the nickel ions are reduced,
- (ii) Co(II) adsorbs onto freshly deposited Ni and begins to be deposited.

The Co(II) deposition was supposed to inhibit subsequent Ni deposition, although it was considered to be unable to block it completely. The anomalous deposition behaviour is slightly affected by the magnetic field. According to Ebadi *et al.* [125], the electrodeposition of Co and Ni are mass transport controlled. Based on this the electrodeposition of Co-Ni films under

magnetic field in this work is also under the influence of mass transport. The additional convection in the electrolyte, induced by the magnetic field, enhances the deposition rate through the MHD stirring. While Co^{2+} and Ni^{2+} are both double charged ions, thus both will experience almost the same Lorentz force, which increases the deposition of Co and Ni to the same extent. Because the larger magnetic moment has Co compared to Ni, the other magnetic forces, such as field gradient force (Eq.(28)) and paramagnetic force (Eq.(27)), will become larger for Co than for Ni. Thus, higher amount of Co in the Co-Ni films in the presence of magnetic field is observed.

II.4.2.2. Electrodeposited Co-Cu films

An interesting case of the high magnetic field effect is noticed, when depositing the Co-Cu films. The phase composition of Co-Cu electrodeposited on Cu/ITO substrate under high magnetic field is presented in Figure 38. The X-ray diffraction pattern of Co-Cu film deposited without an applied magnetic field reveals the alloy formation with simultaneous growth of single Co-hcp phase.

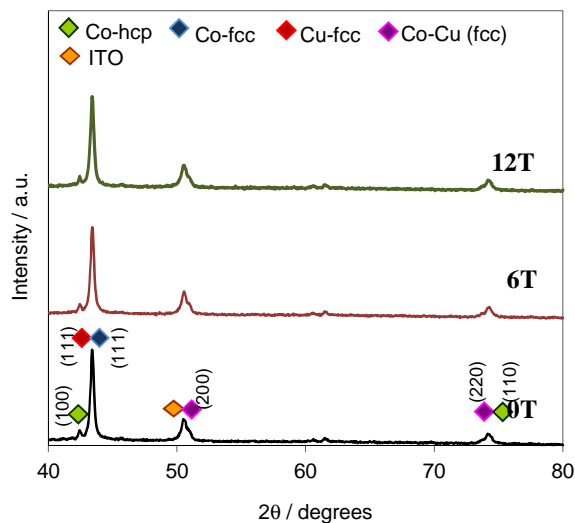


Fig.38. Phase composition of the Co-Cu films electrodeposited on Cu/ITO substrate under HMF; $i = -20\text{mA}/\text{cm}^2$, $t = 1\text{min}$, $\text{pH} = 4$.

A superimposition of the high magnetic field does not modify the character of diffraction patterns, inducing only a slight variation of the diffraction peak intensities. The split of the (111) diffraction peak may arise from the (111) preferred orientation of Cu, because growth of Cu in this direction is favoured [44]. The evidence of preferred Cu growth is given by the SEM analysis (Fig.39). In the case of electrodeposited Co-Cu films, in the absence of external magnetic field, the film consists of two layers: bottom, composed with small particles and very homogenous, and top, characterized by the presence of granular-like crystallites. Under applied magnetic field the growth of crystallites from both layers is induced. The granular-like nucleus begin to grow perpendicularly to the substrate surface and the branched tree-like structure is observed. The particles of bottom layer grow as well, but not as fast as that of the top layer. Under the magnetic conditions of 12T, a whole substrate surface is covered by the well-developed tree-like nucleus.

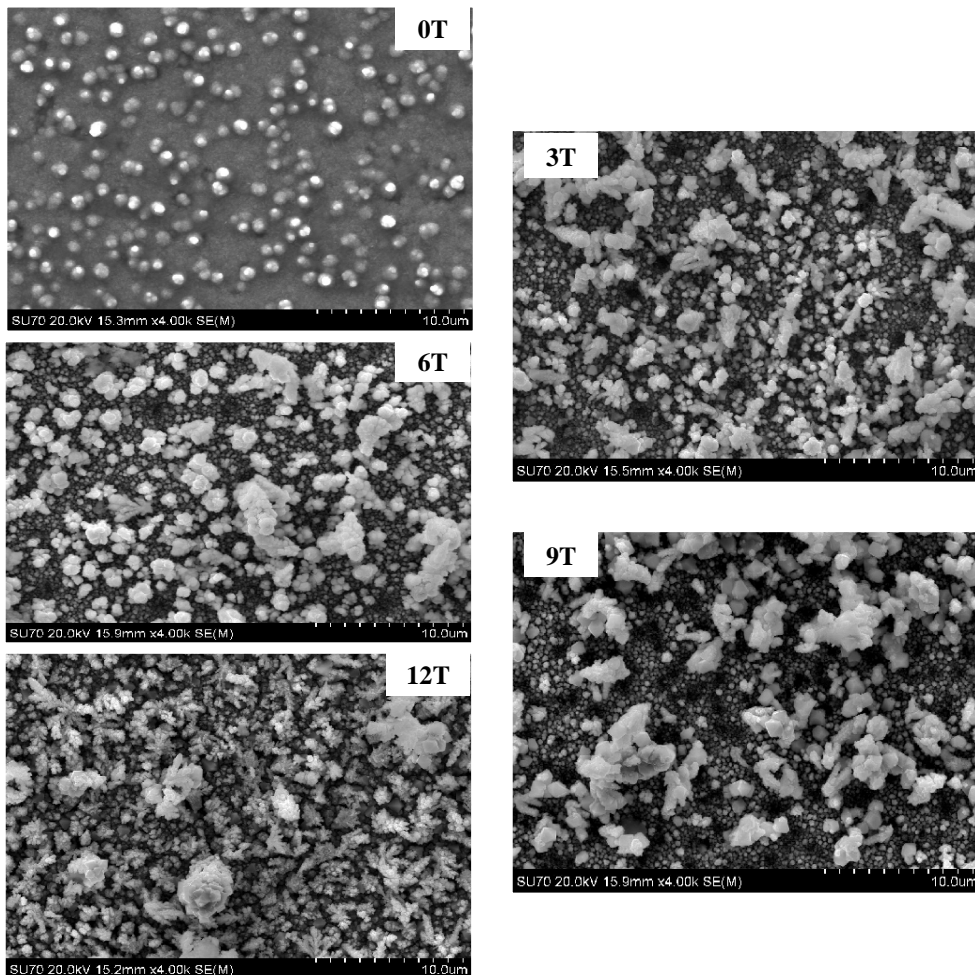


Fig.39. Morphological characteristic of the Co-Cu films electrodeposited on Cu/ITO substrate under HMF; $i = -20\text{mA/cm}^2$, $t = 1\text{min}$, $\text{pH} = 4$.

According to the chemical composition (Fig.40) it is clear that when magnetic field is not imposed during the deposition process, the film consists of almost equal amount of Co and Cu elements. Under magnetic field electrodeposition process the ratio of each element is drastically changed. The content of Co decreases, while that of Cu increases rapidly and under 12T magnetic field the films is composed in 99wt.% from Cu atoms. Thus, the branched tree-like structure is associated with the fast growth of Cu-fcc crystallites under magnetic conditions. The small amount of Co in the films electrodeposited under magnetic field suggests that the Cu tree-like structure is formed with the simultaneous, low incorporation of the Co atoms.

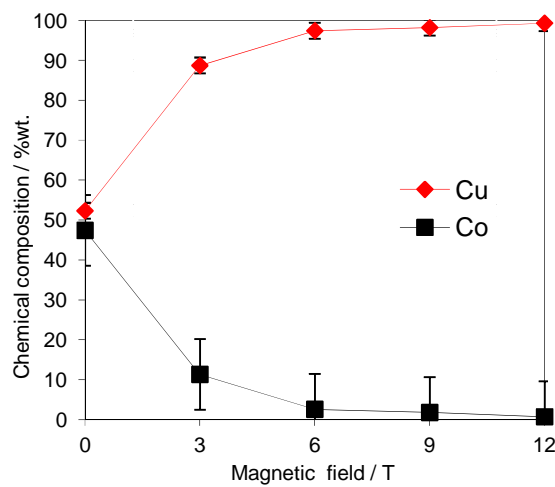


Fig.40. Chemical composition of the Co-Cu films electrodeposited on Cu/ITO substrate under HMF; $i = -20\text{mA/cm}^2$, $t = 1\text{min}$, $\text{pH} = 4$.

Moreover, following Karaagac *et al.* [189], the flower-like growth of electrodeposited Co-Cu films, containing relatively high amount of Cu may be attributed to short range crystalline order and diffusive growth of Cu. Therefore, the surface morphology is strongly influenced by the Cu to Co ratio in the film.

In the mass-controlled region of Co-Cu deposition, the deposited mass of Cu increases with increasing magnetic field. This is due to the MHD effect caused by a higher convection in the electrolyte, as a result of already mentioned Lorentz force. An additional convection not only increases the transport of Cu^{2+} and Co^{2+} ions towards electrode surface, but the rate of hydrogen evolution is increased as well, affecting the growth of deposit. Hydrogen evolution causes gas bubble stirring that changes the hydrodynamics and the mass transfer conditions in the vicinity of the electrode surface. At the first step a Co-Cu layer is formed with a deposition at the fewer

surface steps acting as nuclei. The localized flow of the metal ions to the growing flower-like features leads to the coalescence of hydrogen bubbles, resulting in the branched flower-like crystallites. Locally, high local current densities concentrated around the bubbles, due to their non-conductivity, cause faster growth of finer flower-like crystallites. The microscopic current distribution is changed due to the adsorption of hydrogen bubbles enhanced by superimposed magnetic field, decreasing both conductivity and the effective electrode area. As a final result, the current density distribution and coalescence of hydrogen bubbles create well-defined tree-like structure on different length scales, as seen in Fig.39 under 12T magnetic field.

II.5. Conclusion

The objective of this Chapter was to investigate the correlation between structure and electrodeposition parameters that affect the film growth. In the present work, the examined deposition parameters include electrolytic pH, substrate type and deposition time. Moreover, the effect of an applied external magnetic field during the electrodeposition process on the microstructure formation is determined. Additionally, the electrochemical kinetics and dynamics investigations have been provided, as an example of another approach that allows comprehensively understand the formation and growth of the electrodeposited Co-based films.

The considered pH values include two levels, referring to low (2.7), and high (4.7) pH. It is shown that both structural features: phase composition and surface morphology of Co and Co-Ni films are strongly influenced by the electrolyte pH. In both cases, the electrodeposited films consist of two crystallographic structures of cobalt: hexagonal closed-packed (hcp) and face centered-cubic (fcc). The differences observed in the phase composition and surface morphology, according to the pH level may be explained by the hydrogen evolution reaction and adsorbed intermediate species, such as cobalt and nickel hydroxides, at the cathode surface.

During the electrodeposition of Co and Co-Ni films on Ti substrate, most of the films were characterized by the rough surface. In order to decrease this undesired effect, the Ti substrate has been changed for a thin glass substrate covered by indium tin oxide and reinforced a seed-layer of Ni. The microstructural investigations show that the substrate type affects the phase composition of Co and Co-Ni deposits. Electrodeposited Co and Co-Ni films on Ti are characterized as biphasic, hcp and fcc. The Co film deposited on Ni/ITO possesses only the hcp

structure, while in the case of Co-Ni film the predominant phase is fcc. The phase composition differences are confirmed by the examination of surface morphology, which indicates presence of film crystallites in the particular form associated with each crystallographic structure of Co. Furthermore, the surface quality is improved and more homogeneous, less rough films are obtained. Moreover, the morphological characteristics show that decreasing deposition time from 4 to 1 minute brings about reduction in the crystallites size. The deposition time has an effect on the early stages of electrodeposition. Thus, the nucleation process is dominated, resulting in the nanocrystallite films.

In Chapter I it is discussed that a superimposition of an external magnetic field during the electrodeposition may be another parameter influencing the deposition process, and thus, the microstructure formation of electrodeposits. In this work, the effect of an applied parallel magnetic field, up to 12T, on the microstructure formation and growth of Co and Co-based films is studied. It is shown that an applied magnetic field does not influence on the phase composition, but modify the relative diffraction peak intensity. An exceptional case is the electrodeposited Co-Ni film on Ti substrate, where in comparison with the Co-Ni deposited on Ni/ITO substrate, some compositional changes under magnetic field conditions can be observed. In this case, the influence of magnetic field is similar as that of low pH, where the privilege growth in (220) direction is noticed. Thus, the secondary effects of magnetic field, as for example, on the pH value in the vicinity of electrode surface, are responsible for the structural modifications.

A superimposed magnetic field reduces the crystallites size and layer roughness significantly, resulting in more homogeneous surface. The result is clearly induced by the MHD stirring of the electrolyte, which reduces the thickness of diffusion layer and in turn improves a mass transport toward the electrode surface. Some interesting morphological features under superimposed magnetic field are observed in the electrodeposited Co-Cu and Co-Ni-Cu films. The Co-Cu and Co-Ni-Cu films deposited without an applied magnetic field possess a morphology consisting of mostly roundish shapes and initial stage of the dendritic structures. After superimposition of an external magnetic field the flower-like features develop, which consist of main branches with the shorter side-branches. This is related to the increase of Cu content in the films under magnetic conditions. Therefore, a possible explanation for the flower-like growth in the surface morphology of the Co-Cu and Co-Ni-Cu films may be the diffusive growth of Cu and hydrogen evolution, which is favoured under magnetic conditions.

Furthermore, the results reveal the anomalous co-deposition process of Co-Ni films. The anomalous deposition behaviour is slightly affected by the magnetic field. The additional convection in the electrolyte, induced by the magnetic field, enhances the deposition rate through the MHD stirring. Thus, higher amount of Co in the Co-Ni films in the presence of magnetic field is observed. In the mass-controlled region of Co-Cu and Co-Ni-Cu deposition, the deposited mass of Cu increases with increasing magnetic field.

The effect of an external magnetic field on the electrochemical kinetics and dynamics of electrodeposition process of Co, Co-Ni and Co-Cu films, respectively, is investigated. Considering the electrochemical kinetic behaviour, investigations are based on the chronoamperometric study, where the current-time transient of Co is investigated and nucleation mode is determined. The result shows that the behaviour of nucleation is relatively close to the instantaneous mechanism, but with a non-negligible deviation from the theoretical model. This is explained in terms of hydrogen reduction. The differences observed in the current-time transients of electrodeposited Co and Co-Ni films are due to the change of hydrodynamic conditions in the electrolyte under magnetic field superimposition. The instantaneous nucleation mode of electrodeposited Co and MHD effect on the nuclei growth of Co-Ni films are confirmed by the topographical AFM analysis.

From the electrochemical dynamic investigations of Co-Cu system it has been shown that a homogenous magnetic field does not practically modify the charge-transfer parameters of the process. The weak effects observed in the presence of magnetic field are only due to the change of the electrode area during the metallic electrodeposition and to the effect of MHD convection. In a magnetic field the MHD convection enhances the mass transfer rate of Co^{2+} and Cu^{2+} ions toward the electrode surface as well as hydrogen. The hydrogen is adsorbed at the active sites of substrates, blocking them for the metal ions reduction. Thus, the conditions of electrodeposited substrate surface are changed and the electrochemical respond is modified.

Chapter III

Application approach

III.1. Introduction

Thin films based on the ferromagnetic metals and their alloys are proved to be very promising materials from the application point of view. A great deal of experimental investigation results of the thin ferromagnetic film properties, such as structure, phase composition, electroconductivity, magnetoresistance, the Hall effect, etc., has been accumulated recently. The investigations often concern the study of structure and its influence on the magnetic properties, which can be changed in certain range, by varying the content of alloy elements as well as its structure and phase state. Most of the magnetic materials are prepared by physical means of deposition, such as molecular beam epitaxy (MBE) or sputtering. The electrochemical ways of deposition are an interesting alternative to these techniques, because they are easier to handle and much cheaper. There are already examples, where properties similar to those obtained for vacuum grown samples are observed [190-192]. In addition, electrochemical routes of preparation allow growing structures with high aspect ratio, which are not possible to obtain by MBE deposition. Nevertheless, electrochemical techniques share with the other techniques a high sensitivity of the samples magnetic properties on their crystallographic and chemical structure. Therefore, a detailed structural characterization of the electrodeposited films is of prime importance to understand the properties of samples. Among many methods to impose the desired structure and magnetic properties, magnetic field processing has been given special attention in the last few decades. However, up to date, only a few high magnetic field annealing experiments (in the magnetic field of several Tesla) have been done on magnetic materials, and the mechanism through which the high magnetic annealing field plays a role on microstructure and magnetic properties are still unclear. The annealing treatment may cause phase transition, alloy formation, change of Curie temperature and enhances diffusion at the interface, which adversely affects the magnetic properties.

The followed Chapter - Application approach, is introduced in this thesis in view of the ***COMAGNET*** project, based on the magneto-science fields. The ***COMAGNET*** project is developed by two research groups: Laboratoire d'Ingénierie et Sciences des Matériaux (LISM) at University of Reims Champagne-Ardenne in France, and Key Laboratory of Electromagnetic Processing of Materials (Ministry of Education) at Northeastern University in Shenyang, China. The main interest of this project is to develop Co-based magnetic alloy films and/or oxides, by use of an external magnetic field. The considered here alloy films are CoX, where X stands for

Cu, Ni, Fe, Cr, Pt, etc., whereas, the oxides of interest are, for example, CoFe_2O_4 with different application destination, such as: permanent magnets, magnetic recording media, magnetoresistive and giant magneto-optical materials. The major objective of the *COMAGNET* project is to show that the magnetic properties (coercivity, saturation magnetization, magnetic anisotropy) may be modified by a superimposition of a high magnetic field (HMF) during fabrication process. Originality and innovative aspect of this project is to couple two processes carried out under high magnetic field:

- firstly, development of Co-based alloys and oxides in the nanoscale range by the electrochemical deposition under high magnetic field,
- secondly, performance of the thermal treatments or oxidation of electrodeposited Co-based materials in the presence of magnetic field under controlled atmosphere.

The aim of coupling both, magneto-electrodeposition and magnetic annealing processes is to improve the functionality of Co-based materials.

As it has been already discussed in Chapter I and shown in Chapter II, the electrodeposition process of thin films under magnetic field may affect the surface morphology, crystallographic phase composition and physical properties of the material. It is generally accepted that the magnetic field promotes to obtain denser and more homogeneous deposits, with reduced grain sizes. Moreover, the magnetic field becomes an alternative for brighteners and leveling agents usually added to the electrolytic solution. In the case of deposited cobalt and/or Co-based alloys, such as Fe-Co, a superimposition of magnetic field may modify the microstructure and thus, the magnetic properties of material. On the other hand, materials produced by the electrodeposition technique require thermal treatments under controlled atmosphere in order to improve their functionality. Thus, the part of project focused on electrodeposition under high magnetic field has been coordinated by the LISM Laboratory in Reims, while that on magnetic thermal treatments has been realized by the EPM Laboratory in Shenyang, which possesses significant experience in the field of metallurgy under high magnetic fields, such as solidification, diffusion, and reactions at the film/substrate interface.

From this standpoint, the followed sections consider investigations of:

- effects of magnetic annealing treatment on the microstructure of as-deposited films,
- magnetic properties of as-deposited and post-annealed Co-based films under magnetic field.

III.2. Methodology

The electrodeposited systems considered in this Chapter are listed in Table 7, together with the electrodeposition conditions. The magnetic measurements have been done using Alternating Gradient Force Magnetometer (AGFM) and Vibrating Sample Magnetometer (VSM) (*Annex III*). For each sample, two measurements were performed: with the magnetic field applied in the sample plane (labelled as “in-plane”) along two orthogonal directions, and a third measurement with the magnetic field applied perpendicular to the sample plane (labelled as “out-of-plane”). In all cases, the two in-plane directions turn out to be the same, meaning that there does not seem to be any preferential direction in the sample plane.

Table 7. The electrodeposition conditions of Co-based thin films subjected to the magnetic annealing treatment and magnetic properties analysis.

System	Chemical agent	Concentration <i>mol/L</i>	Solution pH	Solution temperature <i>°C</i>	Current density <i>mA/cm²</i>	Deposition time <i>min</i>	Magnetic field amplitude <i>T</i>
<i>Seed-layers</i>							
Ni / ITO	NiSO ₄ ·7H ₂ O H ₃ BO ₃	0.6 0.4	2.7	30	-10	1	0
Cu / ITO	CuSO ₄ ·6H ₂ O H ₃ BO ₃	0.03 0.4	4.0	50	-20	5 sec	0
<i>Films</i>							
Co/Ni / ITO	CoSO ₄ ·7H ₂ O H ₃ BO ₃	0.6 0.4	4.7	50	-10	1	≤ 1
Co-Ni / ITO	CoSO ₄ ·7H ₂ O NiSO ₄ ·6H ₂ O H ₃ BO ₃ saccharin	0.3 0.7 0.4 0.015	4.7	50	-10	1	≤ 12
Co-Cu/Cu/ITO	CoSO ₄ ·7H ₂ O CuSO ₄ ·6H ₂ O H ₃ BO ₃	0.4 0.03 0.4	4.0	50	-20	1	≤ 12
Co-Ni-Cu/Cu/ITO	CoSO ₄ ·7H ₂ O NiSO ₄ ·6H ₂ O CuSO ₄ ·6H ₂ O H ₃ BO ₃	0.015 0.2 0.01 0.4	4.0	50	-20	1	≤ 1

The Co and Co-Ni films were heat treated at 673K, while the annealing temperature of Co-Cu films was set up at 623K, both lower than the Curie temperature of cobalt, which is 1388 K. The annealing treatment was carried out during 4h under a protective atmosphere of high purity

argon, and then cooled down to the room temperature. A vertical furnace placed inside a superconducting magnet was used (Fig.41). The direction of an external magnetic field was perpendicular to the films surface and the applied magnetic flux density was 0T, 6T, and 12T, respectively.

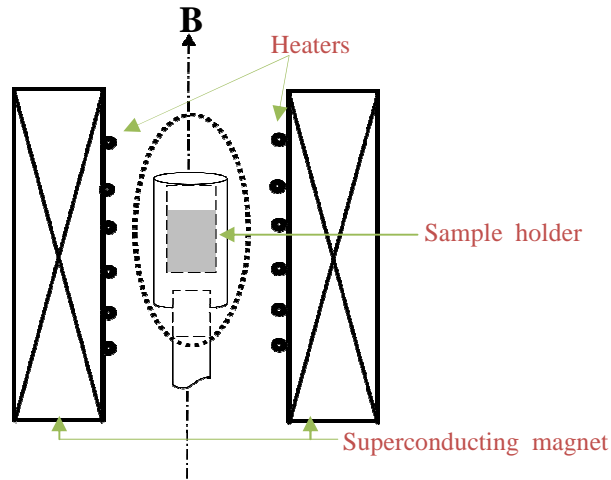


Fig.41. Schematic view of the annealing setup under high magnetic field.

III.3. Electrodeposited Co/Ni/ITO films

III.3.1. Annealing treatment effect on structure and morphology

The electrodeposited Co/Ni/ITO films, with and without an external magnetic field, presented wider elsewhere (Fig.19 - Chapter II.4.1.2), were then annealed under high magnetic field. Since the X-ray diffraction analysis have not shown any structural changes, regardless on the magnetic field amplitude (up to 1T) during electrodeposition, only one example of as-deposited Co/Ni/ITO film, according to the magnetic annealing treatment will be here discussed. Figure 42 presents the phase composition of Co/Ni/ITO film electrodeposited without a superimposed magnetic field and its modification by the magnetic annealing treatment. As it can be expected, the annealing treatment improves the crystallinity of the deposited films and the FWHM narrows down indicating an increase of the grain size. Moreover, the recrystallization effect is preserved under superimposed magnetic field during the process.

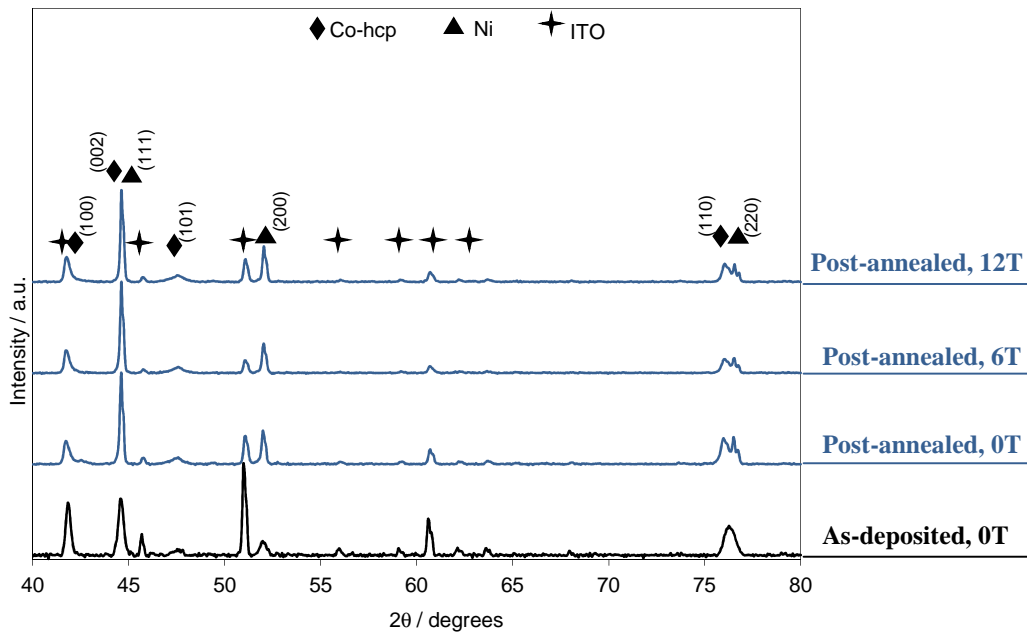


Fig.42. X-ray diffraction patterns of the Co/Ni/ITO films before and after annealing under high magnetic field; *Electrodeposition: $i = -10\text{mA/cm}^2$, $t = 1\text{min}$, $\text{pH} = 4.7$; Annealing: $t = 4\text{h}$, $T = 673\text{K}$.*

In Fig. 42 a variation of the diffraction peaks intensity is observed, as well as slight segregation of the biphasic peak at 2θ angles about 76° , which confirms the presence of Co-(110)-hcp and Ni-(220)-fcc phases under thermal conditions. Moreover, at lower 2θ angles highly intensive biphasic peak of Co-(002)-hcp and Ni-(111)-fcc structures, is observed as well. The presence of both Co and Ni phases in the range of considered above 2θ angles may be clearly seen in Fig.43, which points out also that under magnetic annealing conditions the structural modifications are not further observed.

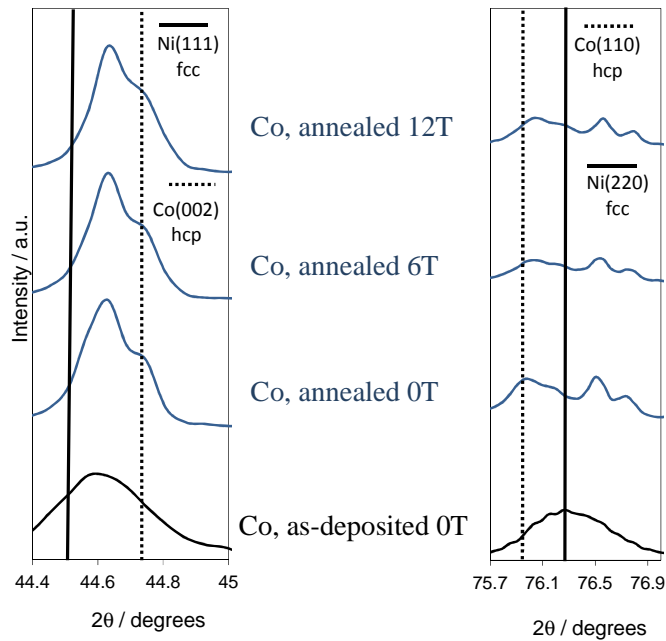


Fig.43. Zoom at the 2θ angles, where the growth of biphasic diffraction peaks of Co/Ni/ITO films is observed; *Electrodeposition: $i = -10\text{mA}/\text{cm}^2$, $t = 1\text{min}$, $\text{pH} = 4.7$; Annealing: $t = 4\text{h}$, $T = 673\text{K}$.*

The presented above result is in a good agreement with the observation made by Bacaltchuk *et al.* [193] and Sheikh-Ali *et al.* [194], who investigated effects of the annealing treatment on the microstructure of ferromagnetic FeSi and diamagnetic ZnAl alloys films, respectively, and found a similar effect.

During thermal treatment, diffusion phenomena can occur. Thus, it can be assumed that due to an increased intensity of the Ni-(200)-fcc diffraction peak, as indicated in Fig.42, the interdiffusion zone at interface of Co and Ni layers under annealing conditions could be presented. The evidence for existence of diffusion regions between these two layers has been determined in the case of thicker Co/Ni/ITO films [195], not included in this study. The X-ray photoelectron spectroscopy (XPS) of the thicker Co/Ni/ITO films annealed with and without a superimposed magnetic field is shown in Fig.44. Taking into account the concentration of Co and Ni the estimated diffusion length increases from $0.92\ \mu\text{m}$ to $1.3\ \mu\text{m}$, when annealing is carried out under superimposed 12T magnetic field. Some other proofs for the existence of interdiffusion zone under thermal treatment are given by Khan and Bhatti [196] and El Asri *et al.* [197]. In Ref. [196], the authors investigated effects of annealing temperature on the magnetic properties of Cu-capped ultrathin Co films. Their results indicate the diffusion of Cu/Co into the Si substrate,

which has been increased by increasing annealing temperature. Thus, the increased diffusion at the interfaces of both Co and Ni layers during magnetic annealing treatment of thin Co/Ni/ITO films considered in this work could be also expected.

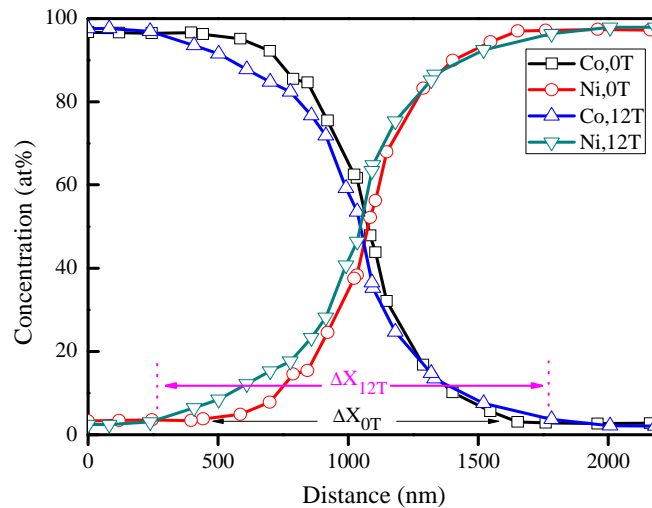


Fig.44. Composition distribution of the Co/Ni/ITO films along the cross-section. Δx stands for the diffusion distance [195]; *Electrodeposition: $i = -10\text{mA/cm}^2$, $t = 4\text{min}$, $\text{pH} = 4.7$; Annealing: $t = 4\text{h}$, $T = 673\text{K}$.*

Thank to the application of SEM and high resolution AFM techniques, useful complementary information on the morphological structure of Co/Ni/ITO films could be observed (Fig.45). The morphological structure of as-deposited Co film (Fig.45.(a)) is composed of hexagonal-shaped crystallites, what is agreed with the XRD observation, revealing the monophasic - hcp structure of Co/Ni/ITO films. Under magnetic annealing treatment (Fig.45.(b),(c)) the Co crystallites are separated in the form of single grains, as evident from the AFM images. These grains are packed very densely, roundish in shape and possess sizes at the nanometer range. Moreover, comparing the scale along the AFM images, it can be clearly seen that thermal treatment improves the surface morphology and a superimposed magnetic field during annealing reinforces this effect by reducing the surface roughness, what in consequence gives more homogeneous Co/Ni/ITO.

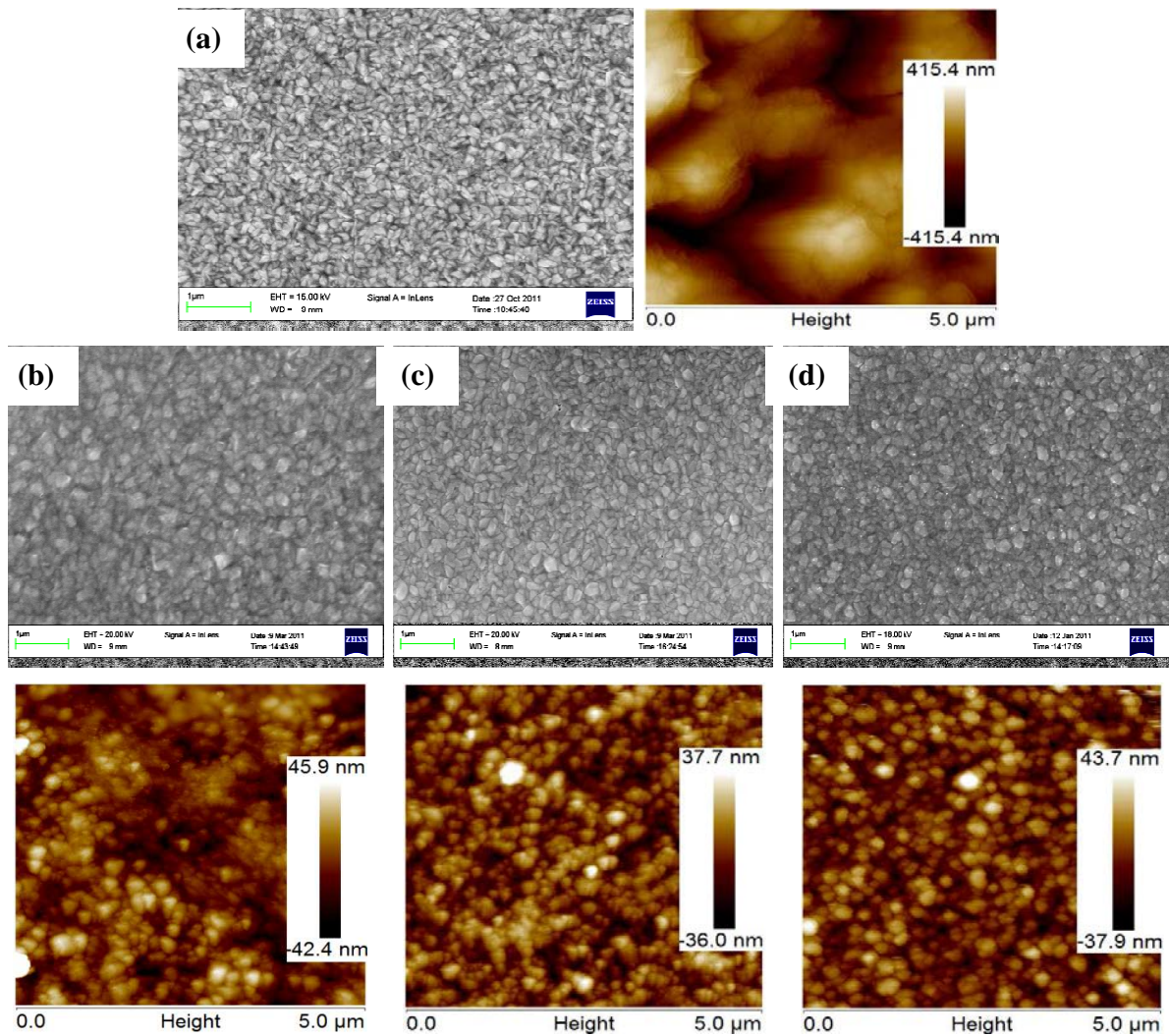


Fig.45. Morphological comparison of the Co/Ni/ITO bilayer thin films as-deposited under 0T (a) and post-annealed under 0T (b), 6T (c) and 12T (d) magnetic field;
Electrodeposition: $i = -10\text{mA}/\text{cm}^2$, $t = 1\text{min}$, $\text{pH} = 4.7$; Annealing: $t = 4\text{h}$, $T = 673\text{K}$.

III.3.2. Determination of the magnetic properties

In order to determine the effects of magnetic fields superimposed during electrodeposition and annealing processes on the magnetic properties of Co/Ni/ITO films the hysteresis loops were recorded. Figure 46 indicates the magnetic characteristic of as-deposited Co/Ni/ITO films. It is observed that film deposited under 1T magnetic field approaches the saturation more quickly than

film deposited in its absence. Moreover, an increase in the coercivity field (H_c), from 45 Oe (as-deposited, 0T) to 78 Oe (as-deposited, 1T), is noticed as well.

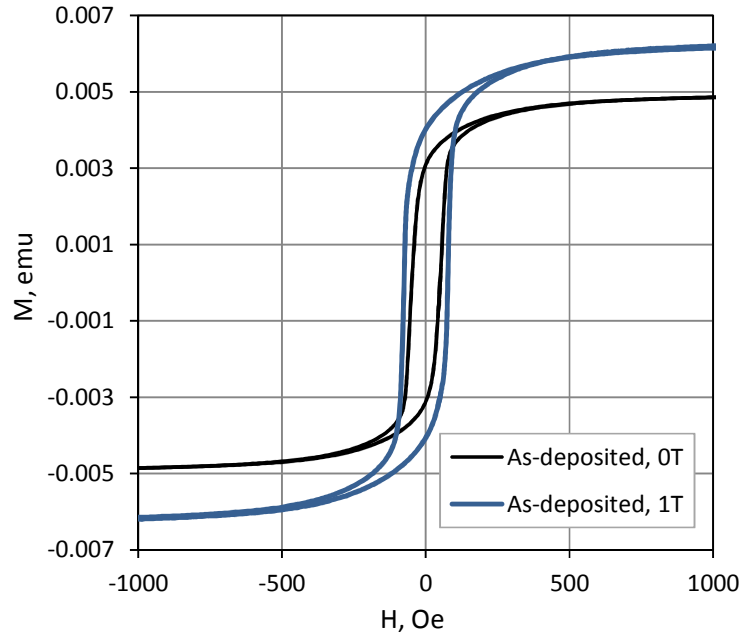


Fig.46. Comparison of the hysteresis loops of Co/Ni/ITO bilayer films electrodeposited without and with a superimposed magnetic field; *Electrodeposition: $i = -10\text{mA}/\text{cm}^2$, $t = 1\text{min}$, $\text{pH} = 4.7$.*

Due to the presence of an external magnetic field an alignment of magnetic moments or production of ordered atomic pairs of unlike atoms along the direction of external applied field is expected. Thus, the variation in coercivity field may occur. Furthermore, the H_c depends on various types of anisotropy, among which the shape anisotropy is very dominant and is of dipolar origin, as stated by Diandra *et al.* [198]. Hence, the higher coercivity of Co/Ni/ITO film deposited under 1T may be attributed to an increased shape anisotropy exhibited by cobalt [199]. Both samples were then annealed under magnetic conditions and the hysteresis loops were again recorded. In both cases, as-deposited under 0 and 1T Co/Ni/ITO films, a drop in approaching the saturation and increase of the coercivity fields are observed (Fig.47).

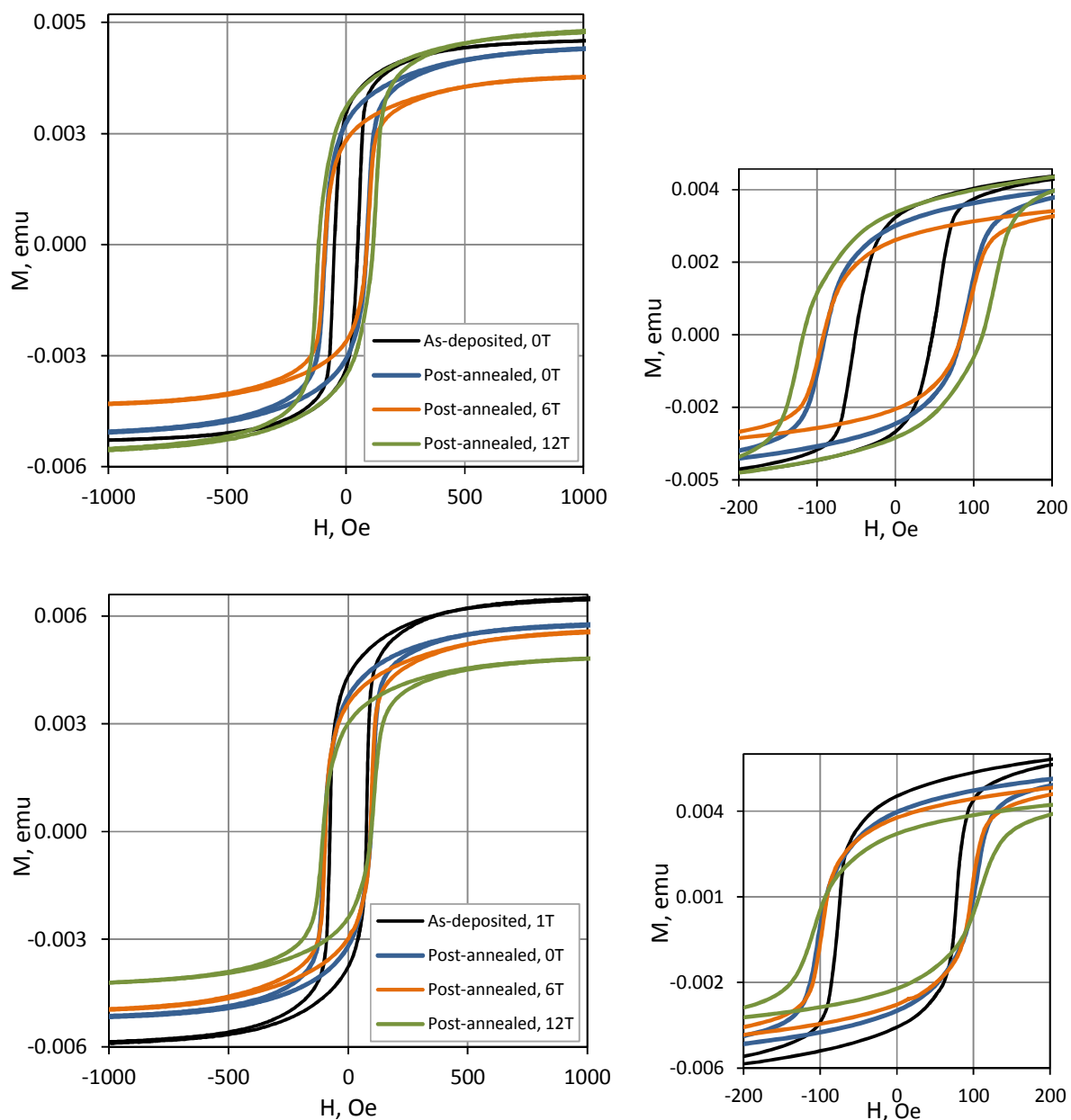


Fig.47. Comparison of the hysteresis loops of Co/Ni/ITO bilayer films electrodeposited under 0 and 1T and annealed under 0, 6 and 12T; *Electrodeposition: $i = -10\text{mA/cm}^2$, $t = 1\text{min}$, $\text{pH} = 4.7$; Annealing: $t = 4\text{h}$, $T = 673\text{K}$.*

A slower approach to the saturation may be due to the increased intermixing of Co and Ni atoms at the interfaces, since the XPS analysis (Fig.44) proved the existence of interdiffusion zone. An increased H_c field is probably due to the mixed effects of recrystallization process and structural modifications. Further annealing under magnetic conditions brings about a slight increase of the

H_c (Fig.48), what is most likely to be caused by enhanced increase of Co grains and structural directionality. However, the presence of interdiffusion zone cannot be neglected as well.

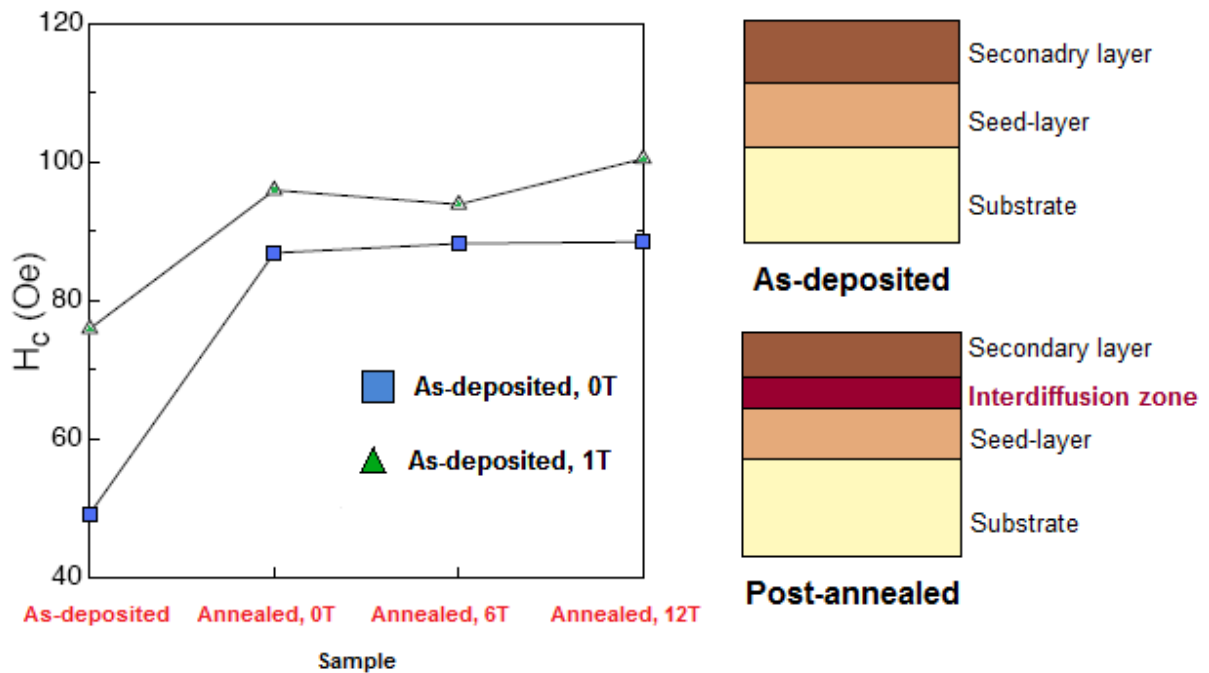


Fig.48. Comparison of the coercivity field of Co/Ni/ITO bilayer films before (as-deposited) and after (post-annealed) annealing treatment; *Electrodeposition: $i = -10\text{mA/cm}^2$, $t = 1\text{min}$, $\text{pH} = 4.7$; Annealing: $t = 4\text{h}$, $T = 673\text{K}$.*

Extended analysis of the magnetic characteristics of post-annealed Co/Ni/ITO bilayer films have been done by use of Magnetic Force Microscope (MFM). Figure 49 presents MFM images of the Co/Ni/ITO films as-deposited and post-annealed, respectively, on the base of AFM images presented in Fig.45. The magnetic structure consists of bubble domains, sometimes affected by the granular morphology. Annealing at 0T results in a magnetic image with almost no contrast. Annealing under 6 and 12T magnetic field results in a magnetic image with some rather well defined contrast. In general, the domains run in random directions in the film plane, i.e. no directionality in the orientation of domains is observed. The domains are displayed as bright and dark areas, which span several grains, but prove unambiguously that they have opposite magnetization components perpendicular to the film surface. Apparently, there is a trend in the samples that points to the appearance of some perpendicular magnetic anisotropy with field annealing, even though the hysteresis loops do not show significant differences among the

samples (Fig.47), since the magnetic measurements based on AGFM/VSM techniques are the volume analysis, examining all the layers occurred on the substrate (Fig.48).

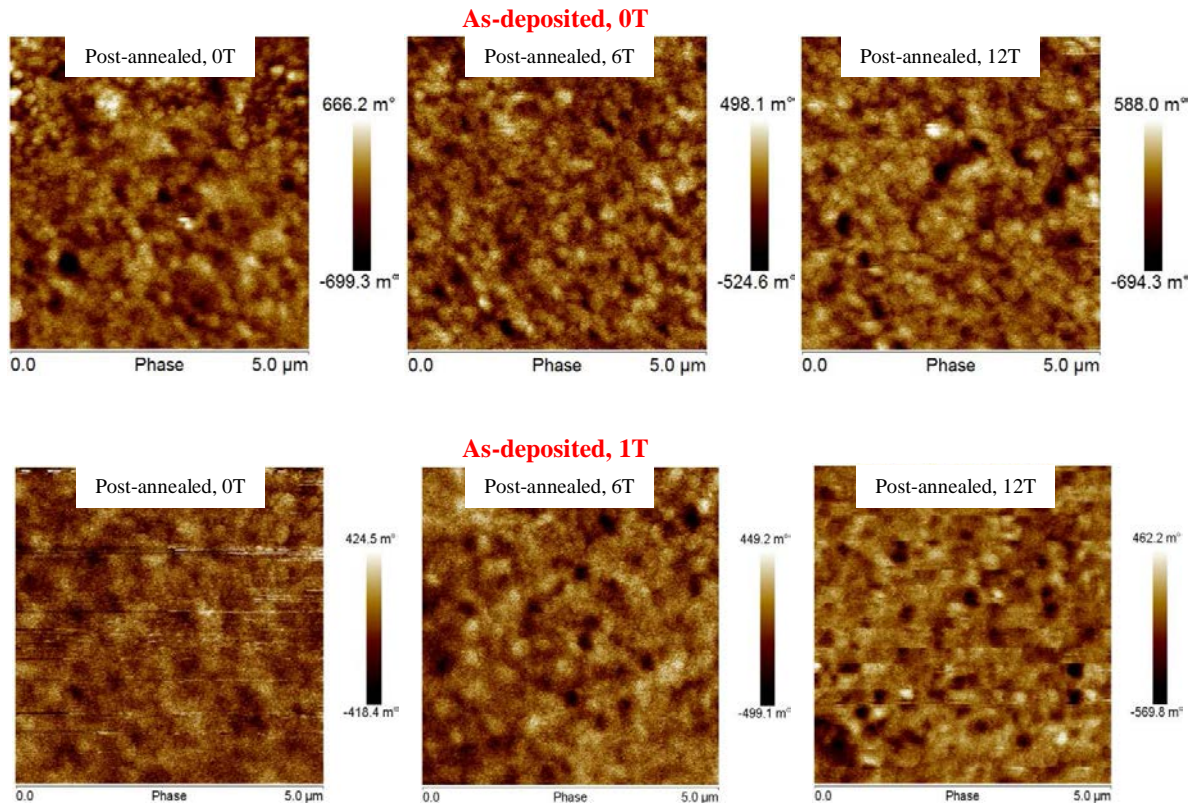


Fig.49. MFM analysis of the Co/Ni/ITO films; *Electrodeposition: $i = -10\text{mA}/\text{cm}^2$, $t = 1\text{min}$, $\text{pH} = 4.7$; Annealing: $t = 4\text{h}$, $T = 673\text{K}$.*

The observed magnetic anisotropy is probably of the grain size origin. When the grains are larger than their single-domain critical size an increase in the H_c is observed. Thus, the magnetic domain structure determines the hysteresis loops of Co/Ni/ITO films, and the domains configuration is affected by the surface morphology (Fig.45).

III.4. Electrodeposited Co-Ni films

III.4.1. Annealing treatment effect on structure and morphology

Figure 50 shows the X-ray diffraction patterns of electrodeposited Co-Ni/ITO film annealed without and with an applied magnetic field. It can be seen that the diffraction peaks of (111) and (200) are clearly defined, what confirms better crystallization of the deposit. It needs to be noticed here that the growth of (200) fcc phase of Co-Ni alloy is not observed in as-deposited sample. Thus, the appearance of this crystallographic plane under annealing conditions may give an evidence for the recrystallization effect of thermal treatment. After annealing the Co-Ni fcc structure and the preferred (111) orientation are preserved. An applied magnetic field during the process does not affect the films structure, even when its amplitude rises up to 12T.

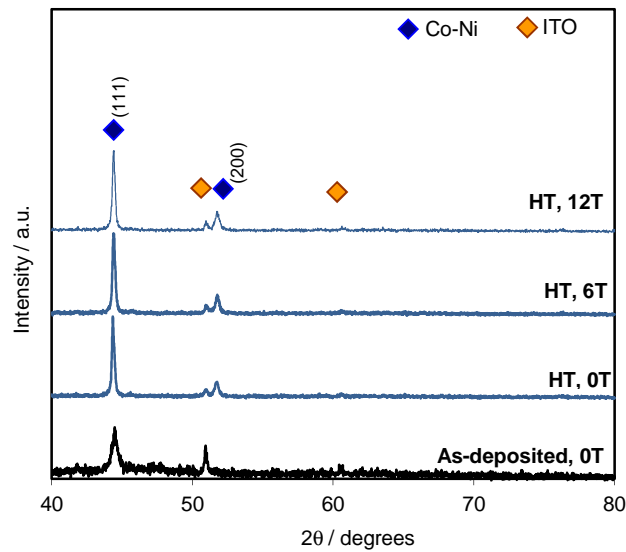


Fig.50. X-ray diffraction patterns of the Co-Ni/ITO alloy films before and after annealing under high magnetic field; *Electrodeposition: $i = -10\text{mA/cm}^2$, $t = 1\text{min}$, $\text{pH} = 4.7$; Annealing: $t = 4\text{h}$, $T = 673\text{K}$.*

Since the magnetic field was applied in the film plane during electrodeposition, therefore more crystals grains are expected to have their easy axis of magnetization parallel to the Co-Ni axis. That is obvious from an increase in the (111) peak intensity of more prominent peak along the (111), when high magnetic field during electrodeposition was superimposed (Fig.51). Under high magnetic field electrodeposition the intensity of (111) plane increases slightly with increasing

field amplitude. During annealing process the strong growth of (111) diffraction peak is observed, which is preserved, when magnetic field is superimposed.

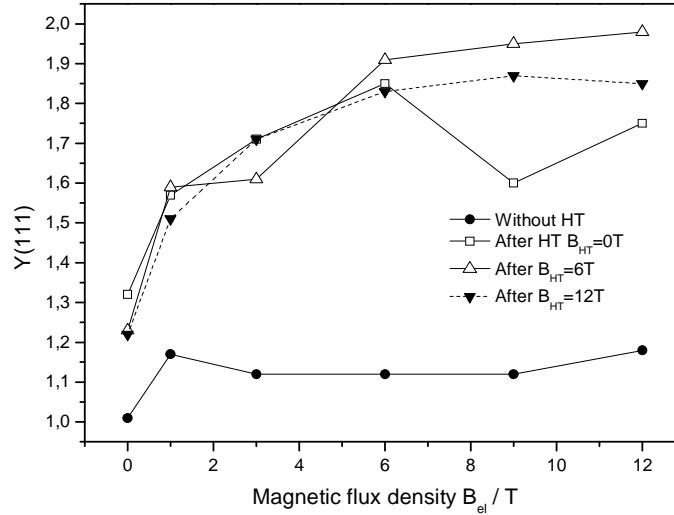


Fig.51. Dependence of the crystal orientation index $Y(111)$ of Co-Ni fcc phase on magnetic flux density. B_{el} – magnetic field during electrodeposition, B_{HT} – magnetic field during annealing; Electrodeposition: $i = -10\text{mA/cm}^2$, $t = 1\text{min}$, $\text{pH} = 4.7$; Annealing: $t = 4\text{h}$, $T = 673\text{K}$.

As it has been shown in the work of Li et al. [200] the high magnetic field annealing tends to align the c-axis of crystals along the direction of annealing field. The density of crystals with c-axis along the magnetic field direction has been noticed to be twice random than that in the samples annealed without a superimposed magnetic field. As a conclusion it was stated that samples annealed without a magnetic field do not show uniaxial crystal anisotropy. In contrary, the texture analysis indicated that annealing under high magnetic field does improve the orientation distribution of crystal and the uniaxial anisotropy is expected for the magnetically annealed samples. Thus, the observation made in this work is in a good agreement with the results shown in [200]. Furthermore, the annealing treatment causes the recrystallization of film nucleus, as indicated on the X-ray diffraction patterns by narrower FWHM of the (111) diffraction peak. As a result, the compact and homogeneous structure is obtained (Fig.52). It can be assumed that the increased compactness may be a consequence of a low volume of disorderly arranged atoms in the grains boundaries formed under magnetic annealing conditions, as compared to the grains themselves. Thus, it may be assumed that magnetic properties may be changed along the as-deposited and post-annealed Co-Ni/ITO samples.

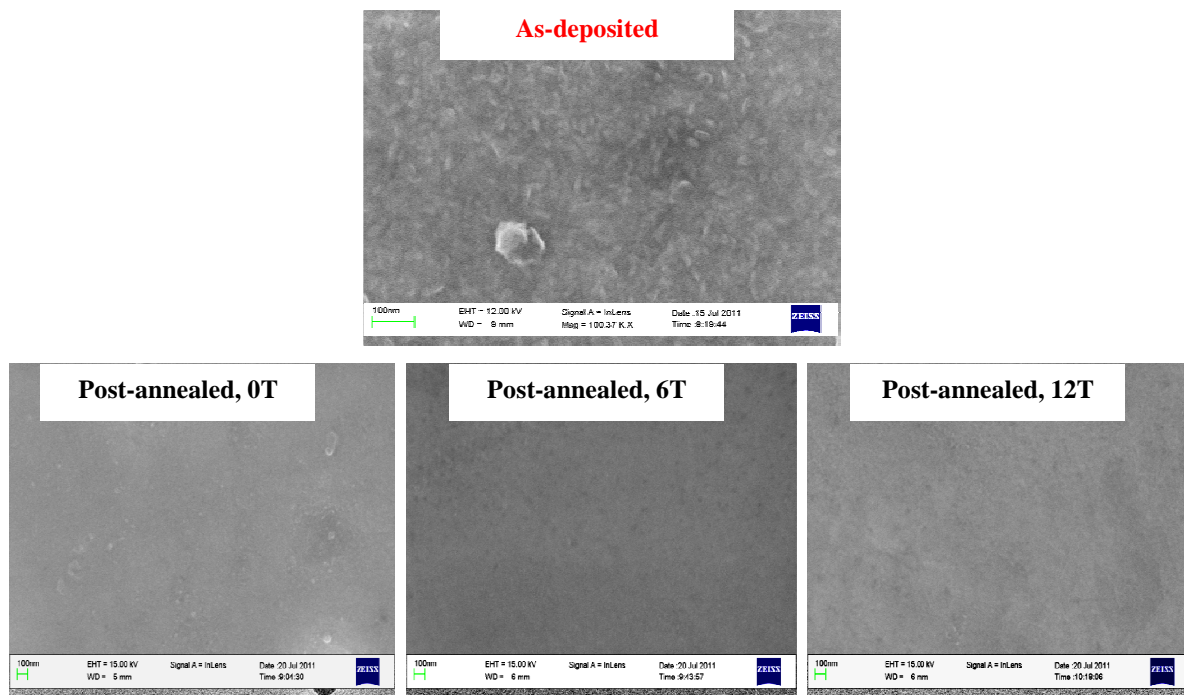


Fig.52. Morphological comparison of the electrodeposited Co-Ni/ITO films before and after annealing process; *Electrodeposition: $i = -10\text{mA}/\text{cm}^2$, $t = 1\text{min}$, $\text{pH} = 4.7$; Annealing: $t = 4\text{h}$, $T = 673\text{K}$.*

III.4.2. Determination of the magnetic properties

Figure 53 indicates the magnetic characteristics of as-deposited Co-Ni/ITO film annealed under high magnetic fields. It is observed that an approach in saturation magnetization of annealed films under magnetic conditions is slightly quicker achieved than that of the sample annealed without a superimposed magnetic field. This may be caused by appearance of the newly formed Co-Ni phase in (200) direction. When annealing treatment is carried out under magnetic conditions the growth of (200) diffraction peak is slightly enhanced (Fig.50), thus an approach in saturation magnetization is faster. According to Tian *et al.* [201], it is mainly because all the Co and Ni atoms grown in this direction have turned into Co-Ni alloy under magnetic conditions, thus this approach in saturation magnetization will not increase so much even though the higher magnetic field will be further superimposed.

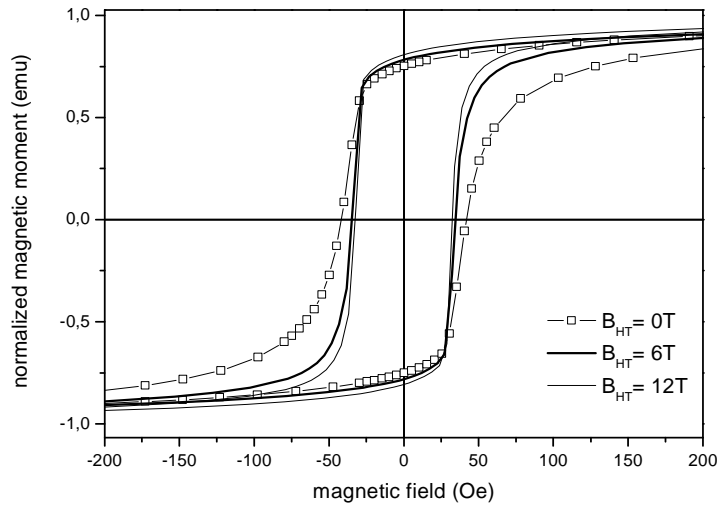


Fig.53. Hysteresis loops of the post-annealed Co-Ni/ITO films deposited without magnetic field;
Electrodeposition: $i = -10\text{mA/cm}^2$, $t = 1\text{min}$, $\text{pH} = 4.7$; Annealing: $t = 4\text{h}$, $T = 673\text{K}$.

Regarding on the coercivity field, it is reduced under magnetic annealing conditions (Fig.54). Since the coercivity is sensitive to the phase, disfigurement, stress, thickness of films, etc., the possible explanation may lay down in the internal stress of as-deposited sample. As it has been discussed in Chapter II, during electrodeposition process besides the reduction of metals the simultaneous hydrogen evolution is observed, which may be adsorbed in the Co-Ni films.

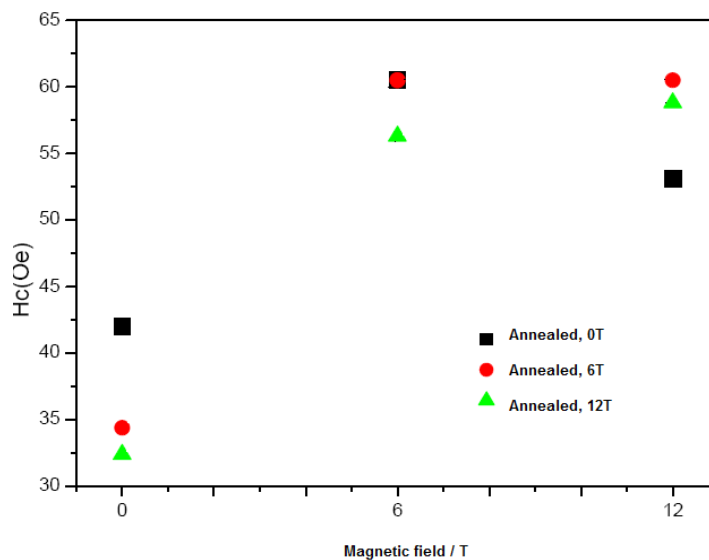


Fig.54. Coercivity field of the as-deposited Co-Ni/ITO films after annealing process;
Electrodeposition: $i = -10\text{mA/cm}^2$, $t = 1\text{min}$, $\text{pH} = 4.7$; Annealing: $t = 4\text{h}$, $T = 673\text{K}$.

Thus, the adsorbed hydrogen is probably separated out during thermal treatment, reducing the internal stress and disfigurement. Furthermore, the Co-Ni films were deposited directly on the ITO substrate with an addition of saccharin, which improves the adhesion ability of the films at the substrate surface. Further action of this additive is to reduce the stress in deposit. Hence, the decrease of H_c by magnetic annealing in the as-deposited Co-Ni film may be also related with the residual strain appearing in the film. In other cases of as-deposited Co-Ni films under 6 and 12T, the observed variation in values of coercivity field under magnetic annealing conditions may be due to the linked effects of stress-free character of as-deposited films and recrystallization process.

III.5. Electrodeposited Co-Cu/Cu/ITO films

The investigations of magnetic annealing treatment of Co-Cu/Cu/ITO films reveal the phase segregation under annealing conditions. The as-deposited Co-Cu/Cu/ITO film is biphasic, composed with Co-Cu-fcc phase grown simultaneously with that of Co-hcp phase (Fig.55). An intensive (111)-fcc diffraction peak indicates that the growth of Co-Cu film is mainly oriented in this direction. Under annealing conditions the (111) plane is disintegrated and very broad diffraction peak in the range of 2θ angles of $44^\circ - 48^\circ$ is observed. The XRD analysis indicates presence of three phases in this region: Co-(100)-hcp, Co-(111)-fcc and Cu-(111)-fcc. Moreover, other diffraction peaks, Co-Cu-(200) and Co-Cu-(220)-fcc+Co-(110)-hcp are shifted towards higher 2θ angles, indicating growth of single Cu phase under annealing conditions. A superimposed magnetic field preserves the induced structural changes.

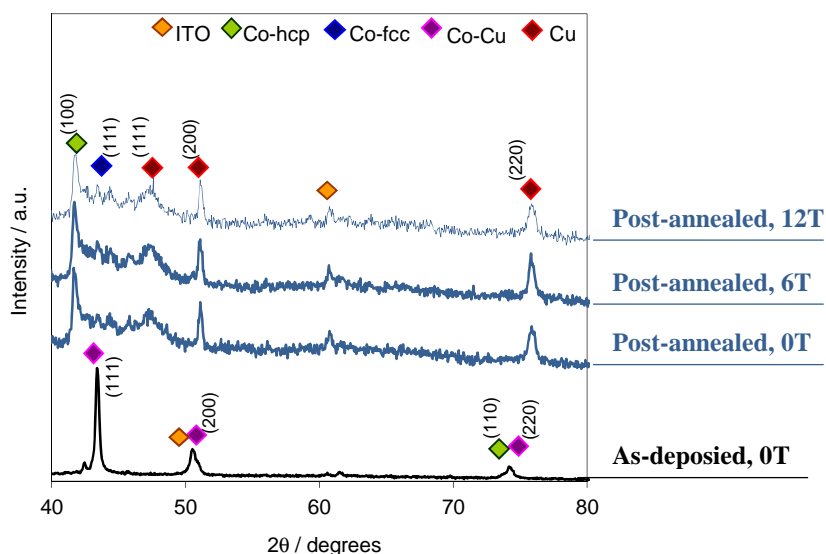


Fig.55. X-ray diffraction patterns of Co-Cu/Cu/ITO alloy films before and after annealing under high magnetic field; *Electrodeposition: $i = -20\text{mA/cm}^2$, $t = 1\text{min}$, $\text{pH} = 4$; Annealing: $t = 4\text{h}$, $T = 623\text{K}$.*

The morphological investigations give an evidence for the observed structural modifications. The morphology of as-deposited Co–Cu films annealed afterwards under magnetic conditions is presented in Fig.56. The Co–Cu film deposited in absence of the magnetic field has a morphology consisting of mostly roundish shapes and initial stage of the dendritic-like structures. For the Co–Cu film deposited under 1T magnetic field, the dendrites and their outgrowth is developed, consisting of main branches with the shorter side-branches formation. The SEM images of post-annealed samples indicate improved growth of these features. As it was discussed in Chapter II, development of the dendritic-like structure of Co–Cu films is of chemical composition origin. Therefore, a possible explanation for the enhanced growth in the surface morphology of films might be the diffusive growth of Cu under annealing conditions. Moreover, it is observed that it is improved by a superimposition of magnetic field. Since, the film consists mainly of Cu structure, thus, the phase composition under magnetic annealing conditions is changed. Furthermore, the XRD analysis indicates growth of Co-hcp phase, what may mean that along the Co–Cu films with high Cu concentration, the regions with high amount of Co atoms exists.

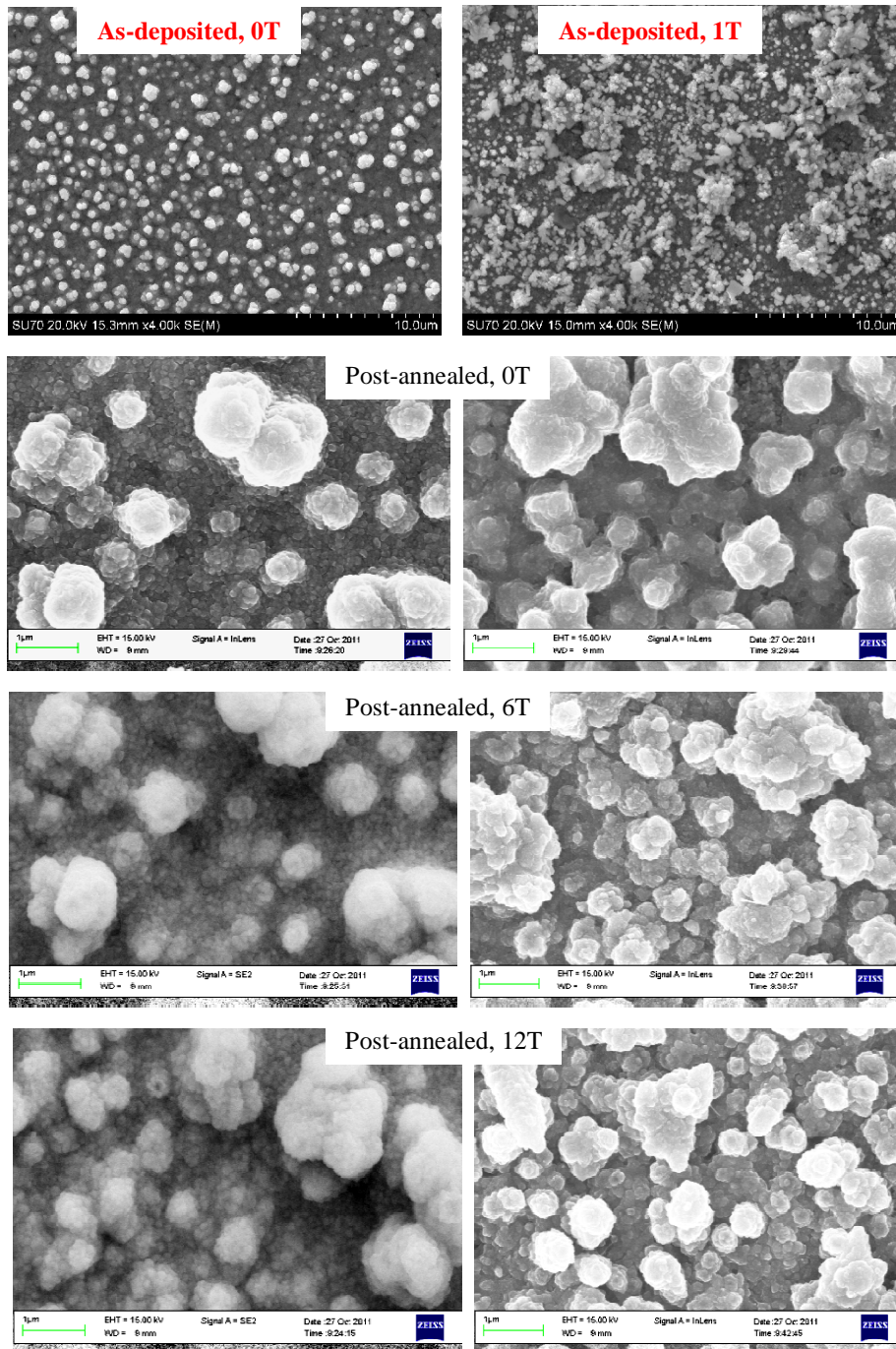


Fig.56. Morphological changes of as-deposited Co-Cu/Cu/ITO films by the annealing process under magnetic field; *Electrodeposition: $i = -20\text{mA/cm}^2$, $t = 1\text{min}$, $\text{pH} = 4$; Annealing: $t = 4\text{h}$, $T = 623\text{K}$.*

Apart from morphological and structural properties, the Co–Cu films grown under magnetic field have different magnetic properties. Figure 57 shows the hysteresis loops for the Co-Cu/Cu/ITO samples electrodeposited under superimposed magnetic field, measured in the film plane. It can

be clearly seen that it is harder to magnetise the Co-Cu film grown under superimposed magnetic field. A drop in approaching the saturation magnetization and increase of hysteresis field is observed, when the Co-Cu films are deposited in the presence of external field. This effect can be attributed to the change of Co:Cu ratio in the film caused by the electrodeposition conditions.

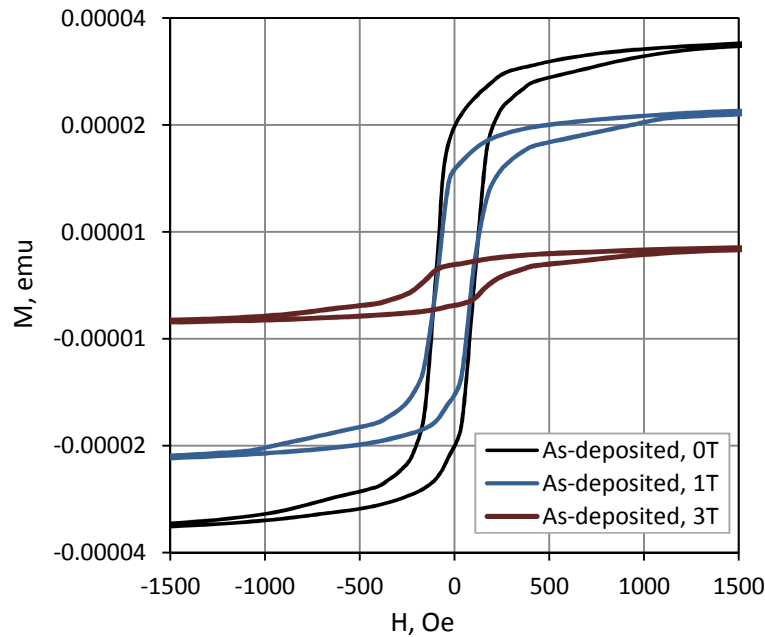


Fig.57. Comparison of the hysteresis loops field of Co-Cu/Cu/ITO alloy films electrodeposited without and with an applied magnetic field; *Electrodeposition: $i = -20\text{mA/cm}^2$, $t = 1\text{min}$, $\text{pH} = 4$;*

When deposition is carried out without an applied magnetic field the chemical composition of Co-Cu film is almost equal for each element (Fig.58). A superimposed magnetic field enhances the deposition rate of copper ions, suppressing that of cobalt. Thus, the Co-Cu films consist mainly of copper crystallites with low incorporation of cobalt nucleus, what is seen in the X-ray diffraction patterns (Fig.55). An evidence of decreased M_s and increased H_c in dependence on Co:Cu ratio is given by Karaagac *et al.* [44,184], whose EDX results have shown that they are strongly affected by increasing amount of non-magnetic Cu component in the film that result in the increased density of dendritic structure as well. Furthermore, the topographical AFM analysis reveals clearly the transition of Co-Cu film crystallites with an increase of magnetic field during electrodeposition (Fig.58). It can be seen, that under external magnetic field the form of Co-Cu

crystallites is changed, from small and rather round particles in much larger rhombic-like features, as observed under 12T magnetic field.

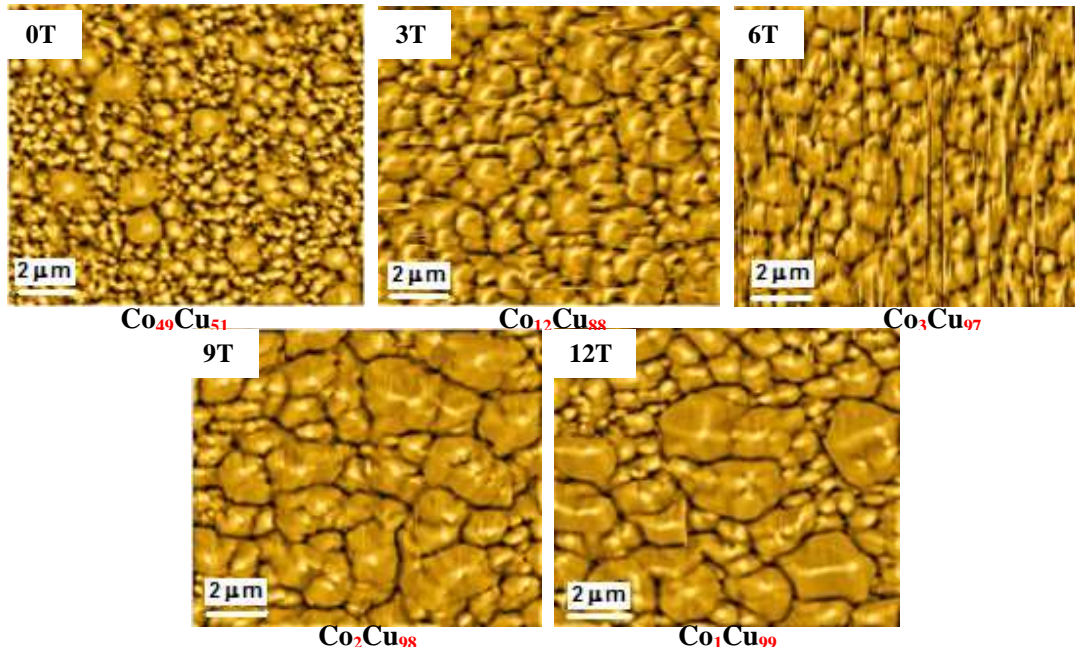


Fig.58. Topographical characteristics of the Co-Cu/Cu/ITO films electrodeposited under high magnetic field. Images were obtained by applying a differentiation procedure to the AFM images by Nova software; *Electrodeposition: $i = -20\text{mA/cm}^2$, $t = 1\text{min}$, $\text{pH} = 4$.*

Since the Co-Cu dendrites are grown in the (111) orientation, perpendicular to the substrate surface, they significantly affect the film thickness and surface roughness, which both strongly increase under magnetic field deposition (Table 8). Thus, for the Co-Cu films deposited under the field higher than 3T the magnetic investigations brings about the anti-hysteresis curves, where no saturation magnetization and hysteresis field was observed.

Table 8. Characteristic features of the Co-Cu/Cu/ITO films influencing magnetic properties.

Magnetic field, T	Nucleus size, nm	Thickness, nm	Roughness, nm	Coercivity field, Oe
0	610	350	37	110
1	750	389	90	115
3	810	450	138	200
6	890	500	143	-
9	910	700	154	-
12	920	860	173	-

III.6. Electrodeposited Co-Ni-Cu/Cu/ITO films

Figure 59 presents the in-plane hysteresis loops of Co-Ni-Cu films deposited with and without an applied magnetic field during electrodeposition. Both samples are full saturated in the high magnetic field. However, the Co-Ni-Cu film deposited under 1T magnetic field is characterized by achieving lower saturation magnetization and coercivity field. This is related with the chemical composition of Co-Ni-Cu films, which is affected by magnetic deposition conditions. An applied external magnetic field causes a decrease of the content of ferromagnetic Co and Ni from 61wt.% and 25wt.%, respectively (when no magnetic field is present), down to 52wt.% and 13wt.%, respectively, (under 1T field). At the same time the content of copper increases, from 14wt.% (0T) up to 35wt.% (1T). Furthermore, the crystallographical characteristic of Co-Ni-Cu film is changed, as indicated by topographical images (Fig.59).

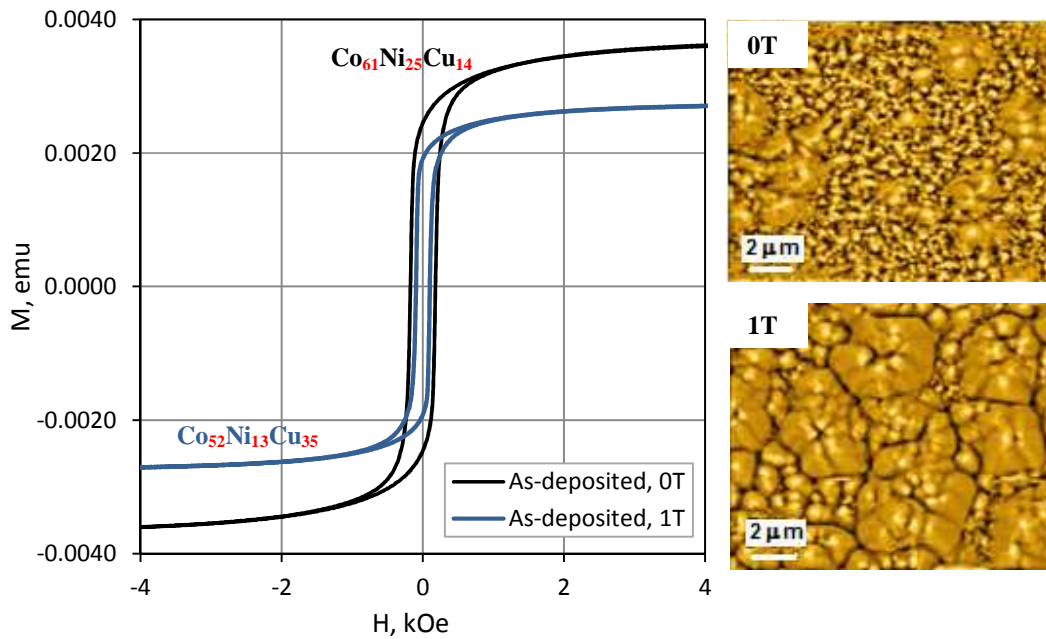


Fig.59. Comparison of the hysteresis loops measured in-plane of Co-Ni-Cu/Cu/ITO films electrodeposited without and with an applied magnetic field; *Electrodeposition: $i = -20\text{mA/cm}^2$, $t = 1\text{min}$, $\text{pH} = 4$.*

Similar, as in the case of binary Co-Cu films, an increased amount of Cu in the layer affects the crystallite growth, which under magnetic field is of dendritic nature. The development of dendritic-like structure under magnetic conditions brings about to improve the surface roughness, which in turn affects the magnetic properties of Co-Ni-Cu films (Table 9).

Table 9. Characteristic features of the Co-Cu/Cu/ITO and Co-Ni-Cu/Cu/ITO films influencing magnetic properties.

Magnetic field, T	Nucleus size, nm	Thickness, nm	Roughness, nm	Hc, Oe	M, emu
<i>Co-Cu/Cu/ITO</i>				in-plane	in-plane
0	610	350	37	125	$35 \cdot 10^{-6}$
1	750	389	90	230	$26 \cdot 10^{-6}$
<i>Co-Ni-Cu/Cu/ITO</i>				in-plane out-of-plane	
0	480	432	171	180 500	$36 \cdot 10^{-4}$
1	640	465	224	100 460	$28 \cdot 10^{-4}$

A superimposed magnetic field during electrodeposition reduces the hysteresis field and slows down the approaching of saturation magnetization however, comparing to that of Co-Cu system it is clearly observed that alloying Co-Cu with Ni certainly improves the magnetic properties of deposited films. Moreover, it is interesting to see that Co-Ni-Cu film deposited under 1T magnetic field possesses almost identical crystallographical characteristic as binary Co-Cu film deposited under 12T (Fig.60). Thus, it is assumed that magnetic properties of Co-Ni-Cu films deposited under higher than 1T magnetic field would be greatly modified.

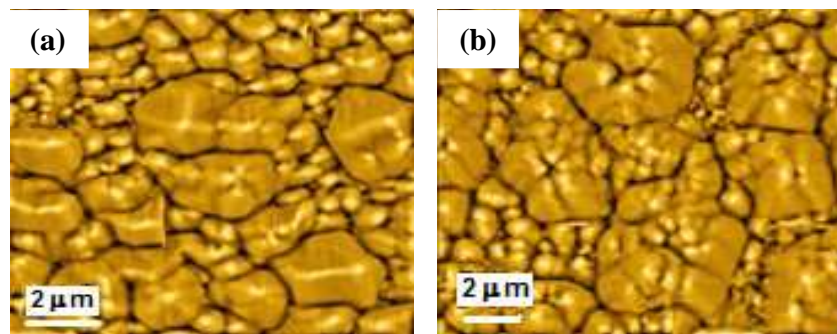


Fig.60. Topography of (a) Co-Cu under 12T and (b) Co-Ni-Cu under 1T magnetic field;
Electrodeposition: $i = -20\text{mA/cm}^2$, $t = 1\text{min}$, $\text{pH} = 4$.

An interesting behaviour is observed, when determining the magnetic measurements of sample in out-of-plane direction to the film surface. Both samples, deposited under 0 and 1T magnetic field, share a similar behaviour with a slow approach to saturation magnetization (Fig.61). Moreover, a clear perpendicular anisotropy, marked by the presence of a relatively large coercive field (approximately 500 Oe) is observed. For the Co-Ni-Cu film deposited under 1T magnetic field the reduced perpendicular anisotropy is seen, and lower coercivity field is achieved (Table 9). The results indicate that easy-axis direction of magnetization is parallel and hard-axis is perpendicular to the film plane.

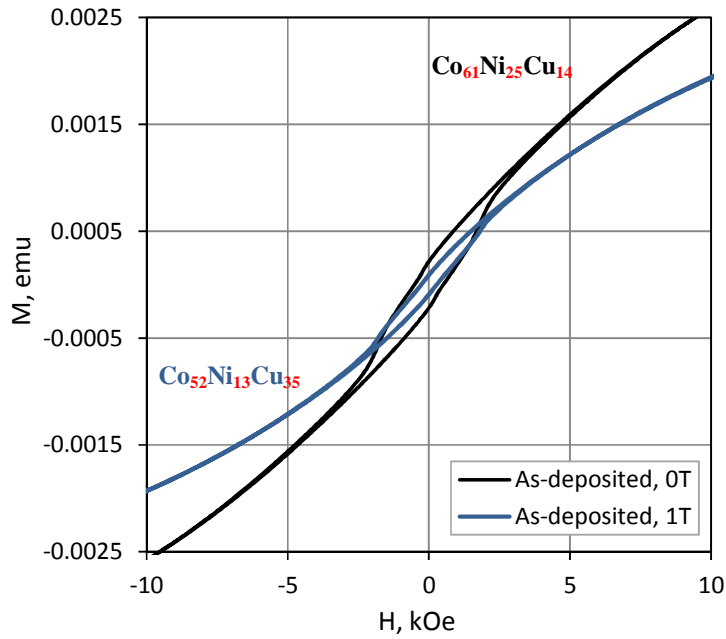


Fig.61. Comparison of the hysteresis loops measured out-of-plane of Co-Ni-Cu/Cu/ITO films electrodeposited without and with an applied magnetic field;
Electrodeposition: $i = -20\text{mA/cm}^2$, $t = 1\text{min}$, $\text{pH} = 4$.

III.7. Conclusion

The magnetic annealing treatment of electrodeposited Co/Ni/ITO, Co-Ni/ITO and Co-Cu/Cu/ITO films, respectively, in dependence on microstructure has been investigated. Furthermore, the magnetic properties of mentioned and additional Co-Ni-Cu/Cu/ITO films have been determined.

It is shown that the crystallographical structure of as-deposited films is improved by annealing treatment. Moreover, it is preserved under superimposed magnetic field during process. Furthermore, it has been shown that annealing processing induces intermixing between seed (Ni, Cu) and secondary layers deposited on ITO substrate, which is enhanced under magnetic conditions of the process. Hence, the magnetic properties of as-deposited samples are strongly affected.

The magnetic field annealing has affected the magnetic properties of Co/Ni/ITO and Co-Ni/ITO films by minimizing the magnetic anisotropy energy of the systems due to the stress relief between grains and directional atomic pair ordering. The direction bonds of dissimilar

atoms (Co, Ni) in the films may affect their asymmetric distribution under superimposed magnetic field, when supposing that its strength is sufficiently high. Furthermore, the magnetic field annealing decreases the dipole magnetostatic interactions of the metal atoms due to the redistribution of pair ordering directions, which are perpendicular to the magnetization direction in each domain, as in the case of Co/Ni/ITO films. Interestingly, an in-plane magnetic anisotropy in the investigated films was always obtained, which origin is seen in a preferential same-like atoms couples formation under magnetic annealing conditions.

A superimposed magnetic field affects the magnetic properties of as-deposited Co-Cu/Cu/ITO and Co-Ni-Cu/Cu/ITO films. The magnetic measurements revealed that magnetic properties of the films depend on the film composition, mainly on the amount of non-magnetic Cu component, which varies under magnetic field conditions. Thus, the morphological and structural changes are observed, which increase the surface/volume ratio and enhance the shape anisotropy.

A detailed knowledge and understanding of the grain structure, magnetic domain structure and the correlation between these features are not only basic research interest, but also of practical significance. From the practical point of view, they are important for tailoring of the materials with the required properties, as indicated in this Chapter. The presented here results are useful for possible production of the Co-based films with a range of magnetic properties for applications, when considering sensors and recording media.

Chapter IV

Theoretical study

IV.1. Introduction

Understanding and control of the evolving surface morphology of different growth modes of electrodeposits is the essential issues in the field of surface science. This especially accounts, when considering a potential application approach, where the microstructure plays a significant role in determining the material properties. Although many aspects of the growth behaviours and material properties have been studied extensively, the investigation of how to obtain ordered structures with better performance is still necessary.

As it is discussed in Chapter I and shown in Chapter II, in the electrochemical deposition process the hydrogen evolution reaction (HER) is one of the important electrochemical reaction from both, theoretical and practical points of view. As it was discussed before, the HER may affects strongly the growth mechanism of electrodeposits, determining their final structure and morphology and thus, properties of the film. The research on HER necessary involves the investigation of this side reaction on well-defined surfaces, what is identified as essential in order to link the atomic-molecular-level properties of the electrochemical interface with the macroscopic kinetic parameters. The interaction of H_2 with transition metals is of the fundamental interest in the fields of hydrogen storage, catalysis and metallurgy. Especially the adsorption of hydrogen on nickel, cobalt and iron is of considerable importance, as these metals are used in hydrogenation (Ni) [202], ammonia synthesis (Fe) [203], or Fischer-Tropsch (Co and Fe) catalysts [204]. Under reaction conditions, the surface of catalytically active metals is often covered by hydrogen. Experimental evidence in support of the HER mechanism includes the observation that the ionization potential of metal clusters increases upon adsorption of hydrogen [205], the strength of the cluster (hydrogen bond) [206] and that the reaction between hydrogen and metal cluster is irreversible at room temperature [207]. The provided density functional theory (DFT) and quantum mechanics (QM) based calculations on transition metal clusters present a real challenge in predicting the magnetic properties of such systems and the importance of spin-orbit coupling and correlation effects. However, they give a huge possibility to design and explain the growth of electrodeposited films under chosen electrodeposition conditions.

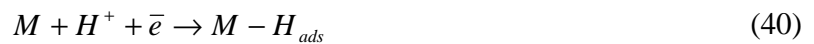
The aim of this theoretical study is to compile the theoretical results of adsorption of hydrogen onto different hkl planes of both cobalt crystallographic structures: hexagonal closed-packed (hcp) and face centered-cubic (fcc), as well as to determine the preferred adsorption surface and site. In the next order, the relation between computational results and that of

experimental ones is made, in order to explain the growth of electrodeposited cobalt, which is further studied in the experimental study in Chapter II. As known so far, this work is the first one, which considers the hydrogen adsorption on both crystallographic structures of cobalt: hexagonal and cubic, including various surfaces and supported by the QM/DFT study with referring to the explanation of experimental results.

IV.2. Role of the hydrogen evolution reaction (HER) in electrodeposition

During electrodeposition process in aqueous solution, hydrogen evolution occurs as a parallel process that consumes part of the applied current and reduces the overall process efficiency. This secondary process can affect the pH at the electrode-electrolyte interface and also modifies the kinetics and mechanism of cobalt electrodeposition [208,209]. As a consequence, the local pH rise can lead to the cobalt hydroxide precipitation over the electrode, which interferes with the formation of metallic deposit, producing a porous structure [35,210,211] and at the same time, may give a rise to the marked mechanical effects, such as hydrogen embrittlement [212].

There are two generally accepted mechanism for HER during the deposition process of the iron group metals and their alloys from the aqueous solution [49]: i) discharge (Volmer reaction) (40) followed by Tafel recombination (41a) or ii) discharge (40) followed by electrochemical desorption (Heyrovsky reaction) (41b):



The rate-determining step is determined by the strength of hydrogen bond with the to-be-adsorbed surface. Reaction (40) is an adsorption step in which a chemical bond $M-H_{ads}$ is formed. A major portion of the adsorbed reacts to give hydrogen molecules followed by a desorption stage according either to reaction (41a), which implies that the H_{ads} atoms are mobile at the metal surface, or to reaction (41b) in which a second proton is involved. A small portion of the adsorbed hydrogen is adsorbed into the metallic lattice, $M(H_{ads})$ as follows [49]:



The interaction of hydrogen with the transition metal surface is a topic of considerable experimental, theoretical and industrial interest. In general, H_{ads} is considered to block active sites that could otherwise be used for the formation of $Me(I)_{ads}$ species. This is supported by the studies conducted on Pt substrates that provide evidence that H_{ads} adsorbs onto and blocks surface sites at the expense of the adsorbed iron-group metal intermediates, e.g. $Ni(I)_{ads}$, $Fe(I)_{ads}$ [12].

IV.2.1. Hydrogen evolution reaction under magnetic field

The magnetically induced forces, which act inside the diffusion layer, affect also the microstructure of the deposited layers. This is mainly caused by the co-deposition and adsorption of hydrogen, which locally inhibits the layer growth. The magnetic fields support desorption of the adsorbed and recombined hydrogen independent on their orientation. Consequently, the inhibition of the local layer growth is reduced by magnetic fields and a more uniform layer can be formed.

An effect of superimposed magnetic field on HER significantly affects the process. This is manifested by a reduced electrode fraction covered by bubbles, reduced bubble size and narrower size distribution. The effect can be divided into two categories: in parallel-to-electrode and perpendicular-to-electrode surface. In the parallel to electrode surface magnetic field, the electric and magnetic fields are perpendicular to each other resulting in a macroscopic convection due to the Lorentz force acting in the bulk, i.e. a classical MHD effect (*Annex I*). A bubble at the electrode surface acts as an obstacle in the flow and a hydrodynamic drag acting on the bubble will be induced [159,213,214]. This leads to a reduced bubble size and its faster desorption from the electrode surface, and as a consequence depolarization of the electrode is noticed [213,215]. Moreover, the coalescence of bubbles is enhanced [216], which leads to their improved desorption from the electrode surface. A schematic representation of these phenomena is shown in Fig.62.

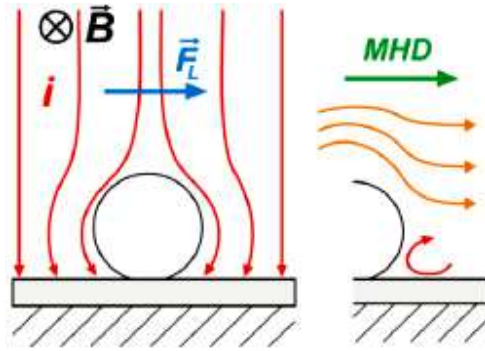


Fig.62. Schematic representation of the current distribution together with direction of Lorentz force (left hand side) and characteristic convection patterns (right hand side) in the vicinity of a bubble obtained in the parallel-to-electrode magnetic field configuration. (Krause et al. [216])

This result is qualitatively the same as obtained under forced convection [213]. The authors have also shown a dramatic reduction of the electrode fraction covered by the bubbles and their improved coalescence under forced convection condition. According to the work of Koza et al. [217], the explanation for faster desorption rate of hydrogen could be as follow: when a hydrogen bubble is formed at the electrode surface, in its vicinity the current distribution is distorted. The current lines are no longer perfectly normal to the electrode surface, but there is also a parallel-to-electrode component (Fig.63.(a)). As a consequence Lorentz force is induced. The Lorentz force acting in the bubble vicinity induces a localized convection close to it (Fig.63.(a)). This effect is analogous to a micro-MHD effect [217].

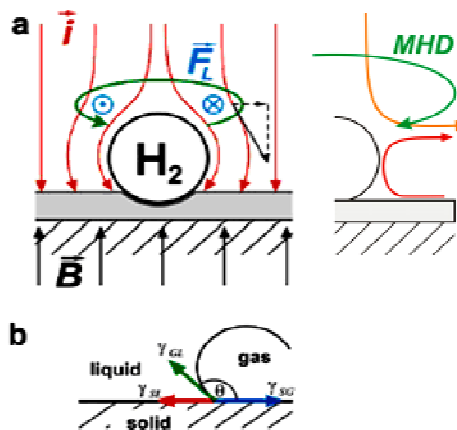


Fig. 63. Schematic representation of the current distribution together with direction of Lorentz force (left hand side) and characteristic convection patterns (right hand side) in the vicinity of a bubble obtained in the perpendicular-to-electrode magnetic field configuration (a), and surface tensions between gas/liquid/solid interfaces (b). (Koza et al. [217])

Following Wassef and Fahidy [219], the hydrogen formation can be divided in three zones with respect to the current density. The first zone corresponds to low current densities, where the hydrogen formation is negligible. The second zone characterizes moderate current densities, at which stagnant hydrogen bubbles are formed and adhere to the cathode surface. The third zone occurs at high overpotentials, where bubble formation is very intensive and it is no longer stationary. When the deposition is carried out without a magnetic field the morphology of the deposits suggested that HER is in the second zone where stationary bubbles are formed (Fig.64.(a)) and adhere to the electrode surface.

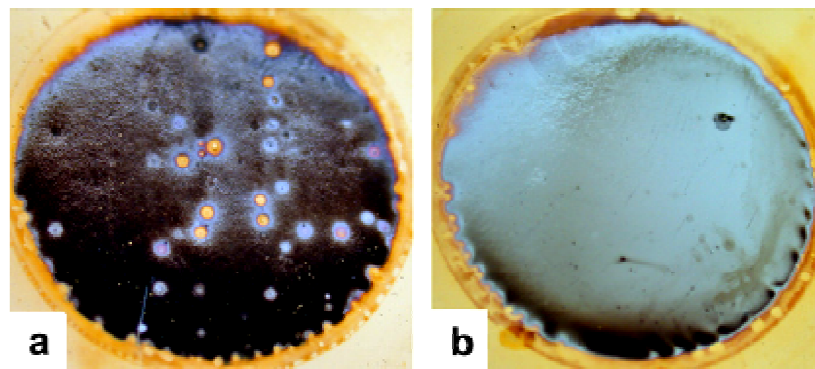


Fig.64. Optical micrographs of CoFe deposits: (a) deposited without magnetic field and (b) deposited with $B = 1\text{T}$ [217].

The hydrogen bubbles will be desorbed from the electrode surface (Fig.64.(b)), if they reach critical size. This critical size depends on the surface tensions between bubble, electrode surface and electrolyte:

$$\gamma_{SL} = \gamma_{SG} - \gamma_{GL} \cos \theta \quad (43)$$

where γ_{SL} , γ_{SG} and γ_{GL} are surface tensions of solid/liquid, gas/solid and gas/liquid interferences, respectively; θ is a contact angle. Moreover, bubble might be removed from the electrode surface only if its pressure is higher than the atmospheric and hydrostatic pressures. When a magnetic field is applied to the electrode, a localized convection introduces a hydrodynamic drag force, which acts on the hydrogen bubble, which is an obstacle in the flow. The contact angle increases (Fig.63.(b)) and smaller hydrogen bubbles can be removed from the electrode surface. As a consequence, an enhanced desorption of hydrogen is observed (Fig.64.(b)). Additionally it has to be mentioned that magnetic field induced convections are very

complex already at flat electrodes without gas evolution especially in small cell geometries as shown by Cierpka et al. [220]. After coalescence, the large bubble is immediately removed from the electrode surface. This, in turn, induces micro-convective phenomena below the desorbed bubble [221], the pressure field is affected and the bubble in the vicinity is sucked away from the electrode surface.

Desorption of the hydrogen from the electrode surface might be also supported due to a local field gradient force, which may act in the very vicinity of the ferromagnetic electrode. Such a local field gradient force may arise due to the stray fields in the material [222], close to the hydrogen bubble. Hydrogen is diamagnetic and thus is repulsed out of the magnetic fields [124]. As a result the equilibrium state for the HER is shifted because the partial pressure of hydrogen at the electrode surface is reduced:

$$E_{H_2/2H^+} = E_{H_2/2H^+}^0 + \frac{RT}{2F} \ln \frac{a_{H^+}^2}{p_{H_2}} \quad (44)$$

where E_{H_2/H^+} is the equilibrium potential of the HER, E_{H_2/H^+}^0 is the standard potential of the hydrogen electrode, R is the universal gas constant, T is temperature, a_{H^+} is the activity of the hydrogen ions and p_{H_2} is the partial pressure of hydrogen. Koza et al. [223] investigated the effect of a low magnetic field superimposed with parallel and perpendicular orientation relative to the electrode surface on the electrocrystallization of Co, Fe and Co-Fe alloys. Their work reported that in the case of perpendicular-to-electrode configuration, at moderate deposition times during the deposition of Co-Fe alloys increased hydrogen evolution reaction current was observed. This current enhancement for the HER was attributed to the faster desorption of hydrogen from the electrode surface in the magnetic field, caused by the stray fields in the ferromagnetic deposit which may lead to the local field gradients acting on the hydrogen bubble.

IV.3. Density Functional Theory (DFT) background

Density functional theory (DFT) describes the electronic states of atoms, molecules and materials in terms of the three-dimensional electronic density of the system, which is a great simplification over wave function theory (WFT), which involves a $3N$ -dimensional anti-

symmetric wave function for a system with N electrons. DFT has now become the preferred method for electronic structure theory for complex chemical systems, in part because of its cost scales more favourably with system size than does the cost of correlated WFT. This is true even in organic chemistry, but the advantage of DFT is still greater for metals, especially transition metals.

IV.3.1. Early Density Functional Theory: Thomas Fermi Model

A first approximation to studies at the atomic level was made using Newtonian mechanics and classical electromagnetism. Due to the failure to explain the structure and complexity of atomic systems, new theories had to be proposed. Thomas and Fermi gave the first formal derivation of a density functional approach for a system of electrons in an external potential, due to nuclei [224,225]. In their model the total energy of an inhomogeneous electron gas is written as a functional of the electronic density, $\rho(\vec{r})$. This was an initial approximation to the exact solution of the many-electron Schrödinger equation and the associated wave function $\Psi(r_1, r_2, \dots, r_N)$, and is the most primitive version of DFT.

$$E_{TF}[\rho(\vec{r})] = T_{TF}[\rho(\vec{r})] + E_{en}[\rho(\vec{r})] + E_{ee}[\rho(\vec{r})] \quad (45)$$

In the Thomas-Fermi (TF) model, the electronic density $\rho(\vec{r})$ completely characterizes the ground state of the system. As the TF model neglects exchange (included in the Hartree-Fock method, as a consequence of the anti-symmetry of the wave function, i.e. the Pauli exclusion principle) and the correlation effects; the energy functional $E_{TF}[\rho(\vec{r})]$ is expressed as the contribution of the kinetic energy ($T_{TF}[\rho(\vec{r})]$), the electron-nucleus attraction ($E_{en}[\rho(\vec{r})]$) and electron-electron repulsion ($E_{ee}[\rho(\vec{r})]$). In the TF model, the kinetic energy is expressed as a functional of the electronic density $\rho(\vec{r})$.

$$T_{TF}[\rho(\vec{r})] = C_F \int \rho^{5/3}(\vec{r}) d\vec{r} \quad (46)$$

hence, the energy functional can be written as follows:

$$E_{TF}[\rho(\vec{r})] = C_F \int \rho^{5/3}(\vec{r}) d\vec{r} - Z \int \frac{\rho(\vec{r})}{r} d\vec{r} + \frac{1}{2} \iint \frac{\rho(\vec{r})\rho(\vec{r}^j)}{|\vec{r} - \vec{r}^j|} d\vec{r} d\vec{r}^j \quad (47)$$

with $C_F = \frac{3}{10}(3\pi^2)^{2/3} = 2.871$ calculated from the jellium model. The TF model assumes that the electronic density $\rho(\vec{r})$ minimizes the energy functional $E_{TF}[\rho(\vec{r})]$, with the constrain:

$$N = N[\rho(\vec{r})] = \int \rho(\vec{r}) d\vec{r} \quad (48)$$

where integrating over $\rho(\vec{r})$, gives the total number of electrons, N . Using the Lagrange multipliers method in order to find a stationary point for $E[\rho(\vec{r})]$, using the constrain (48):

$$\frac{\delta}{\delta\rho(\vec{r})} \left[E_{TF}[\rho(\vec{r})] - \mu_{TF} \left(\int \rho(\vec{r}) d\vec{r} - N \right) \right] = 0 \quad (49)$$

the variations in electronic density of the energy functional $E_{TF}[\rho(\vec{r})]$, can be expressed as an Euler-Lagrange equation, where:

$$\frac{\delta E_{TF}[\rho(\vec{r})]}{\delta\rho(\vec{r})} = \mu_{TF} \quad (50)$$

$$\mu_{TF} = \frac{\delta E_{TF}[\rho(\vec{r})]}{\delta\rho(\vec{r})} = \frac{5}{3} C_F \rho^{2/3}(\vec{r}) - \phi(\vec{r}) \quad (51)$$

where

$$\phi(\vec{r}) = \frac{Z}{r} - \int \frac{\rho(\vec{r}^j)}{|\vec{r} - \vec{r}^j|} d\vec{r} \quad (52)$$

Equation (52) can be solved using the density constrain (Eq.(48)), and the resulting density is then inserted in Eq.(47), in order to give the total energy of the system. The TF model is a very simple theory for describing total energies of atoms, which set up the foundations for a more complex DFT [226,227].

IV.3.2. Modern Density Functional Theory

For the case of N interacting electrons (in the ground-state), their interactions can be described as the sum of the kinetic energy (\hat{T}), external potential (\hat{V}) and Coulombic (\hat{V}_{ee}) operators. The corresponding Hamiltonian operator (\hat{H}):

$$\hat{H} = \hat{T} + \hat{V} + \hat{V}_{ee} \quad (53)$$

which can be expressed, in a similar way, in the following analytic form:

$$\hat{H} = -\sum_{i=1}^N \frac{1}{2} \nabla_i^2 + \sum_{i=1}^N v(\vec{r}_i) + \frac{1}{2} \sum_{i=1}^N \sum_{i \neq j} \frac{1}{|\vec{r}_i - \vec{r}_j|} \quad (54)$$

where $v(\vec{r}_i)$ represents the external potential. The Hamiltonian \hat{H} described in the equation above, takes into account the adiabatic Born–Oppenheimer approximation. The Born–Oppenheimer approximation treats the atomic nucleus as being fixed in position, with respect to the electronic motion, due to large mass differences between the atomic nucleus and the electron. This represents a decoupling of the motion of the electrons and the motion of the nucleus; hence one needs to solve the Schrödinger equation only for the electronic part [228]. The foundations of modern DFT were published in the classic papers of Kohn and Sham [229]. They developed an exact variational principle formalism in which ground state properties, such as: total electronic energy, equilibrium positions and magnetic moments are expressed in terms of the total electronic density $\rho(\vec{r})$. The theorems are explained below: Hohenberg and Kohn Theorem: the ground state density $\rho(\vec{r})$ of a system of interacting electrons in some external potential $v(\vec{r})$ determines potential uniquely, as well as the ground state wave-function $\psi(r_{1,\dots,r_N})$. This theorem also states that: since electronic density $\rho(\vec{r})$ determines total number of electrons, N and the external potential $v(\vec{r})$; $\rho(\vec{r})$ also provides full description of all the ground-state observables, which are functionals of $\rho(\vec{r})$. Another statement of the Hohenberg–Kohn theorem states: the ground energy E_0 and the ground-state density $\rho(\vec{r})$ of a system characterized external potential $v(\vec{r})$ can be obtained by using the variational principle (involving only the density). In other words, the ground state energy E_0 can be expressed as a functional the ground state density $E_v[\rho(\vec{r})]$ otherwise the inequality prevails [226]:

$$E_0 = E_v[\rho_0(\vec{r})] < E_v[\rho(\vec{r})] \quad (55)$$

The theory also established the existence of a universal functional, $F[\rho(\vec{r})]$ which is independent of the external potential $v(\vec{r})$, i.e. which has the same functional form for any system considered. The universal functional $F[\rho(\vec{r})]$ can be expressed as the sum of the kinetic energy of the gas of non-interacting Kohn–Sham electrons ($T_s[\rho(\vec{r})]$), the Coulombic electron–electron interaction, and the exchange–correlation term ($E_{xc}[\rho(\vec{r})]$) as follows:

$$F[\rho(\vec{r})] = T_s[\rho(\vec{r})] + \frac{1}{2} \iint \frac{\rho(\vec{r})\rho(\vec{r}^j)d\vec{r}d\vec{r}^j}{|\vec{r} - \vec{r}^j|} + E_{xc}[\rho(\vec{r})] \quad (56)$$

The $E_{xc}[\rho(\vec{r})]$ term is expressed as the sum of the correlation ($E_c[\rho(\vec{r})]$) and the exchange energy ($E_x[\rho(\vec{r})]$). In the $E_{xc}[\rho(\vec{r})]$ term, the correlation energy $E_c[\rho(\vec{r})]$ is expressed as the difference between the true kinetic energy $T[\rho(\vec{r})]$ and $T_s[\rho(\vec{r})]$:

$$E_c[\rho(\vec{r})] = T[\rho(\vec{r})] - T_s[\rho(\vec{r})] \quad (57)$$

Therefore, the total energy of a system ($E_v[\rho(\vec{r})]$), under a external potential, $v(\vec{r})$ can be expressed as:

$$E_v[\rho(\vec{r})] = F[\rho(\vec{r})] + \int \rho(\vec{r})v(\vec{r})d\vec{r} \quad (58)$$

Using the variational principle with the constraint (48) the ground state density satisfies the stationary principle:

$$\delta \left[E_v[\rho(\vec{r})] - \mu \left(\int \rho(\vec{r})d\vec{r} - N \right) \right] = 0 \quad (59)$$

which gives the Euler–Lagrange equation:

$$\frac{\delta E_v[\rho(\vec{r})]}{\delta \rho(\vec{r})} = v(\vec{r}) + \frac{\delta F[\rho(\vec{r})]}{\delta \rho(\vec{r})} \quad (60)$$

From the Hohenberg–Kohn theorems, it was possible to derive the Kohn–Sham (KS) equations [226,227,229]. The KS equations solve the problem of the complex many electron Schrödinger equations, by transforming them into a set of N single electron equations, which need to be solved self-consistently.

$$\left[-\frac{1}{2}\nabla^2 + v(\vec{r}) + \int \frac{\rho(\vec{r}')}{|\vec{r} - \vec{r}'|} d\vec{r}' + v_{\chi^e}[n(\vec{r})] \right] \psi_i(\vec{r}) = \epsilon_i \psi_i(\vec{r}) \quad (61)$$

with an electronic density:

$$\rho(\vec{r}) = \sum_{i=1}^N |\psi_i(\vec{r})|^2 \quad (62)$$

where ψ_i is a mono-electronic wave function. In Eq.(61), the exchange-correlation potential, $v_{\chi^e}[n(\vec{r})]$ is expressed as the partial derivative of the $E_{\chi^e}[\rho(\vec{r})]$ term, with respect to the electronic density, $\rho(\vec{r})$:

$$\frac{\delta E_{\chi^e}[\rho(\vec{r})]}{\delta \rho(\vec{r})} = v_{\chi^e}[\rho(\vec{r})] \quad (63)$$

This means that it is necessary to start from some initial electronic density ($\rho_0(\vec{r})$) and proceed to solve Eq.(61). A new density, which is used to solve Eq.(61) until self-consistency is reached [226,227,229]. DFT does not provide a description of how to construct the exchange-correlation functional, $E_{\chi^e}[\rho(\vec{r})]$ it only stipulates the existence of $E_{\chi^e}[\rho(\vec{r})]$ as a universal functional of the density $\rho(\vec{r})$ which is valid for all systems. Several approximations have been constructed (for the accurate description of the exchange-correlation energy, $e_{\chi^e}[\rho(\vec{r})]$) such as the local-density approximation (LDA) [225]. This formulation is established in the original Kohn–Sham theory, and the idea is that a system with inhomogeneous charge distribution is treated as having a locally-homogeneous spatial uniform distribution of $\rho(\vec{r})$:

$$E_{\chi^e}^{LDA}[\rho(\vec{r})] = \int \rho(\vec{r}) e_{\chi^e}[\rho(\vec{r})] d\vec{r} \quad (64)$$

where $e_{\chi^e}[\rho(\vec{r})]$ is the exchange and correlation energy per particle of a uniform electron gas of density e . LDA offers a good level of accuracy for highly-homogeneous systems, and even for realistic non-homogeneous systems; while one of the drawbacks is its overestimation of binding energies for molecules and solids [230,231]. Some other high-level approximations to the $e_{\chi^e}[\rho(\vec{r})]$ have been made, such as the generalized gradient approximation (GGA) [230,232,233], for which the exchange-correlation energy (for a spin-unpolarized system) is expressed as:

$$E_{\chi^e}^{GGA}[\rho(\vec{r})] = \int f[\rho(\vec{r}), \nabla\rho(\vec{r})] d\vec{r} \quad (65)$$

in which the density $\rho(\vec{r})$ is expanded in terms of the gradient (∇) operator. This approximation is valid for systems with slowly-varying densities. In order to solve the Kohn–Sham equations, it is usually needed to select a suitable (sufficiently large) finite basis set (in theory one will need an infinite basis set for a precise description of the molecular orbital). The wave-fuction ψ can be expressed in terms of Gaussian-type-orbitals (GTOs), in either cartesian or polar coordinates:

$$\psi(\vec{r}) = Ax^{l_x} y^{l_y} z^{l_z} \exp(-\xi r^2) \quad (66)$$

where A is a normalization constant, l determines the orbital, ξ is related to the width of the curve, and the r^2 gives the curve a Gaussian shape [234]. Finally, there are also hybrid functionals, which mix HF and DFT exchanges.

IV.3.3. DFT literature review on the adsorption of hydrogen

Among the numerous theoretical calculation methodologies, DFT has been generally used in many adsorption systems, and also, the calculated results were in good agreement with the experimental results. In this regard, many researchers have studied hydrogen adsorption, dissociation and diffusion on metallic surfaces. Pozzo and Alfe [235] studied the effect of doping transition metal elements on hydrogen dissociation on Mg(0001) surface. Their calculation show that doping the surface with transition metals on the left of periodic table eliminates the barrier for dissociation of the molecule, but the H atoms bind very strongly to them, while transitions metals on the right of periodic table do not bind H, but unfortunately they reduce the barrier to dissociate H₂ significantly. Huo et al. [236] investigated the hydrogen adsorption onto Fe(111) surface and their found that there are three adsorption sites for H atom, that is: the top site, the top-shallow bridge site and the quasi 4-fold site (Fig.65). Among them at all coverages the most favoured one is the top-shallow bridge site, followed by the quasi 4-fold site. Furthermore, the small diffusion barriers indicate that the H ad-atoms have a large mobility at the Fe(111) surface.

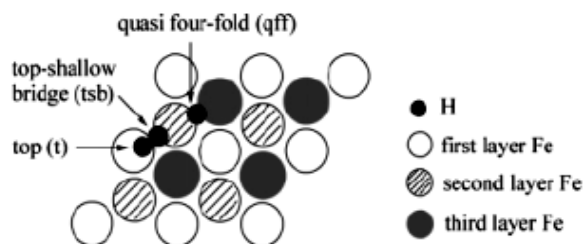


Fig.65. H atom adsorption sites on Fe(111) surface (Huo et al.[236]).

Pasti et al. [237] has shown that the mobility of adsorbed H may be directly correlated to the strength of adsorbate-substrate interaction. The relationship between the adsorption energies and the mobility of adsorbate holds not only for clean transition metal surfaces, but also for metal overlayers and subsurface alloys, as it was also shown by Weng et al. [238]. The authors studied kinetics and mechanism for the adsorption, dissociation and diffusion of hydrogen in nickel and nickel/yttria-stabilized zirconia (Ni/YSZ) and they found that the migration of H-atom in the YSZ slab was very high and that the existence of vacancy can enhance the diffusion of hydrogen through the interface of the Ni/YSZ slab.

In particular, the interaction of hydrogen with cobalt surfaces has not been studied as extensively as for example nickel or iron, however, the literature suggests that behaviour of hydrogen on cobalt is similar to nickel. Based on work function measurements taken as a function of surface coverage, Christmann [202] suggested that adsorbate-adsorbate interaction exist for hydrogen on a Ni(111) surface and therefore, a similar surface coverage dependence on cobalt would be expected. In one of the comparison between hydrogen bonding on nickel and cobalt, Zotwiak et al. [239] indicated that hydrogen is significantly more strongly adsorbed on cobalt, with a heat of adsorption 13-14.5 kcal/mol larger than that on nickel. Bridge et al. [240] reported the chemisorption energy of hydrogen on Co(0001) surface and found the sticking coefficient of hydrogen adsorption was independent of surface coverage up to $\Theta=0.5$. At higher coverages, the sticking coefficient was a strong function of surface coverage. The energetic picture of hydrogen chemisorption over Ni(111) and Co-(001)-hcp quantified in the study of Klinke and Broadbelt [241], suggests that metal-hydrogen bond strength are largely independent of valence-electron occupation and surface coverage. Also, the observed differences in the binding energy of hydrogen between the possible adsorption sites for both studied metals suggest that the diffusion barrier of hydrogen on these surfaces is quite small.

IV.4. Theoretical model of hydrogen adsorption at cobalt surfaces

It is well known that the determination of adsorption energies is one of the most critical aspects of the cluster modelling of surfaces [242]. For small clusters usually the adsorption energies oscillate with the cluster size even if the bonding nature remains the same [243]. Another related problem is that for some systems the optimized geometric parameters show that there is a bond between adsorbate and metal cluster. However, from the energetic considerations the overall system cluster+adsorbate is unbonded with respect to the dissociation limit with local minima on the energy surface [244]. At the transition metal surfaces the hydrogen usually adsorbs dissociatively. At temperatures higher than 80K this process takes place spontaneously, what means that the energy gain due to the formation of two individual metal-H bonds (adsorption) surmounts the energy, which is required for the dissociation of molecule. The net energy gain appears as a heat of adsorption and the energy of a single metal-H bond can be calculated [245].

IV.4.1. Calculation details

In the present work the interactions of H and H⁺ with Co surfaces are studied. For that purpose the density functional theory (DFT) approach was used. The cobalt metal surfaces were modelled by CaRIne 3.1 with upload version to CaRIne 4.0 software [246], which gave a possibility to choose from the Bravais unit cells database, two varieties of a crystallographic structure related to the metallic cobalt: hexagonal and face-centered cubic. It must be noticed here that due to the schemes of Bravais lattice commonly present in the literature, the hcp structure is represented by the model shown in Fig.66.

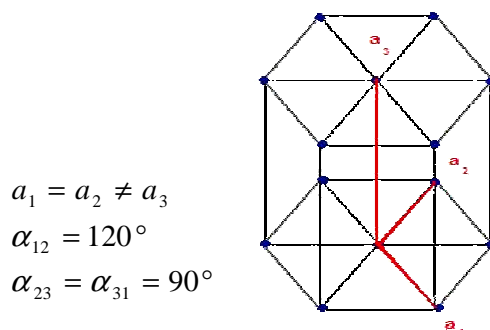


Fig.66. The Bravais lattice indicating hexagonal simple structure of cobalt.

Because our background was the lattice database included into CaRIne software the calculations were limited to the 1/3 part of a whole system assigned to the proper Co hexagonal centered-packed structure which is marked on the model presented in Fig.67. The number of structural isomers dramatically increases with increasing cluster size. Because structural information on both, bare and hydrogenated metal clusters is scarce, calculations have been done only for the systems containing 8 and 14 cobalt atoms, for which the number of possible geometric isomers is limited.

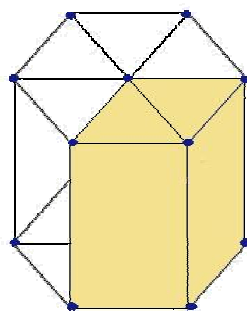
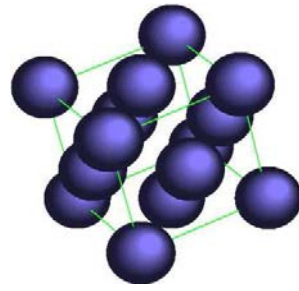


Fig.67. The Bravais lattice indicating a simple hexagonal structure of cobalt with marked calculation part.

By the Miller indices hkl the crystallographic planes for each single cluster of both cobalt structures were determined. Figure 68 represents the surfaces of cobalt with determined hkl planes, which have been used during the calculations.

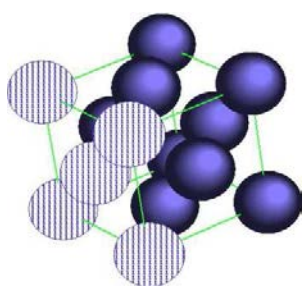
Calculations were performed in the framework of density functional theory using the GAUSSIAN09 packages [247]. All calculations were done using the LANL2DZ basis set, which treats the Co valence shell with a double- ξ basis set and all the remainder shell electrons with the effective core potential of Hay and Wadt [248]. The B3LYP hybrid functional as well as CAM-B3LYP and PBE functionals were used. The B3LYP functional includes a mixture of Hartree-Fock (HF) and DFT exchange terms [249] associated with the gradient corrected correlation functional of Lee et al. [250]. The CAM-B3LYP functional is Yanai's et al. [251] long range corrected version of B3LYP using the Coulomb-attenuating method, while the PBE functional is the 1996 gradient-corrected functional of Perdew, Burke and Ernzerhof [252,253].



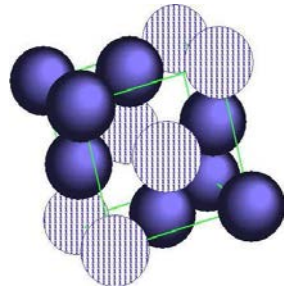
$$a = b = c = 3.548 \text{ \AA}$$

$$\alpha = \beta = \gamma = 90^\circ$$

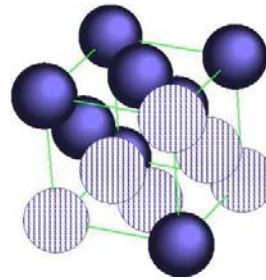
Co - fcc



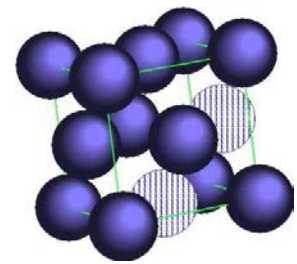
(100) plane



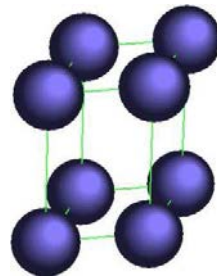
(110) plane



(111) plane



(220) plane



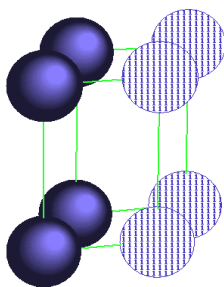
$$a = b = 2.5071 \text{ \AA}$$

$$c = 4.0686 \text{ \AA}$$

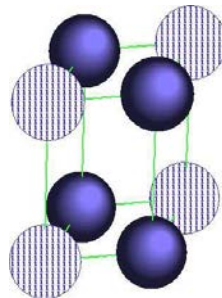
$$\alpha = 120^\circ$$

$$\beta = \gamma = 90^\circ$$

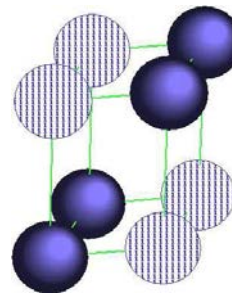
Co - hcp



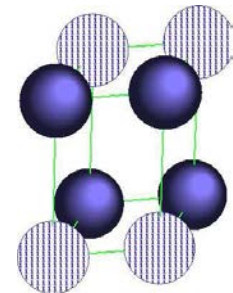
(100) plane



(110) plane



(101) plane



(011) plane

Fig.68. Crystallographic structures of cobalt with marked planes determined by CaRIne 3.1 software and geometrical parameters.

The following computational procedure has been applied. Firstly, based on the fixed atoms coordinates, which build a Co cluster and were obtained by CaRIne software, various spin multiplicities were tried to find the more stable one with the smallest spin contamination. Next, single atomic hydrogen and hydrogen ion were added to each crystallographic plane of Co surface. The positions of hydrogen atom and hydrogen cation were allowed to relax, while other atomic parameters were fixed to maintain a high degree of symmetry in the calculations.

The adsorption energies can be used to estimate the strength of an atom-surface interaction and for determining the most energetically favourable adsorbing surface. The adsorption energy E_{ads} was calculated by the traditional equation:

$$E_{ads} = E_{H/surface} - (E_{surface} + E_H) \quad (67)$$

where E_H is in this case the energy of hydrogen atom and/or ion, $E_{surface}$ is the energy of clean Co surface and $E_{H/surface}$ is the total energy of hydrogen adsorbed on the Co surface. Negative values of E_{ads} denote adsorption that is more stable than the corresponding clean surface and the free atom.

The adsorption of H atom can be oriented on the cobalt surface toward three different symmetrical sites: top, bridge and threefold. Hydrogen adsorbed on the stable site of a perfect crystal distorts the positions of surrounding substrate metal atoms. As explained by Nilekar *et al.* [254] mobility of adsorbed species on a transition metal surface, which is the function of E_{ads} , might play a key role in the transport of species during the catalytic reactions, growth of the surface nanostructures and many other important processes.

IV.4.2. Face-centered cubic structure

Table 10 contain the calculation results: system energy (E), adsorption energy (E_{ads}) of hydrogen atom and hydrogen ion, and hydrogen adsorption sites developed at the different crystallographic planes of hexagonal and cubic cobalt surfaces. The first calculations were related with the choice of multiplicity value in order to obtain the lowest cluster energy. Considering the Co-cubic cluster the proper ones were 29 for B3LYP and CAM-B3LYP and 31 for PBE calculation methods. In the case of Co-hexagonal cluster the calculations determined multiplicity of 19 for B3LYP and PBE and 21 for CAM-B3LYP methods.

Table 10. Calculation results for the different planes of Co-cubic system.

System	Calculation method	Multiplicity	E Hartree	E_{ads} kcal/mol	Adsorption site
H	B3LYP		-0.49891		
	CAM-B3LYP		-0.49534		
	PBE		-0.49588		
H ⁺			0.0		
<i>(100) plane</i>					
Co ₁₄	B3LYP	29	-2031.21467		
	CAM-B3LYP	29	-2030.12019		
	PBE	31	-2031.36287		
Co ₁₄ +H	B3LYP	28	-2031.81227	-61.9	}
		30	-2031.80246	-55.8	
	CAM-B3LYP	28	-2030.75681	-88.7	
		30	-2030.74517	-81.4	
	PBE	30	-2031.95405	-59.8	
		32	-2031.94010	-51.0	
Co ₁₄ +H ⁺	B3LYP	29	-2031.61795	-253.1	}
	CAM-B3LYP	29	-2030.56613	-279.8	
	PBE	31	-2031.75043	-243.2	
<i>(110) plane</i>					
Co ₁₄	B3LYP	29	-2031.14085		
	CAM-B3LYP	29	-2030.02987		
	PBE	31	-2031.22902		
Co ₁₄ +H	B3LYP	28	-2031.74146	-63.8	}
		30	-2031.74836	-68.1	
	CAM-B3LYP	28	-2030.60896	-52.6	
		30	-2030.63283	-67.5	
	PBE	30	-2031.83424	-68.6	
		32	-2031.82209	-61.0	
Co ₁₄ +H ⁺	B3LYP	29	-2031.55287	-258.5	}
	CAM-B3LYP	29	-2030.46600	-273.7	
	PBE	31	-2031.62877	-250.8	
<i>(111) plane</i>					
Co ₁₄	B3LYP	29	-2031.17821		
	CAM-B3LYP	29	-2030.09039		
	PBE	31	-2031.28466		
Co ₁₄ +H	B3LYP	28	-2031.77822	-63.4	}
		30	-2031.77637	-62.3	
	CAM-B3LYP	28	-2030.71939	-83.9	
		30	-2030.71455	-80.8	
	PBE	30	-2031.87681	-60.4	
		32	-2031.87422	-58.8	
Co ₁₄ +H ⁺	B3LYP	29	-2031.60829	-269.9	}
	CAM-B3LYP	29	-2030.55600	-292.2	
	PBE	31	-2031.68324	-250.1	
<i>(220) plane</i>					
Co ₁₅	B3LYP	32	-2176.21254		
	CAM-B3LYP	28	-2175.02818		
	PBE	33	-2176.35378		
Co ₁₅ +H	B3LYP	31	-2176.83546	-77.8	}
		33	-2176.83382	-76.8	
	CAM-B3LYP	27	-2175.66181	-86.8	
		29	-2175.68728	-102.8	
	PBE	31	-2176.95734	-67.6	
		33	-2176.95763	-67.7	
Co ₁₅ +H ⁺	B3LYP	32	-2176.64080	-268.7	}
	CAM-B3LYP	28	-2175.47905	-282.9	
	PBE	32	-2176.75809	-253.7	

The high index (220) plane for Co-cubic cluster was calculated additionally since the XRD analyses have detected its presence in the electrodeposited Co films. Details and relationship of the X-ray diffraction patterns with the adsorbed hydrogen will be discussed in the next section. Calculated energies of pure cobalt and hydrogen surfaces allow calculating and comparing the adsorption energies between defined cobalt crystallographic planes. A negative value of E_{ads} indicates that the adsorption process is exothermic (stable), while a positive value stands for its endothermic (unstable) character. The calculated adsorption energies for all the considered planes of Co-cubic show negative values relative to the gas phase hydrogen atom, indicating the stable adsorption process. The most remarkable observation is that the adsorption energies of cationic hydrogen are much lower than these related to the adsorbed atomic hydrogen.

From Table 10, we can derive some tendencies. For the atomic hydrogen adsorption, the most stable site occurs for the (220) plane whatever the functional (adsorption energy included between -102.8 and -67.6 kcal/mol). The tendency for the less stable site leads to the (100) plane (B3LYP and PBE with an adsorption energy of -55.8 and -51.0 kcal/mol respectively) and the (110) plane (CAM-B3LYP with an adsorption of -52.6 kcal/mol).

For the hydrogen ion, two most stable sites emerge: the (111) plane (B3LYP and CAM-B3LYP with the adsorption energy of -269,9 and -292,2 kcal/mol, respectively) and the (220) plane (B3LYP and PBE with the adsorption energy of -268.7 and -253.7 kcal/mol, respectively). The less stable sites were the same two sites as for the atomic hydrogen: the (100) plane (B3LYP and PBE with the adsorption energy of -253.1 and -243.2 kcal/mol, respectively) and the (110) plane (CAM-B3LYP with the adsorption of -273.7 kcal/mol).

Because the positions of adsorbed H and H⁺ on cobalt surfaces were free to relax another observed feature in the calculations is a favour site, at which hydrogen is bonded to the cobalt cluster. According to Table 10 two different sites of adsorbed hydrogen are noticed. The characteristic of both sites is presented in Fig.69. The most favoured one is a bridge site. However, for (111) and (220) planes a 3-fold site is also noticed, depending on the chosen functional. In both cases the CAM-B3LYP functional gives a strong 3-fold bonding, while in B3LYP and PBE the adsorption site varies with the orientation plane.

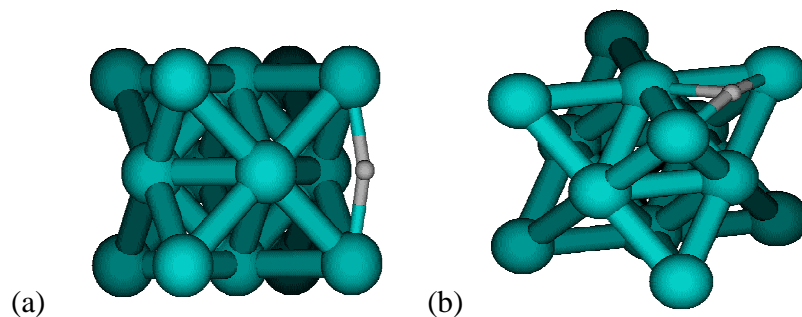


Fig.69. Example of the adsorption sites of hydrogen at cubic-Co surface: (a) – bridge site, (b) – 3-fold site.

The literature gives some evidences that on the greater part of transition metal surface the hydrogen atoms prefer sites with a high local coordination [255]. Molecular hydrogen does not have a permanent dipole moment, but it possesses a large quadrupole moment and polarizability. Hence, when it approaches a charged site it can bind to that site through ion-quadrupole and ion-induced dipole interactions [202]. At the cobalt surface with 2-fold symmetry the sites with the highest coordination were found to be 3-fold coordinated [245]. The 3-fold site is the most stable binding site for hydrogen. Similar feature was observed in the work of Jiang and Carter [256], who characterized the atomic hydrogen adsorption on Fr (110) surface and found that the 3-fold site is the only one stable minimum, while the bridge sites are the transition states for H diffusion. For the high index plane (211) of Fe surface it was shown that hydrogen is adsorbed at the 3-fold coordinated site [257]. The presented results confirm these observations, however they also clearly indicate that the adsorption site is determined not only by the plane hkl coordinates, but also by the chosen multiplicity and functional used during the calculation.

IV.4.3. Hexagonal closed-packed structure

Similar calculations have been done for the Co-hexagonal system, for which the chosen cobalt surfaces included (101), (110), (011) and (100) planes. Table 11 represents the collected results of calculated energies, adsorption energies and determined hydrogen adsorption sites. The considered multiplicities for Co-hexagonal cluster were 19 in the case of B3LYP and PBE functional and 21, when the calculations were run with the CAM-B3LYP functional. Considering the adsorption energy of Co-hexagonal cluster it can be seen that E_{ads} is again more negative for the case of adsorbed cationic hydrogen for all the considered cobalt-hexagonal surfaces.

Table 11. The calculation results for the different planes of Co-hexagonal system.

System	Calculation method	Multiplicity	E Hartree	Eads kcal/mol	Adsorption site
H	B3LYP		-0.49891		
	CAM-B3LYP		-0.49534		
	PBE		-0.49588		
H ⁺			0.0		
<i>(100) plane</i>					
Co ₈	B3LYP	19	-1160.51663		
	CAM-B3LYP	21	-1159.87489		
	PBE	19	-1160.46143		
Co ₈ +H	B3LYP	18	-1161.12365	-67.8	} bridge
		20	-1161.11354	-61.5	
	CAM-B3LYP	20	-1160.49398	-77.7	
		22	-1160.43686	-41.8	
	PBE	18	-1161.08837	-82.2	
		20	-1161.07793	-75.7	
Co ₈ +H ⁺	B3LYP	19	-1160.91404	-249.4	} bridge
	CAM-B3LYP	21	-1160.26545	-245.1	
	PBE	19	-1160.87657	-260.5	
<i>(110) plane</i>					
Co ₈	B3LYP	19	-1160.43719		
	CAM-B3LYP	21	-1159.61668		
	PBE	19	-1160.35790		
Co ₈ +H	B3LYP	18	-1161.02377	-55.0	} bridge
		20	-1161.01839	-51.6	
	CAM-B3LYP	20	-1160.32819	-135.6	
		22	-1160.26738	-97.5	
	PBE	18	-1160.94156	-55.1	
		20	-1160.96920	-72.4	
Co ₈ +H ⁺	B3LYP	19	-1160.83288	-248.3	} bridge
	CAM-B3LYP	21	-1160.18177	-354.6	
	PBE	19	-1160.74528	-243.1	
<i>(101) plane</i>					
Co ₈	B3LYP	19	-1160.50511		
	CAM-B3LYP	21	-1159.87911		
	PBE	19	-1160.47886		
Co ₈ +H	B3LYP	18	-1160.12200	-74.0	} bridge
		20	-1160.11366	-68.8	
	CAM-B3LYP	20	-1160.40716	-20.5	
		22	-1160.43803	-39.9	
	PBE	18	-1160.08178	-67.2	
		20	-1160.08001	-66.1	
Co ₈ +H ⁺	B3LYP	19	-1160.91301	-256.0	} bridge
	CAM-B3LYP	21	-1160.26387	-241.4	
	PBE	19	-1160.87024	-245.6	
<i>(011) plane</i>					
Co ₈	B3LYP	19	-1160.49094		
	CAM-B3LYP	21	-1159.87313		
	PBE	19	-1160.45798		
Co ₈ +H	B3LYP	18	-1161.10590	-72.8	} bridge
		20	-1161.10220	-70.5	
	CAM-B3LYP	20	-1160.48723	-74.5	
		22	-1160.43100	-39.2	
	PBE	18	-1161.05760	-65.1	
		20	-1161.05753	-65.0	
Co ₈ +H ⁺	B3LYP	19	-1160.90024	-256.8	} bridge
	CAM-B3LYP	21	-1160.26484	-245.8	
	PBE	19	-1160.85742	-250.6	

Table 11 derives also some tendencies, but less clear than those for the Co-cubic system. For the atomic hydrogen adsorption, the obtained most stable site is different for each functional: the (101) and (011) planes for B3LYP (adsorption energy of -74.0 and -72.8 kcal/mol, respectively), the (110) plane for CAM-B3LYP (adsorption energy of -135.6 kcal/mol) and the (100) plane for PBE (adsorption energy of -82.2 kcal/mol). The tendency for the less stable site leads to the (110) plane (B3LYP and PBE with the adsorption energy of -51.6 and -55.1 kcal/mol, respectively) and the (101) plane (CAM-B3LYP with the adsorption of -20.5 kcal/mol). For the adsorption of hydrogen ion, the same most stable sites for each functional as those for the atomic hydrogen were obtained: the (101) and (011) planes for B3LYP (adsorption energy of -256.0 and -256.8 kcal/mol, respectively), the (110) plane for CAM-B3LYP (adsorption energy of -354.6 kcal/mol) and the (100) plane for PBE (adsorption energy of -260.5 kcal/mol). As for the less stable site, two sites in B3LYP are determined: the (100) and (110) planes (adsorption energy of -249.4 and -248.3 kcal/mol, respectively), and one site for both, CAM-B3LYP and PBE, which is (101) plane with the adsorption energy of -241.4 and -245.6 kcal/mol, respectively. The last observation is related to the preferential adsorption site. In all the cobalt-hexagonal surface cases and for both types of hydrogen there is only one type of adsorption site determined as a bridge site.

IV.5. Structure formation determined by hydrogen evolution reaction

IV.5.1. Effect of pH

In the Chapter II the XRD analyses of electrodeposited cobalt films, according to the pH variation as well as effect of an external magnetic field are presented. This section is focused on the explanation of phase formation of cobalt deposits observed in Chapter II, by involving the quantum calculations of hydrogen adsorption described above. Figure 70 shows the X-ray diffraction patterns of cobalt films grown under different pH values. Considering the phase composition of cobalt film deposited at low pH (2.7), only one diffraction peak is detected and assigned to the presence of mixed hcp(110)+fcc(220) phases.

In general, cobalt is stabilized in a hexagonal centered-packed phase, but depending on the deposition conditions it is possible to form biphasic films. It has been reported [82] that the growth of Co-fcc phase in a solution with a low pH value is due to the formation of cobalt hydride, which is metastable and facilitated by adsorption and incorporation of atomic hydrogen. Based on this statement as well as according to the calculated E_{ads} (Table 10 and Table 11) it can be assumed that the intensive growth of mixed hcp(110)+fcc(220) peak could be related with higher volume fraction of fcc phase than hcp.

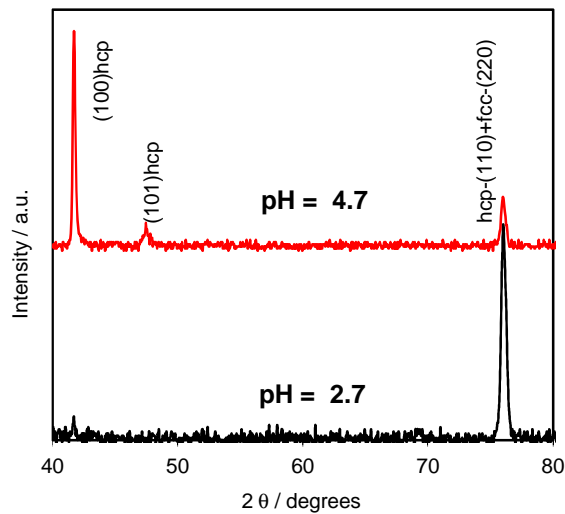


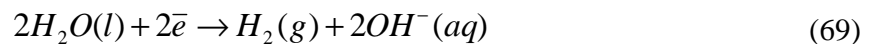
Fig.70. X-ray diffraction patterns of the electrodeposited Co films at different bath pH.

According to the E_{ads} , the fcc-(220) phase is more favourable to create a stable bond with hydrogen. Thus, more metastable cobalt hydrides are formed giving strong signal of the presence of fcc phase in the XRD patterns. On the other hand, the adsorbed hydrogen can suppress slightly the growth of cobalt crystallites in the direction of fcc-(220), allowing at the same time for the privileged growth of hcp-(110) phase, which adsorbs the hydrogen with less stable bonding than that of fcc-(220). The evidence for the presence of fcc phase as a majority in the cobalt film deposited at low pH is also given by the fine-grained morphology already presented in our previous work [258]. Raising the pH value up to 4.7 the X-ray diffraction pattern indicates a change in the phase composition of cobalt film. The growth of biphasic diffraction peak observed at pH 2.7 is less intensive at higher pH value. The additional hcp peaks of (100) and (101) planes at lower 2θ angles are observed.

The modification of phase composition of cobalt formed at higher pH level can be related to the presence of cobalt hydroxides, which slow down the growth rate of biphasic diffraction peak and as a result favour the growth of other hexagonal phases of cobalt. Thus, a higher precipitation of Co-hexagonal phase is observed. This causes a rotation of the hexagonal crystallites of cobalt around the c-axis from (110) to energetically more stable (100), what in consequence gives re-orientation of the film. After an occupation of all the active sites by hydrogen at (100) surface it will begin to occupy the active sites of (101) surface. To confirm this theory by the E_{ads} of hydroxides at the cobalt surfaces, further quantum calculation are currently provided and will be the subject of future work.

IV.5.2. Effect of magnetic field

As it has been discussed before and also reported in many previous publications [125,215,259-260], a superimposed magnetic field during the electrodeposition process from aqueous solutions can affect the hydrogen evolution reaction and thus, the hydrogen adsorption process at the electrode surface. In the process carried out under superimposed magnetic field, the MHD convection can enhance the ionic mass transfer rate of hydrogen toward the cathode surface. However, the competition between deposition rates of hydrogen and deposited metals can be observed. Ebadi et al. [125] studied the electrodeposition process of Ni-Co alloys under magnetic field. They have shown that the deposition of the alloy is much enhanced compared to the hydrogen evolution reaction. In mildly acidic solutions, the HER can arise from the following reactions:



Due to the Lorentz force that is efficient on the solution in the vicinity of the electrode, the HER is increasing with magnetic field, but not as much as the increase of metals on the electrode surface because the concentration of hydrogen ion is much smaller than metallic ion concentrations. These deliberations may help in the explanation of the differences between the X-ray diffraction patterns of Co films deposited without (Fig.70) and with an applied magnetic field (Fig.71). Comparing Fig.70 and Fig.71 it can be seen that the phase composition of cobalt films

is not changed when electrodepositing under magnetic field. Similar observation was reported in the work of Koza *et al.* [216]. However, a superimposition of magnetic field affects the peaks intensity in the case of pH 4.7. The intensity of diffraction peaks at this high pH varies, when the magnetic field of 1T is applied. These modifications are due to the change of hydrogen evolution and cobalt rates caused by an accelerated mass transport in the electrolyte, which is due to the additional convection introduced by B-field. A lower hydrogen evolution rate and higher that of cobalt ions causes that the active sites of electrode surface are faster occupied by the metal than by the hydrogen. Thus, the growth of other cobalt planes is possible, as it can be seen in the cobalt film deposited at low pH, where additional growth of (100)-hcp peak is observed (Fig.71).

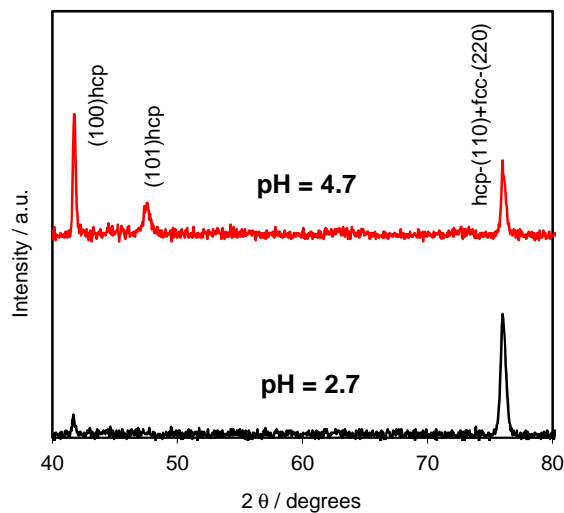


Fig.71. X-ray diffraction patterns of the electrodeposited Co films under 1T magnetic field.

In this case, hydrogen will look for the most stable active sites at the electrode surface, free for adsorption. Following Nakahara *et al.* [35], the rate of atomic hydrogen incorporation might be proportional to the hydrogen evolution rate. Thus, under magnetic field conditions the high rate of hydrogen incorporation could form a metastable cobalt hydride, which might facilitate the growth of Co-cubic structure. This suggests that the magnetic field acts on the phase formation in the same way as a low pH level.

IV.6. Conclusion

The DFT calculations were performed to examine the adsorption energy of atomic and cationic hydrogen on various low index Co surfaces: cubic – (100), (110), (111) and hexagonal - (100), (110), (101), (011), as well as high index cubic-(220) surface. The preferential adsorption sites were also determined. At all of the flat surfaces of cobalt, DFT calculations show that the hydrogen is preferentially bonded to the most coordinated sites, which in this study is a bridge site. However, the adsorption site of hydrogen is determined by the cluster size, which can result in different adsorption sites as in the case of Co-cubic, where the 3-fold site was also observed. Depending on the surface orientation, adsorption site and calculation method the adsorption energies of atomic as well as cationic hydrogen varies slightly. Among all the calculated cobalt surfaces for both, fcc and hcp phases the adsorption energies show tendencies for more and less favoured planes to be adsorbed, depending on the chosen functional. Considering the fcc phase, the most stable bond between cobalt and hydrogen is formed at the surfaces of: (220) for atomic hydrogen and (220) + (111) for ionic hydrogen. As the less stable surfaces in both, cationic and ionic hydrogen cases are (100) and (110). According to the hcp phase, the most stable bonding between cobalt and atomic and ionic hydrogen is created at (101), (011), (110) and (100) surfaces. Consequently, the less stable are (110) and (101) for atomic hydrogen and (100), (110) and (101) for ionic hydrogen.

The DFT study of hydrogen adsorption helped to distinguish the phase formation of cobalt film grown at low pH level (2.7), where biphasic film was obtained. The calculation of E_{ads} has shown that the hydrogen is favoured to create a stable bond with (220) surface of cubic-Co, what in turn allows forming the cobalt hydrides. Thus, it can be estimated that the volume fraction of fcc phase in the cobalt deposits is higher than that of hcp phase. At the same time, the growth in the fcc-(220) direction is suppressed and growth of other planes of cobalt is observed, such as hcp-(110). In the case of high pH (4.7), the phase formation is dependent on the formation and adsorption of hydroxides at the cobalt surfaces, rather than single hydrogen. To confirm this observation, further quantum calculations are required. It has been shown as well, that an applied external magnetic field affects the mass transport in the electrolyte, by providing an additional convection. Hence, the deposition rates of metal and hydrogen are influenced by a B-field, modifying only the intensities of diffraction peaks.

General conclusion

The presented work is focused on the experimental and theoretical studies of the electrodeposition mechanism of Co-based films, including single Co, binary Co-Ni, Co-Cu and ternary Co-Ni-Cu alloy films. The modeling and structure-properties relationship by a multi-scale approach was investigated.

The preliminary study involves determination and optimization of the electrodeposition parameters in order to obtain nanocrystalline films with satisfied surface quality and promising magnetic properties. It is shown that the electrolytic pH, to-be-deposited type of substrate and deposition time are of high importance in the fabrication of nanoscale materials. Among them, the electrolytic pH is the one, which has the greatest effect on structure formation. The considered pH values included two levels, referring to low (2.7), and high (4.7) pH. It is shown that both structural features: phase composition and surface morphology of Co and Co-Ni films are strongly influenced by the electrolyte pH. In both cases, the electrodeposited films are consisted of two crystallographic structures of cobalt: hexagonal closed-packed (hcp) and face centered-cubic (fcc). The differences observed in the phase composition and surface morphology, according to the pH level are explained by the hydrogen evolution reaction and adsorbed intermediate species, such as cobalt and nickel hydroxides at the cathode surface.

During the electrodeposition of Co and Co-Ni films on Ti substrate, most of the films were characterized by rough surface. Thus, in order to eliminate this undesired effect a thin glass substrate covered by indium tin oxide and reinforced by Ni seed-layer has been chosen. The microstructural investigations show that the substrate type affects the phase composition of Co and Co-Ni deposits. Electrodeposited Co and Co-Ni films on Ti are characterized as biphasic, hcp and fcc. The Co film deposited on Ni/ITO possesses only the hcp structure, while in the case of Co-Ni film the predominant phase is fcc. The phase composition differences are confirmed by the examination of surface morphology, which indicates the film crystallites in the form assigned to each crystallographic structure of Co. Furthermore, the surface quality has been improved and more homogeneous, less rough films were obtained. Moreover, the morphological characteristic show that decreasing deposition time brings about reduction in the crystallites size. The deposition time has an effect on the early stages of electrodeposition. Thus, at shorter times the nucleation process is dominated, resulting in the nanocrystallite films.

The film growth as well as its quality can be strongly affected by a superimposition of an external magnetic field. The electrodeposition process was carried out under parallel to the electrode surface magnetic fields, with magnets strength up to 12T. The results reveal that the induced forced convection in the electrolyte changes the hydrodynamic conditions and thus, affects the structure and morphology of the obtained films. No significant effects of the magnetic field on the phase composition are observed. Nevertheless, the relative intensity of X-ray diffraction peaks is affected by the magnetic field electrodeposition conditions. Thus, the secondary effects of magnetic field, as for example, on the pH value in the vicinity of the electrode surface are responsible for the structural modifications. A superimposed magnetic field affects the crystallites size and layer roughness significantly, resulting in more homogeneous surface. The result is clearly induced by the MHD stirring of the electrolyte, which reduces the thickness of diffusion layer and in turn improves a mass transport toward the electrode surface. Due to the stirring effect, the MHD convection improves the electrode coverage by removing the gas bubbles sticking to the electrode surface and as a consequence, more homogeneous Co-based films are obtained. Furthermore, the results reveal the anomalous co-deposition process of Co-Ni films, characterized by higher amount of Co in the film than in the electrolytic solution. The anomalous deposition behaviour is slightly affected by the magnetic field. In the mass-controlled region of Co-Cu and Co-Ni-Cu deposition, the deposited mass of Cu increases with increasing magnetic field.

The effect of an external magnetic field on the electrochemical kinetics and dynamics of electrodeposition process of Co, Co-Ni and Co-Cu films is also investigated. It is shown that the kinetics-dynamics-structure relationship is basically determined by the adsorption behaviour of co-deposited hydrogen and other intermediates species, such as metal hydroxides. Considering the electrochemical kinetic behaviour, the investigations are based on the chronoamperometric study, where the current-time transient of Co is investigated and nucleation mode is determined. The result shows that the behaviour of nucleation is relatively close to the instantaneous mechanism, but with a non-negligible deviation from the theoretical model. This is explained in terms of hydrogen reduction. The differences observed in the current-time transients of electrodeposited Co and Co-Ni films are due to the change of hydrodynamic conditions in the electrolyte under magnetic field superimposition. From the electrochemical dynamic investigations of Co-Cu system it is shown that a homogenous magnetic field does not practically modify the charge-transfer parameters of the process. The weak effects observed in the presence

of magnetic field are only due to the change of the electrode area during the metallic electrodeposition and to the effect of MHD convection.

The magnetic annealing treatment of electrodeposited Co/Ni/ITO, Co-Ni/ITO and Co-Cu/Cu/ITO films, respectively, in dependence on microstructure is investigated. Furthermore, the magnetic properties of mentioned and additional Co-Ni-Cu/Cu/ITO films are also determined. It is shown that the crystallographical structure of as-deposited films is improved by annealing treatment. Moreover, it is preserved under superimposed magnetic field during process. The annealing processing induces intermixing between seed (Ni, Cu) and secondary layers deposited on ITO substrate, which is enhanced under magnetic conditions. Hence, the magnetic properties of as-deposited samples are strongly affected. Interestingly, an in-plane magnetic anisotropy was always obtained, which origin is seen in a preferential same-like atoms couples formation in the magnetic field annealing direction. A superimposed magnetic field affects the magnetic properties of as-deposited Co-Cu/Cu/ITO and Co-Ni-Cu/Cu/ITO films. The magnetic measurements reveal that magnetic properties of the films depend on the film composition, mainly on the amount of non-magnetic Cu component, which varies under magnetic field conditions. Thus, the morphological and structural changes are observed, which increase the surface/volume ratio and enhance the shape anisotropy.

The DFT calculations were performed to examine the adsorption energy of atomic and cationic hydrogen on various low index Co surfaces: cubic – (100), (110), (111) and hexagonal - (100), (110), (101), (011), as well as high index cubic-(220) surface. The preferential adsorption sites are also determined. At all of the flat surfaces of cobalt, DFT calculations show that the hydrogen is preferentially bonded to the most coordinated sites, which in this study is a bridge site. However, the adsorption site of hydrogen is determined by the cluster size, which can result in different adsorption sites as in the case of Co-cubic, where the 3-fold site is also observed. Depending on the surface orientation, adsorption site and calculation method the adsorption energies of atomic as well as cationic hydrogen varies slightly. Among all the calculated cobalt surfaces for both, fcc and hcp phases the adsorption energies show tendencies for more and less favoured planes to be adsorbed, depending on the chosen functional. The DFT study of hydrogen adsorption helps to distinguish the phase formation of cobalt film grown at low pH level (2.7), where biphasic film is obtained. The calculation of E_{ads} shows that the hydrogen is favoured to create a stable bond with (220) surface of cubic-Co, what in turn allows forming the cobalt hydrides. Thus, it can be estimated that the volume fraction of fcc phase in the cobalt deposits is

higher than that of hcp phase. At the same time, the growth of fcc-(220) orientation is suppressed and growth of other planes of cobalt, such as hcp-(110) is observed. In the case of high pH (4.7), the phase formation is dependent on the formation and adsorption of hydroxides at the cobalt surfaces, rather than single hydrogen. To confirm this observation, further quantum calculations are required. It is shown as well, that an applied external magnetic field affects the mass transport in the electrolyte, by providing an additional convection. Hence, the deposition rates of metal and hydrogen are influenced by a magnetic field, modifying only the intensities of diffraction peaks.

The present work is a novel approach in understanding the experimental results by introduction of the theoretical studies. It gives a new way and possibility to combine theory with practice and opens discussion on the relation of these two domains in order to achieve deeper comprehension of the studied electrochemical systems.

Annex

I. Magnetohydrodynamic (MHD) effect

The effect of a magnetic field on electrochemical processes is usually observed through the magnetohydrodynamic effect, which origin lies in the Lorentz force. For conventional MHD effects, the theoretical and experimental examinations have been often performed by means of the magnetic fields directed parallel to the electrode surface, since the Lorentz force becomes the largest, when a magnetic field is applied vertically to the electrolytic current.

The MHD effect was studied by Aogaki *et al.* [261,262] and the magneto-hydrodynamic electrode (MHDE) was used for the analysis of electrochemical reaction in a magnetic field (Fig.1).

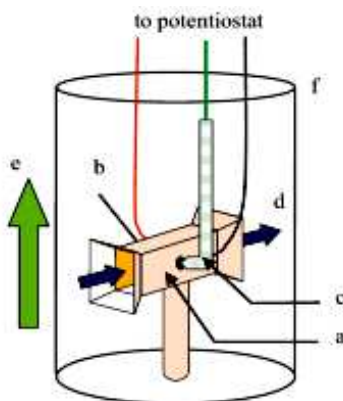


Fig.1. MHD electrode: a-working electrode, b-counter electrode, c-Luggin capillary, d-MHD flow, e-magnetic flux density, f-vessel (Aogaki [262]).

The MHD electrode was composed of a rectangular channel with two open ends. On the inner walls of channel, a pair of electrodes (working and counter), each with the same area was placed face to face and electrolytic current flows between them. The electrode potential of working electrode was regulated by a reference electrode inserted from behind through a Luggin capillary. Magnetic field was applied vertically to the current, in parallel orientation to the electrode surface, so that Lorentz force was generated along the channel, and as shown in Fig.1., the solution inside the channel started to move along the electrodes. Momentum balance of the induced fluid motion is expressed by the following Navier-Stokes equation:

$$\frac{\partial \bar{u}}{\partial t} + (\bar{u} \cdot \nabla) \bar{u} = -\frac{1}{\rho} \nabla P + \nu \nabla^2 \bar{u} + \frac{1}{\rho} \bar{i} \times \bar{B} \quad (1)$$

where \bar{u} is the velocity, P is the pressure, ρ is the density and ν is the kinematic viscosity. The solution flow under the MHD effect is called the MHD flow, which is self-organized through an autocatalytic process between fluid motion and mass transfer. To see the process comprehensively, first consider the electrolytic current flowing by the mass transfer of active species. Mass balance of active ionic species in the presence of a large amount of supporting electrolyte is expressed by:

$$\frac{\partial C}{\partial t} + (\bar{u} \cdot \nabla) C = D \nabla^2 C \quad (2)$$

Current density at the electrode is, from Fick's law, the y-component vertical to the electrode, which is given as:

$$i = z_m F D \left(\frac{\partial C}{\partial y} \right)_{y=0} \quad (3)$$

where z_m is the charge number, F is the Faraday constant, D is the diffusion constant and C is the concentration of active species. Therefore, by the Lorentz force per unit volume i_B , the solution, according to Eq.(1), starts to flow in the velocity u along the electrode, where B is the z-component of the magnetic flux density and u is the x-component of the velocity. On the other hand, the flowing solution enhances the mass transfer, so that the concentration of active species changes according to Eq.(2). The concentration gradient $(\partial C / \partial y)_{y=0}$ together with the velocity u also increases. As a result, the current density i in Eq.(3) again increases. All these processes are cycled until the steady state is achieved. In the case, where the channel height and the velocity are large, the flow mode becomes inviscid, so that the average current density is given by:

$$\bar{i} = H^* (C_s - C_w)^{4/3} B^{1/3} \quad (4)$$

where

$$H^* = 0.753 (z_m F D)^{4/3} (\nu / D)^{4/9} \nu^{-2/3} \rho^{-1/3} \gamma^{1/3} (\sqrt{x_2} - \sqrt{x_1})^{4/3} (x_2 - x_1)^{-4/3} \quad (5)$$

and C_s and C_w are bulk and surface concentrations, respectively. x_1 and x_2 are the x-coordinates of both ends of the electrode, γ is the cell constant. When the channel height and the velocity are small, the solution flows in viscous mode, and the average current density is:

$$\bar{i} = K^* (C_s - C_w)^{3/2} B^{1/2} \quad (6)$$

where

$$K^* = 0.504(z_m F)^{3/2} Dh^{1/2} (\eta l)^{-1/2} \quad (7)$$

h is the channel height, η the viscosity and l the electrode length.

The MHD flow moves in quite a different mode from the fluid motion driven by mechanical force. For example, in the rotating disk electrode the solution velocity is one-sidedly determined by external mechanical force, whereas the velocity of MHD flow is controlled in close relation to the electrode reactions. In the vicinity of the electrode MHD flows contain minute vortex structures called “micro-MHD flows”, which are a kind of non-equilibrium fluctuation of MHD flows. Therefore, the micro-MHD flows can interact with other non-equilibrium fluctuations such as concentration fluctuation, so that electrode reactions receive specific effects called the micro-MHD effects from micro-MHD flows. The most important point is that although micro-MHD flows affect the mass transfer of active species, the mass transport process is not always promoted, but sometimes suppressed. If the reaction contains some autocatalytic process of non-equilibrium fluctuations, such fluctuations are often suppressed by the micro-MHD flows, and the total reaction rate decreases as well as the characteristic morphologies emerge on the deposited surface, where regular patterns composed of micro-holes called “the micro-mystery circles”, are formed [263,264].

1.1. MHD in electrochemical processing

The largest effect of the Lorentz force and consequently the largest MHD effect are achieved with magnetic fields parallelly oriented to the electrode surface (i.e., when the external magnetic field is oriented perpendicularly to the direction of the ion flux). During the electrolysis under parallel fields, the Lorentz force induces conductive flow of the electrolyte close to electrode surface. A magnetically stimulated convection leads to a decrease in the thickness of the diffusion layer, thus the diffusion-limited current is increased. This will lead to a decrease in the degree of diffusion control of the electrodeposition process, because the current density at a fixed value of overpotential η , and then, the activation part of deposition overpotential required for the charge transfer η_a should be larger in the presence than in the absence of an effect of

magnetic field. If the applied overpotential remains the same, the remaining overpotential η_{diff} must decrease.

As a rule, it was adopted that the limiting diffusion current density depends on magnetic field, as $i_L \propto B^{1/3}$. According to the equations

$$\eta = \frac{b_c}{2.3} \ln \frac{i}{i_0} + \frac{b_c}{2.3} \ln \frac{1}{1 - (i/i_L)} \quad (8)$$

$$\eta_{diff} = \frac{b_c}{2.3} \ln \frac{1}{1 - (i/i_L)} \quad (9)$$

where b_c is the cathodic Tafel slope and i_0 and i_L are the exchange and the limiting current densities respectively, increasing the limiting current density leads to a decrease of the degree of diffusion control of the deposition process, and then the electrodeposition process occurs at some overpotential, which is effectively lower. This overpotential at which a metal electrodeposition occurs, when the exchange in the hydrodynamic conditions is caused by the effect of an imposed magnetic field represents the effective overpotential of electrodes process. Based on the results obtained by Sudibyo *et al.* [265], who studied the magnetic field effect on Co electrodeposition at room temperature the limiting current increases proportionately to the magnitude of magnetic strength. The increment of limiting current indicated the increasing of mass transport on electrodeposition process. This increment of limiting current can be linked to the presence of MHD effect. The convective flow will create mixing in the diffusion area and reduce the thickness of its Nernst diffusion layer in front of the electrode effectively. As the Nernst diffusion layer decrease, the limiting current density will increase. The change in the magnetic field strength leads to the variation of limiting current, but the value of diffusion coefficient is unchanged.

1.2. Nucleation determined by the electrochemical fluctuations

Nucleation is classified into two types: 2D nucleation, expanding lateral growth and 3D nucleation, protruding vertical growth. According to the work of Aogaki *et al.* [261], these two types of nucleation come from different non-equilibrium fluctuations (Fig.2.). One is the asymmetrical fluctuation (Fig.2.a), which arises from electrochemical reactions in an electrical double layer. As it is shown in the figure, this fluctuation one-sidedly changes from an

electrostatic-equilibrium state toward a cathodic reaction side controlling 2D nucleation. The other one (Fig.2.b) is the symmetrical fluctuation changing around an average value of its physical quantity in a diffusion layer. This fluctuation controls 3D nucleation. The symmetrical fluctuation suppresses the 3D nucleation of order of $0.1 \mu\text{m}$ to yield a flat surface (the 1st micro-MHD effect). After a long-term deposition in the same magnetic field conditions, instead of leveling, semi-spherical secondary nodules with the order of $10\text{-}100 \mu\text{m}$ in diameters are self-organized from 2D nuclei with the other non-equilibrium, asymmetrical fluctuations (the 2nd micro-MHD effect) [263].

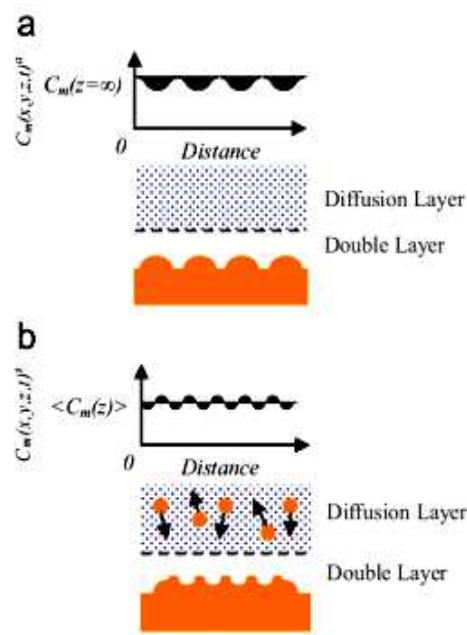


Fig.2. Non-equilibrium fluctuations in electrodeposition: a - asymmetrical concentration fluctuation, b - symmetrical concentration fluctuations, (Aogaki [261]).

At early stage of electrodeposition in the absence of magnetic field (Fig.3.), there are two different kinds of unstable processes of fluctuations.

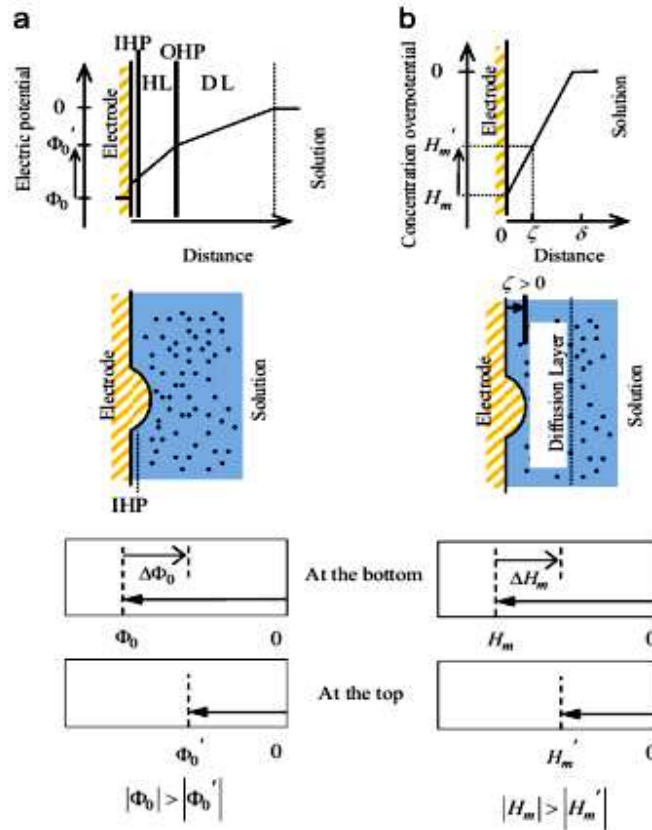


Fig.3. Schematic figures of the instability of 2D and 3D nucleation in the early stage of electrodeposition in the absence of magnetic field: a – 2D nucleation in electric double layer, b – 3D nucleation in diffusion layer, (Aogaki [261]).

The first one takes place in an electrical double layer (Fig.3.a). In the case of electrodeposition without any specific adsorption of anion, the potential in a diffuse layer of the double layer becomes positive. Supposing that a minute 2D nucleus is accidentally formed in the diffuse layer, at the top of nucleus, its negative overpotential decreases with the nucleation, so that with the unstable growth of the fluctuation the 2D nucleus is self-organized. As the reaction proceeds, outside the double layer, a diffusion layer yielded (Fig.3.b). In electrodeposition, since the concentration gradient is positive, the top of a 3D nucleus contacts with higher concentration than other parts. This means that the concentration overpotential decreases at the top of nucleus. As a result, mass transfer is enhanced there, the symmetrical concentration fluctuation turns unstable and the 3D nucleus is self-organized. In a parallel magnetic field the symmetrical concentration fluctuation is interfered by the micro-MHD flows, so that the 3D nucleation always has a tendency for suppression. However, after long-term deposition, since the rate-determining step to control 2D nucleation changes from the electron transfer process concerning the double-layer

overpotential to the mass transfer process concerning the concentration overpotential, the decrease of the concentration overpotential at a 2D nucleus triggers instability. The total of the double-layer overpotential and the concentration overpotential is kept constant, so that on the contrary of the initial deposition mentioned above, the increase of the double-layer overpotential decreases the rate-controlling concentration overpotential inducing new instability that in turn newly generates larger micro-MHD flows by the Lorentz force through the increase of the fluctuation of electrolytic current. This type of instability actually occurs under proton adsorption. In the secondary nodule formation (the 2nd micro-MHD effect), due to such mechanism, it has been found that the flow mode of the solution changes from a laminar MHD flow to a convective micro-MHD flow induced by the unstable concentration fluctuations, so that the diffusion layer thickness slowly decreases with time increasing electrolytic current. As a result, the mass transfer to 2D nuclei is enhanced and the secondary nodules are self-organized [266].

1.3. Early stages of electrodeposition and MHD

Matsushima et al. [267] studied the magnetic field effect on the initial stages of electrodeposition of different metals. Along them, they noted in the case of Cu deposition that the limiting current density was increased. Because they excluded presence of macroscopic MHD convection by the Lorentz force, the observed enhancement was explained by the fact that, in the vicinity of deposits surface, the current density vector has a component parallel to the deposit plane and it is not locally parallel to the magnetic field, as it is shown in Fig.4.

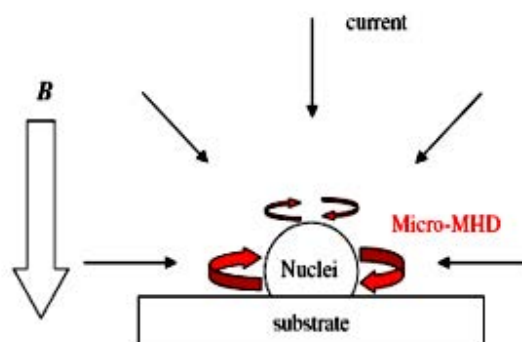


Fig.4. Schematic illustration of the micro-MHD convection flow; (Matsushima et al. [267]).

Such local distortion of the electric field produces a microscopic vortex convection that is called micro-MHD. Therefore, the ionic mass transfer in the B-field could be enhanced by the attending localized stirring effect. Moreover, from the current density plots, which can be straightforwardly interpreted in terms of nucleation rate, was the time to current density peak corresponding to a given overvoltage. This quantity was increased in the presence of magnetic field and this effect obviously hints at a depression of the nucleation rate. Furthermore, the peak current was apparently reduced in the magnetic field. These two pieces of evidence suggest that nucleation or deposition rate tends to be inhibited in the magnetic field. One possible explanation of the current-inhibiting effects of a magnetic field, highlighted in this research work, would be that the MHD effect influences the transient formation from a three-dimensional to a two-dimensional diffusion field, unless the magnetic field changes the nucleation rate. It is well known, that a 3D diffusion field is formed around nuclei within a short moment [268]. Then, the fields overlap each other to build a 2D diffusion field, where the current flow decreases due to the smaller flux area compared to a 3D field. That is, their results would phenomenologically suggest that a 2D diffusion field would be formed faster in the magnetic field. Another explanation could be that the surface diffusion at the ad-atoms towards the cluster is affected by the magnetic field. As the ad-atoms bear a charge they would be subjected to a Lorentz force. As a first approximation, the movement of the ad-atoms could be described as two-dimensional cyclotronic trajectories around the clusters, giving rise to a spiraling ad-atom flux around the nucleus. As a net result the residence time of the ad-atoms on the crystal plane onto which a nucleus is formed would be higher and the crystal growth would thus be inhibited. Since the high-overpotential region, a higher surface concentration of ad-atoms exists; this inhibiting effect of the magnetic field is expected to be less marked. An alternative explanation might be that the cluster energy is affected by the magnetic field. This would be an effect that is proportional to the volume of the cluster and to magnetic field [269].

II. Electrochemical stationary techniques

II.1. Chronoamperometry

In this technique, the electrode potential is abruptly changed from E1 (the electrode is usually in the equilibrium state at this potential) to E2 and the resulting current variation is recorded as a function of time. The interpretation of the results is typically based on a planar

electrode in a stagnant solution and an extremely fast interfacial redox reaction as compared to mass transfer.

Chronoamperometry has been widely used to characterize the kinetic behavior of insertion materials. The typical assumption for the analysis of the chronoamperometric curve (or current transient) of insertion materials is that the diffusion of the active species governs the rate of the whole insertion process. This means the following: the interfacial charge-transfer reaction is so kinetically fast that the equilibrium concentration of the active species is quickly reached at the electrode surface at the moment of potential stepping. The instantaneous depletion (or accumulation) of the concentration of active species at the surface caused by the chemical diffusion away from the surface to the bulk electrode (or to the interface away from the bulk electrode) is completely compensated by the supply from the electrolyte (or release into the electrolyte). This is referred to hereafter as the potentiostatic boundary condition. The interface between the electrode and current collector is typically under the impermeable boundary condition where the atom cannot penetrate into the back of the electrode [270].

II.2. Voltammetry

Voltammetry is basically referred to techniques with the common characteristics that the potential of the working electrode is controlled and the resulting current flow is measured. One of the most general applications is linear-sweep voltammetry (LSV), where the potential is linearly scanned over time in either the negative or positive direction. Cyclic voltammetry is a set of LSV experiments in which anodic and cathodic scans are repeated alternately. That is, at the end of the first scan of LSV, the scan in the reverse direction is continued. This cycle can be repeated a number of times. The voltammogram gives information on the possible redox reactions of the system, including the Faradaic insertion and extraction reaction. Furthermore, the presence of a surface reaction and its reversibility during the atom insertion-extraction process can be successfully examined. The voltammetric response of the insertion electrode, similar to chronoamperometry, is analyzed by the diffusion-controlled model [270].

II..3. Electrochemical Impedance Spectroscopy

Electrochemical impedance theory is a well-developed branch of AC theory that describes the response of a circuit to an alternating current or voltage as a function of frequency. In DC theory, which is a special case of AC theory where the frequency equals 0 Hz, resistance is defined by Ohm's Law:

$$E = I \cdot R \quad (10)$$

Using Ohm's Law, it is possible to apply a DC potential (E) to a circuit, measure the resulting current (I), and compute the resistance (R), or determine any term of the Equation (10) if the other two are known. A resistor is the only element that impedes the flow of electrons in a DC circuit. In AC theory, where the frequency is non-zero, the analogous equation is:

$$E = I \cdot Z \quad (11)$$

As in Equation (10), E and I are here defined as potential and current, respectively. Z is defined as impedance, the AC equivalent of resistance. In addition to resistors, capacitors and inductors impede the flow of electrons in AC circuits.

In an electrochemical cell, slow electrode kinetics, slow preceding chemical reactions, and diffusion can all impede electron flow, and can be considered analogous to the resistors, capacitors, and inductors that impede the flow of electrons in an AC circuit. Figure 5 shows typical plot of a voltage sine wave (E) applied across a given circuit and the resultant AC current waveform (Eq. (10)).

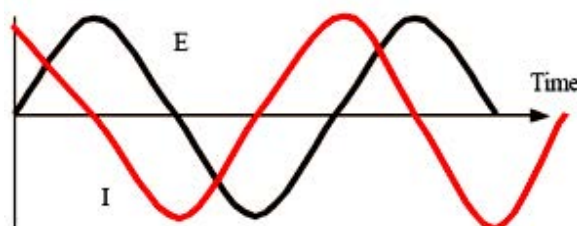


Fig.5. AC Waveforms for an applied potential and a resulting current [266].

The two traces are different not only in amplitude, but are also shifted in time. When a sinusoidal potential excitation (Eq.(12)) is applied to the electrode/solution interface, cause an out of phase current response with respect to the applied sinusoidal (Eq.(13))

$$E_{(t)} = E_0 \sin(\omega \cdot t) \quad (12)$$

$$I_{(t)} = I_0 \sin(\omega t + \varphi) \quad (13)$$

Where $E_{(t)}$ and $I_{(t)}$ are instantaneous potential and current, respectively; E_0 and I_0 are rest potential and current, respectively; ω is a frequency, t is a time and φ is a phase shift. In the case of a purely resistive network, the two waveforms would not be shifted. They would be exactly in phase, differing only in amplitude.

It is possible to study an equivalent circuit by deriving its impedance equation expressed as a real part $Z'(\omega)$ and an imaginary part $Z''(\omega)$ (Eq.(14)). However, it is simpler to perform a measurement on the circuit and analyze the resulting plot. As a result a good picture of the real and imaginary impedance components and of the phase shift characteristics as a function of frequency is obtained.

$$Z_{(\omega)} = \frac{I_0 \sin(\omega t + \varphi)}{E_0 \sin(\omega t)} = Z'_{(\omega)} + iZ''_{(\omega)} \quad (14)$$

The Randles cell (Fig.6) models the electrochemical impedance of an interface and fits many chemical systems. It is easy to equate the circuit components in the Randles with familiar physical phenomena, such as adsorption or film formation.

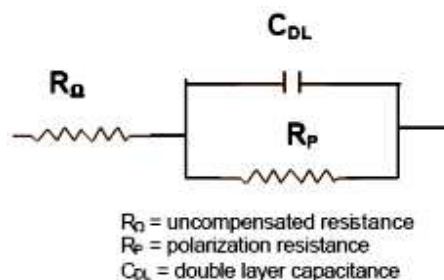


Fig.6. Equivalent circuit for a single electrochemical cell [271].

R_{Ω} is the ohmic or uncompensated resistance of the solution between the working and reference electrodes. R_p is the polarization resistance or charge-transfer resistance at the electrode/solution interface. C_{DL} is the double layer capacitance at this interface. If the polarization or charge-transfer resistance is known, it is possible to calculate the electrochemical reaction rates. Double-

layer capacitance measurements can provide information of adsorption and desorption phenomena.

The plot in Figure 7 illustrates the expected response of the simple circuit in Fig.6. This is the Nyquist plot which is one of the most popular format for evaluating electrochemical impedance data.

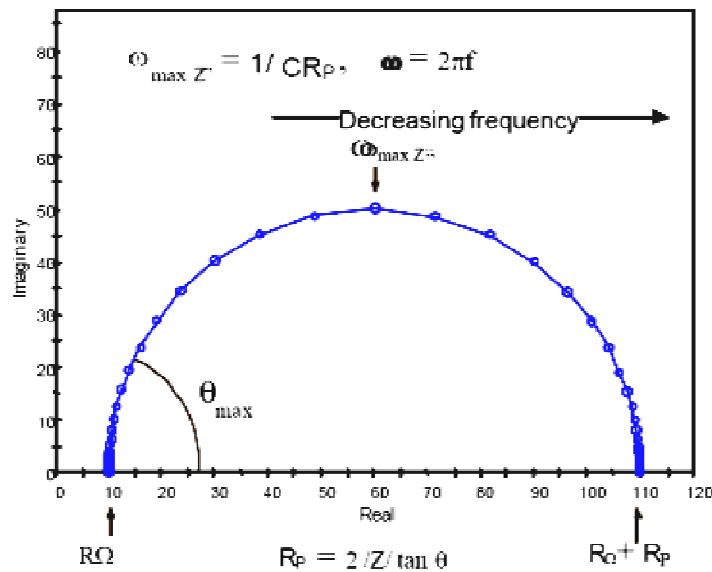


Fig.7. Nyquist plot for a simple electrochemical system [271].

The Nyquist plot has several advantages. The primary one is that the plot format makes it easy to see the effects of the ohmic resistance. If we will take a data at sufficiently high frequencies, it is easy to extrapolate the semicircle toward the left, down to the x axis to read the ohmic resistance. The shape of the curve does not change when the ohmic resistance changes. Consequently, it is possible to compare the results of two separate experiments that differ only in the position of the reference electrode. Another advantage of this plot is that it emphasizes circuit components that are in series, such as $R\Omega$. However, the Nyquist plot format also has some disadvantages. For example, frequency does not appear explicitly. Secondly, although the ohmic resistance and polarization resistance can be easily read directly from the Nyquist plot, the electrode capacitance can be calculated only after the frequency information is known. As shown in Fig.7, the frequency corresponding to the top of the semicircle, $\omega(\theta = max)$ can be used to calculate the capacitance if R_p is known.

III. Surface characterization techniques

III.1. X-ray Diffraction (XRD)

X-ray Diffraction is a powerful non-destructive technique for characterizing crystalline materials. While most other analytical techniques provide elemental or molecular information from a sample, XRD is unique in providing a wide variety of information on structures, crystalline phases, preferred crystal orientations (texture), and other structural parameters, such as crystallite size, percent crystallinity, strain, stress and crystal defects.

In XRD analysis a sample is illuminated by a collimated X-ray beam of specific known wavelength. If the material is crystalline, it possesses a three dimensional ordering or structure with repeat units of atomic arrangement (unit cells). X-rays are diffracted by the repeating lattice spacings of crystalline materials, whereas X-rays are simply scattered by amorphous materials. X-ray diffraction occurs at specific angles (2θ) with respect to the lattice spacings defined by Bragg's Law:

$$n\lambda = 2d \sin \theta \quad (15)$$

where n is an integer denoting the order of the reflection, λ is the x-ray wavelength, d is the lattice spacing of the crystal planes of interest, and θ is the diffraction angle (Fig.8). Bragg's Law is satisfied, when the pathlength difference of the X-rays (indicated in green) is equal to $n\lambda$. The diffraction angle θ is half the angle between the incident and diffracted X-rays.

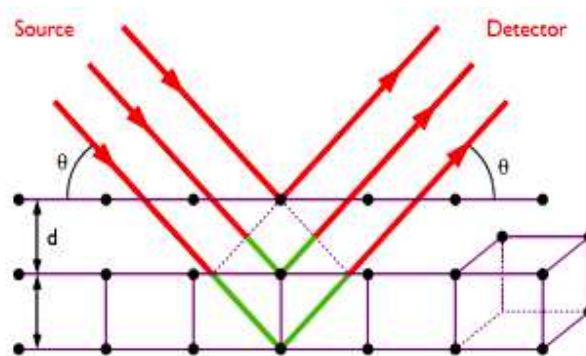


Fig.8. Schematic representation of X-rays diffraction in a crystalline material [267].

Any change of difference in lattice spacing results in a corresponding shift in the diffraction lines. Consequently, the X-ray diffraction pattern is the fingerprint of periodic atomic arrangements in a

given material. Diffraction patterns can be checked against large libraries of patterns from known materials in order to identify/quantify the phases present in a sample.

A Bruker D8 Advance X-ray Diffractometer (Fig.9.a) with CuK_α radiation has been employed to obtain XRD patterns using standard Bragg-Brentano (θ - 2θ) geometry (Fig.9.b). In the Bragg-Brentano geometry the X-ray source (X-ray tube focus) and the detector are always situated on the same circle. The samples surface is tangential to the center of the circle and touches the geometrical diffractometer axis. At the same time the flat sample surface is always tangential to the focusing circle which contains the X-ray focus and the receiving slits of the detector. The focusing conditions will be fulfilled exactly when the X-ray source, the detector and the sample source are situated on the same circle. If the sample has a flat surface, the surface must be tangential to the focusing circle and its normal vector must be bisect the angle between direction to the source and the detector. The condition is the main distinction of the Bragg-Brentano method.

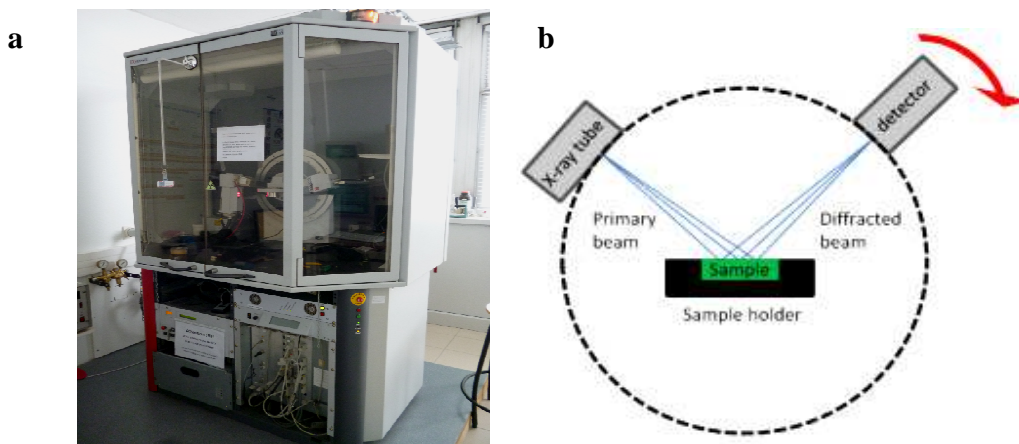


Fig.9. X-ray diffractometer used for the structural analysis (a) with a classical Bragg-Brentano reflection geometry (b) [272].

III.2. Scanning Electron Microscope (SEM)

The scanning electron microscope uses a focused beam of high-energy electrons to generate a variety of signals at the surface of solid specimens. A beam of electrons is produced at the top of the microscope by an electron gun. The electron beam travels through electromagnetic fields and lenses, which focus the beam down toward the sample. The signals that derive from

electron-sample interaction reveal information about the sample including external morphology (texture), chemical composition, and crystalline structure and orientation of materials making up the sample. Once the beam hits the sample, electrons and X-rays are ejected from the sample. Detectors collect these X-rays, backscattered electrons and secondary electrons and convert them into a signal that is sent to a screen. A two-dimensional image is generated that displays spatial variations in these properties. The SEM is also capable of performing analyses of selected point locations on the sample. This approach is especially useful in qualitatively or semi-qualitatively determining chemical composition, crystalline structure, and crystal orientations.

In the present work the coating's morphology has been investigated by the use of scanning electron microscopes of following types: JOEL JEM-2010 ARP, FE-SEM SUPRA 35 and JOEL JSM 6460LA coupled with EDS JEL 1300 microprobe.

III.3. Energy-Dispersive X-ray Spectroscopy (EDS)

Interaction of an electron beam with a sample target produces a variety of emissions, including X-rays. An energy-dispersive detector is used to separate the characteristic X-rays of different elements into an energy spectrum, and EDS system software is used to analyze the energy spectrum in order to determine the abundance of specific elements. EDS can be used to find the chemical composition of materials down to a spot size of a few microns, and to create elements composition maps over a much broader raster area. Together, these capabilities provide fundamental compositional information for a wide variety of materials.

EDS systems are typically integrated into an SEM instrument. EDS system includes a sensitive X-ray detector, a liquid nitrogen dewar for cooling, and software to collect and analyze energy spectra. The detector is mounted in the sample chamber of the main instrument at the end of a long arm, which itself cooled by liquid nitrogen. An EDS detector contains a crystal that absorbs the energy of incoming X-rays by ionization, yielding free electrons in the crystal that become conductive and produce an electrical charge bias. The X-ray absorption thus converts the energy of individual x-rays into electrical voltages of proportional size. The electrical pulses correspond to the characteristic X-rays of the element.

III.4. Wavelength Dispersive X-ray Fluorescence (WD-XRF)

WD-XRF is one of two generated types of X-ray fluorescence instrumentation used for elemental analysis applications. In WDXRF spectrometers, all of the elements in the sample are excited simultaneously. The different energies of the characteristic radiation emitted from the sample are diffracted into different directions by an analyzing crystal or monochromator (similar to the action of a prism dispersing different colors of visible light into different directions). By placing the detector at a certain angle, the intensity of X-rays with a certain wavelength can be measured. Sequential spectrometers use a moving detector on a goniometer to move it through an angular range to measure the intensities of many different wavelengths. Simultaneous spectrometers are equipped with a set of fixed detection systems, where each system measures the radiation of a specific element. The principle advantages of WD-XRF systems are high resolution (typically 5 – 20 eV) and minimal spectral overlaps.

III.5. X-ray Photoelectron Spectroscopy (XPS)

XPS is the most widely used surface analysis technique because of its relative simplicity in use and data interpretation. It is a quantitative spectroscopic technique that measures the element composition, empirical formula, chemical state and electronic state of the elements that exist within a material. The analysis principle of XPS is quite simple. The sample is irradiated with mono-energetic X-rays, causing photoelectrons to be emitted from the sample surface. An electron energy analyzer determines the binding energy of the photoelectrons. XPS requires ultra-high vacuum conditions. However, it can be used to analyze the surface chemistry of materials in their initial state, or after some treatments, such as annealing, cutting, etc..

III.6. Atomic Force Microscopy (AFM)

The atomic force microscopy belongs to a family of techniques dedicated to nanoscale surface characterization. The AFM provides a three-dimensional profile of the surface, by measuring forces between a sharp probe (tip) and surface at very short distance (0.2 – 10 nm). The probe is supported on a flexible cantilever. The AFM tip touches the surface and records the small force between the probe and the surface. The obtained topography image corresponds to the

measured height values $z(x,y)$ for a given area A , defined by a window scan size L . Each height value is associated to a pair of surface coordinates (x,y) , and the image is described by a matrix with N lines and M columns which corresponds to the surface (x,y) points being the matrix elements the height $z(x,y)$. The dominant interactions at short probe-sample distances are Van der Waals interactions.

III.7. Magnetic Force Microscopy (MFM)

Magnetic force microscopy is a family of techniques used to measure magnetic fields using an AFM. It employs a magnetic tip, which is brought close to a sample and interacts with the magnetic stray fields near the surface. The strength of the local magnetostatic interaction determines the vertical motion of the tip as it scans across the sample. The MFM technique uses a magnetically coated sharp tip attached to a flexible cantilever. The tip is placed close to the sample surface (5-100 nm) and interacts with the stray field emanating from the sample. The image is formed by scanning the tip laterally with respect to the sample and measuring the force (or force gradient) as a function of position. An image taken with a magnetic tip contains information about both the topography and the magnetic properties of a surface.

MFM is a non-contact technique, and both static and dynamic operating modes can be applied. The static mode detects the magnetic force acting on the tip, whereas the dynamic mode measures the force derivative acting on the tip. The force derivative can originate from a wide range of sources, including electrostatic probe-sample interactions, van der Waals forces, damping, or capillary forces. However, MFM relies on those forces that arise from a long-range magnetostatic coupling between probe and sample. This coupling depends on the internal magnetic structure of the probe, which greatly complicates the mechanism of contrast formation.

Magnetic force microscopy is able to investigate with high resolution magnetic domain structure, reading and recording information in magnetic media, magnetization reversal processes etc.

III.8. Vibrating Sample Magnetometer (VSM)

The vibrating sample magnetometer has become a widely used instrument for determining magnetic properties of a large variety of materials: diamagnetics, paramagnetics,

ferromagnetics, ferromagnetics and antiferromagnetics. It operates on Faraday's Law of Induction, which tells that a changing magnetic field will produce an electric field. This electric field can be measured and can give information about the changing magnetic field.

In principle, if a sample of any material is placed in a uniform magnetic field, created between the poles of an electromagnet, a dipole moment will be induced. If the sample vibrates with sinusoidal motion a sinusoidal electrical signal can be induced in suitable placed pick-up coils. The signal has the same frequency of vibration and its amplitude will be proportional to the magnetic moment, amplitude, and relative position with respect to the pick-up coils system. The induced voltage in the pickup coil is proportional to the sample's magnetic moment, but does not depend on the strength of the applied magnetic field. In a typical setup, the induced voltage is measured through the use of a lock-in amplifier using the piezoelectric signal as its reference signal. By measuring in the field of an external electromagnet, it is possible to obtain the hysteresis curve of a material.

III.9. Alternating Field Gradient Magnetometer (AFGM)

The AGMF determines the magnetic moment of a sample by measuring the force exerted on a magnetic dipole by a magnetic field gradient. The force is measured by mounting the sample on a piezoelectric biomorph, which creates a voltage proportional to the elastic deformation and, hence, to the force acting on the sample. By driving an alternating voltage and by tuning the frequency of the field gradient to the mechanical resonance of the sample mounted on the piezoelectric element by a glass capillary, a very high sensitivity can be achieved.

The main advantage of the AFGM is its relative immunity to external magnetic noise and the resulting high signal-to-noise ratio and short measuring time.

List of References

- [1] Jiang S.P., Chen Y.Z., You J.K., Chen T.X., Tseung A.C.C., *J. Electrochem. Soc.* 137 (1990) 3374.
- [2] Jiang S.P., Tseung A.C.C., *J. Electrochem. Soc.* 137 (11) (1990) 3387.
- [3] Jeffrey M.I., Choo W.L., Breuer P.L., *Miner. Eng.* 13 (2000) 1231.
- [4] Pradhan N., Subbaiah T., Das S.C., *J. Appl. Electrochem.* 27 (1997) 713.
- [5] Cui C.Q., Jiang S.P., Tseung A.C.C., *J. Electrochem. Soc.* 137 (1990) 3418.
- [6] Vazques-Arenas J., Pritzker M., *J. Electrochem. Soc.* 157 (2010) D283.
- [7] Zech N., Podlaha E.J., Landolt D., *J. Electrochem. Soc.* 146 (1999) 2892.
- [8] Matlosz M., *J. Electrochem. Soc.* 140 (1993) 2272.
- [9] Epelboin I., Jousselein M., Wiart R., *J. Electroanal. Chem.* 119 (1981) 61.
- [10] Epelboin I., Jousselein M., Wiart R., *J. Electroanal. Chem.* 157 (1983) 75.
- [11] Wiart R., *Electrochim. Acta* 35 (1990) 1587.
- [12] Sasaki K.Y., Talbot J.B., *J. Electrochem. Soc.* 140 (1993) 669.
- [13] Cheng C.C., West A.C., *J. Electrochem. Soc.* 140 (1997) 3050.
- [14] Vazquez-Arenas J., Pritzker M.D., *Electrochim. Acta* 55 (2010) 8376.
- [15] Matsushima J.T., Trivinho-Strixino F., Pereira E.C., *Electrochim. Acta* 51 (2006) 1960.
- [16] Campbell F.C., Ed., *Elements of Metallurgy and Engineering Alloys*, ASM International, 2008.
- [17] Vincenzo A., Cavallotti P.L., *Electrochim. Acta* 49 (2004) 4079.
- [18] Krause A., Uhlemann M., Gebert A., Schultz L., *Thin Solid Films* 515 (2006) 1694.
- [19] Cerisier M., Attenborough K., Jedryka E., Wojcik M., Nadolski S., Van Haesendonck, Celis J.P., *J. Appl. Phys.* 89 (2001) 7083.
- [20] Eagleton T.S., Farr J.P.G., *Trans. IMF* 80 (2002) 9.
- [21] Dille J., Charlier J., Winand R., *J. Mater. Sci.* 32 (1997) 2637.
- [22] Cohen-Hyams T., Kaplan W.D., Yahalom J., *Electrochem. Solid State Lett.* 5 (2002) C75.
- [23] Cadorna L., Cavallotti P., *Electrochim. Metall.* 1 (1966) 364.
- [24] Pangarov N.A., Vitkova S.D., *Electrochim. Acta* 11 (1966) 1733.
- [25] Pangarov N.A., *J. Electroanal. Chem.* 9 (1965) 70.
- [26] Sard R., Schwartz C.D., Weil R., *J. Electrochem. Soc.* 113 (1966) 424.
- [27] Breckpot R., *An. R. Soc. Esp. Fis. Quim.* 61B (1965) 51.
- [28] Armyanov S., Vitkova S.D., *Surf. Technol.* 7 (1978) 319.
- [29] Finch G.I., Wilman H., Yang L., *Disc. Faraday Soc.* 1 (1947) 144.
- [30] Croll I.M., May B.A., in: *Electrodeposition Technology Theory and Practice*, ECS Proc. 87-17, Romankiw L.T., Turner D.R. (Eds.), ECS Pub., Pennington, New Jersey, 1987.

- [31] Froment M., Maurin G., C.R. Acad. Sci. Paris 266C (1968) 1017.
- [32] Nakano H., Nakahara K., Kawano S., Oue S., Akiyama T., Fukushima H., J. Appl. Electrochem. 32 (2002) 43.
- [33] Scoyer J., Winand R., Surf. Technol. 5 (1977) 169.
- [34] Reddy A.K.N., J. Electroanal. Chem. 6 (1963) 141.
- [35] Nakahara S., Mahajan S., J. Electrochem. Soc. 127 (1980) 283.
- [36] Gaigher H.L., Van Der Berg N.G., Electrochim. Acta 21 (1976) 45.
- [37] Cavallotti P.L., Galbiati E., Chen T., in: Electroplating Engineering and Waste Recycle, Snyder D.D., Landau U., Sard R. (Eds.), ECS Pub., Pennington, New Jersey, 1983.
- [38] Cavallotti P.L., Caironi G., Surf. Technol. 7 (1978) 1.
- [39] Chen T., Cavallotti P.L., Appl. Phys. Lett. 41 (1982) 205.
- [40] Chen T., Cavallotti P.L., IEEE Trans. Magn. 18 (1982) 1125.
- [41] Cojocar P., Magagnin L., Gomez E., Valles E., J. Alloys Compd. 503 (2010) 454.
- [42] Bahadormanesh B., Dolati A., J. Alloy Compd. 504 (2010) 518.
- [43] Zhao F., Franz S., Vincenzo A., Cavallotti P.L., Sansotera M., Navarrini W., Electrochim. Acta 56 (2011) 9644.
- [44] Karaagac O., Alper M., Kockar H., J. Magn. Magn. Mat. 322 (2010) 1098.
- [45] Qiu R., Zhang D., Wang P., Zhang X.L., Kang Y.S., Electrochim. Acta 58 (2011) 699.
- [46] Gomez E., Ramirez J., Valles E., J. Appl. Electrochem. 28 (1998) 71.
- [47] Mentar L., Ionics 18 (1-2) (2012) 223.
- [48] Tian L., Xu J., Xiao S., Vacuum 86 (2011) 27.
- [49] Orinakova R., Orinak A., Vering G., Talian I., Smith R.M., Arlinghaus H.F., Thin Solid Films 516 (2008) 3045.
- [50] Alper M., Kockar H., Safak M., Celalettin Baykul M., J. Alloys Com. 453 (2008) 15.
- [51] Mizushima I., Chikazawa M., Watanabe T., J. Electrochem. Soc. 143 (1996) 1978.
- [52] Fenineche N., Coddet C., Saida A., Surf. Coat. Technol. 41 (1990) 75.
- [53] Alper M., Schwarzacher W., Lane S.J., J. Electrochem. Soc. 144 (1997) 2346.
- [54] Nabiyouni G., Schwarzacher W., J. Magn. Magn. Mat. 156 (1996) 355.
- [55] Bergenstorf Nielsen C., Horsewell A., Ostergard M.J.L., J. Appl. Electrochem. 27 (1997) 839.
- [56] Chan K.C., Chan W.K., Qu N.S., J. Mater. Process. Technol. 89-90 (1999) 447.
- [57] Santos J.S., Matos R., Trivinho-Strixino F., Pereira E.C., Electrochim. Acta 53 (2007) 644.
- [58] Elsherief A.E., J. App. Electrochem. 33 (2003) 43.
- [59] Sivasubramanian R., Sangaranarayanan M.V., Mat. Chem. Physics 103 (2012) 448.
- [60] Ergeneman O., Sivaraman K.M., Pane S., Pellicer E., Teleki A., Hirt A.M., Baro M.D., Nelson B.J., Electrochim. Acta 56 (2011) 1399.

- [61] Riemer S., Gong J., Sun M., Tabakovic I., *J. Electrochem. Soc.* 159 (2009) D439.
- [62] Brankovic S.R., Haislmaier R., Vasiljevic N., *Electrochem. Solid State Lett.* 10 (2007) D67.
- [63] George J., Bae S.-E., Litvinov D., Rancheler J., Brankovic S.R., *J. Electrochem. Soc.* 155 (2008) D589.
- [64] Bakonyi I., Peter L., *Prog. Mat. Sci.* 55 (2010) 107.
- [65] Tripathy B.C., Singh P., Muir D.M., *Metall. Trans. B* 32 (2001) 395.
- [66] Zech N., Landolt D., *Electrochim. Acta* 45 (2000) 3461.
- [67] Hoare J.P., *J. Electrochem. Soc.* 133 (1986) 2491.
- [68] Tilak B.V., Gendron A.S., Mosoiu M.A., *J. Appl. Electrochem.* 7 (1977) 495.
- [69] Ji J., Cooper W.C., Dreisinger D.B., Peters E., *J. Appl. Electrochem.* 25 (1995) 642.
- [70] Yin K.M., Lin B.T., *Surf. Coat. Technol.* 78 (1996) 205.
- [71] Abyaneh M.Y., Hashemi-pour M., *Trans. Inst. Met. Finish.* 72 (1993) 23.
- [72] Horkans J., *J. Electrochem. Soc.* 126 (1979) 1861.
- [73] Vazquez-Arenas J., Altamirano-Garcia L., Treeratanaphitak, Pritzker M., Luna-Sanchez R., Cabrera-Sierra R., *Electrochim. Acta* 65 (2012) 234.
- [74] Osaka T., Sawaguchi T., Mizutani F., Yokoshima T., Takai M., Okinaks Y., *J. Electrochem. Soc.* 146 (9) (1999) 3295.
- [75] Lallemand F., Ricq L., Wery M., Bercot P., Pagetti J., *Surf. Coat. Technol.* 179 (2004) 314.
- [76] Haider S.Z., Malik K.M.A., Ahmed K.J., Hess H., Riffel H., Hursthouse M.B., *Inorg. Chim. Acta* 72 (1983) 21.
- [77] Manhabosco T.M., Muller I.L. *Surf. Coat. Technol.* 202 (2008) 3585.
- [78] Li Y., Jiang H., Wang D., Ge H., *Surf. Coat. Technol.* 202 (2002) 4952.
- [79] Ghosh S.K., Bera T., Saxena C., Bhattacharya S., Dey G.K., *J. Alloys Compd.* 475 (2009) 676.
- [80] Brankovic S.R., Kagajwala B., George J., Majkic G., Stafford G., Ruchhoeft P., *Electrochim. Acta.* 83 (2012) 387.
- [81] Golodnitsky D., Rosenberg Y.U., Ulus A., *Electrochim. Acta* 47 (2002) 2707.
- [82] Sasaki K.Y., Talbot J.B., *J. Electrochem. Soc.* 147 (2000) 189.
- [83] Armyanov S., *Electrochim. Acta* 45 (2000) 3323.
- [84] Krause T., Arulnayagam L., Pritzker M., *J. Electrochem. Soc.* 144 (1997) 960.
- [85] Yin K.-M., *J. Electrochem. Soc.* 144 (1997) 1560.
- [86] Dahms H., Croll I.M., *J. Electrochem. Soc.* 112 (1965) 771.
- [87] Gomez E., Valles E., *J. Electroanal. Chem.* 421(1997) 157.
- [88] Fabri Miranda F.J., Barcia O.E., Diaz S.L., Mattos O.R., Wiart R., *Electrochim. Acta* 41 (1996) 1041.
- [89] Brenner A., *Electrodeposition of Alloys*, vol. 1-2, Academic Press, Inc, NY, 1963.

- [90] Golodnitsky D., Gaudin N.V., Volyanuk G.A., *J. Electrochem. Soc.* 147 (11) (2000) 4156.
- [91] Sasaki K.Y., Talbot J.B., *J. Electrochem. Soc.* 142 (3) (1995) 775.
- [92] Safranek W.H., *Properties of Electrodeposited Metals and Alloys*, New York, London, 1974, p. 206.
- [93] Zech N., Podlaha E.J., Landolt D., *J. Electrochem. Soc.* 146 (8) (1999) 2886.
- [94] Singh V.B., Singh V.N., *Plating Surf. Finish.* 63 (1976) 34.
- [95] Golodnitsky D., Gaudin N.V., Voluanuk G.A., *Plating Surf. Finishing* 2 (1998) 65.
- [96] Vagramyan A.T., Fatuera T.A., *J. Electrochem. Soc.* 110 (1963) 1030.
- [97] Gadad S., Harris T.M., *J. Electrochem. Soc.* 145 (11) (1998) 3699.
- [98] Goldbach S., De Kermadec R., Lapique F., *J. Appl. Electrochem.* 30 (2000) 277.
- [99] Tilak B.V., Genderon A.S., Mosoin M.A., *J. Appl. Electrochem.* 7 (1977) 495.
- [100] Bai A., Hu C.C., *Electrochim. Acta* 47 (2002) 3447.
- [101] Zech N., Podlaha E.J., Landolt D., *J. Electrochem. Soc.* 146 (1999) 2886.
- [102] Zech N., Podlaha E.J., Landolt D., *J. Electrochem. Soc.* 146 (1999) 2892.
- [103] Vazquez-Arenas J., Pritzker M., *Electrochem. Acta* 66 (2012) 139.
- [104] Lupi C., Dell'Era A., Pasquali M., Imperatori P., *Surf. Coat. Technol.* 205 (2011) 5394.
- [105] Dille J., Charlier J., Winard R., *J. Mat. Sci.* 321 (1997) 2637.
- [106] Newman R.C., *Proc. Phys. Soc. B* 69 (1956) 432.
- [107] Tochitskii T.A., Nemtserich L.V., *Russ. J. Electrochem.* 39 (2003) 301.
- [108] Peter L., Bakonyi I., *Electrodeposition and Properties of Nanoscale Magnetic/Non-magnetic Metallic Multilayer Films*, in: *Electrocrystallization in Nanotechnology*, G. Staikov (Eds), Wiley VCH.
- [109] Peter L., Kupay Z., Padar J., Cziraki A., Kerner Zs., Bakonyi I., *Electrochim. Acta* 49 (2004) 3613.
- [110] Huang Q., Podlaha E.J., *J. Electrochem. Soc.* 151 (2004) C119.
- [111] Fujimara Y., Enomoto H., *J. Electrochem. Soc.* 147 (2000) 1840.
- [112] Li D.Y., Szpunar J.A., *J. Mater. Sci.* 28 (1993) 5554.
- [113] Matsushima H., Fukunaka Y., Yasuda H., Kikuchi S., *IsIj Int.* 45 (2005) 1001.
- [114] Matsushima H., Bund A., Plieth W., Kikuchi S., Fukunaka F., *Electrochim. Acta* 53 (2007) 161.
- [115] Chouchane S., Levesque A., Douglade J., Rehemania R., Chopart J.-P., *Surf. Coat. Technol.* 201 (2007) 6212.
- [116] Tabakovic I., Riemer S., Vas'ko V., Sapozhnikov V., Kief M., *J. Electrochem. Soc.* 150 (2003) C635.
- [117] Koza J., Uhlemann M., Gebert A., Schultz L., *J. Solid State Electrochem.* 12 (2008) 181.
- [118] Msellak K., Chopart J.-P., Jbara O., Aaboubi O., Amblard J., *J. Magn. Magn. Mat.* 281 (2004)

295.

- [119] Uhlemann M., Krause A., Chopart J.-P., Gebert A., *J. Electrochem. Soc.* 152 (2005) C817.
- [120] Tabakovic I., Riemer S., Sun M., Vas'ko V.A., Kief M.T., *J. Electrochem. Soc.* 152 (2005) C851.
- [121] Ispas A., Matsushima H., Plieth W., Bund A., *Electrochim. Acta* 52 (2007) 2785.
- [122] Koza J., Uhlemann M., Geber A., Schultz L., *JOSSEC* 12 (2002) 181
- [123] Krause A., Uhlemann M., Gebert A., Schultz L., *Electrochim. Acta* 49 (2004) 4127.
- [124] Hinds G., Coey J.M.D., Lyons M.E.G., *Electrochem. Commun.* 3 (2001) 215.
- [125] Ebadi M., Basirun W.J., Alias Y., *J. Chem. Sci.*, 122 (2010) 279.
- [126] "Fundamentals of Magnetic Field Effects" in *Magneto-Science. Magnetic Field Effects on Materials: Fundamentals and Applications.*, M. Yamaguchi, Y. Tanimoto, Ed., Kodansha Springer, Japan, 2006.
- [127] Olivier A., Chopart J.-P., Amblard J., Merienne E., Aaboubi O., *ACH – Models Chem.* 137 (2000) 2.
- [128] Chopart J.-P., Devos O., Aaboubi O., Merienne E., Olivier A., in : *Proceedings of the 3rd International Conference on Transfer Phenomena in Magnetohydrodynamics and Electroconducting Flows*, Aussois, France, September 22-26, 1997, p. 63.
- [129] O'Brien R.N., Santhanam K.S.V., *J. Appl. Electrochem.* 27 (1997) 573.
- [130] O'Brien R.N., Santhanam K.S.V., *J. Appl. Electrochem.* 20 (1990) 427.
- [131] Waskaas M., Kharkats Y.I., *J. Phys. Chem. B* 103 (1999) 4976.
- [132] Waskaas M., *J. Phys. Chem.* 97 (1993) 6970.
- [133] Bund A., Kohler S., Kuhnlein H.H., Plieth W., *Electrochim. Acta* 49 (2003) 147.
- [134] Rabah K.L., Chopart J.-P., Schloerb H., Saulnier S., Aaboubi O., Uhlemann M., Elmi D., Amblard J., *J. Electroanal. Chem.* 571 (2004) 85.
- [135] Leventis N., Dass A., *J. Am. Chem. Soc.* 127 (2005) 4988.
- [136] Weier T., Eckert K., Muhlenhoff S., Cierpka C., Bund A., Uhlemann M., *Electrochem. Commun.* 9 (2007) 2497.
- [137] Coey J.M.D., Rhen F.M.F., Dunne P., McMurry S., *J. Solid State Electrochem.* 11 (2007) 711.
- [138] Tschulik K., Sueptitz R., Koza J., Uhlemann M., Mutschke G., Weier T., Gebert A., Schultz L., *Electrochim. Acta* 56 (2010) 297.
- [139] Tschulik K., Koza J.A., Uhlemann M., Gebert A., Schultz L., *Electrochem. Commun.* 11 (2009) 2241.
- [140] Tschulik K., Yang X., Mutschke G., Uhlemann M., Eckert K., Sueptitz R., Schultz L., Gebert A., *Electrochem. Commun.* 13 (2011) 946.
- [141] Mutschke G., Tschulik K., Weier T., Uhlemann M., Bund A., Frohlich J., *Electrochim. Acta* 55

(2010) 9060.

- [142] Sueptitz R., Koza J., Uhleman M., Gebert A., Schultz L., *Electrochim. Acta* 54 (2009) 2229.
- [143] Yu Y., Wei G., Hu X., Ge H., Yu Z., *Surf. Coat. Technol.* 204 (2010) 2669.
- [144] Grant K.M., Hemmert J.W., White H.S., *J. Electroanal. Chem.* 500 (2001) 95.
- [145] Pullins M.D., Grant K.M., White H.S., *J. Phys. Chem. B* 105 (2001) 8989.
- [146] Motoyama M., Fukunaka Y., Kikuchi S., *Electrochim. Acta* 51 (2005) 897.
- [147] Sugiyama A., Hashiride M., Morimoto R., Nagai Y., Aogaki R., *Electrochim. Acta* 49 (2004) 5115.
- [148] Krause A., Koza J., Ispas A., Uhlemann M., Gebert A., Bund A., *Electrochim. Acta* 52 (2007) 6338.
- [149] Bund A., Ispas A., *J. Electroanal. Chem.* 575 (2005) 221.
- [150] Coey J.M.D., Hinds G., *J. Alloys Compd.* 326 (2001) 238.
- [151] Fahidy T.Z., *Prog. Surf. Sci.* 68 (2001) 155.
- [152] Matsushima H., Fukunaka Y., Ito I., Bund A., Plieth W., *J. Electroanal. Chem.* 587 (2006) 93.
- [153] Matsushima H., Nohira T., Ito Y., *Electrochem. Solid State Lett.* 7 (2004) C81.
- [154] Matsushima H., Nohira T., Mogi I., Ito Y., *Surf. Coat. Technol.* 179 (2004) 245.
- [155] Koza J.A., Karnbach F., Uhlemann M., McCord J., Mickel Ch., Gebert A., Baunach S., Schultz L., *Electrochim. Acta* 55 (2010) 819.
- [156] Georgescu V., Baub M., *Surf. Sci.* 600 (2006) 4195.
- [157] Ganesh V., Vijayaraghavan D., Lakshminarayanan V., *App. Surf. Sci.* 240 (2005) 286.
- [158] Taniguchi T., Sassa K., Yamada T., Asai S., *Mater. Trans. JIM* 41 (2000) 981.
- [159] Devos O., Olivier A., Chopart J.-P., Aaboubi O., Maurin G., *J. Electrochem. Soc.* 145 (1998) 401.
- [160] Chiba A., Kitamura K., Ogawa T., *Surf. Coat. Technol.* 27 (1986) 83.
- [161] Aaboubi O., Chopart J.-P., Douglade J., Olivier A., Gabrielli C., Tribollet B., *J. Electrochem. Soc.* 137 (1990) 1796.
- [162] Krause A., Uhlemann M., Gebert A., Schultz L., *Thin Solid Films* 515 (2006) 1694.
- [163] Morimoto R., Sugiyama A., Aogaki R., *Electrochemistry* 72 (2004) 421.
- [164] Koehler S., Bund A., *J. Phys. Chem. B* 110 (2006) 1485.
- [165] O'Reilly C., Hinds G., Coey J.M.D., *J. Electrochem. Soc.* 148 (2001) C674.
- [166] Devos O., Aaboubi O., Chopart J.-P., Olivier A., Tribollet B., *J. Phys. Chem. A* 104 (2000) 1544.
- [167] Ispas A., Matsushima H., Bund A., Bozzini B., *J. Electroanal. Chem.* 629 (2009) 174.
- [168] Daltin A.-L., Bohr F., Chopart J.-P., *Electrochim. Acta* 54 (2009) 5813.
- [169] Daltin A.-L., Chopart J.-P., *Crystal Growth and Design*, 10 (2010) 2267.

- [170] Daltin A.-L., Addad A., Baudart P., Chopart J.-P., *Cryst. Eng. Comm.* 13 (2011) 3373.
- [171] Dini J.W., *Electrodeposition*, Noyes Publications, Park Ridge, NJ, 1993.
- [172] Nallet P., Chassaing E., Walls M.G., Hytch M.J., *J. Appl. Phys.* 79, (1996) 6884.
- [173] Sard R., Schwartz C.D., Weil R., *J. Electrochem. Soc.* 113, (1966) 424.
- [174] Bergenstorf Nielsen C., Horsewell A., Ostergard M.J.L., *J. Appl. Electrochem.* 27, (1997) 839.
- [175] Chan K.C., Chan W.K., Qu N.S., *J. Mater. Process. Technol.* 89-90, (1999) 447.
- [176] Osafo-Acquaah A., Foster D.G., Jorne J., *J. Electrochem. Soc.* 155, (2008) D270.
- [177] Diao Z., Dunne P.A., Zangari G., Coey J.M.D., *Electrochem. Commun.* 11 (2009) 740.
- [178] Matsushima H., Ispas A., Bund A., Plieth W., Fukunaka Y., *J. Solid State Electrochem.* 11, (2007) 737.
- [179] Scharifker B., Hills G., *Electrochim. Acta* 28 (1983) 879.
- [180] Palomar-Pardave M., Scharifker B.R., Arce E.M., Romero-Romo M., *Electrochim. Acta* 50, (2005) 4736.
- [181] Koza J.A., Uhlemann M., Gebert A., Schultz L., *Electrochim. Acta* 53 (2008) 5344.
- [182] Koza J.A., Mogi I., Tschulik K., Uhlemann M., Mickel Ch., Gebert A., Schultz L., *Electrochim. Acta* 55, (2010) 6533.
- [183] Grujicic D., Pesic B., *Electrochim. Acta* 49, (2004) 4719.
- [184] Karaagac O., Kockar H., Alper M., Hacıismailoglu M., *J. Magn. Magn. Mater.* 324, (2012) 3834.
- [185] Pantleon K., Somers M.A.J., *J. Appl. Phys.* 100, (2006) 114319.
- [186] Rafailovic L.D., Minic D.M., Karnthaler H.P., Wosik J., Trisovic T., Nauer G.E., *J. Electrochem. Soc.* 157 (2010) D295.
- [187] Fan C., Piron D.L., *Electrochim. Acta* 41, (1996) 1713.
- [188] Correia A.N., Machado S.A.S., *Electrochim. Acta* 45, (2000) 1733.
- [189] Karaagac O., Kockar H., Alper M., *IEEE Trans. Magn.* 46, (2010) 3973.
- [190] Alper M., Attenborough K., Baryshev V., Hart R., Lashmore D.S., Schwarzacher W., *J. Appl. Phys.* 75 (1994) 6543.
- [191] Lebbad N., Voiron J., Nguyen B., Chainet E., *Thin Solid Films* 275, (1994) 216.
- [192] Schindler W., Kirschner J., *Phys. Rev. B* 55, (1997) R1989.
- [193] Bacaltchuk C.M.B., Castello-Branco G.A., Ebrahimi M., Garmestani H., Rollett A.D., *Scr. Mater.* 48, (2003) 1343.
- [194] Sheikh-Ali A.D., Molodov D.A., Garmestani H., *Scr. Mater.* 46, (2002) 857.
- [195] Zhao Y., Li D., Wang Q., Franczak A., Levesque A., Chopart J.-P., He J., *Mat. Lett.* 106 (2013) 190.
- [196] Khan R.A., Bhatti A.S., *J. Magn. Magn. Mater.* 323, (2011) 340.

- [197] El Asri T., Raissi M., Vizzini S., Maachi A.E., Ameziane E.L., D'Avitaya F.A., Lazzari J.L., Coudreau C., Oughaddou H., Aufray B., Kaddouri A., *Appl. Surf. Sci.* 256, (2009) 2731.
- [198] Diandra L.L., Reuben D.R., *Chem. Mater.* 8, (1996) 1770.
- [199] An Z., Pan S., Zhang J., *J. Phys. Chem. C* 113, (2009) 1346.
- [200] Li D.S., Garmestani H., Yan S.-S., Elkawni M., Bacaltchuk M.B., Schneider–Muntau H.J., Liu J.P., Saha S., Barnard J.A., *J. Magn. Magn. Mat.* 281, (2004) 272.
- [201] Tian J., Xu J., Qiang Ch., *Appl. Surf. Sci.* 257, (2011) 4689.
- [202] Christmann K., *Surf. Sci. Rep.* 9 (1988) 1.
- [203] Somorjai G.A., *Introduction to Surface Chemistry and Catalysis*, Wiley, New York, 1994.
- [204] Anderson R.B., *The Fischer-Tropsch Synthesis*, Academic Press, Orlando FL, 1984.
- [205] Zakin M. R., Cox D.M., Whetten R.L., Trevor D.J., Kaldor A., *Chem. Phys. Lett.* 135 (1987) 223.
- [206] Liu F., Armentrout P.B., *J. Chem. Phys.* 122 (2005) 194320.
- [207] Geusic M.E., Morse M.D., Smalley R.E., *J. Chem. Phys.* 82 (1985) 590.
- [208] Vermeiren P., Leysen R., Vandenborre H., *Electrochim. Acta* 30 (1985) 1253.
- [209] Gabe D.R., *J. Appl. Electrochem.* 27 (1997) 908.
- [210] Gaigher H.L., Van der Berg N.G., *Electrochim. Acta* 21 (1976) 45.
- [211] Ursache A., Goldbach J.T., Russell T.P., Tuominen M.I., *J. Appl. Phys.* 97 (2005) 10J322.
- [212] Szeles C., Vertes A., *J. Phys. F. Met. Phys.* 17 (1987) 2031.
- [213] Eigeldinger J., Vogt H., *Electrochim. Acta* 45 (2000) 4449.
- [214] Ida T., Matsushima H., Fukunaka Y., *J. Electrochem. Soc.* 154 (2007) E112.
- [215] Diao Z., Dunne P.A., Zangari G., Coey J.M.D., *Electrochem. Commun.* 11 (2009) 740.
- [216] Koza J.A., Muhlenhoff S., Żabiński P., Nikrityuk P.A., Eckert K., Uhlemann M., Gebert A., Weier T., Schultz L., Odenbach S., *Electrochim. Acta* 56 (2011) 2665.
- [217] Koza J.A., Uhlemann M., Gebert A., Schultz L., *Electrochem. Commun.* 10 (2008) 1330.
- [218] Shinohara K., Hashimoto K., Aogaki R., *Electrochemistry* 70 (2002) 773.
- [219] Wassef O., Fahidy T.Z., *Electrochim. Acta* 21 (1976) 727.
- [220] Cierpka C., Weier T., Gerbeth G., Uhlemann M., Eckert K., *J. Solid State Electrochem.* 11 (2007) 687.
- [221] Vogt H., *Electrochim. Acta* 38 (1993) 1412.
- [222] Tacke R.A., Janssen L.J.J., *J. Appl. Electrochem.* 25 (1995) 1.
- [223] Koza J.A., Uhlemann M., Gebert A., Schultz L., *Electrochim. Acta* 53 (2008) 5344.
- [224] Thomas L.H., *Proc. Camb. Phil. Soc.* 23 (1927) 542.
- [225] Fermi E., *Z. Phys.* 48 (1928) 73.
- [226] Parr R.G., Yang W., *Density-Functional Theory of Atoms and Molecules*, Oxford University

Press, Oxford, 1989.

- [227] Finnis M., *Interatomic Forces in Condensed Matter*, Oxford University Press, Oxford, 2003.
- [228] Atkins P.W., Friedman R.S., *Molecular Quantum Mechanics*, 3rd edn. Oxford University Press, Oxford, 1997.
- [229] Kohn W., Sham L.S., *Phys. Rev.* 140(4A) (1965) A1133.
- [230] Kohn W., *Rev. Mod. Phys.* 71(5) (1999) 1253.
- [231] Kheun A., Singh D.J., Umrigar C.J., *Phys. Rev. B* 51 (1995) 4105.
- [232] Perdew J.P., Wang Y., *Phys. Rev. B* 33 (1986) 8800.
- [233] Perdew J.P., Chevary J.A., Vosko S.H., Jackson K.A., Pederson M.R., Singh D.J., Fiolhaus C., *Phys. Rev. B* 46 (1992) 6671.
- [234] Jensen F., *Introduction to Computational Chemistry*, Springer, Berlin, 1999.
- [235] Pozzo M., Alfe D., *Int. J. Hydrogen Energy* 34 (4) (2009) 1922.
- [236] Huo Ch.-F., Li Y.-W., Wang J., Jiao H., *J. Phys. Chem. B* 109 (2005) 14160.
- [237] Pasti I.A., Gavrilov N.M., Mentus S.V., *Adv. Phys. Chem.* doi:10.1155/2011/305634.
- [238] Weng M.H., Chen H.-T., Wang Y.-Ch., Ju S.-P., Chang J.-G., Lin M.C., *Langmuir* 28 (2012) 5596.
- [239] Zotwiak J.M., Bartholomew C.H., *J. Catal.* 83 (1983) 107.
- [240] Bridge M., Comrie C., Lambert R., *J. Catal.* 58 (1979) 28.
- [241] Klinke D.J., Broadbelt L.J., *Surf. Sci.* 429 (1999) 169.
- [242] Pacchioni G., Bagus P.S., Parmigiani F., *Cluster Models for Surface and Bulk Phenomena*, NATO ASI Series B, vol. 283, Plenum Press, New York, 1992.
- [243] Herman K., Bagus P.S., Nelin C.J., *Phys. Rev. B* 35, (1987) 9467.
- [244] Bernardo C.G.P.M., Gomes J.A.N.F., *J. Mol. Str. (Theochem)* 629, (2003) 251.
- [245] Ernst K.H., Schwarz E., Christmann K., *J. Chem. Phys.* 101, (1994) 5388.
- [246] Boudias C., Monceau D., *CaRIne Crystallography*, www.carine.crystallography.pagespro-orange.fr
- [247] Gaussian09, Revision A.02, M.J. Frisch, G.W. Trucks, H.B. Schlegel, G.E. Scuseria, M.A. Robb, J.R. Cheeseman, G. Scalmani, V. Barone, B. Mennucci, G.A. Petersson, H. Nakatsuji, M. Caricato, X. Li, H.P. Hratchian, A.F. Izmaylov, J. Bloino, G. Zheng, J.L. Sonnenberg, M. Hada, M. Ehara, K. Toyota, R. Fukuda, J. Hasegawa, M. Ishida, T. Nakajima, Y. Honda, O. Kitao, H. Nakai, T. Vreven, J.A. Montgomery, Jr., J.E. Peralta, F. Ogliaro, M. Bearpark, J.J. Heyd, E. Brothers, K.N. Kudin, V.N. Staroverov, R. Kobayashi, J. Normand, K. Raghavachari, A. Rendell, J.C. Burant, S.S. Iyengar, J. Tomasi, M. Cossi, N. Rega, J.M. Millam, M. Klene, J.E. Knox, J.B. Cross, V. Bakken, C. Adamo, J. Jaramillo, R. Gomperts, R.E. Stratmann, O. Yazyev, A.J. Austin, R. Cammi, C. Pomelli, J.W. Ochterski, R.L. Martin, K. Morokuma, V.G.

- Zakrzewski, G.A. Voth, P. Salvador, J.J. Dannenberg, S. Dannenberg, S. Dapprich, A.D. Daniels, O. Farkas, J.B. Foresman, J.V. Ortiz, J. Cioslowski, D.J. Fox, Gaussian, Inc., Wallingford CT, 2009; www.gaussian.com; www.surfsara.nl/systems/shared/software/gaussian
- [248] Hay P.J., Wadt W.R., *J. Chem. Phys.* 82, (1985) 270.
- [249] Becke A.D., *J. Chem. Phys.* 98, (1993) 5648.
- [250] Lee C., Yang W., Parr R.G., *Phys. Rev. B* 37, (1988) 785.
- [251] Yanai T., Tew D.P., Handy N.C., *Chem. Phys. Lett.* 393, (2004) 51.
- [252] Perdew J.P., Burke K., Ernzerhof M., *Phys. Rev. Lett.* 77, (1996) 3865.
- [253] Perdew J.P., Burke K., Ernzerhof M., *Phys. Rev. Lett.* 78, (1997) 1396.
- [254] Nilekar A.U., Greeley J., Mavrikakis M., *Angewandte Chemie – International Edition*, vol. 49, n. 42, (2006) 7046.
- [255] Haiping W., Xuemin W., Fangfang G., Mingjie Z., Weidong W., Tiecheng L., *Physica B* 405, (2010) 1792.
- [256] Jiang D.E., Carter E.A., *Surf. Sci.* 547, (2003) 85.
- [257] Muller K., *Prog. Surf. Sci.* 42, (1993) 245.
- [258] Franczak A., Levesque A., Bohr F., Douglade J., Chopart J.-P., *App. Surf. Sci.* 258, (2012) 8683.
- [259] Kohlmann F.J., *A Technological Handbook for Industry*, GLI International, A Hach Company Brand, (2003) 6.
- [260] Matsushima H., Ispas A., Bund A., Plieth W., Fukunaka Y., *J. Solid State Electrochem.* 11, (2007) 737.
- [261] Aogaki R., Morimoto R., Asanuma M., *J. Mag. Mat.* 322 (2010) 1664.
- [262] Aogaki R., *J. Chem. Phys.* 103 (1995) 8602.
- [263] Aogaki R., *Magnetohydrodynamics* 39 (2003) 453.
- [264] Aogaki R., Sugiyama A., in: *Proceedings of the Symposium on New Magneto-Science 2002*, Tsukuba-Japan, November 6-8, 2002, p. 136.
- [265] Sudibyo, Ismail A.B., Uzir H.H., Idris M.N., Aziz N., *J. Sci. Eng. Technol.* 2 (2009) 41.
- [266] Aogaki R., Morimoto R., Sugiyama A., *ECS Trans.* 13 (16) (2008) 15.
- [267] Matsushima H., Ispas A., Bund A., Bozzini B., *J. Electroanal. Chem.* 615 (2008) 191.
- [268] Milchev A., Zapryanova T., *Electrochim. Acta* 51 (2006) 2926.
- [269] Shapira Y., Bindilatti V., *J. Appl. Phys.* 92 (2002) 4155.
- [270] Pyun S.-I. et al., *Electrochemistry of Insertion Materials for Hydrogen and Lithium*, Monographs in Electrochemistry., Springer-Verlag, Berlin-Heidelberg 2012, doi: 10.1007/978-3-642-29464-8_2.
- [271] Basic of electrochemical impedance spectroscopy; Princeton Applied Research application note

AC-1; www.princetonappliedresearch.com/products/appnotes.cfm.

[272] Mitchell S., Perez-Ramirez J., *Surface Science and Methods in Catalysis.*, Advanced Catalysis Engineering Institute for Chemical and Bioengineering, ETH Zurich, Switzerland.